ACS SYMPOSIUM SERIES 1034

# Functional Polymer Nanocomposites for Energy Storage and Conversion

EDITED BY

Qing Wang and Lei Zhu

Downloaded by 89.163.35.42 on June 21, 2012 | http://pubs.acs.org
Publication Date (Web): March 11, 2010 | doi: 10.1021/bk-2010-1034.fw001

# Functional Polymer Nanocomposites for Energy Storage and Conversion

Downloaded by 89.163.35.42 on June 21, 2012 | http://pubs.acs.org
Publication Date (Web): March 11, 2010 | doi: 10.1021/bk-2010-1034.fw001

ACS SYMPOSIUM SERIES **1034**

# Functional Polymer Nanocomposites for Energy Storage and Conversion

**Qing Wang**, Editor
*The Pennsylvania State University*

**Lei Zhu**, Editor
*Case Western Reserve University*

Downloaded by 89.163.35.42 on June 21, 2012 | http://pubs.acs.org
Publication Date (Web): March 11, 2010 | doi: 10.1021/bk-2010-1034.fw001

**Sponsored by the**
**ACS Division of Polymeric Materials: Science and Engineering**

American Chemical Society, Washington, DC

Downloaded by 89.163.35.42 on June 21, 2012 | http://pubs.acs.org
Publication Date (Web): March 11, 2010 | doi: 10.1021/bk-2010-1034.fw001

**Library of Congress Cataloging-in-Publication Data**

Functional polymer nanocomposites for energy storage and conversion / Qing Wang, editor ; Lei Zhu, editor ; sponsored by the ACS Division of Polymeric Materials: Science and Engineering, American Chemical Society.
p. cm. -- (ACS symposium series ; 1034)
Includes bibliographical references and index.
ISBN 978-0-8412-2543-5 (alk. paper)
1. Storage batteries--Materials. 2. Polymers--Electric properties. 3. Nanocomposites (Materials) 4. Conducting polymers. I. Wang, Qing. II. Zhu, Lei. III. American Chemical Society. Division of Polymeric Materials: Science and Engineering.
TK2941.F86 2010
621.31'242--dc22
2010003305

The paper used in this publication meets the minimum requirements of American National Standard for Information Sciences—Permanence of Paper for Printed Library Materials, ANSI Z39.48n1984.

Copyright © 2010 American Chemical Society

Distributed by Oxford University Press

All Rights Reserved. Reprographic copying beyond that permitted by Sections 107 or 108 of the U.S. Copyright Act is allowed for internal use only, provided that a per-chapter fee of $40.25 plus $0.75 per page is paid to the Copyright Clearance Center, Inc., 222 Rosewood Drive, Danvers, MA 01923, USA. Republication or reproduction for sale of pages in this book is permitted only under license from ACS. Direct these and other permission requests to ACS Copyright Office, Publications Division, 1155 16th Street, N.W., Washington, DC 20036.

The citation of trade names and/or names of manufacturers in this publication is not to be construed as an endorsement or as approval by ACS of the commercial products or services referenced herein; nor should the mere reference herein to any drawing, specification, chemical process, or other data be regarded as a license or as a conveyance of any right or permission to the holder, reader, or any other person or corporation, to manufacture, reproduce, use, or sell any patented invention or copyrighted work that may in any way be related thereto. Registered names, trademarks, etc., used in this publication, even without specific indication thereof, are not to be considered unprotected by law.

PRINTED IN THE UNITED STATES OF AMERICA

Downloaded by 89.163.35.42 on June 21, 2012 | http://pubs.acs.org
Publication Date (Web): March 11, 2010 | doi: 10.1021/bk-2010-1034.fw001

# Foreword

The ACS Symposium Series was first published in 1974 to provide a mechanism for publishing symposia quickly in book form. The purpose of the series is to publish timely, comprehensive books developed from the ACS sponsored symposia based on current scientific research. Occasionally, books are developed from symposia sponsored by other organizations when the topic is of keen interest to the chemistry audience.

Before agreeing to publish a book, the proposed table of contents is reviewed for appropriate and comprehensive coverage and for interest to the audience. Some papers may be excluded to better focus the book; others may be added to provide comprehensiveness. When appropriate, overview or introductory chapters are added. Drafts of chapters are peer-reviewed prior to final acceptance or rejection, and manuscripts are prepared in camera-ready format.

As a rule, only original research papers and original review papers are included in the volumes. Verbatim reproductions of previous published papers are not accepted.

**ACS Books Department**

Downloaded by 89.163.35.42 on June 21, 2012 | http://pubs.acs.org
Publication Date (Web): March 11, 2010 | doi: 10.1021/bk-2010-1034.pr001

# Preface

With the soaring of global oil prices and global warming, energy crisis has become a pressing issue that challenges everyone's standard of life, societal security, economy, and even global environment. Advanced functional materials including polymer nanocomposites start to play an unprecedented role in our ultimate objective of sustainable and clean energy production, energy transportation, storage, and end usage. A number of developments and achievements in polymer nanocomposites have been documented during the past decade. Nevertheless, a focus on applications of functional polymer nanocomposites for energy storage and conversion, which are emerging research topics worldwide, has not yet been introduced in previous ACS meetings or associated symposium series books. The objectives of this timely ACS symposium series book are multifold. 1) This symposium book is to highlight the frontier scientific research and technologies in polymer nanocomposites for energy storage and conversion from international and the U.S. academic institutions and industries in recent years. 2) It is our purpose to enlighten the future development and directions of polymer nanocomposites for energy storage and conversion. 3) This symposium book endeavors to enhance the national awareness of the feasibility and importance of polymer nanocomposites for energy storage and conversion. This symposium book focuses on three contemporary energy topics: electric energy storage, fuel cells, and photovoltaics.

## Polymer Nanocomposites for Electrical Energy Storage

Nowadays, electrical energy storage has become increasingly important in our daily life, not only because of its versatile utilization in mobile electronic devices such as cell phones, lap-top computers, and personal digital devices, but also due to its new applications in transportation (i.e., electric vehicles, ships, and airplanes), power conditioning, pulsed power, and effective commercialization of renewable resources such as solar and wind power. The demanded storage size ranges from milliwatts for sensors to megawatts for large power conditioning or load-leveling stations. Basic electric energy storage devices include batteries, double-layer electrochemical capacitors (supercapacitors and pseudocapacitors), dielectric capacitors, and fuel cells. In general, batteries have a high energy density (Wh/kg or Wh/m$^3$), but their power density (W/kg or W/m$^3$) is low. On the contrary, capacitors have a high power density but a low energy density. Both of them can find appropriate end uses, depending on the ultimate need.

In this symposium book, we focus on polymer nanocomposites for dielectric capacitor applications. The current state-of-the-art dielectric (or solid-state) capacitors (e.g., biaxially oriented polypropylene) suffer from relatively low energy density because of their relatively low dielectric constants. Enhancing dielectric constant but retaining high dielectric breakdown and reasonably low dielectric loss are the major challenges in this field. Currently, polymer nanocomposites impregnated with high dielectric constant ceramic nanoparticles hold a promise of increasing the film dielectric constant. The challenges are how to tailor the polymer-ceramic nanoparticle interfaces to retain high dielectric breakdown and low dielectric loss. Rational nanomaterials synthesis and processing to ensure uniform dispersion of nanoparticles and tailored interfacial properties are endeavored.

Downloaded by 89.163.35.42 on June 21, 2012 | http://pubs.acs.org
Publication Date (Web): March 11, 2010 | doi: 10.1021/bk-2010-1034.pr001

## Polymer Nanocomposites for Fuel Cells

Intense academic and industrial research efforts have focused on proton-exchange membrane fuel cells (PEM FCs) due to the promise of commercialization and mass production. Although PEM FCs have great commercial potentials, significant technical challenges still await technological resolution and improvements, such as retaining high proton conductivity at high temperatures and low relative humidity, reducing mechanical and chemical degradation, better water management, etc. Modification of polyelectrolyte membranes to permit operation at high temperature and low relative humidity appears to be a promising strategy. To pursue this goal, different approaches have been investigated, such as 1) selecting alternative high performance polyelectrolyte membranes based on solid-state proton conductive materials; 2) modifying PEMs with hygroscopic inorganic materials to improve their water retention property at temperatures above 100 °C; and 3) modifying PEMs with inorganic proton conductors to obtain reasonable proton conductivity which will be hardly dependent on the water contents. Although synthesis of new high performance proton conductive polymers for PEM FC applications is promising, many molecular and structural parameters are difficult to manipulate and obtain high fuel cell performance. An alternative approach to achieve high proton conductivity in PEMs at reduced relative humidity is polymer nanocomposite membranes. Incorporation of hygroscopic inorganic materials such as silica into PEM membranes may retain water in the membranes, and thus keep high proton conductivity at high temperatures. Most approaches have focused on the incorporation of hydrophilic inorganic proton-conducting dopants into PEM membranes, such as heteropolyacids (HPAs) and isopolyacids (IPAs). HPAs are the acid form of heteropolyanions and have extremely high proton conductivity up to 0.2 $S \cdot cm^{-1}$ at 25 °C. Examples of HPAs are phosphotungstic acid (PTA), silicotungstic acid (STA), phosphomolybdic acid, silicomolybdic acid, and layered phosphates such as zirconium hydrogen phosphate, tungsten hydrogen phosphate, and vanadium hydrogen phosphate. These solid acids can also assist in the improvement of thermal and mechanical stability, water absorption, and resistance to reactant crossover. In addition, metal and metal oxide nanoparticles can be incorporated into polyelectrolyte membranes to reduce radical degradation via hydrogen peroxide.

## Polymer Nanocomposites for Photovoltaics

Direct conversion of sunlight into electricity has been explored for decades as a source of clean alternative energy, with wafer based silicon solar cells being the most common type of cells in today's solar energy market. Solar energy currently contributes much less than 1% to the U.S. energy portfolio because silicon-based devices are still expensive on a cost per Watt basis due to the costly materials processing that is required. There has been considerable interest recently in the development of photovoltaic devices in which the active matrix consists of conducting polymers. This interest has been motivated by the potential of organic polymers to offer economic viability for solar energy conversion owing to their inherent advantages of low cost, ease of processing, and light weight. An encouraging breakthrough for the high efficiency of optical-to-electrical power conversion has been achieved in cells fabricated using organic-inorganic hybrid structures, in which inorganic semiconductor nanocrystals are introduced to utilize their high electron mobility and overcome charge-transport limitations associated with organic polymers. These hybrids allow remarkable electronic and optical properties of organic semiconductors to be combined with their inorganic counterparts, thus presenting great opportunities for unique photophysical, photochemical, and electrochemical properties. In organic solar cells, excitons, created by the absorption of light, must be able to diffuse to the interface between the *p*-type conjugated polymers and *n*-type inorganic nanocrystals where charge separation can occur to generate free charge carriers. As the exciton diffusion length in organic materials is often limited to about 10 nm, a bicontinuous and nanoscopic phase-separated mixture of conjugated polymers and nanoparticles is thereby favorable for charge creation and transport. In order to exploit the cooperative electronic and optical properties of nanoparticles and conducting polymers, the construction of appropriate polymer nanocomposite assemblies with an accurate control of the spatial organization over a range of length scales becomes necessary. The efficiency of single layer organic solar cells has reached a plateau in recent years with devices based on the composite of regioregular poly(3-hexylthiophene) (RR-P3HT) and methanofullerene [6,6]-phenyl $C_{61}$-butyric acid methyl ester (PCBM) yielding the highest performance. These devices are able to collect over 90% of the photo-generated charge carriers under short circuit conditions, although the collection efficiency drops considerably at the maximum power point. Current efforts to optimize the efficiency of organic solar cells have largely focused on improving the overlap of the optical absorption spectrum of the polymers with the terrestrial solar spectrum and on maximizing the open-circuit voltage of the devices. This symposium book will present the latest progress on design,

Downloaded by 89.163.35.42 on June 21, 2012 | http://pubs.acs.org
Publication Date (Web): March 11, 2010 | doi: 10.1021/bk-2010-1034.pr001

synthesis and characterization of polymer nanocomposites for organic-based solar cells.

The financial supports for this symposium from ACS Division of Polymeric Materials Science and Engineering and National Science Foundation (DMR-0936980) are highly acknowledged.

**Qing Wang**

Department of Materials Science and Engineering
The Pennsylvania State University
University Park, PA 16802
814-863-0042 (telephone)
814-865-2917 (fax)
wang@matse.psu.edu (e-mail)

**Lei Zhu**

Department of Macromolecular Science and Engineering
Case Western Reserve University
Cleveland, OH 44106
216-368-5861 (telephone)
216-368-4202 (fax)
lxz121@case.edu (e-mail)

Downloaded by 89.163.35.42 on June 21, 2012 | http://pubs.acs.org
Publication Date (Web): March 11, 2010 | doi: 10.1021/bk-2010-1034.pr001

Downloaded by 89.163.35.42 on June 21, 2012 | http://pubs.acs.org
Publication Date (Web): March 11, 2010 | doi: 10.1021/bk-2010-1034.ch001

## Chapter 1

# Nanostructure-Level Modeling of Nonlinear Energy Storage in Polymer-Ceramic Nanocomposites

**Jeffrey P. Calame**[*]

**Electronics Science and Technology Division, Naval Research Laboratory, Washington, DC 20375**
**[*]Jeffrey.calame@nrl.navy.mil**

Three-dimensional finite difference dielectric simulation routines have been developed to predict the overall dielectric behavior of a composite, based on the constituent properties and a computer representation of the micro- to nanostructure. The methodology allows for a nonlinear dependence of constituent polarization vs. the local electric field. Studies on nonlinear titanate-like inclusions in a linear matrix have been performed for both spheres-in-a-simple-cubic-lattice (SSCL) and randomly positioned spheres configurations. For a relatively low saturation inclusion material (similar to simple titanates), when arranged in a SSCL fashion at filling fraction $p = 0.3$ in a matrix with a dielectric constant of 12, the composite energy storage is reduced by nonlinear effects from the expected 2.5 J/cm$^3$ down to 1.04 J/cm$^3$ at 140 V/micron applied field. The energy storage situation is improved by using inclusions with 5 times higher saturation polarization, reaching 10 J/cm$^3$ at $p = 0.4$ with 300 V/micron applied field.

## Introduction

A critical issue in composite dielectrics is the prediction of the overall properties of the composite based on constituent properties. Given a microstructure or nanostructure of the composite, one would like to be able to predict, using computer simulations, the real and imaginary parts of the

In Functional Polymer Nanocomposites for Energy Storage and Conversion; Wang, Q., et al.;
ACS Symposium Series; American Chemical Society: Washington, DC, 2010.

Downloaded by 89.163.35.42 on June 21, 2012 | http://pubs.acs.org
Publication Date (Web): March 11, 2010 | doi: 10.1021/bk-2010-1034.ch001

small-signal dielectric permittivity ($\varepsilon'$ -$j\varepsilon''$), the energy storage at high electric fields, etc., without resorting to free parameters. The ultimate goal is the complete modeling of composite materials for capacitors, including both micro- and nanoscale features (individual particles, ensembles of particles in a matrix) and the truly nanoscopic features (interfacial effects, coatings, local dipolar interactions in surface layers, etc.). Such a capability would allow experimental synthesis to be focused on the most promising structural approaches, without the need to physically test each idea. It would also be critical for understanding tradeoffs between competing requirements, for example energy storage vs. breakdown. Within a specific class of micro- or nanostructures, the computational capability would provide explicit guidance to synthesis efforts, for example allowing the intelligent selection of particle shapes, loading fractions, surface coatings, and hierarchical assembly strategies. Finally, the computational techniques will provide a means of understanding experimental results on existing and new materials.

Historically, most of the modeling of this type has been based on small signal, linear dielectric permittivities for the constituents. This is appropriate for conventional polymer dielectric materials like polypropylene, which is highly linear even at high electric field strengths, and for many other materials at low electric field strengths. However, many emerging materials being considered for high density energy storage applications are either ferroelectric, paraelectric, or antiferroelectric. Examples include PVDF polymers, P(VDF-TrFE-CFE) terpolymers, and titanate ceramics. Hence, the linear assumption is ultimately not appropriate, and needs to be replaced with full nonlinear modeling.

This chapter describes the modeling of the overall polarization and energy storage behavior of particulate composites, in situations that include a representative nonlinear dependence of constituent polarization vs. the local electric field. The formalism at present does not include hysteresis. Therefore, it is appropriate for nonlinear paraelectrics during both charging and discharging, but for ferroelectrics it is only applicable for charging from an initial uncharged state. Studies on nonlinear titanate-like inclusions in a linear polymer matrix are performed for both a spheres-in-a-simple-cubic-lattice (SSCL) configuration and for a randomly positioned spheres configuration. The behavior of the composite energy density as a function of applied field receives particular attention.

## Simulation Methodology

The modeling of permittivity in spherical particle composites for the linear constituent case has been described thoroughly in a prior publication (*1*). In brief summary, the geometry of a portion of the micro- or nanostructure, including background matrix material and particle shapes, orientations, and arrangements, is represented in a three dimensional cellular model space ($n_d$ cells/axis, $n_d^3$ total cells). The dielectric permittivity of the model space is computed using finite difference quasi-electrostatic simulations. The appropriate bulk permittivities at the frequency of interest are assigned to the individual cubical model space cells

Downloaded by 89.163.35.42 on June 21, 2012 | http://pubs.acs.org
Publication Date (Web): March 11, 2010 | doi: 10.1021/bk-2010-1034.ch001

depending on whether the cell is filled (i.e. within a particle) or is background matrix material. Located at the vertices between these cells are grid points at which potentials will be computed. The potentials on the top and bottom faces of the overall model space are fixed at a values of 1.0 and 0, respectively, to represent an externally applied voltage to the microstructure. Symmetry conditions are applied to the sides of the model space. To obtain the solution, the potentials and electric fields are found by iterative enforcement of Gauss' Law at each grid point until convergence is obtained. The effective composite permittivity $\varepsilon_c$ in this linear situation is found from the ratio of boundary charge on the bottom (or top) of the model space to the applied potential.

For the new nonlinear studies, in which the constituents are assumed to have nonlinear polarization versus applied field characteristics, a significantly modified approach was used. In the new formulation a vector displacement $\boldsymbol{D}$ vs. vector $\boldsymbol{E}$ relationship is assumed in which $\boldsymbol{D}$ is in the same direction as $\boldsymbol{E}$, but the magnitude of $\boldsymbol{D}$ is a nonlinear function $f$ of the magnitude of $\boldsymbol{E}$. In this initial approach hysteresis is not included, so only nonlinear paraelectrics (or ferroelectrics charging from an uncharged state) can be modeled, but the formulation will be broadened in the future to include hysteresis and thus both the charging and discharging of ferroelectrics. One still retains the finite difference approach, based on simultaneously enforcing Ñ•$\boldsymbol{D}$=0 at the vertex points of each cell. However, to include nonlinear behavior in the models, the formulation is changed to allow $\boldsymbol{D}=f(|\boldsymbol{E}|)(\boldsymbol{E}/|\boldsymbol{E}|)$. In the new formulation, one defines a related secondary function $g$ for each of the materials as the ratio of the magnitude of $\boldsymbol{D}$ to the magnitude of $\boldsymbol{E}$, so that $\boldsymbol{D} = g(|\boldsymbol{E}|)\boldsymbol{E}$. Thus, the finite difference model will now solve the system of equations enforcing Ñ•$(g(|\boldsymbol{E}|)\boldsymbol{E})=0$. When enforcing this at the vertex points during solution, one must take the average electric field within each of the model space cells surrounding the vertex, and compute the field-dependent value of $g$ in each cell using a lookup table approach, with the appropriate curve selected to correspond to the material composition of the cell. The process is iteratively repeated throughout the model space until convergence is obtained. Following this, the energy storage density is computed using the integrals of $\boldsymbol{E}$•d$\boldsymbol{D}$ within each cell and then summing these over then entire model space.

## Results

A simple model of the polarization curves for nonlinear titanate-like ceramic inclusions was used for the studies, as shown in Fig. 1. The curves are based on a hyperbolic tangent functionality. Two cases are shown with different saturation polarizations, the lower one having a saturated surface charge density of 0.0287 $\mathrm{Cm}^{-2}$ (similar to single cation titanate ceramics), and with the higher one being possibly representative of more idealized materials (compound cation titanate ceramics) with a saturated surface charge density of 0.15 $\mathrm{Cm}^{-2}$. Both curves have an initial (low field) relative permittivity of 1200.

Downloaded by 89.163.35.42 on June 21, 2012 | http://pubs.acs.org
Publication Date (Web): March 11, 2010 | doi: 10.1021/bk-2010-1034.ch001

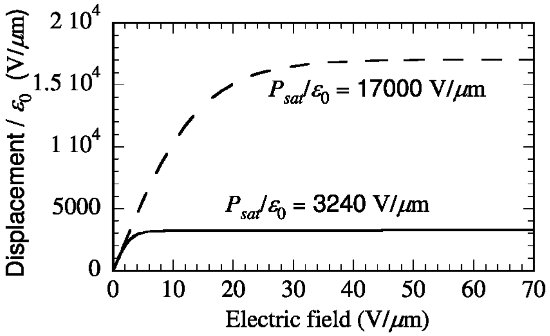

*Figure 1. Assumed nonlinear polarization curves for inclusions with two different saturation polarizations.*

Finite difference simulations were performed for a SSCL configuration of nonlinear inclusions in a background polymer, where the background polymer had a perfectly linear dielectric constant of 12. The geometry is shown in Fig. 2(a) and (b). The nonlinear simulation results for the composite behavior are shown in Fig. 2(c), where the inclusions are assumed to exhibit the low-saturation ***D*** vs. ***E*** curve of Fig. 1. The volumetric filling fraction $p$ of the spheres is 0.3. Also shown for comparison is the result if the inclusions hypothetically maintained their linear low field permittivity of 1200. Very clearly the effect of the nonlinear behavior is to cause much less energy to be stored than expected based on the linear calculation. The nonlinear calculation shows the expected quadratic dependence at low fields, below about 50 V/$\mu$m. However, at higher fields, the increase in energy density slows down towards a behavior that is roughly linearly proportional to applied field. The effect is very significant; at 140 V/$\mu$m applied field, the nonlinear composite energy storage is 1.04 J/cm$^3$ compared to the 2.5 J/cm$^3$ expected if the system remained linear.

Studies of nonlinear energy storage in the SSCL ceramic-polymer composite (with the low-saturation polarization ceramic inclusions) as functions of filling fraction were also carried out, for a wide range of applied electric fields. The results are shown in Fig. 3. Unlike in the linear case where an increase in filling fraction raises the permittivity and thus the energy storage, the nonlinear case is more complicated. Instead, at low applied fields, raising the filling fraction will first increase the energy storage, and then after some optimum, further increases in $p$ will reduce the energy storage. For example, in Fig. 3, at 50 V/$\mu$m the optimum filling fraction is about 0.4, while at 125 V/$\mu$m the optimum $p$ is only about 0.2. Above a certain applied field, there is no optimum, and any nonzero value of $p$ is deleterious.

Only relatively low stored energy densities have been shown to be achievable with composites having inclusions with a saturation polarization of 0.0287 Cm$^{-2}$ ($P_{sat}/\varepsilon_0 = 3240$ V/$\mu$m). To achieve higher stored energies, inclusions having higher values of $P_{sat}$ are needed. This is likely possible with more complex titanates than those behaving similarly to plain barium titanate. If a saturation polarization of 0.15 Cm$^{-2}$ ($P_{sat}/\varepsilon_0$ = 17,000 V/$\mu$m) could be achieved, as depicted by the dashed

Downloaded by 89.163.35.42 on June 21, 2012 | http://pubs.acs.org
Publication Date (Web): March 11, 2010 | doi: 10.1021/bk-2010-1034.ch001

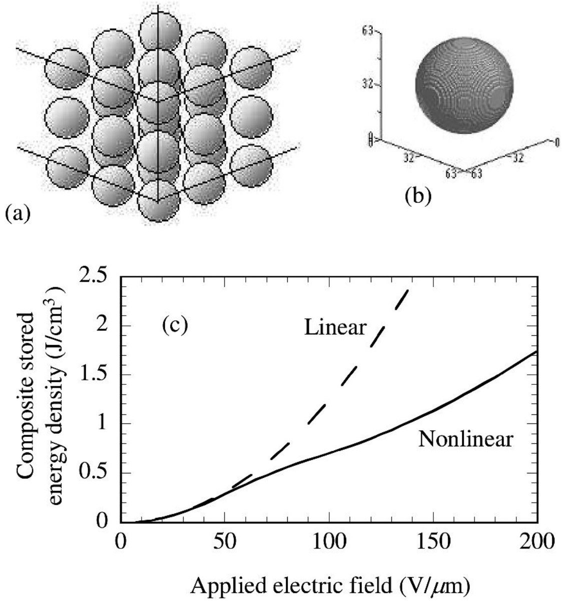

*Figure 2. (a) Schematic of SSCL configurations of inclusions in a polymer matrix, (b) simulation geometry of single spherical inclusion plus symmetry boundary conditions, and (c) results of nonlinear finite difference simulations of the ceramic-polymer composite energy storage (solid line) in comparison to linear results (dashed line).*

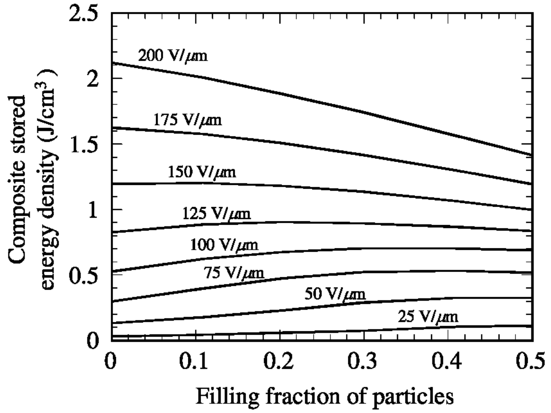

*Figure 3. Nonlinear ceramic-polymer composite energy storage in a SSCL configuration, when the inclusions have the low saturation D vs. E curve*

curve in Fig. 1, then the energy storage situation improves markedly. Nonlinear calculations were carried out for a SSCL configuration using the inclusions with the higher saturation polarization. Figure 4 shows the stored energy vs. filling fraction, for a wide range of applied electric fields. At 208 V/$\mu$m, the stored energy

Downloaded by 89.163.35.42 on June 21, 2012 | http://pubs.acs.org
Publication Date (Web): March 11, 2010 | doi: 10.1021/bk-2010-1034.ch001

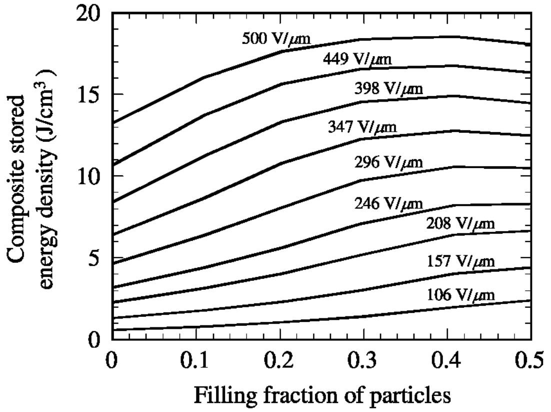

*Figure 4. Nonlinear ceramic-polymer composite energy storage in a SSCL configuration, when the inclusions have the high saturation D vs. E curve.*

increases substantially as the filling fraction is increased from 0 to the optimum value of $p \sim 0.45$ for that field. Even at the highest field studied, 500 V/$\mu$m, there still exists a clearly defined optimum value of filling fraction for energy storage, which is near $p = 0.4$ (yielding 18.6 J/cm$^3$). The numerical values of stored energy are much more encouraging throughout the plot, reaching above 10 J/cm$^3$ over a wide range of parameters.

Finally, comparisons have been made between randomly positioned sphere configurations and SSCL configurations. The overall behavior is very similar to Fig. 4, except that the optimum energy storage is obtained at somewhat lower values of $p$ in the random case in comparison to the SSCL case. For example, at 500 V/$\mu$m, as can be seen in Fig. 5, the optimum $p$ drops to about 0.25. However, the optimum energy density in the random case at $p \sim 0.25$ is 17 J/cm$^3$ at 500 V/$\mu$m, which is somewhat less than the optimum value of 18.6 J/cm$^3$ at $p \sim 0.4$ in the SSCL case at the same applied field. Thus, there appears to be a very slight advantage to the SSCL ordered arrangement compared to the random arrangement, when nonlinear energy storage is considered.

## Summary

Simulations of the energy storage of particulate composite dielectrics have been performed for the situation in which nonlinear inclusions are dispersed in a linear dielectric matrix. A hyperbolic tangent model for the nonlinear ***D*** vs. ***E*** behavior of the inclusions, without hysteresis, was assumed. Nonlinear behavior has a strong influence on the composite energy storage, including significant reductions in energy density if the inclusion saturation polarization is not high enough. Specifically, for a relatively low saturation inclusion material ($P_{sat}$ = 0.0287 $Cm^{-2}$, similar to simple titanates), when arranged in a SSCL fashion with filling fraction $p = 0.3$ in a matrix with a dielectric constant of 12, the composite energy storage is reduced by nonlinear effects from the expected

Downloaded by 89.163.35.42 on June 21, 2012 | http://pubs.acs.org
Publication Date (Web): March 11, 2010 | doi: 10.1021/bk-2010-1034.ch001

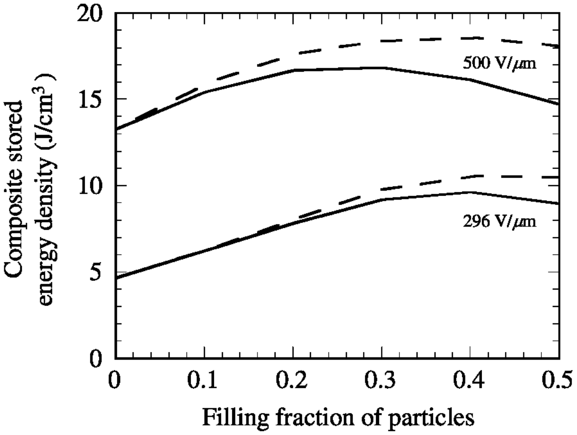

*Figure 5. Nonlinear energy storage comparison between random spheres (soild lines) and SSCL (dashed lines) configurations for two values of applied electric field, when the inclusions have the high saturation D vs. E curve.*

2.5 J/cm$^3$ down to 1.04 J/cm$^3$ at 140 V/$\mu$m applied field. However, the energy storage situation is markedly improved by using inclusions with 5 times higher saturation polarization ($P_{sat} = 0.15$ Cm$^{-2}$, likely achievable with compound cation titanates), reaching 10 J/cm$^3$ at $p = 0.4$ with 300 V/$\mu$m applied field and 15 J/cm$^3$ with 400 V/$\mu$m. Additional research is needed to further quantify the impact of particle arrangements. Further work is also required to include hysteresis in the polarization curves and repeat the calculations in the various geometries.

## Acknowledgments

This work was supported by the Office of Naval Research.

## References

1. Calame, J. P. *J. Appl. Phys.* **2006**, *99*, 084101.

Downloaded by CORNELL UNIV on June 21, 2012 | http://pubs.acs.org
Publication Date (Web): March 11, 2010 | doi: 10.1021/bk-2010-1034.ch002

## Chapter 2

# Nanodielectrics for Energy Storage from First Principles Computations

**N. Shi[1] and R. Ramprasad[*,2]**

**[1]Shocking Technologies, Inc., 5870 Hellyer Ave, San Jose, CA, USA**
**[2]Chemical, Materials and Biomolecular Engineering, Institute of Materials Science, University of Connecticut, Storrs, CT, USA**
**[*]rampi@ims.uconn.edu**

First-principles computational methologies are presented to study the impact of surfaces and interfaces on the dielectric and electronic properties of dielectric nanocomposites at the nanoscale. The two important factors controlling energy strorage capacitbity, dielectric constant and dielectric breakdown strength, are specifically addressed. The variation of dielectric constant across $SiO_2$-polymer interfaces has been correlated to interfacial chemical bonding enviorments, using the theory of the local dielectric permittiviy. The local electronic structure variation across $SiO_2$-polymer interfaces, including band bending, band offsets and the creation of interfacial trap states have been demonstrated using a layer-decomposed density of states analysis. The enhancement of dielectric breakdown strength is understood qualitatively in termas of interface electronic structure and electron-phonon interactions.

## Introduction

Dielectric materials play a dominant role in modern electronics and electrical power systems due to their capability for storing and controlling electrical energies. As the requirements grow for highly miniaturized, more reliable, electrical power systems, as well as energy storage capacitors, development of high power and energy density dielectric materials becomes a major enabling technology (*1*–*3*). Among various dielectric materials, polymers are presently

In Functional Polymer Nanocomposites for Energy Storage and Conversion; Wang, Q., et al.;
ACS Symposium Series; American Chemical Society: Washington, DC, 2010.

Downloaded by CORNELL UNIV on June 21, 2012 | http://pubs.acs.org
Publication Date (Web): March 11, 2010 | doi: 10.1021/bk-2010-1034.ch002

the materials of choice for energy storage applications because of their relatively high energy density, high electric breakdown field, low dielectric loss, fast speed, flexibility, easy processablity, and graceful failure.

Driven by a need for increased electrical energy density in polymeric capacitor thin films, the scientific and technological communities are in the midst of a vigorous search for methods of increasing the dielectric constant and/or dielectric breakdown strength of polymeric thin films. Among the means of achieving these goals are (1) creating polymer-inorganic nanocomposites, and (2) polymeric multi-layers.

Regardless of the approach, a fundamental understanding of the factors that control electronic and dielectric properties in polymers, and the new opportunities and challenges offered by interfaces and nanomaterials is essential to make further progress. Phenomena such as charge conduction, dielectric response, and dielectric degradation or breakdown are the result of complex and numerous critical processes operating at multiple temporal and spatial length scales. For example, the response of the capacitor dielectric to an external electric field will be determined by the presence of defects states, in addition to the polarization contributions due to ions and electrons of the system. More importantly, as feature sizes or dimensions in multiple component systems shrink to the atomic or nanoscale, the structure and chemistry at interfaces, and size-dependent alternations in the properties of the nano-sized systems, become important and can sometimes dominate the overall properties. For instance, while atomic level interfacial features such as dangling bonds, under- or over- coordination, multiple oxidation states, impurities, etc., may be less important in larger scale systems owing to the smaller volume fraction occupied by the interfacial region, the consequences of such effects especially on electrical properties can reach unanticipated magnitudes in nanoscale systems (*4–7*). Thus it is important to characterize the electronic and dielectric properties of interface-containing materials in the nanoregime.

In this paper, we will present recent developments in the *ab initio* computational modeling arena, which constitute an initial understanding of the relationship between interfacial structure and properties, including interfacial polarization, dielectric response and electronic structure. Specially, (i) the extent to which surface/interface effects modify the static and optical local dielectric permittivity, (ii) the evolution of the local electronic structure across interfaces as a function of position, and (iii) electron-phonon interaction, are addressed.

## Methods and Models

An accurate treatment of physical systems at submicroscopic scale (atomic/electronic level) can only be accomplished through the use of quantum mechanics. The electronic energies and the associated electronic wave functions from quantum mechanics allows for the determination of physical quantities such as stability of atomic structure, vibrational and phonon frequencies, force constants and elastic moduli, and so on. Quantum mechanics-based calculations have an additional

Downloaded by CORNELL UNIV on June 21, 2012 | http://pubs.acs.org
Publication Date (Web): March 11, 2010 | doi: 10.1021/bk-2010-1034.ch002

appeal due to the fact that they are *inherently parameter-free* and do not rely on any experimental input other than the values of the electronic and ionic charges and masses, and so have been variously called as "First principles" or "*ab initio*" methods (*8–11*).

Of all the quantum mechanics-based methods currently in use, density functional theory (DFT) provides an efficient, accurate and fundamental route to the *ab initio* numerical computation of electronic, atomic, molecular and solid-state properties (*8–11*). It offers the best trade-off between practicality and accuracy at the present time for the parameter-free computation of several ground-state properties, such as the total energy, charge density, and atomic forces, as well as structural, vibrational, thermochemical and dielectric properties.

Within DFT, the following eigenvalue equation is solved:

$$[-\nabla^2 + V_{eff}(r)]\psi(r) = \varepsilon\psi(r) \tag{1}$$

where the first term in brackets represents the electronic kinetic energy (with $\nabla$ being the gradient operator), and the second term, $V_{eff}(r)$, represents the effective potential energy seen by an electron. $V_{eff}(r)$ contains all the electron-electron and electron-nuclear interactions, as well as the potential due to an external electric field. $\psi$ and $\varepsilon$ are the electronic wave functions and energy, respectively.

All calculations reported here were performed using the local density approximation (LDA) or the generalized gradient approximation (GGA) within DFT as implemented in the local orbital SIESTA (*11*) code. Within these implementations, the electronic wave functions are expanded either using a set of local functions or plane waves. Electron-ion interactions are represented using suitable pesudopotentials, one for each element. As validation of the results of DFT computations, structural parameters for the selected model systems relevant to this work are provided in Table 1, and compared with experiments. Results on Si, two different phases of silica and hafnia, polyethylene (PE), and poly vinyledene fluoride (PVDF) are listed. As can be seen DFT is able to predict structural details with reasonable accuracy.

## Dielectric Response at Interface

Owing to the fundamentally different chemistries at surfaces and interfaces compared to the bulk part of a material, the dielectric response is expected to be different in these regions. In fact, our recent work on the scaling with thickness of the dipole moment induced due to an external electric field in ultra-thin $SiO_2$ and $HfO_2$ slabs has resulted in the realization that the dielectric properties in the surface regions are considerably different from those of the bulk (*17*, *18*). Nevertheless, a quantitative estimation of the dielectric constant or polarization at surface and interface regions was not possible using this approach.

More recently, we have introduced a practical method for the calculation of the position dependent dielectric permittivity of multilayer systems in the presence of finite electric fields (*19*, *20*). These techniques go beyond the

**Table 1. Comparison of calculated structural parameters of bulk Si, $SiO_2$, $HfO_2$, PE, PVDF, and vinylsilanediol with experimental values. All distances are in Å. Data are from (*17*, *18*) and references therein**

| *System* | *Lattice constant /bond length* | *DFT* | *Expt.* |
|---|---|---|---|
| Si | a | 5.43 | 5.43 (*12*) |
| $SiO_2$ (α-quartz) | a/c | 4.91/5.41 | 4.92/5.41 (*13*) |
| $SiO_2$ (b-cristobalite) | a | 7.49 | 7.17 (*14*) |
| HfO2 (cubic) | a | 5.02 | 5.08 (*15*) |
| HfO2 (tetragonal) | a/c | 4.99/5.06 | 5.14/5.25 (*15*) |
| PE | C-C/C-H | 1.51/1.12 | 1.54/1.10 (*16*) |
| PVDF | C-H/C-F | 1.09/1.36 | 1.10/1.34 (*16*) |
| Vinylsilanediol | C=C/Si-C/Si-H | 1.34/1.83/1.51 | 1.34/1.89/1.48 (*16*) |

Downloaded by CORNELL UNIV on June 21, 2012 | http://pubs.acs.org
Publication Date (Web): March 11, 2010 | doi: 10.1021/bk-2010-1034.ch002

traditional ways of determining the dielectric permittivity of bulk (*21–25*) and superlattice (*26*) systems. The simplicity of this latter method to determine the local position dependent permittivity arises from the fact that most standard DFT implementations can be used as-is without the need for additional major code development; more importantly, this approach can treat finite systems such as slabs, with the bulk dielectric properties (optical and static) resulting as a by-product. A local permittivity function was introduced to describe variations of the dielectric response over length scales of the order of interatomic distances, which can conveniently be calculated from the local field induced self-consistent charge density profile. The optical part of the position dependent polarization and permittivity is obtained in terms of the field-induced displacements of just the electronic charge density with the ions held fixed at their field-free equilibrium positions, while the static part is determined from both the induced electronic and ionic displacements.

The local microscopic dielectric polarization $\vec{p}(r)$ can be obtained from the field induced charge density $\rho_{ind}(r)$ through the in-medium Maxwell equation (*27*):

$$\nabla \cdot \vec{p}(r) = -\rho_{ind}(r) \tag{2}$$

In the case of multi-layered (1-dimensional) systems with the layers oriented along the *x*-*y* plane, such as those considered here, Equation (2) reduces to:

$$\frac{d}{dz}\overline{p}(z) = -\overline{\rho}_{ind}(z) \tag{3}$$

where $\overline{p}(z)$ and $\overline{\rho}(z)$ are the polarization and induced charge density along the *z*-axis, respectively, averaged along the *x*-*y* plane. The induced charge density $\overline{\rho}_{ind}(z)$ can be evaluated as the difference of the total charge densities due to positive (+δ)

Downloaded by CORNELL UNIV on June 21, 2012 | http://pubs.acs.org
Publication Date (Web): March 11, 2010 | doi: 10.1021/bk-2010-1034.ch002

and negative (-δ) external electric fields along the *z* direction. In the present work, δ was chosen to be 0.01 V/Å. The solution of Equation (3) is the following:

$$\overline{p}(z) = \overline{p}_{-\infty} - \int_{-\infty}^{z} \overline{\rho}_{ind}(z')dz' \quad (4)$$

For the case when our slab system is located about the $z = 0$ plane, the constant $\overline{p}_{-\infty}$ can be set to zero as it corresponds to the polarization at -∞, a region where charge density is zero.

Using the above procedure, both the optical (high frequency) and the static (low frequency) microscopic polarization can be calculated, respectively, by either allowing just the electrons, or both the electrons and the atoms, to respond to the applied external electric field, $E_{ext}$. The local permittivity profile can then be computed from the local polarization using:

$$\varepsilon(z) = \frac{\varepsilon_0 E_{ext}}{\varepsilon_0 E_{ext} - \overline{p}(z)} \quad (5)$$

The optical and static local permittivities can be obtained from $\overline{p}(z)$ corresponding to the optical and static cases, respectively (*19*, *20*). Further details about the theory of the local dielectric permittivity can be found elsewhere (*20–22*).

## Dielectric Response at Interfaces

Polymeric systems constitute an important class of materials for capacitor and insulation technologies (*27*). Nevertheless, a quantitative understanding of the electrical response of such systems is still lacking (*28*, *29*). Nanocomposites made by blending oxide nanoparticles with polymers are known to display higher effective permittivities than expected from the permittivities of the components, indicating the role played by enhanced interfacial polarization (*30–34*). Here, we explore factors that could result in such permittivity enhancements in polymeric systems.

The $SiO_2$-polymer interface system considered here is composed of $SiO_2$ in the α-quartz phase of thickness 15.96 Å, and the polymer chain was approximated by a $C_{12}H_{26}$ molecule. Figure 1 shows the dielectric constant as a function of position along the $SiO_2$-polymer interface normal. Similar behavior of dielectric constant is observed as with the Si–$SiO_2$ interface. The agreement is excellent for the dielectric constant in the interior region of $SiO_2$ and polymer ($C_{12}H_{26}$) with the corresponding experimental single component bulk values, and the dielectric constant on the $SiO_2$ side of the interface is enhanced. Analysis of the Mulliken charges of the atoms indicates that C atoms closest to the interface are in their nominal oxidation states (i.e., in oxidation states similar to that of C atoms in the interior of the polymer chain), whereas the Si and O atoms close to the interface are in varying oxidation states similar to that in the Si–$SiO_2$ case (*18*).

Our conclusion of permittivity enhancement at the interface is thus consistent with some prior experimental work (*33*). Nevertheless, an important point needs to be made. The $SiO_2$-polymer system modeled here corresponds to a situation in which the $SiO_2$ surface is "untreated" (which is the experimental situation involving "blends" as in (*33*). However, typical polymeric nanocomposites are made using silane-treated $SiO_2$ (*2*, *34–36*). Silane treatment accomplishes the twin purposes of passivation of dangling bonds on silica surfaces by the silane-based initiator molecules, and in the creation of chemical bonds between the initiator and the polymer chains. Thus, silane treatment is expected to *decrease* the polarizability and permittivity at the interface. In fact, recent experimental work indicates that the incorporation of silane-treated $SiO_2$ nanoparticles into polyethylene results in decreased effective permittivities (although the permittivity of $SiO_2$ is higher than that of the host polymer (*34*). A more comprehensive analysis of $SiO_2$-polymer interfaces is necessary to understand the circumstances that would result in a permittivity increase or decrease at the interface.

Incidentally, incorporation of silane-treated $SiO_2$ nanoparticles into polyethylene also resulted in increased dielectric breakdown strength (*34*), while incorporation of micron-sized particles did not. It thus appears that the interface between $SiO_2$ and polyethylene plays a critical role in controlling the dielectric constant as well as the dielectric strength. These issues are explored further in the work later.

It is worth mentioning that although the method of the local dielectric permittivity has been applied to only coherent interfaces between dissimilar materials so far, this approach to computing the local polarization and permittivity can be used to systematically explore a variety of realistic situations, including atomic-level defects (e.g., vacancies), disorder, impurities and initiator species at the interface.

## Electronic Structure at Interfaces

When two materials are brought into contact, the wave function of electrons inside each material will interact with each other at the interface and results in the changes of electronic structure at the interface with respect to that in the interior. The electronic structures at interfaces, such as work function, Schottky barrier (SB), band offset, interfacial states, Fermi level (FL) pinning, etc., largely control the characteristics of electronic devices. Furthermore, as the surface of an insulating material or at the interface between two otherwise defect-free insulators, one generally finds under-coordinated atoms. These sub-optimal bonding situations lead to unoccupied and/or occupied states within the band gap of the insulators, which are localized physically at the surface or interface (as opposed to the delocalized bulk Bloch states), and are generally referred to as surface/interface states, defects states, or "trap" states. These defect states are important in two respects. They can alter the polarizability of the surface/interface

Downloaded by CORNELL UNIV on June 21, 2012 | http://pubs.acs.org
Publication Date (Web): March 11, 2010 | doi: 10.1021/bk-2010-1034.ch002

Downloaded by CORNELL UNIV on June 21, 2012 | http://pubs.acs.org
Publication Date (Web): March 11, 2010 | doi: 10.1021/bk-2010-1034.ch002

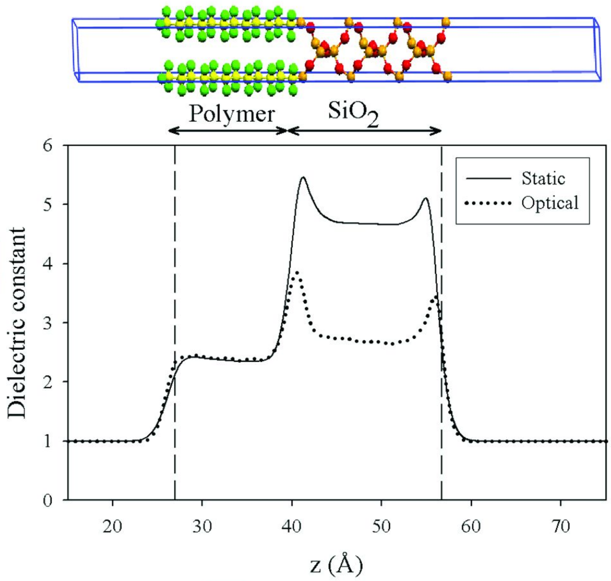

*Figure 1. Above: Atomic model of $SiO_2$-polymer. Below: Static (solid) and optical (dotted) dielectric constant of $C_{12}H_{25}$-$SiO_2$ stack as a function of position z normal to the interface.*

region, as has been discussed in the previous section, and they can significantly control charge carrier conduction through the insulator. It is latter possibility that is important in a study of breakdown phenomena.

In the case of coherent interfaces between dissimilar insulators, no dangling bonds would exist, and hence, one would not find defect states at the interface. Nevertheless, the energetic positions of the conduction and valence band edges in one material will be offset relative to those of the other material. In addition, the band edges could vary with position resulting in band bending due to transfer of charge from one material to the other at the interface.

It is important to characterize both the band offsets across the interface and the existence of trap states at the interface. Below, we present and approach to study the position dependent variation of the valence and conduction bands across interfaces, and the emergence of trap states at interfaces, using the layer-decomposed density of states (LaDOS) method (*37*, *38*). We than apply this method to Si-$HfO_2$ and polymer-$SiO_2$ interfaces.

Compared with the conventional “bulk plus band lineup” method, the layer-decomposed density of states (LaDOS) approach enables more detailed insights of the electronic structures at the interface (*37*, *38*). LaDOS decomposes the total DOS of the entire heterojunction in terms of its origins from various atoms of the system on a layer-by-layer basis through projecting the electronic wave function onto the local orbitals of each atom (*37*, *38*). Since we are primarily interested in multi-layered systems, the layer decomposition provides the position dependence of the electronic structure that we seek.

In Functional Polymer Nanocomposites for Energy Storage and Conversion; Wang, Q., et al.;
ACS Symposium Series; American Chemical Society: Washington, DC, 2010.

Downloaded by CORNELL UNIV on June 21, 2012 | http://pubs.acs.org
Publication Date (Web): March 11, 2010 | doi: 10.1021/bk-2010-1034.ch002

Within DFT such as the one adopted here, the electronic wave function $|\Psi_i\rangle$ can be projected onto the atomic orbitals $|\phi_{al}\rangle$ as (*37*, *38*)

$$|\Psi_i\rangle = \sum_{al} \langle \phi_{al} | \Psi_i \rangle | \phi_{al} \rangle \tag{6}$$

where *i*, *a*, and *l* are the indices for the electronic wave function, atom, and the atomic orbital, respectively, and the Dirac notation is adopted for simplicity. The density of states $g_{al}(\varepsilon)$, where ε is the electronic energy, arising from a specific atom *a* with atomic orbital *l* can be defined as:

$$g_{al}(\varepsilon) = \sum_{i} \left| \langle \phi_{al} | \Psi_i \rangle \right|^2 \delta(\varepsilon - \varepsilon_i) \tag{7}$$

where δ represents the Dirac delta function.

The contribution of all the atomic orbitals in one specific atomic layer results in the LaDOS of that layer. This method allows for the mapping of position dependent conduction and valence band edge profiles across a multi-layered system, which helps identify not only defect states at interfaces and point defects but also the variation of band offsets due to specific bonding environment.

Recent experiments involving silane-treated $SiO_2$ nanoparticles incorporated in polyethylene has shown an increase in dielectric breakdown strength, whereas untreated $SiO_2$ displays only a modest change in the breakdown strength. It has also been postulated that interface states could act as potential electron traps, thereby scavenging “hot” electrons, and increasing the breakdown strength. A systematic investigation of the various types of oxide-polymer interfaces focusing on interface states will help identify trends related to dielectric breakdown strengths, and can aid in the rational design of polymeric systems with superior dielectric properties.

In order to probe the specific role played by the silane treatment of $SiO_2$, we consider models of $SiO_2$-polymer interfaces in the presence of a silane-based species at the interface. The chemical route to the incorporation of silane-treated $SiO_2$ nanoparticles into the polymer involves two separate steps. The $SiO_2$ nanoparticles into the polymer involve two separate steps. The $SiO_2$ nanoparticles are first treated with silane or its derivatives, resulting in $SiO_2$ surfaces decorated with the silane-based initiator species. Next, the facile attachment of polymer chains to the initiator species is accomplished. In this work, the initiator is represented by a vinlysilanediol ($SiH(OH)_2CHCH_2$) molecule, and the polymer chain is $C_6H_7F_7$, representing polyvinylidene difloride (PVDF). We find that attachment of the vinysilandilol initiator of the $SiO_2$ surface (with a binding energy of -0.58 eV) and the subsequent attachment of $C_6H_7F_7$ to the initiator (with a binding energy of -0.98 eV) are themodyanamically favored.

Figure 2 shows the structure of a $SiO_2$-vinylsianediol-PVDF heterojunction, where vinylsianediol is represented by $SiH(OH)_2CHCH_2$, together with its LaDOS profile. As can be seen, the LaDOS in the middle parts of $SiO_2$ and polymer regions indicates large and uniform band gaps, while in the initiator region the band edges do not smoothly evolve from the $SiO_2$ end to the PVDF end. Rather,

Downloaded by CORNELL UNIV on June 21, 2012 | http://pubs.acs.org
Publication Date (Web): March 11, 2010 | doi: 10.1021/bk-2010-1034.ch002

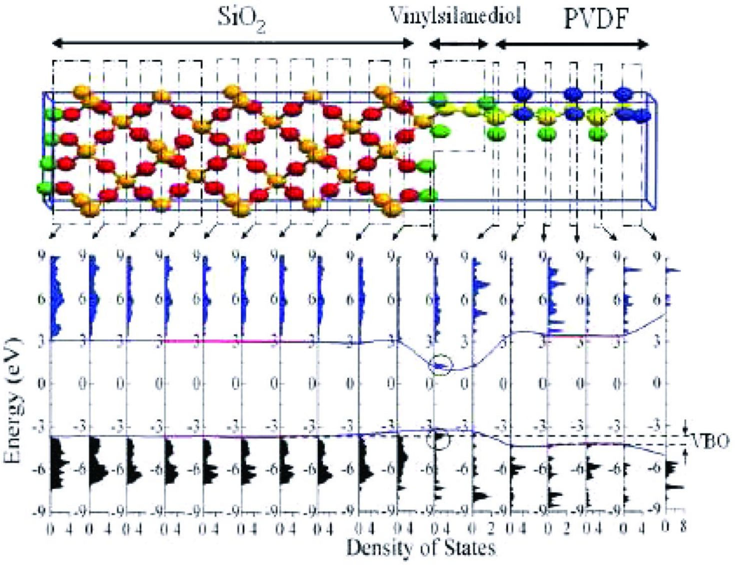

*Figure 2. $SiO_2$-$SiH(OH)_2CHCH_2$-PVDF heterojunction model and its LaDOS profile. The zero of energy is Fermi energy. The defect states are highlighted by circles.*

an occupied and an unoccupied defect states appear in the band gap, which can be attributed to the double bond in the vinylsilanediol initiator. Since these defect states are close to the band edges, they serve as shallow traps for electrons or holes. The electron traps can potentially "cool" conduction electrons and result in higher breakdown strengths. It is noted that the defect states disappear when the vinylsilanediol initiator is replaced by a silane initiator. Hence it appears that the appropriate choice of initiators is critical for the electronic properties of the interfaces.

DFT based computations give reasonable descriptions of interfacial electronic structures such as barrier height and band offsets after some corrections. Particularly the LaDOS approach has demonstrated its strength for the study of electronic structure details at interfaces. It will be very helpful for investigating the electronic properties of a wide variety of nanostructured systems where the impact of surfaces, interfaces, and atomic level defects is important.

## Electron-Phonon Interactions

The method of LaDOS based on DFT gives reasonable descriptions of interfacial electronic structures such as barrier height and band offsets after some corrections. Particularly, the electronic structure details at interfaces were accurately illustrated. Although these aspects are consistent with the observed increase in breakdown strength of $SiO_2$-polymer composites, several questions remain unanswered. Firstly, mechanisms for the dissipation of the energy released

Downloaded by CORNELL UNIV on June 21, 2012 | http://pubs.acs.org
Publication Date (Web): March 11, 2010 | doi: 10.1021/bk-2010-1034.ch002

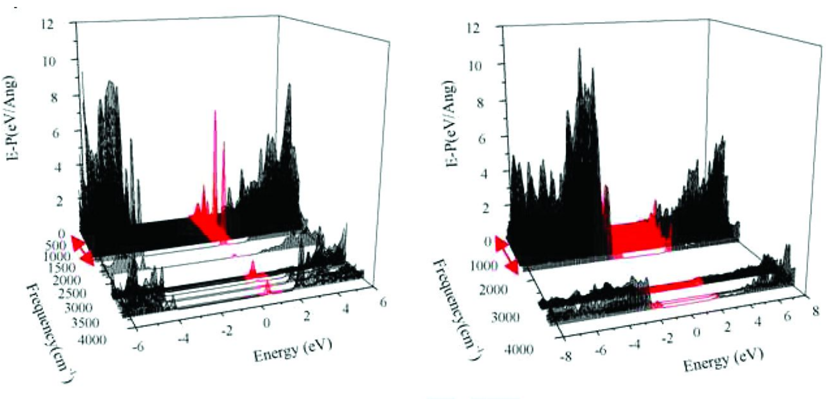

*Figure 3. Electron-phonon coupling for the $SiO_2$-vinysilanediol-PE interface (left) and the $Al_2O_3$-vinysilanediol-PE interface. The arrows indicate $SiO_2$ phonon modes and $Al_2O_3$ phonon modes, respectively.*

during the cooling process need to be addressed. A potential mechanism could be the enhanced interaction between electrons in the polymer and phonons in $SiO_2$. It is well know that enhanced electron-phonon coupling in $SiO_2$ in one of the reasons for its high breakdown strength. Secondly, the role of the initiator species needs to be clarified, as the trap states appear to be determined largely by the nature of the initiator. Thirdly, a variety of $SiO_2$ and other oxide (e.g., $Al_2O_3$) surfaces should be studied to understand systematic trends across a wider class of situations.

Phonons are collective, quantized vibrations of groups of atoms, which when excited propagate through a material. Our computational method for the estimation of the interaction of electrons and phonons (i.e., excitation of phonons by energy released due to electron trapping) involved two steps. First, the phonon band structure, or spectrum, was determined, resulting in all the phonon frequencies and eigenmodes. Second, for each phonon eigenmode, the atoms of the system were displaced from their equilibrium atomic configuration as per that mode, and the associated shifts in the electronic levels were determined. With the knowledge of the phonon frequencies, modes and changes of the eigenenergies caused by the phonon modes, we can estimate the electron-phonon coupling parameter in units of energy per mode displacement length.

The interaction of electrons and phonon in $SiO_2$-polymer and $Al_2O_3$-polymer interfaces were investigated through this procedure. The geometric model for silica-polymer interface considered here has a total number of 89 atoms resulting in 247 phonon modes, while the alumina-polymer interface had a total number of 65 atoms resulting in 195 phonon modes. The calculated electron-phonon coupling for $SiO_2$-polymer interface is shown in Figure 3 (left).

As can be seen, the coupling of electrons at the interface state with phonons is high, similar to the behavior of the $SiO_2$ with O vacancies. Furthermore, the electron-phonon interaction parameter for this interface system is significantly higher than in other cases. Further analysis indicates that the phonon modes contributing to the highest electron-phonon coupling at the defect states originate from the displacement of the interfacial atoms (the atoms in vinylsilandiol). This high electron-phonon coupling could provide the reason for the high breakdown strength in the presence of interfaces.

In order to explore the impact of other oxide on the dielectric breakdown strength in the composites, the electron-phonon coupling in alumina-polymer interface was determined. As shown in Figure 3 (right), the electron-phonon coupling in this case is relatively low at the interface trap energy levels in comparison with the silica-polymer interface. The weak interaction between the phonons and electrons in the defect states indicates that the energy loss is less efficient in alumina containing composites in contrast to the silica-polymer interface.

Downloaded by CORNELL UNIV on June 21, 2012 | http://pubs.acs.org
Publication Date (Web): March 11, 2010 | doi: 10.1021/bk-2010-1034.ch002

## Summary

Understanding the fundamental relationships between the atomic level interfacial structure and electrical properties such as dielectric response and breakdown is critical. In this work, we have presented several *ab inito* based computational results that probe such structure-property relationships in systems of emerging technological importance. The theory of the local dielectric permititivy has been used to understand the variations of the static and optical dielectric constant across idealized Si-polymer interfaces over length scales of the order of interatomic distances. These variations have been correlated to the chemistry at the interfaces, such as dangling bonds and multiple oxidation states. The layer-decomposed density of states approach has been used to compute the electronic structure variation across $SiO_2$-polymer interfaces. This procedure has been used to capture band bending, band offsets and creation of trap states at interfaces. Finally, we also discussed a qualitative way in which electron-phonon interactions can be captured, which we have used to correlate with available breakdown observations. Although further work over a wider range of systems and situations is necessary, the computational tools and their applications described here constitute a promising direction for a more thorough analysis of the impact of surfaces, interfaces, and atomic level defects on the dielectric and electronic properties of a wide variety of nanostrucured systems.

## Acknowledgments

Several helpful discussions with Dr. Steven A. Boggs (Unviersity of Connecticut) and Dr. Lei Zhu (Case Western Reserve University) are gratefully acknowledged. This work was supported by grants from the ACS Petroleum Research Fund, the Office of Naval Research, the Electrical Power Research Institute and the National Science Foundation.

# References

1. Nalwa, H. S. *Handbook of Low and High Dielectric Constant Materials and Their Applications*: Academic Press: San Deigo, 1999.
2. Cao, Y.; Irwin, P. C.; Younsi, K. *IEEE Trans, Dielect. Elect. Insulation* **2004**, *797*.
3. Sargeant, W.; Zirnheld, J.; MacDougall, F. *IEEE Trans. Plasma Sci.* **1998**, *26*, 1368.
4. Green, M. L.; Gusev, E. P.; Degreave, R.; Garfunkel, E. L. *J. Appl. Phys.* **2001**, *90*, 2057.
5. Roberson, J. *Solid-State Electron.* **2005**, *49*, 283.
6. Xiong, K.; Roberson, J.; Gibson, M. C.; Clark, S. J. *Appl. Phys. Lett* **2005**, *87*, 183505.
7. Xiong, K.; Roberson, J.; Clark, S. J. *Appl. Phys. Lett.* **2006**, *89*, 022907.
8. Martin, R. *Electronic Structure: Basic Theory and Practical Methods*; Cambridge University Press: New York, 2004.
9. Hohenberg, R.; Kohn, W. *Phys. Rev.* **1964**, *136*, B864.
10. Kohn, W.; Sham, L. J. *Phys. Rev.* **1965**, *140*, A1133.
11. Soler, J. M.; Artacho, E.; Gale, J.; Garcia, A.; Junquera, J.; Ordejon, P.; Sanchez-Portal, D. *J. Phys.: Condens. Matter* **2002**, *14*, 2745–2779.
12. Kittel, C. Data collected in *Introduction to Solid State Physics*, 5th ed.; Wiley: New York, 1976; and references therein.
13. Levin, L.; Prewitt, C. T.; Weidner, D. J. *Phys. Rev. B* **1992**, *46*, 1–14.
14. WyckoffR. W. G. *Crystal Structure*, 4th ed.; Intersicence: New York, 1974; and references therein.
15. Picaud, E.; Smogunove, A.; Dal Corso, A.; Tosatti, E. *J. Phys.: Condens. Matter* **2003**, *15*, 3731–3740.
16. Rubinstein, M.; Colby, R. *Polymer Physics*; Oxford University Press: New York, 2003.
17. Shi, N.; Ramprasad, R. *Phys. Rev. B.* **2006**, *74*, 045318–045321.
18. Shi, N.; Ramprasad, R. *J. Comput. Aided Mater. Des.* **2006**, *10820*, 133–139.
19. Ramprasad, R.; Shi, N. *Phys. Rev. B* **2005**, *72*, 052107–052110.
20. Shi, N.; Ramprasad, R. *Appl. Phys. Lett.* **2005**, *87*, 262102–262104.
21. Giustino, F.; Pasquarello, A. *Phys. Rev. B.* **2005**, *71*, 144104–144116.
22. Giustino, F.; Umari, P.; Pasquarello, A. *Phys. Rev. Lett.* **2003**, *91*, 267601–267604.
23. Zhao, X.; Vanderbilt, D. *Phys. Rev. B.* **2002**, *65*, 233106–233109.
24. Zhao, X.; Vanderbilt, D. *Phys. Rev. B.* **2002**, *65*, 075105–075114.
25. Sayan, S.; Emge, T.; Garfunkel, E.; Zhao, X.; Wielunski, L.; Bartynski, R.; Vanderbilt, D.; Suehle, J.; Suzer, S.; Banaszak-Holl, M. *J. Appl. Phys.* **2004**, *96*, 7485–7491.
26. Botti, S.; Vast, N.; Reining, L. et al. Ab initio calculations of the anisotropic dielectric tensor of GaAs/AlAs supperlattices, *Phys. Rev. Lett.* **2002**, *89*, 216803.
27. Jackson, J. D. *Classical Electrodynamics*; University of Califonia: Berkeley, 1998.
28. Boggs, S. *IEEE Trans. Dielectr. Electr. Insul.* **2005**, *12* (00), 929–938.

Downloaded by CORNELL UNIV on June 21, 2012 | http://pubs.acs.org
Publication Date (Web): March 11, 2010 | doi: 10.1021/bk-2010-1034.ch002

29. Teyssedre, G.; Laurent, C. *IEEE Trans. Dielectr. Insul.* **2005**, *12*, 857–875.
30. Ray, S. S.; Okamoto, M. *Prog. Polym. Sci.* **2003**, *28*, 1539–1641.
31. Rao, Y.; Wong, C. P. *J. Appl. Polym. Sci.* **2004**, *92*, 2228–2231.
32. O'Brian, Si.; Brus, L.; Murray, C. B. *J. Am. Chem. Soc.* **2001**, *123*, 12085–12086.
33. Murugaraj, P.; Mainwaring, D.; Mora-Huertas, N. *J. Appl. Phys.* **2005**, *98*, 054034–054309.
34. Roy, M.; Nelson, J. K.; MacCrone, R. K.; Schadler, L. S.; Reed, C. W.; Keefe, R.; Zenger, W. *IEEE Trans. Dielectr. Electr. Insul.* **2005**, *12*, 629–43, 1273.
35. Nelson, J. K. *IEEE Intern. Sympos. Electr. Insul.* **2006**, 452–457.
36. Kaufhold, M.; Schafer, K.; Bauer, K.; Bethge, A.; Risse, J. *IEEE Electr. Insul. Mag.* **2002**, *18* (2), 27–36.
37. Shi, N.; Ramprasad, R. *IEEE Trans. Dielectr. Electr. Insul.* **2008**, *15*, 170–177.
38. Shi, N. Properties of Nanoscale Dielectrics from First Principles Computations. Ph.D. Thesis, University of Connecticut: Storrs, CT, 2008.

Downloaded by CORNELL UNIV on June 21, 2012 | http://pubs.acs.org
Publication Date (Web): March 11, 2010 | doi: 10.1021/bk-2010-1034.ch002

Downloaded by UNIV OF DELAWARE MORRIS LIB on June 22, 2012 | http://pubs.acs.org
Publication Date (Web): March 11, 2010 | doi: 10.1021/bk-2010-1034.ch003

## Chapter 3

# Achieving Fast Discharge and Low Loss in Poly(vinylidene fluoride-*co*-chlorotrifluoroethylene)-*graft*-Polystyrene Films by Confined Ferroelectricity

**Fangxiao Guan,[1] Zhongzhe Yuan,[1] Jing Wang,[1] and Lei Zhu*,[1,2]**

**[1]Polymer Program, Institute of Materials Science and Department of Chemical, Materials and Biomolecular Engineering, University of Connecticut, Storrs, Connecticut 06269-3136**
**[2]Department of Macromolecular Science and Engineering, Case Western Reserve University, Cleveland, Ohio 44106-7202**
***lei.zhu2@case.edu**

Although a high electric energy density was recently reported for defect-modified poly(vinylidene fluoride) (PVDF) copolymers at millisecond discharge, they usually deliver less energy at a high pulse rate. In this work, a low loss polystyrene (PS) was grafted as side chains onto the P(VDF-CTFE) main chain. After crystallization of PVDF, dielectric PS side chains were segregated to the crystalline-amorphous interface, forming a finite confinement dielectric layer for ferroelectric PVDF crystals. We speculated that less space charge was induced during electric poling because of the nanoscale confinement effect. Consequently, a fast discharge speed and a relatively high energy density were achieved.

## Introduction

A high energy density pulse discharge capacitor is an important electric energy storage unit for numerous practical applications including electromagnetic generation, Marx generators, pulsed laser, and particle accelerators, where high energy density and low loss at high repetition rates are required (*1*). Currently, the state-of-the-art pulse discharge film capacitors are made from biaxially oriented polypropylene (BOPP) because of its high electric breakdown strength (730 MV/m at 63.2% Weibull failure probability and ~600 MV/m at 1% Weibull failure probability for a test area of 2.0 $cm^2$) (*2*) and very low dielectric loss (<0.0002 at 1 kHz) (*3*). BOPP is a linear dielectric material and its electric energy density ($U_e$) can be described by a linear function; $U_e = \int EdD = 0.5\varepsilon_r\varepsilon_0 E^2$, where E is the electric field, D is the electric displacement, $\varepsilon_r$ is the relative dielectric constant (2.2 for BOPP and independent of electrical fields), and $\varepsilon_0$ is the vacuum permittivity. However, BOPP cannot deliver high energy densities due to its low dielectric constant.

Poly(vinylidene fluoride) (PVDF) is a well-known ferroelectric polymer that exhibits both high dielectric constant ($\varepsilon_r$ = 10-20) and high DC breakdown strength (comparable to that of BOPP) (*4–7*). However, its typical dielectric loss (tanδ) at 1 kHz is nearly 0.02 at ambient temperature because of electric dipole relaxation. Furthermore, relatively easy phase transformations between the paraelectric α-phase and ferroelectric phases (δ,γ and β-phases) at elevated electric fields (*4*, *5*) enhance the cooperative ferroelectricity in PVDF crystals. Early polarization saturation of the ferroelectric phase decreases the electric energy discharge in PVDF. By modifying PVDF with bulky comonomers, such as chlorotrifluoroethylene (CTFE) (*6–11*) and hexafluoropropylene (HFP), P(VDF-CTFE) and P(VDF-HFP) random copolymers recently achieved an energy density as high as 17-25 $J/cm^3$ at ~600 MV/m for millisecond discharge (*6*, *7*). The high energy density is attributed to a relaxor ferroelectric behavior (*12*) achieved by introduction of bulky -Cl atoms (or $-CF_3$ side groups) into the PVDF main chain to breakup large α-form crystallites. One feature of the relaxor ferroelectric behavior is a broadly distributed phase transformation zone (*13*). However, the physical origin of the so-called relaxor ferroelectricity has not been well understood and quantified, and its relationship with different crystalline morphologies and crystal orientations has yet to be elucidated.

Both PVDF and its copolymers exhibit nonlinear dielectric and ferroelectric behaviors with nonlinear permittivity. The linear permittivity is a function of electric field and exhibits a maximum at the coercive field ($E_c$) (*14*). The nonlinear behavior at elevated electric fields complicates a direct calculation of the stored and discharged electric energy densities from the linear permittivity.

Additionally, PVDF and its copolymers differentiate themselves from other pyroelectric material by the thermally reversible polarization (*15*), which is induced by the space charge injection mechanism (*16*)(*17*). Space charge has been further recognized as the origin of high piezoelectric and pyroelectric effects for PVDF (*15*). Analogously, the high energy density of PVDF and its copolymers can also be explained by cooperative polarization-induced space charges via either charge injection, positive hole injection, or local charge splitting (*16*, *18*, *19*). However, it is also because of the slow discharge process of these induced space charges (*18*, *19*), PVDF and its copolymers deliver significantly less energy at fast pulses (*1*). For example, bubble-blown P(VDF-CTFE) films had a 40% loss in discharged energy density when the discharge time decreased from 1 ms to 1 μs (*7*). It was also shown that the injected charges could distribute non-uniformly in pulse poled PVDF films (*17*). Sometimes, they were trapped in a transition

Downloaded by UNIV OF DELAWARE MORRIS LIB on June 22, 2012 | http://pubs.acs.org
Publication Date (Web): March 11, 2010 | doi: 10.1021/bk-2010-1034.ch003

Downloaded by UNIV OF DELAWARE MORRIS LIB on June 22, 2012 | http://pubs.acs.org
Publication Date (Web): March 11, 2010 | doi: 10.1021/bk-2010-1034.ch003

zone, separating the poled part from the non-poled part and thus stabilizing the macroscopic polarization after complete discharge of the poled PVDF film.

To enable PVDF and its copolymers for advanced dielectric applications such as pulse power, an obvious strategy is to solve the practical problem related to the slow discharge of cooperative polarization-induced space charges accumulated in PVDF between the poled crystal and amorphous region. In this report, we utilized a novel concept of nanoconfinement effect to modify the ferroelectric property of PVDF crystals. Specifically, we grafted low loss dielectric polymer side chains, polystyrene (PS), onto the P(VDF-CTFE) copolymer main chain. After crystallization-induced microphase separation, PS was segregated to the crystal periphery, forming a dielectric confinement layer around the PVDF lamellar crystals. As a result, the long distance coupling (*20*) among ferroelectric crystals (or ferroelectric domains) was interrupted and less space charge was induced in the polymer matrix. A fast discharge speed and a low loss were achieved in these ferroelectric/dielectric composite films.

## Experimental Section

### Materials

P(VDF-CTFE) (Dyneon® 31008 with 7.0 mol% CTFE) was provided by courtesy of 3M. Its number-average molecular weight ($M_n$) is 180,000 g/mol and polydisperisity index (PDI) is 1.5. Statistically, each main chain contains ~180 -Cl sites. Styrene (Aldrich, 99%) was passed through a silica gel column to remove the inhibitor before use. Azobisisobutyronitrile (AIBN) was recrystallized from methanol and stored in the refrigerator. CuCl (Aldrich, 99.995+%), $CuCl_2$ (Aldrich, 99.999%), 2,2'-bipyridine (BPy, Acros, 99+%), tri(*n*-butyl)tin hydride ($nBu_3SnH$, Aldrich, 99.99%), *N*-methylpyrrolidinone (NMP, Aldrich, HPLC grade), tetrahydrofuran (THF, Aldrich, HPLC grade), and *N*,*N*-dimethylformamide (DMF, Acros, HPLC grade) were used as received without further purification.

### Graft Copolymerization of Styrene from P(VDF-CTFE) Using Atom Transfer Radical Polymerization (ATRP)

A typical graft copolymerization of styrene from P(VDF-CTFE) using ATRP (see Scheme 1) is modified from a previous report (*21*). First, a 500 mL Schlenk flask was charged with 2 g of P(VDF-CTFE), 2.33 g (14.89 mmol) of 2,2'-bipyridine, 0.4 g (4.02 mmol) of CuCl, and 54.3 mg (0.402 mmol) of $CuCl_2$. The reaction mixture was degassed for three times with nitrogen/vacuum cycles. 23 mL (205 mmol) of styrene and 28 mL of NMP were purged with dry nitrogen for about 1 h and transferred into the Schlenk flask by a nitrogen protected syringe. After all reaction agents were well mixed, the polymerization was carried out at 120 °C for 24 h. The viscous reaction mixture was diluted with acetone and passed through a column filled with fumed silica gel, followed by precipitation in 1:1 vol./vol. methanol/water. The crude product was redissolved in DMF and precipitated in 1:1 methanol/water for three times. Finally, the resulting graft copolymer, P(VDF-CTFE)-*g*-PS, was dried in a vacuum oven at room temperature for 2 d.

### Dechlorination of As-Synthesized P(VDF-CTFE)-*g*-PS

A typical dechlorination reaction of the as-synthesized P(VDF-CTFE)-*g*-PS is adapted from a previous report (*10*). First, a 500-mL round-bottom flask was charged with 3 g of P(VDF-CTFE)-*g*-PS copolymer, 285 mg (1.11 mmol) of AIBN, 180 mL of THF and 60 mL of NMP. The reaction solution was purged with nitrogen for about 1 h. Afterwards, the reaction mixture was stirred at 60 °C for 30 min, and 0.914 mL (2.22 mmol) tri(*n*-butyl)tin hydride ($n\mathrm{Bu_3SnH}$) was added dropwise by a syringe. The dechlorination reaction was carried out at 60 °C for 24 h before it was quenched with methanol. The reaction mixture was precipitated in 1:1 vol./vol. methanol/water and washed with hexane. The crude product was redissolved in DMF and precipitated in 1:1 methanol/water for three times. Finally, the product was dried in a vacuum oven at room temperature for 3 d.

Downloaded by UNIV OF DELAWARE MORRIS LIB on June 22, 2012 | http://pubs.acs.org
Publication Date (Web): March 11, 2010 | doi: 10.1021/bk-2010-1034.ch003

### Instruments and Characterization

$^1$H and $^{19}$F NMR spectra were recorded on a Bruker DMX-400 NMR spectrometer. Size exclusion chromatography (SEC) was performed in a DMF mobile phase using a Viscotek GPCMax VE2001 with a TDA 302 viscometer/light scattering/UV-Vis/refractive index (RI) quadruple detector. DSC thermograms were obtained using a TA Instruments Q20 differential scanning calorimeter (DSC) at a heating rate of 10 °C/min. Two-dimensional (2D) wide-angle X-ray diffraction (WAXD) experiment was performed on an Oxford Xcalibur Diffractometer with an ONYX CCD area detector. The wavelength of Cu $K_\alpha$ X-ray was 0.1542 nm. 2D small-angle X-ray scattering (SAXS) was performed at the synchrotron X-ray beamline X27C at National Synchrotron Light Source, Brookhaven National Laboratory. The wavelength of synchrotron X-ray was 0.1371 nm. Fuji imaging plates were used as detectors, and digital images were obtained using a Fuji BAS-2500 scanner. The typical data requisition time was 1 min. One-dimensional (1D) X-ray profiles were obtained by integration from 2D X-ray images. The *d*-spacing was calibrated using silver behenate with the first-order reflection at the scattering vector $q = 1.076\ \mathrm{nm}^{-1}$, where $q = (4\pi\sin\theta)/\gamma$ with $\theta$ being the half scattering angle.

The dissipation factor was evaluated by using a Fourier transform dielectric spectrometer (IMASS Time Domain Dielectric Spectrometer) in a frequency range from $10^{-4}$ to $10^4$ Hz.

The discharged energy density ($U_e$) was measured by an LCR circuit with a self-built 3-way solid state high voltage switch (see Figure 1), similar to that

Downloaded by UNIV OF DELAWARE MORRIS LIB on June 22, 2012 | http://pubs.acs.org
Publication Date (Web): March 11, 2010 | doi: 10.1021/bk-2010-1034.ch003

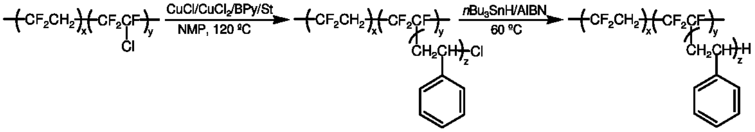

*Scheme 1. Synthesis of P(VDF-CTFE)-g-PS graft copolymers using atom transfer radical polymerization (ATRP), followed by dechlorination with nBu$_3$SnH*

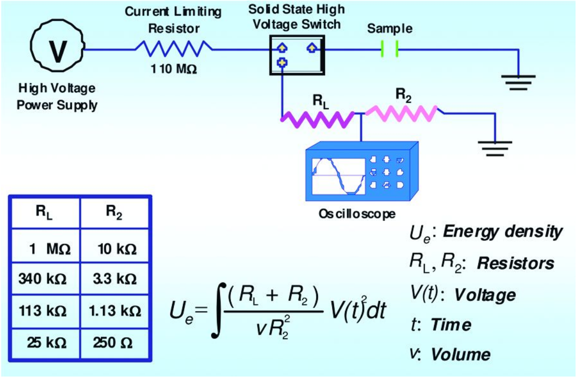
Current Limiting Resistor
110 MΩ
Solid State High Voltage Switch
Sample
V
High Voltage Power Supply
$R_L$
$R_2$
Oscilloscope

| $R_L$ | $R_2$ |
|---|---|
| 1 MΩ | 10 kΩ |
| 340 kΩ | 3.3 kΩ |
| 113 kΩ | 1.13 kΩ |
| 25 kΩ | 250 Ω |

$$U_e = \int \frac{(R_L + R_2)}{vR_2^2} V(t)^2 dt$$

$U_e$: Energy density
$R_L$, $R_2$: Resistors
$V(t)$: Voltage
$t$: Time
$v$: Volume

*Figure 1. A self-designed capacitor discharge circuit. $R_L$ is the load resistor. $R_L$ and $R_2$ can be changed to vary the discharge times, where $R_L/R_2$ is kept at 100. The turn-on time of the solid-state high voltage switch is less than 500 ns.*

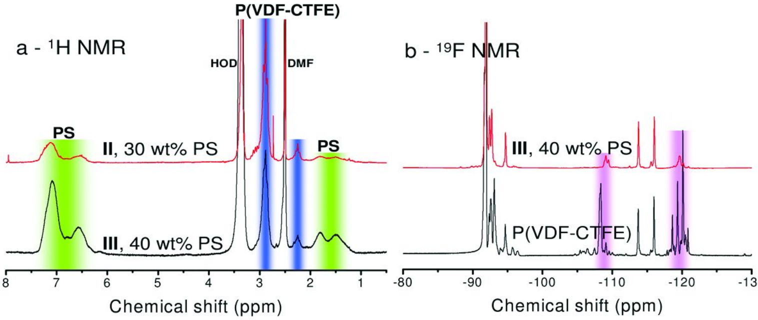

*Figure 2. (a) $^1$H and (b) $^{19}$F NMR spectra of P(VDF-CTFE) and P(VDF-CTFE)-g-PS graft copolymers with 30 and 40 wt% PS, respectively. In the $^1$H NMR spectra in (a), PS signals are located at 1.0-2.0 and 6.2-7.4 ppm, and P(VDF-CTFE) peaks are located at 2.2-2.4 and 2.7-3.1 ppm. In the $^{19}$F NMR spectra in (b), Cl-related F signals are located at -122~-118 and -109~-107 ppm.*

reported in the literature (*7*). Typical turn-on time for the solid-state high voltage switch is less than 500 ns. First, the switch was located at position 1 and a capacitor film sample was charged for 10 seconds to reach a desired voltage by a high voltage power supply. Then, the switch was switched to position 2, and the stored electric energy in the capacitor film sample was discharged through resistors $R_L$ and $R_2$.

$R_L$ could be varied so that the capacitor discharge behavior could be analyzed over a broad time range. The voltage, $V_2$ on the resistor $R_2$ was monitored by an oscilloscope. Finally, $U_e$ was calculated from the $V_2$ profile as a function of time (see Figure 7).

# Results and Discussion

## Synthesis and Characterization of P(VDF-CTFE)-*g*-PS Graft Copolymers

The successful grafting of PS side chains from the -Cl sites in P(VDF-CTFE) is proved by $^{19}$F NMR, as shown in Figure 2. Comparing the $^{19}$F NMR spectra for neat P(VDF-CTFE) and its PS-graft copolymer in Figure 2b, the Cl-related $^{19}$F signals substantially decreased for P(VDF-CTFE)-*g*-PS, indicative of the successful grafting of PS from the -Cl sites. We also performed a control experiment by replacing P(VDF-CTFE) with PVDF under the same reaction condition for ATRP, and no PS could be grafted from pure PVDF. This result clearly indicated that PS side chains were exclusively grafted from the -Cl sites in P(VDF-CTFE). The PS content was calculated from $^{1}$H NMR results shown in Figure 2a and summarized in Table 1.

SEC results for P(VDF-CTFE) and its PS-graft copolymer (40 wt% PS) are shown in Figure 3. After purification, no PS homopolymer was seen in the SEC curve for P(VDF-CTFE)-*g*-PS(40%), indicative of a high purity of the final product. Inversion of the differential RI signal for the graft copolymer from that for neat P(VDF-CTFE) suggested that PS was grafted from P(VDF-CTFE), because PS has a higher RI and P(VDF-CTFE) has a lower RI than DMF (*21*). Finally, a slight decrease in the retention volume for the P(VDF-CTFE)-*g*-PS compared with P(VDF-CTFE) suggested an increase in molecular weight after grafting reaction.

## Characterization of Crystalline Morphology in P(VDF-CTFE)-*g*-PS

Crystalline morphology in P(VDF-CTFE)-*g*-PS graft copolymers was studied by DSC, SAXS and WAXD techniques. Introduction of PS graft significantly lowered the PVDF crystallinity. For example, the PVDF crystallinity was as low as 26 wt% in P(VDF-CTFE)-*g*-PS(30%), which only corresponded to ca. 12 vol.% when the PS volume was considered, as shown in Figure 4. PS grafts increased the glass transition temperature from -27 °C for P(VDF-CTFE) up to 75 °C with 30 wt% PS. However, PS grafts did not affect much on the melting temperature.

The decrease in PVDF crystallinity after grafting PS was also confirmed from WAXD profiles in Figure 5B. Furthermore, it was inferred that the PVDF crystalline lamellar thickness in P(VDF-CTFE)-*g*-PS must have decreased as compared to that in pure PVDF, because the line width for the mixed $(021/111/120)_\alpha$ reflections was substantially broader. In addition, PS grafts eliminated the formation of β-crystals even after 500% uniaxial stretching. In

Downloaded by UNIV OF DELAWARE MORRIS LIB on June 22, 2012 | http://pubs.acs.org
Publication Date (Web): March 11, 2010 | doi: 10.1021/bk-2010-1034.ch003

Downloaded by UNIV OF DELAWARE MORRIS LIB on June 22, 2012 | http://pubs.acs.org
Publication Date (Web): March 11, 2010 | doi: 10.1021/bk-2010-1034.ch003

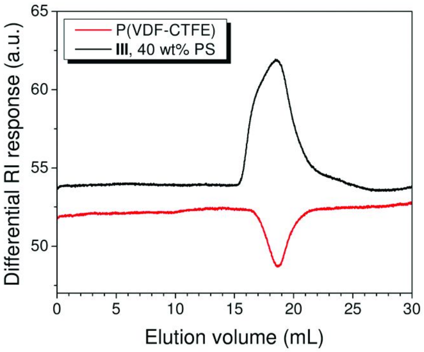

*Figure 3. Size-exclusion chromatography (SEC) of P(VDF-CTFE) and the P(VDF-CTFE)-g-PS graft copolymer with 40 wt% PS. DMF was used as the eluting solvent.*

**Table 1. Molecular Characterization Data for P(VDF-CTFE)-*g*-PS with Different PS Contents (*22*) (Reprinted from ref. (*22*). Copyright 2009 American Institute of Physics)**

<table>
<tr><td colspan="5"><i>P(VDF-CTFE), CTFE mol% = 0.07, $M_n = 1.8x10^5$ g/mol, $M_w/M_n = 1.5$, $T_m = 166$ °C</i></td></tr>
<tr><td><i>P(VDF-CTFE)-g-PS</i></td><td><i>PS (wt%)</i>[a]</td><td><i>$M_n^{PS}$ (g/mol)</i>[b]</td><td><i>$T_g$ (°C)</i></td><td><i>$T_m$ (°C)</i></td></tr>
<tr><td><b>I</b></td><td>25</td><td>328</td><td>35</td><td>163, 169</td></tr>
<tr><td><b>II</b></td><td>30</td><td>421</td><td>75</td><td>166</td></tr>
<tr><td><b>III</b></td><td>40</td><td>656</td><td>70</td><td>167</td></tr>
</table>

[a] Determined by $^1$H NMR. [b] Assuming all Cl in P(VDF-CTFE) initiated ATRP of styrene and all PS grafts had the same length.

(biaxially stretched) PVDF film, some β-crystals co-existed with α-crystals, as evidenced by the existence of the $(110/200)_\beta$ reflections in Figure 5B.

After PVDF crystallized, bulky PS grafts were excluded from the PVDF crystal as structural defects and thus formed a finite interface layer. In fact, a density fluctuation-induced disordered phase was observed in the melt at 180 °C for the graft copolymers, as evidenced by the correlation hole scattering in SAXS results in Figure 5A. However, no distinct microphase separation was observed from high magnification TEM images (data not shown) of microtomed thin-sections stained by $RuO_4$. There might be a few reasons. First, the PVDF crystallinity was low and the crystallite size was small. Second, PS grafts were too short (less than 10 monomer units) to form a distinguishable interface. Although PS would microphase separate from PVDF crystals after PVDF crystallization, it may still partially mixed with the surrounding amorphous PVDF matrix. This may be the reason that even $RuO_4$ did not provide a good contrast between PVDF crystals and $RuO_4$-stained PS.

Uniaxial stretching oriented PVDF crystals in P(VDF-CTFE)-*g*-PS films, as evidenced in Figure 6. When the X-ray beam was directed perpendicular to the

Downloaded by UNIV OF DELAWARE MORRIS LIB on June 22, 2012 | http://pubs.acs.org
Publication Date (Web): March 11, 2010 | doi: 10.1021/bk-2010-1034.ch003

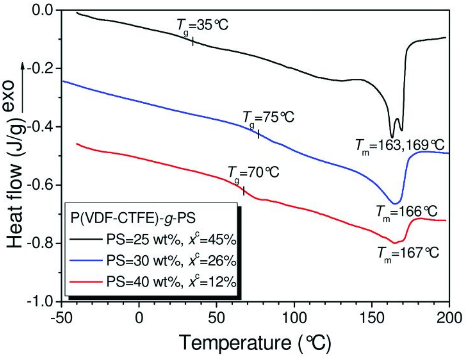

*Figure 4. Differential scanning calorimetry (DSC) curves for P(VDF-CTFE)-g-PS graft copolymers with different PS contents.*

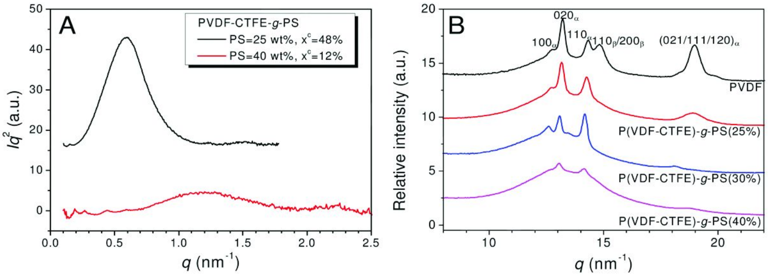

*Figure 5. A. Lorentz-corrected small-angle X-ray scattering (SAXS) profiles for P(VDF-CTFE)-g-PS samples with 25 and 40 wt% PS at 180 °C. B. Wide-angle X-ray diffraction (WAXD) profiles for PVDF and P(VDF-CTFE)-g-PS graft copolymer films with 25, 30 and 40 wt% PS at room temperature.*

drawing direction and parallel to the film, 2D WAXD patterns of both biaxially oriented PVDF (Figure 6a) and uniaxially oriented P(VDF-CTFE)-*g*-PS (Figure 6b) showed that $(100)_\alpha$ and $(110)_\alpha$ reflections for the α-form PVDF crystal centered on the equator, suggesting that PVDF chains are parallel to the drawing direction. Since folded PVDF chains are perpendicular to the crystalline lamellae, PVDF lamellar crystals should oriented perpendicular to the film.

### Dielectric Properties of P(VDF-CTFE)-*g*-PS Graft Copolymer Films

Room temperature discharge measurements were carried out at an electric field of ca. 250 MV/m to avoid electric aging or early breakdown. Typical discharge curves at different discharge times for a commercial capacitor grade PVDF (63.2% Weibull failure probability = 600 MV/m and the Weibull slope β = 12.2 for a test area of 2 cm$^2$) and P(VDF-CTFE)-*g*-PS(30%) films are shown in Figure 7. The experimental discharge time $t_0$ is defined as the time for the discharged energy in $R_L$ to reach 90% of the final value at an infinitely long time,

Downloaded by UNIV OF DELAWARE MORRIS LIB on June 22, 2012 | http://pubs.acs.org
Publication Date (Web): March 11, 2010 | doi: 10.1021/bk-2010-1034.ch003

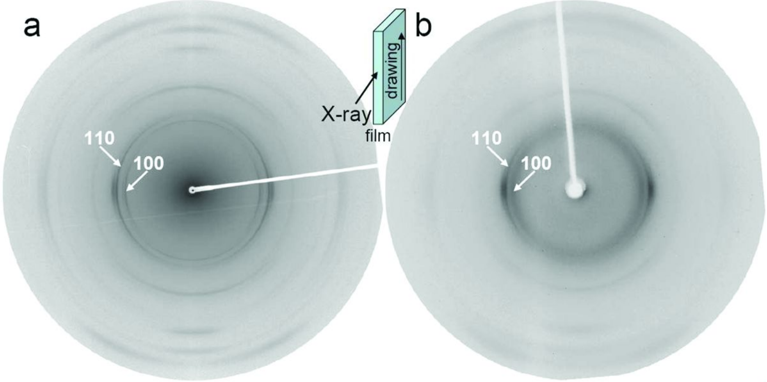

*Figure 6. 2D wide-angle X-ray diffraction (WAXD) patterns for (a) biaxially oriented PVDF and (b) uniaxially oriented P(VDF-CTFE)-g-PS(30%) films with the incident X-ray beam perpendicular to the drawing direction.*

and can be obtained directly from the discharge profiles (*7*). Figure 8a summarizes the $U_e$ as a function of the $t_0$ for PVDF, P(VDF-CTFE)-*g*-PS(30%), and BOPP. From this figure, the total discharged energy in the PVDF capacitor film increased with the $t_0$. This is similar to the results reported for the P(VDF-CTFE) 91/9 films recently (*7*). If we assume that all the energy was discharged when $R_L$ was above 1 MΩ, then the stored energy density $U_0=U_e$ and the time dependent loss can be defined as $1-U_e/U_0$. For example, when $R_L$ = 25 kΩ and $t_0$ = 22 μs, only 72% of the stored energy can be released and the time dependent loss for the PVDF capacitor film was as high as 0.28.

In contrast, P(VDF-CTFE)-*g*-PS(30%) had a faster discharge, which was close to that of BOPP (see Figure 8a). From this figure, the $U_e$ for P(VDF-CTFE)-*g*-PS(30%) was nearly constant when $R_L$ varied from 25 kΩ to 1 MΩ, and $t_0$ varied from 8 to 300 μs. This means that the stored energy density in P(VDF-CTFE)-*g*-PS(30%) can be completely discharged in a relatively short time, and the time dependent loss is almost zero.

Figure 8b compares the experimental discharge time $t_0$ with the theoretical discharge time for PVDF, P(VDF-CTFE)-*g*-PS, and BOPP. For a linear dielectric material, the theoretical relaxation time (τ) is defined from the voltage drop profile during discharge:

$$V(t) = V_0 e^{-t/\tau} \tag{1}$$

$$\tau = R_L C \tag{2}$$

Where *t* is time, $V_0$ is the starting voltage, $V(t)$ is the voltage at time *t*, and *C* is the capacitance of the capacitor. From the electric circuit in Figure 1, the

Downloaded by UNIV OF DELAWARE MORRIS LIB on June 22, 2012 | http://pubs.acs.org
Publication Date (Web): March 11, 2010 | doi: 10.1021/bk-2010-1034.ch003

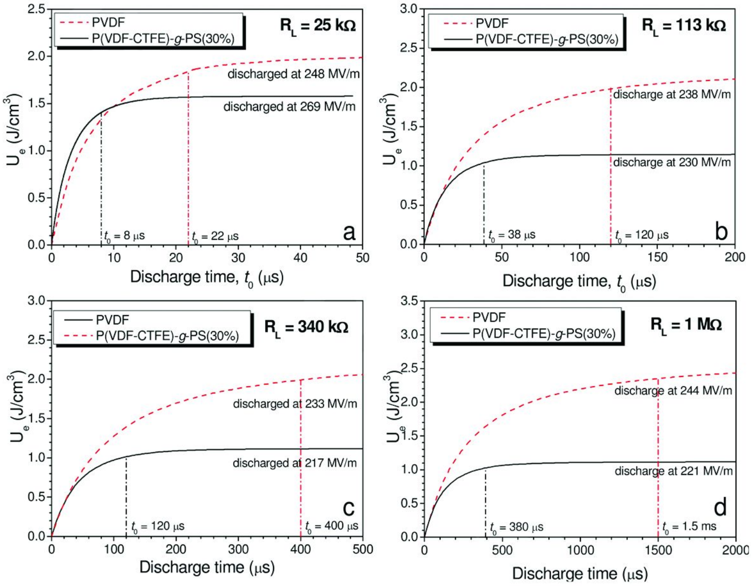

*Figure 7. Typical discharged energy density profiles for PVDF and P(VDF-CTFE)-g-PS(30%) at ca. 250 MV/m. The load resistor $R_L$ is (a) 25 kΩ, (b) 113 kΩ, (c) 340 kΩ, and (d) 1 MΩ, respectively.*

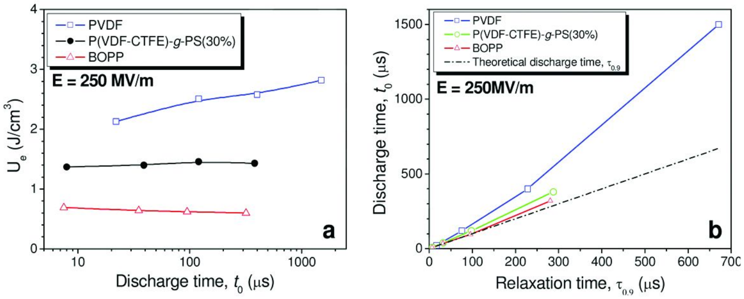

*Figure 8. (a) Discharged energy density $U_e$ as a function of the discharge time $t_0$ obtained at ca. 250 MV/m for PVDF, P(VDF-CTFE)-g-PS, and BOPP, respectively. (b) Comparison of the experimental discharge time $t_0$ with the theoretical discharge time $\tau_{0.9}$ at 250 MV/m for PVDF, P(VDF-CTFE)-g-PS, and BOPP, respectively (22). Reprinted from reference (22). Copyright 2009 American Institute of Physics.*

discharged energy density $U_e$ can be derived from the voltage discharge profile as a function of time:

$$U_e = \frac{1}{v}\int_0^t V(t)I(t)dt = \frac{1}{v}\int_0^t V_2 \cdot \frac{R_L + R_2}{R_2} \cdot \frac{V_2}{R_2} \cdot dt = 0.5M\tau V_0^2(1-e^{-2t/\tau}) \qquad (3)$$

Downloaded by UNIV OF DELAWARE MORRIS LIB on June 22, 2012 | http://pubs.acs.org
Publication Date (Web): March 11, 2010 | doi: 10.1021/bk-2010-1034.ch003

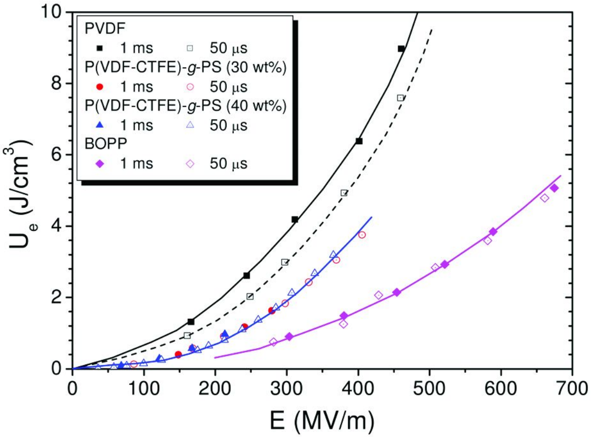

*Figure 9. Discharged energy density as a function of applied electric field for PVDF, P(VDF-CTFE)-g-PS graft copolymers, and BOPP at different discharge times, 1 ms and 50 μs, respectively (22). Reprinted from reference (22). Copyright 2009 American Institute of Physics.*

Where *v* is the volume of the capacitor film, *I*(*t*) is the current, $V_2$ is the voltage on $R_2$, and $M = (R_L + R_2)/(v \cdot R_2^2)$. At *t*→∞, $U_e(\infty) = 0.5 M \tau V_0^2$. Therefore, $U_e = U_e(\infty) \cdot (1 - e^{-2t/\tau})$, and theoretical discharge time at 90% of $U_e(\infty)$, $\tau_{0.9}$, can be obtained as:

$$\tau_{0.9} = [-0.5 \ln(1 - 0.90)]\tau = 1.15\,\tau \tag{4}$$

Obviously, P(VDF-CTFE)-*g*-PS(30%) and BOPP had a fast discharge time, which was comparable to the theoretical $\tau_{0.9}$. Instead, PVDF showed a substantially longer discharge time than $\tau_{0.9}$, which can be attributed to the slow discharge of polarization-induced space charges in PVDF at an elevated electric field of 250 MV/m.

The discharged energy densities as a function of the applied electric field for various samples are shown in Figure 9. The discharged energy density for PVDF at 1 ms was consistently higher than that at 50 μs, and this demonstrated the typical slow discharge of induced space charges. P(VDF-CTFE)-*g*-PS samples exhibited lower discharged energy density as compared to that of PVDF, but still more than twice that of BOPP. This can be attributed to less space charge induced in the system. For two P(VDF-CTFE)-*g*-PS samples with different crystallinities ($x_c$ = 26 and 12 wt% for 30 and 40 wt% PS contents, respectively), the discharged energy densities at different discharge times (50 μs and 1 ms when $R_L$ = 25 kΩ and 1 MΩ, respectively) were nearly the same, indicating that they both had a relatively fast discharge (< 8 μs) of all the electric energy stored. Note that a fast discharge is typical for a linear dielectric material such as BOPP, since it does

Downloaded by UNIV OF DELAWARE MORRIS LIB on June 22, 2012 | http://pubs.acs.org
Publication Date (Web): March 11, 2010 | doi: 10.1021/bk-2010-1034.ch003

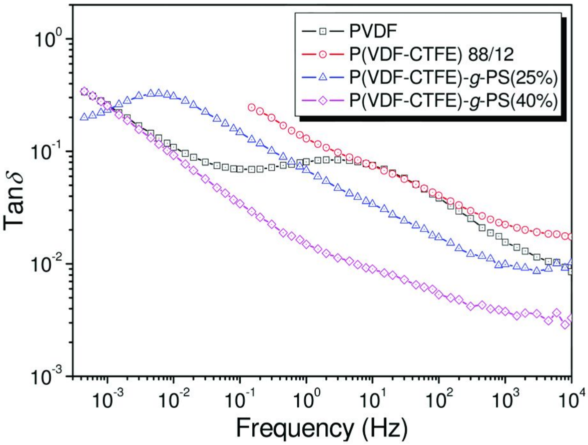

*Figure 10. Dissipation factor (tanδ) as a function of frequency for PVDF, P(VDF-CTFE) 88/12, P(VDF-CTFE)-g-PS graft copolymers, respectively.*

not have any induced space charges. Interestingly, the discharged energy density for the high crystallinity sample was the same as that for the low crystallinity sample, suggesting that crystallinity is not so important here, and this needs further investigation in the future.

The frequency-dependent loss of P(VDF-CTFE)-*g*-PS films can be determined by measuring the dissipation factor, tan*δ*. Figure 10 shows the dissipation factor of P(VDF-CTFE)-*g*-PS copolymer over a frequency range from $10^{-4}$ to $10^4$ Hz. The result for P(VDF-CTFE) 88/12 is also showed in Figure 10 for comparison. It can be seen that the dissipation factor for P(VDF-CTFE)-*g*-PS graft copolymers were consistently lower than both PVDF and P(VDF-CTFE) 88/12. Especially, P(VDF-CTFE)-*g*-PS(40%) had the lowest frequency dependent loss, i.e., 0.003 at 1 kHz. Apparently, this reduction in loss can be attributed to the incorporated low loss PS grafts and the increased amorphous content.

To understand the fast discharge and low loss behavior for P(VDF-CTFE)-*g*-PS graft copolymers, space charge accumulation at the crystalline/amorphous interface and polarization contributions from both amorphous and crystalline (α and β) phases need to be considered (see schematics in Figure 11). First, introducing dielectric PS grafts into P(VDF-CTFE) substantially decrease the α-phase crystallinity (see Table 1 and DSC results in Figure 4) and thus increased the amorphous content. Amorphous PVDF has a linear but weak polarization, while the crystals have a non-linear and strong polarization as a function of the applied electric field (*23*). Consequently, less PVDF crystallinity will result in less induced space charge. This is the reason why P(VDF-CTFE)-*g*-PS stores less energy than PVDF (and also its copolymers). Second, for PVDF, polar crystalline phases (δ- and β-forms) can be induced at elevated electric fields, and thus dipoles in these polar crystalline phases will orient along the external electric field. As a result, space charges have to be induced at the crystalline-amorphous interfaces to compensate local polarization (*16*, *18*, *19*), and they will further induce and stabilize polarization in the crystalline phase. This is the reason why

Downloaded by UNIV OF DELAWARE MORRIS LIB on June 22, 2012 | http://pubs.acs.org
Publication Date (Web): March 11, 2010 | doi: 10.1021/bk-2010-1034.ch003

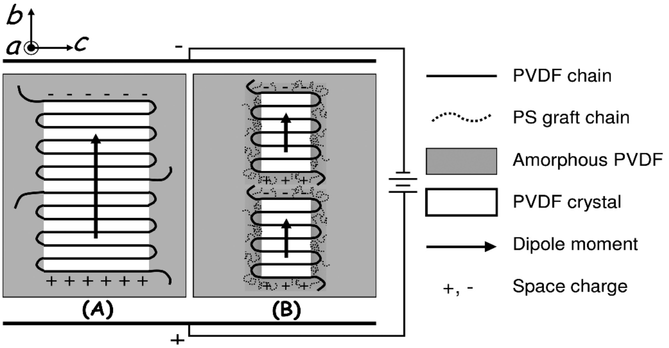

*Figure 11. Schematic representation of electric poling-induced dipole moment orientation (dark arrows) and space charge distribution in (A) PVDF and (B) P(VDF-CTFE)-g-PS, respectively. The PVDF chain (or c) axes along the drawing direction are perpendicular to crystalline lamellae in the film (22). Reprinted from reference (22). Copyright 2009 American Institute of Physics.*

PVDF and its random copolymers can store more charges/energy than linear dielectrics (Figure 9). In the discharge process, space charges need to be removed to disorient the dipole moment to its random state and give out the stored electric energy. However, the removal of interfacial charges takes time, and this is the reason why PVDF delivers significantly less energy for fast pulses (*18*, *19*, *24*). For P(VDF-CTFE)-*g*-PS graft copolymers, PVDF crystals are confined by a layer of glassy and dielectric PS after PVDF crystallization. We speculate that the paraelectric (α) to ferroelectric (δ and β) phase transitions and dipole orientation may become more difficult due to the confinement effect. As a result, the induced space charge is less than that in PVDF (see Figure 11). Meanwhile, due to the interruption from dielectric PS confining layers, depolarization field penetration may be destroyed, and long-range dipole-dipole coupling becomes lost.

## Conclusions

In sum, fast discharge and low loss were achieved in P(VDF-CTFE)-*g*-PS graft copolymers because of less space charge induced in the sample due to the confinement effect from the nonpolar PS interfaces surrounding the PVDF crystals.

## Acknowledgments

The authors are in debt to Prof. Steven Boggs at University of Connecticut for helpful discussion. Ms. Essay W. Shu helped the design and fabrication of the discharge energy density measurement LCR circuit. Financial support from ONR (N00014-05-1-0338) is greatly acknowledged.

# References

1. MacDougall, F.; Ennis, J.; Yang, X. H.; Seal, K.; Phatak, S.; Spinks, B.; Keller, N.; Naruo, C.; Jow, T. R. In *Large High Energy Density Pulse Discharge Capacitor Characterization*, IEEE International Pulsed Power Conference, Monterey, CA, 2005; pp 1−4.
2. Ho, J.; Ramprasad, R.; Boggs, S. *IEEE Trans. Dielectr. Electr. Insul.* **2007**, *14*, 1295–1301.
3. Rabuffi, M.; Picci, G. *IEEE Trans. Plasm. Sci.* **2002**, *30*, 1939–1942.
4. Lovinger, A. J. *Science* **1983**, *220*, 1115–1121.
5. Tashiro, K. Crystal Structure and Phase Transition of PVDF and Related Copolymers. In *Ferroelectric Polymers: Chemistry, Physics, and Applications*, 1st ed.; Nalwa, H. S., Ed.; Dekker: New York, 1995; pp 63−182.
6. Chu, B. J.; Zhou, X.; Ren, K. L.; Neese, B.; Lin, M. R.; Wang, Q.; Bauer, F.; Zhang, Q. M. *Science* **2006**, *313*, 1887–1887.
7. Zhou, X.; Chu, B. J.; Neese, B.; Lin, M. R.; Zhang, Q. M. *IEEE Trans. Dielectr. Electr. Insul.* **2007**, *14*, 1133–1138.
8. Wang, Z. M.; Zhang, Z. C.; Chung, T. C. M. *Macromolecules* **2006**, *39*, 4268–4271.
9. Lu, Y. Y.; Claude, J.; Neese, B.; Zhang, Q. M.; Wang, Q. *J. Am. Chem. Soc.* **2006**, *128*, 8120–8121.
10. Lu, Y. Y.; Claude, J.; Zhang, Q. M.; Wang, Q. *Macromolecules* **2006**, *39*, 6962–6968.
11. Zhang, Z. C.; Chung, T. C. M. *Macromolecules* **2007**, *40*, 783–785.
12. Ranjan, V.; Yu, L.; Nardelli, M. B.; Bernholc, J. *Phys. Rev. Lett.* **2007**, *99*, 047801.
13. Samara, G. A. *J. Phys.: Condens. Matter* **2003**, *15*, R367–R411.
14. Furukawa, T.; Nakajima, K.; Koizumi, T.; Date, M. *Jpn. J. Appl. Phys.* **1987**, *26*, 1039–1045.
15. Pfister, G.; Abkowitz, M.; Crystal, R. G. *J. Appl. Phys.* **1973**, *44*, 2064–2071.
16. Mizutani, T.; Nagata, T.; Ieda, M. *J. Phys. D: Appl. Phys.* **1984**, *17*, 1883–1887.
17. Butenko, A. F.; Fedosov, S. N.; Sergeeva, A. E. Trapping of Compensating Charges in Corona Poled PVDF Films. http://arxiv.org/abs/0704.3449, 2007.
18. von Seggern, H.; Fedosov, S. N. *Appl. Phys. Lett.* **2002**, *81*, 2830–2832.
19. Fedosov, S. N.; von Seggern, H. *J. Appl. Phys.* **2008**, *103*, 014105.
20. Stephanovich, V. A.; Luk'yanchuk, I. A.; Karkut, M. G. *Phys. Rev. Lett.* **2005**, *94*, 047601.
21. Zhang, M. F.; Russell, T. P. *Macromolecules* **2006**, *39*, 3531–3539.
22. Guan, F. X.; Yuan, Z. Z.; Shu, E. W.; Zhu, L. *Appl. Phys. Lett.* **2009**, *94*, 052907.
23. Rollik, D.; Bauer, S.; Gerhard-Multhaupt, R. *J. Appl. Phys.* **1999**, *85*, 3282–3288.
24. Womes, M.; Bihler, E.; Einsenmenger, W. *IEEE Trans. Dielectr. Electr. Insul.* **1989**, *24*, 461–468.

Downloaded by UNIV OF DELAWARE MORRIS LIB on June 22, 2012 | http://pubs.acs.org
Publication Date (Web): March 11, 2010 | doi: 10.1021/bk-2010-1034.ch003

## Chapter 4

# Ferroelectric Polymer Based Nanocomposites for Electrical Energy Storage

**Junjun Li, Paisan Khanchaitit, and Qing Wang***

**Department of Materials Science and Engineering, The Pennsylvania State University, University Park, Pennsylvania 16802, USA**
***wang@matse.psu.edu**

Downloaded by PENNSYLVANIA STATE UNIV on June 21, 2012 | http://pubs.acs.org
Publication Date (Web): March 11, 2010 | doi: 10.1021/bk-2010-1034.ch004

Polyvinylidene fluoride (PVDF)-based ferroelectric polymers exhibit much higher electrical energy storage capability than other linear dielectric polymers. To further improve and tailor the dielectric properties of polymers, nanocomposites based on ceramic nanoparticles and polymer matrices have been prepared as a means of engineering dielectric property and energy storage capacity.

## Introduction

The continued success of dielectric polymers in capacitor applications imposes a challenge to improve energy density of these materials for advanced electronic devices and electric power systems with reduced weight, size and cost (*1–3*). Recently, nanocomposites composed of ceramic particles and polymer matrices have been prepared as a means of engineering dielectric property and energy storage capacity (*4*). The idea underlying this composite approach is to integrate complementary elements, such as high dielectric permittivity from the inorganic dopants and high breakdown strength from the polymer matrix, for a substantially enhanced energy density (*5*). In general, the energy density of a diphasic composite is the sum of the energy density of each constituent. In most of the ceramic-polymer composites, the volume fractions of the two constituents are on the same order of magnitude. Therefore, to achieve a high energy density of a composite, a sizeable energy density from each constitute must be needed.

The polymers currently used as matrices in the dielectric nanocomposites, including polyethylenes, poly(methyl methacrylate)s, epoxy resins, and

In Functional Polymer Nanocomposites for Energy Storage and Conversion; Wang, Q., et al.;
ACS Symposium Series; American Chemical Society: Washington, DC, 2010.

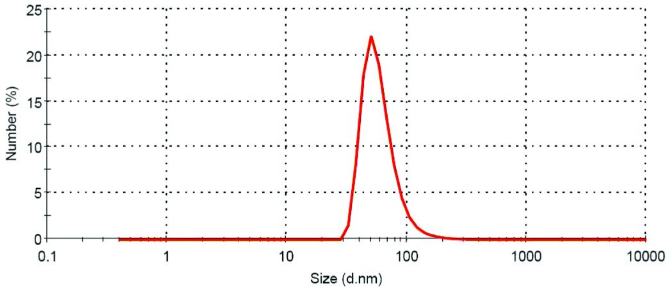

*Figure 1. The particle size distribution of surface-modified $BaTiO_3$ particles in DMF (1mg/ml) by DLS.*

Downloaded by PENNSYLVANIA STATE UNIV on June 21, 2012 | http://pubs.acs.org
Publication Date (Web): March 11, 2010 | doi: 10.1021/bk-2010-1034.ch004

polyimides, usually possess dielectric permittivities of ~2-5 that are significantly lower than their inorganic counterparts, thus severely limiting the energy density obtained in the polymer matrix and consequently, in the resulting composites (*6–9*). Ferroelectric poly(vinylidene fluoride) (PVDF) and its copolymers, such as poly(vinylidene fluoride-*co*-trifluoroethylene) [P(VDF-TrFE)] and poly(vinylidene fluoride-*co*-hexafluoropropylene) [P(VDF-HFP)], have also been utilized in the formation of the dielectric nanocomposites, owing to their relatively high dielectric permittivity at approximate 10 (*10–13*). The unique dielectric properties of PVDF based polymers originate from the presence of highly electronegative fluorine on the polymer chains and the spontaneous alignment of the C-F dipoles in the crystalline phases (*14*). However, dispersion of inorganic fillers in these fluorinated polymers is always problematical because of the low surface energy of the polymers. The agglomeration of the ceramic dopants gives rise to electron conduction for a high dielectric loss and undesirable porosity for dielectric failure at much lower fields. Surface-functionalization of nanoparticles was normally adopted to improve the miscibility of polymer matrices and ceramic dopants. In the first part of this contribution, nanocomposites comprised of the ferroelectric polymers and surface-functionalized $BaTiO_3$ nanoparticles were prepared. The effect of polymer matrix on the energy storage capability of the nanocomposites has been examined.

On the other hand, although most of the current studies on dielectric nanocomposites are focused on the enhancement of dielectric permittivity, the inclusion of nanoparticles with permittivities on the order of hundreds and even thousands into polymers, which generally possess a permittivity less than 10, might not be desirable for an appreciable increase in energy density. As the filler has a much greater permittivity than the polymer matrix, most of the increase in effective dielectric permittivity comes from an increase in the average field in the polymer matrix with very little of the energy being stored in the high permittivity filler phase (*15*). Furthermore, the presence of a large contrast in permittivity between two phases gives rise to a highly inhomogeneous electric field and thus a significantly reduced effective breakdown strength of the composite (*16*). In the second part, we describe the high-energy-density polymer nanocomposites based on surface-functionalized $TiO_2$ nanocrystals as dopant in a ferroelectric poly(vinylidene fluoride-ter-trifluoroethylene-ter-chlorotrifluoroethylene) (P

(VDF- TrFE-CTFE)). The choices of polymer matrix and the dopant are based on the fact that P(VDF- TrFE-CTFE) and $TiO_2$ filler possess comparable dielectric permittivities. High dielectric performance in the nanocomposites is realized via the large enhancement in polarization response at high electric fields and changes in polymer microstructure induced by the nanofillers.

## Experimental

### Sample Preparation

Ferroelectric poly(vinylidene fluoride-*co*-chlorotrifluoroethylene) [P(VDF-CTFE) 91/9 mol %] and poly(vinylidene fluoride-*ter*-trifluoroethylene-*ter*-chlorotrifluoroethylene) [P (VDF-TrFE-CTFE) 78.8/5.4/15.8 mol %] were employed as matrices in the nanocomposites investigated herein. P(VDF-TrFE-CTFE) was synthesized by a suspension polymerization of VDF and CTFE followed by a partial dechlorination of CTFE (*17*, *18*).

Crystalline $BaTiO_3$ nanoparticles were prepared via decomposition of ethylene diamine modified titanium(IV) isopropoxide and barium hydroxide in aqueous solution (*19*). The nanoparticles were characterized by X-ray diffraction (XRD), scanning electron microscopy (SEM), transmission electron microscopy (TEM), and Fourier transform infrared spectroscopy (FTIR) (*19*).

The $TiO_2$ nanoparticles with a rod-shaped dimension (~20 nm× 70 nm) were prepared via a hydrothermal reaction of titanium tetraisopropoxide ($Ti(O\mathit{i}Pr)_4$) and hydrogen peroxide at 100 °C for 12 h. The surfaces of the $TiO_2$ nanoparticles were then modified by refluxing in aqueous $CO_2$-free barium hydroxide solution for 2 h under Ar atmosphere following a procedure described elsewhere (*20*).

The nanocomposite films were prepared by mixing the polymer and nanoparticles in N,N-dimethylformamide (DMF). This mixture was stirred using Vibra-Cell high intensity ultrasonic processor (VC-505) at 20% power for 15 min to break agglomeration, and then poured onto clean glass slide and dried at 70 °C, followed by further annealing at 120 °C in a vacuum oven to remove the remaining trace of solvent. The resulting films were further melt pressed at 200°C for P(VDF-CTFE) based composites and 160 °C for P(VDF-TrFE-CTFE) based composites under 3000 psi.

### Materials Characterizations

Molecular weights and polydispersity of the P(VDF-CTFE) and P (VDF-TrFE-CTFE) were determined in a DMF mobile phase at a flow rate of 1.0 mL/min using gel permeation chromatography. The instrument is Viscotek Model 302 triple detection system equipped with refractive index, right angle light scattering and viscometer detectors, and the columns were Viscogel I-Series for intermediate polar polymers. The thermal transition data were obtained by a TA Instrument Q100 differential scanning calorimeter at a heating rate of 10 °C/min.

Downloaded by PENNSYLVANIA STATE UNIV on June 21, 2012 | http://pubs.acs.org
Publication Date (Web): March 11, 2010 | doi: 10.1021/bk-2010-1034.ch004

Downloaded by PENNSYLVANIA STATE UNIV on June 21, 2012 | http://pubs.acs.org
Publication Date (Web): March 11, 2010 | doi: 10.1021/bk-2010-1034.ch004

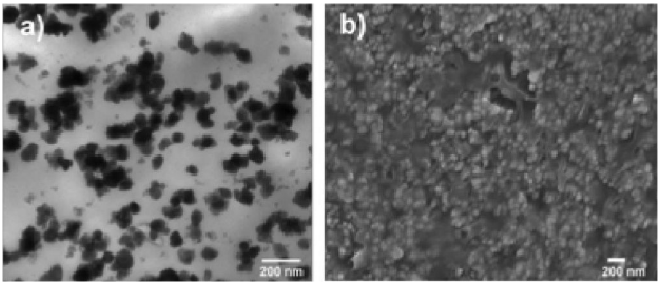

*Figure 2. (a) TEM image of P(VDF-CTFE)-$BaTiO_3$composites with 5 vol % $BaTiO_3$. (b) Cross-sectional FE-SEM image of the P(VDF-TrFE-CTFE)-$BaTiO_3$nanocomposite thin film containing 23 vol % $BaTiO_3$.*

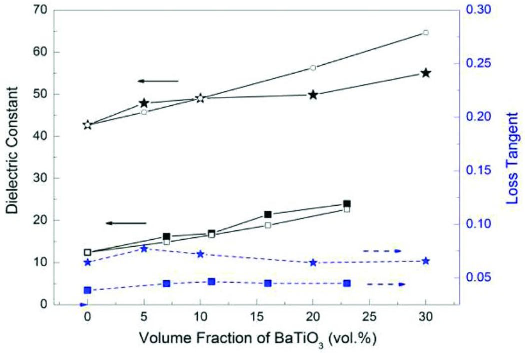

*Figure 3. Dielectric constant and loss tangent of the P(VDF-TrFE-CTFE)-$BaTiO_3$ (star) and P(VDF-CTFE)-$BaTiO_3$ (square) nanocomposites measured at 1 kHz and room temperature. Open circles and squares are the calculated effective permittivity from the Lichtenecker law for the P(VDF-TrFE-CTFE) and P(VDF-CTFE) based composites, respectively.*

Wide-angle X-ray diffraction measurements were conducted using a Scintag diffractometer with Cu Kα radiation (wavelength $\lambda$=0.154 nm). Transmission scanning microscopy experiments were performed using JEOL JEM-1200 EX II TEM equipment and the sample was made by cryo-microtome. The uniformity of nanocomposites was examined by field-emission scanning electron microscope JEOL 6700F (FESEM) of the fractured surface. To examine the dielectric properties of composites, circular gold electrodes with diameter of 2.6 mm and a typical thickness of 30 nm were sputtered on both sides of the films for the electric measurements. Dielectric constant and loss at room temperature were measured using an Agilent LCR meter (E4980A). Dielectric relaxation spectroscopy of the polymer and nanocomposites at frequencies ranging from 100 to 1 MHz has been investigated using a LCR meter equipped with a temperature chamber. The temperature range is -50 - 100 °C. The energy density of samples was measured by a modified Sawyer-Tower circuit.

Downloaded by PENNSYLVANIA STATE UNIV on June 21, 2012 | http://pubs.acs.org
Publication Date (Web): March 11, 2010 | doi: 10.1021/bk-2010-1034.ch004

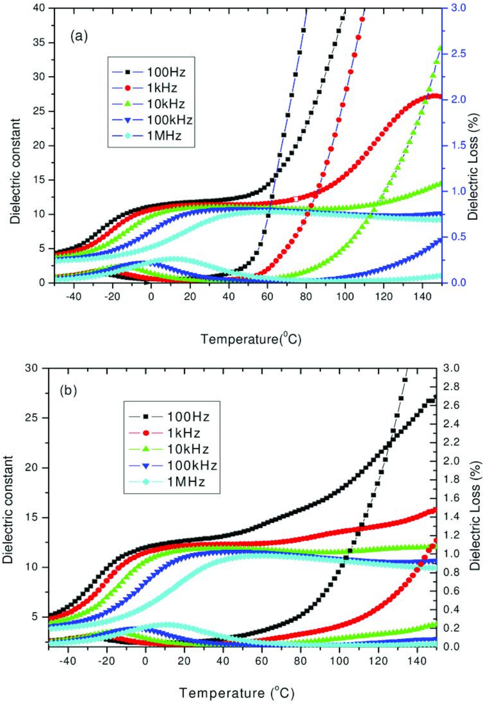

*Figure 4. Temperature dependence of dielectric responses of a) P (VDF-CTFE) and b) P (VDF-CTFE) –$BaTiO_3$ with 11 vol % $BaTiO_3$ at different frequencies in the cooling process [dielectric constant (from top to bottom), and dielectric loss (from bottom to top)]: 0.1 k, 1 k, 10 k, 100 k, and 1 MHz.*

# Polymer-$BaTiO_3$ Nanocomposites

## Structure and Morphology

The chemical composition of the resulting P(VDF-CTFE) polymer was calculated according to the integrals of the characteristic peaks in $^1H$ and $^{19}F$ NMR spectra (*21*). The absolute weight-average molecular weight of the polymer, determined by gel permeation chromatography (GPC) in DMF, is ~240 kDa with a polydispersity of 3.40.

The chemical functionalization of the $BaTiO_3$ nanoparticles with ethylene diamine moieties on the surface renders the particles a greatly enhanced dispersibility in organic solvents and in turn a homogeneous distribution in the polymer matrix. The dynamic light scattering (DLS) measurements (Figure 1) disclose an average aggregation size of ~60 nm for the suspension of the ethylene diamine-stabilized $BaTiO_3$ nanoparticles in DMF. The uniformity of the nanocomposite films is evidenced in the cryo-microtomed TEM and cross-sectional field-emission SEM (FE-SEM) images as shown in Figure 2, where the $BaTiO_3$ nanoparticles are homogeneously dispersed in the polymer

Downloaded by PENNSYLVANIA STATE UNIV on June 21, 2012 | http://pubs.acs.org
Publication Date (Web): March 11, 2010 | doi: 10.1021/bk-2010-1034.ch004

matrix with an average particle size of ~50-70 nm. The typical thickness of the nanocomposite film for the dielectric measurements is ~25 μm.

## Dielectric Properties

A dielectric permittivity of 180 at 1 kHz was determined on the ethylene diamine-functionalized $BaTiO_3$ nanoparticle using impedance spectroscopy (*22*). Dielectric permittivity and loss tangent of pristine polymer and nanocomposties were measured from 100 Hz to 2 MHz (*23*). The variation of the weak-field dielectric permittivity and loss tangent with the nanoparticle concentration in the nanocomposites is plotted in Figure 3. The dielectric permittivity steadily increases with the increase of the $BaTiO_3$ content, which is ascribed to a higher permittivity of the filler relative to the polymer matrix. At a 20 vol % content of the $BaTiO_3$ nanoparticle, P(VDF-TrFE-CTFE) based nanocomposite exhibits a dielectric permittivity of 50, whereas a permittivity of 24 was found in the P(VDF-CTFE) based nanocomposite. The effective dielectric permittivity of the nanocomposite was calculated based on the Lichtenecker logarithmic rule, which is commonly used in a two-phase composite system: $\log \varepsilon = y_1 \log \varepsilon_1 + y_2 \log \varepsilon_2$, where $y_1$ and $y_2$ denote the volume fractions of ceramic fillers and polymer matrix which have dielectric permittivities of $\varepsilon_1$ and $\varepsilon_2$, respectively (*24*). As shown in Figure 3, the calculated results agree reasonably well with the experimental data except at high BaTiO3 concentrations (>20 vol %) in the P(VDF-TrFE-CTFE)-based composites where the Lichtenecker logarithmic law overpredicts those measured. It is also noteworthy that the dielectric loss of the nanocomposites arises primarily from the polymer matrices and is almost independent of the volume content of the $BaTiO_3$ filler, further indicating a minimized agglomeration of the filler in the nanocomposites.

Temperature dependence of the dielectric permittivity and loss tangent of the polymers and nanocomposites at frequencies ranging from $10_2$ to $10_6$ Hz has been investigated using a LCR meter equipped with a temperature chamber at 1 V bias. As illustrated in Figure 4, the dielectric spectra of the nanocomposites are dominated by the dielectric responses of the polymer matrix. For the polymers, the dielectric relaxation peaks shift progressively toward high temperatures with an increase of frequency, corresponding to glass-transition related micro-Brownian motions of chain segments in the amorphous region. At temperatures above 60 °C, both the dielectric permittivity and loss increase markedly with temperature at low frequencies, which are usually interpreted as the Maxwell-Wagner-Sillars (MWS) interfacial polarization in heterogeneous systems and conduction from space charge. The introduction of the $BaTiO_3$ nanoparticles into the polymers drastically decreases the weak-field dielectric permittivity and loss at high temperatures (>60 °C) and low frequencies (e.g., 100 Hz), implying that an increased trapping density in the nanocomposites suppresses the space charge effect and reduces the conduction loss (*25*). The surface groups of the $BaTiO_3$ and the nanoparticle/polymer interface are possible charge trapping centers.

Downloaded by PENNSYLVANIA STATE UNIV on June 21, 2012 | http://pubs.acs.org
Publication Date (Web): March 11, 2010 | doi: 10.1021/bk-2010-1034.ch004

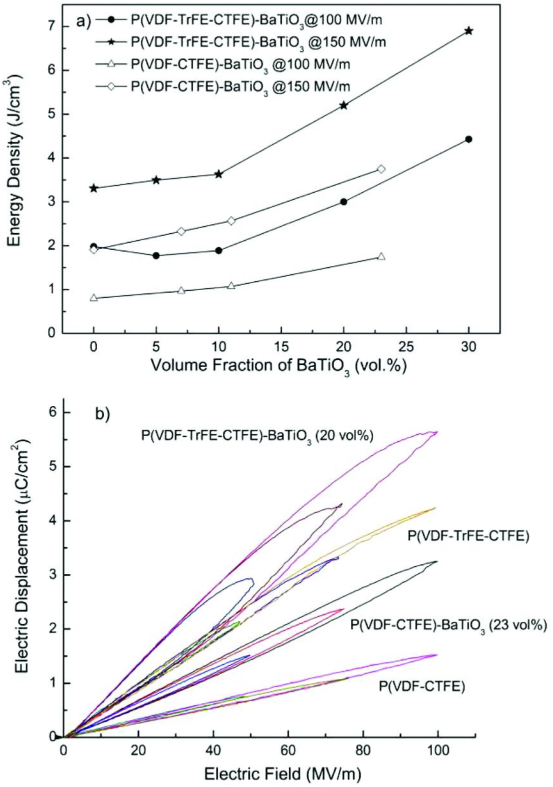

*Figure 5. (a) The dependence of energy density on the BaTiO3content in the P(VDF-TrFE-CTFE) and P(VDF-CTFE) based nanocomposites measured under 100 and 150 MV/m. (b) Electric displacement-field (D-E) loop measured under different applied fields at room temperature and 10 Hz for the polymers and nanocomposites.*

The electrical energy density of the polymers and nanocomposites was measured at various electric field. As summarized in Figure 5, the addition of the $BaTiO_3$ nanoparticles into the polymers greatly increases the energy density of the materials. At 150 MV/m, the stored energy density of the P(VDF-TrFE-CTFE) composite with 30 vol % $BaTiO_3$ is 7.0 J/cm$^3$, which corresponds to a ~120% improvement compared with pure P(VDF-TrFE-CTFE) with a energy density of 3.2 J/cm$^3$. For P(VDF-CTFE), the achieved stored energy density nearly doubles from 1.9 J/cm$^3$ to 3.7 J/cm$^3$ for the nanocomposite containing 23 vol % $BaTiO_3$ nanoparticles under the same field. These energy densities far exceed those reported in the composites based on the conventional polymers such as epoxy and polyethylene, which are less than 3 J/cm$^3$ in most cases (*8*, *9*). Importantly, the P(VDF-TrFE-CTFE) based nanocomposites generally exhibit much higher energy densities than the corresponding composites based on P(VDF-CTFE). This is in accordance with the weak-field trend presented in Figure 3 and can be attributed

Downloaded by PENNSYLVANIA STATE UNIV on June 21, 2012 | http://pubs.acs.org
Publication Date (Web): March 11, 2010 | doi: 10.1021/bk-2010-1034.ch004

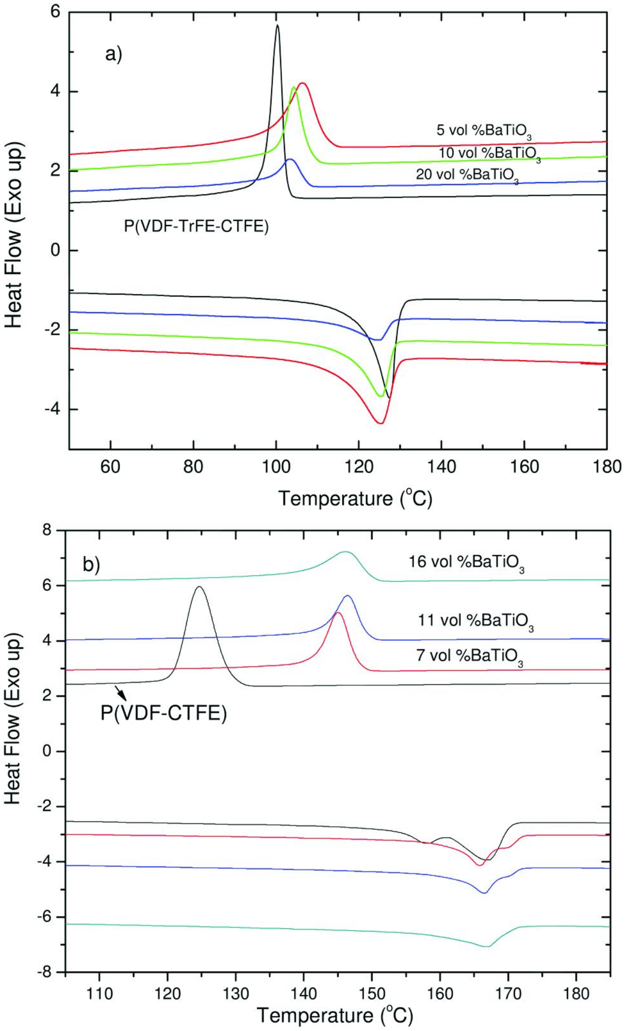

*Figure 6. DSC profiles of a) P (VDF-TrFE-CTFE) and nanocomposites with $BaTiO_3$; b) P (VDF-CTFE) and nanocomposites with $BaTiO_3$*

to larger electric displacement achieved in the P(VDF-TrFE-CTFE) matrix. As exampled in Figure 5b, under a field of 100 MV/m the electric displacement reaches more than 5.6 μC/cm$^2$ in the P(VDF-TrFE-CTFE) composite with 20 vol % $BaTiO_3$, while the electric displacement in the composite composed of P(VDF-CTFE) and the same volume content of $BaTiO_3$ is less than 3.3 μC/cm$^2$. Similarly, the incorporation of the nanoparticles notably raises the electric displacement, which accounts for the remarkably improved energy densities in the nanocomposites over the pristine polymer. As also shown in Figure 5b, compared to the polymer matrix, the nanocomposites exhibit increased polarization hysteresis and dielectric loss, which also increase progressively with the applied field. These results are consistent with earlier studies, indicating strong charge

Downloaded by PENNSYLVANIA STATE UNIV on June 21, 2012 | http://pubs.acs.org
Publication Date (Web): March 11, 2010 | doi: 10.1021/bk-2010-1034.ch004

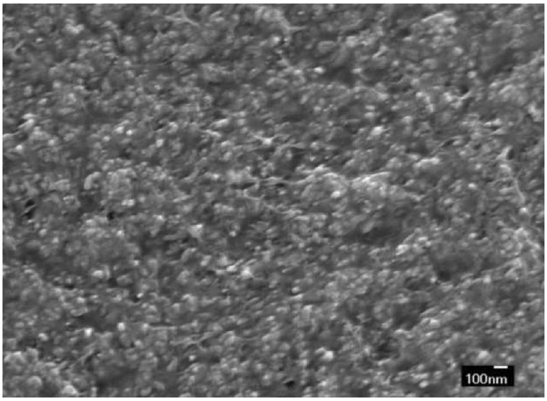

*Figure 7. Cross-sectional FE-SEM image of the nanocomposite thin film containing 30 vol% $TiO_2$*

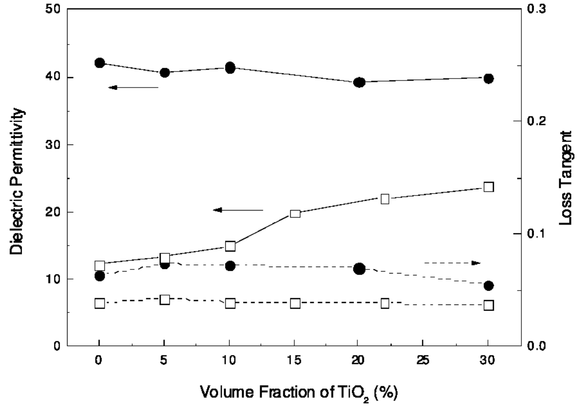

*Figure 8. Dielectric permittivity and loss tangent of the P(VDF-TrFE-CTFE)-$TiO_2$ (circle) and P(VDF-CTFE)-$TiO_2$ (square) nanocomposites measured at 1 kHz and room temperature with a 1 V bias.*

injection and trapping in the composites because the $BaTiO_3$ nanoparticles with a higher permittivity greatly enhance the local electric field dropped across the polymer phase (*26*).

## Thermal Properties

It is well-known that the polarization and dielectric properties of the PVDF based ferroelectric polymers originate from their crystalline domains (*14*). To acquire the influence of the $BaTiO_3$ nanoparticles on the crystallization behavior of the polymer matrix, differential scanning calorimery (DSC) measurements were carried out. The DSC profiles of the polymers and nanocomposites recorded during heating and cooling scans are displayed in Figures 6. The introduction of the nanoparticles into the polymers raises the crystallization temperatures, from ~100 °C for P(VDF-TrFE-CTFE) to ~106 °C for the nanocomposite containing 5 vol % $BaTiO_3$. An even larger shift of about 20 °C has been observed in the P(VDF-CTFE) composite with 7 vol % $BaTiO_3$ nanoparticles, illustrating the role of the nanoparticles as a nucleating agent in the crystallization of the polymer matrix. Consistent with the change in the crystallization temperatures, the heat of fusion in the nanocomposites increases from 18.3 J/g from P(VDF-TrFE-CTFE) to 20.7 J/g for the composite with 5 vol % $BaTiO_3$ nanoparticles, which corresponds to a change of the degree of crystallinity from 21% for the neat polymer to 24% for the composites. On the contrary, the melting temperatures decrease in the composites compared to that in the polymer. This suggests that the presence of the nanoparticles in the matrix decreases the crystal size of the polymer, which is in agreement with the decrease of the crystallization temperatures and the heat of fusion with further increasing of the volume fraction of the $BaTiO_3$ nanoparticle (*27*). Nevertheless, it is believed that the enhanced electric displacement yielded from the nanoparticles, rather than the changes in the crystallinity of the polymer matrix, is mainly responsible for the observed increase in the energy density in the nanocomposites (*13*).

Downloaded by PENNSYLVANIA STATE UNIV on June 21, 2012 | http://pubs.acs.org
Publication Date (Web): March 11, 2010 | doi: 10.1021/bk-2010-1034.ch004

## Polymer-$TiO_2$ Nanocomposites

### Morphology

The formation of Ba-OH surface groups greatly enhances the dispersibility of the $TiO_2$ nanoparticles in organic media. As revealed in DLS measurements, the surface-modified $TiO_2$ nanoparticles can be dispersed in DMF with an average aggregation size of ~60 nm and an overall size below 100 nm. Figure 7 shows a cross-sectional field-emission scanning electron microscopic (FESEM) image of the nanocomposite containing 30 vol% $TiO_2$. The $TiO_2$ nanoparticles are homogeneously dispersed in the polymer matrix with an average size about 50-70 nm, suggesting that the particles are successfully transformed from solution to solid states with minimized agglomeration.

### Dielectric Properties

The dielectric permittivity of the barium hydroxide-functionalized $TiO_2$ nanoparticles was determined ~42 at room temperature and 1kHz by impedance spectroscopy using an appropriate equivalent circuit model (*22*). Figure 8 illustrates the frequency-dependent dielectric permittivity and loss tangent at different loading. Since the P(VDF-TrFE-CTFE) matrix has a similar dielectric constant (~47 at 1kHz) with the $TiO_2$ filler, a marked change of the low-field dielectric permittivity was not observed in the nanocomposites. As a comparison, the composites of [P(VDF-CTFE) 91/9 mol%] with the $TiO_2$ nanoparticles were also fabricated. The gradual increase of dielectric permittivity with the concentration of $TiO_2$ in the P(VDF-CTFE) nanocomposites is attributed to higher dielectric permittivity of the filler relative to the polymer matrix which has a permittivity of 12. In both composites, the loss tangents show little variation as a function of the $TiO_2$ concentration, further indicating that the surface-modified nanoparticles are well-dispersed in the polymers and consequently, the dielectric loss mainly originates from the polymer matrix.

Downloaded by PENNSYLVANIA STATE UNIV on June 21, 2012 | http://pubs.acs.org
Publication Date (Web): March 11, 2010 | doi: 10.1021/bk-2010-1034.ch004

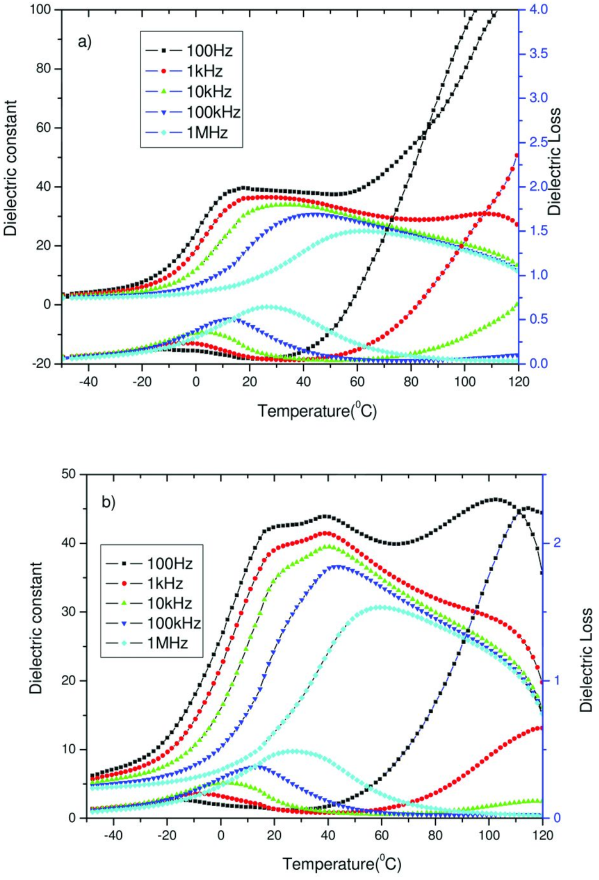

*Figure 9. Temperature dependence of dielectric responses of a) P (VDF-TrFE-CTFE) and b) P (VDF-TrFE-CTFE) –$TiO_2$ with 10 vol % $TiO_2$ at different frequencies in the heating process [dielectric constant (from top to bottom), and dielectric loss (from bottom to top)]: 0.1 k, 1 k, 10 k, 100 k, and 1 MHz.*

Downloaded by PENNSYLVANIA STATE UNIV on June 21, 2012 | http://pubs.acs.org
Publication Date (Web): March 11, 2010 | doi: 10.1021/bk-2010-1034.ch004

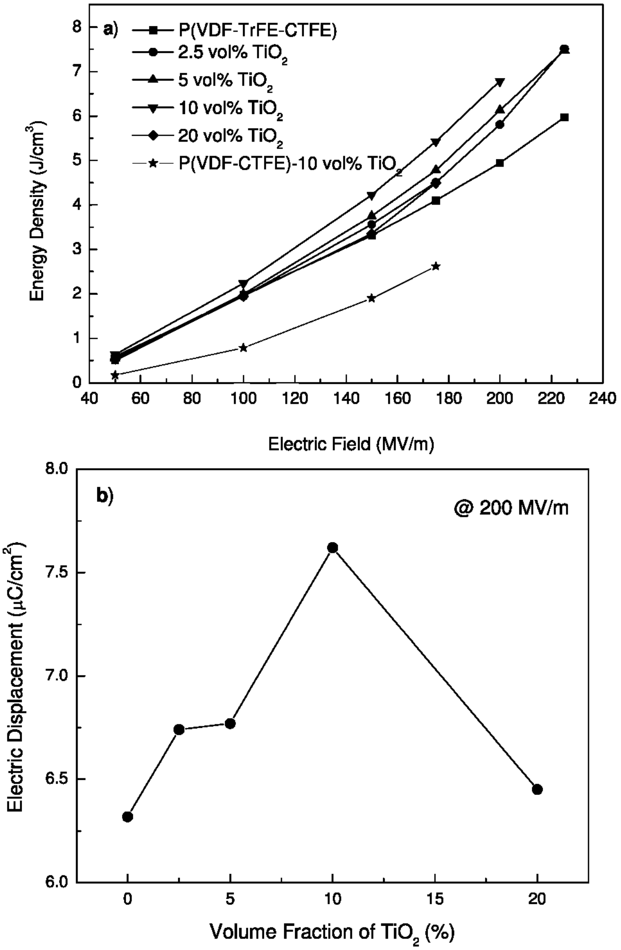

*Figure 10. a) The stored energy density of the polymer and nanocomposites as a function of the applied field. b) The dependence of maximum electric displacement on the $TiO_2$ content in the nanocomposites at 200 MV/m.*

The temperature dependent dielectric permittivity shows broad peak at 23 °C in P(VDF-TrFE-CTFE) is the consequence of the kinetics related to freezing of dipolar motion in ferroelectric relaxor (*28*). (Figure 9) Incorporation of $TiO_2$ nanoparticles into the polymer shows the appearance of a new dielectric anomaly at 38 °C, which can be ascribed to the dipolar glass freezing transition from the polymer chains surrounding the nanoparticles. In accordance with the changes in crystalline size and thermal transition temperatures discussed in the following section, the presence of the particles restricts the chain mobility of nearby polymers and thus enhances activation energy of the transition. A shift of the dielectric relaxation peak towards a lower temperature and a reduced dielectric loss tangent are also observed, which is indicative of interface polarization

Downloaded by PENNSYLVANIA STATE UNIV on June 21, 2012 | http://pubs.acs.org
Publication Date (Web): March 11, 2010 | doi: 10.1021/bk-2010-1034.ch004

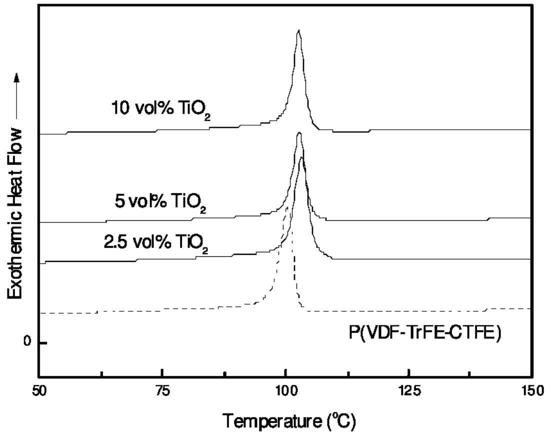

*Figure 11. DSC curves of the polymer and nanocomposites during the cooling cycle.*

interaction and an increased trap density in the nanocomposites (*29*). Thermally stimulated current (TSC) measurements have been performed on the polymers and the nanocomposites, where the samples are first poled at room temperature by applying an electric field of 10 MV/m for 10 min and then are heated with a ramp rate of 4 °C/min. It was found that the nanocomposites generate two-orders-of-magnitude higher TSC than the polymer matrix, confirming that large amounts of charge are trapped presumably around the polymer/nanoparticle interface regions under an applied electric field.

A strong dependence of the energy density of the P(VDF-TrFE-CTFE) nanocomposites on the $TiO_2$ concentration has been revealed in Figure 10, where the energy density of the composites was found to maximize at around 10 vol% $TiO_2$ content. A further increase in the $TiO_2$ concentration leads to a decreased energy density. This trend is likely associated with the interface effect which is proportional to the interfacial area (*30*). For a composite containing 10 vol% nanoparticles with a 20 x 70 nm rod-shaped dimension and ideally uniform dispersion, the calculated inter-particle distance is around 40 nm. As the thickness of the interface region is generally estimated to be ~20 nm, the volume fraction of the polymer chains residing in the interfacial area reaches a maximum at a 10 vol% content of nanoparticles. The large interface area in the nanocomposites would produce the Maxwell-Wagner-Sillars (MWS) interfacial polarization at low frequencies and/or leads to an “interaction zone” with Gouy-Chapman diffuse layer, thereby greatly affecting polarization and dielectric responses of the polymer matrix (*29*, *30*). Indeed, as shown in Figure 10b, the incorporation of the $TiO_2$ nanoparticles into the polymer induces an improved electric displacement, which accounts for high energy densities observed in the nanocomposites. Under an applied field of 200 MV/m, the maximum displacement in the neat polymer is 6.3 $\mu C/cm^2$. The electric displacement of the nanocomposites monotonically increases to 7.62 $\mu C/cm^2$ as the $TiO_2$ content increases to 10 vol%. The decrease in electric displacement and energy density with the further increase of the nanoparticle concentration is presumably caused by the coalescing of the interface region and a reduction of the interface effect.

## Effect of $TiO_2$ on Microstructure

Differential scanning calorimery (DSC), dynamic mechanical analysis (DMA) and WAXD measurements have been carried out to examine the effect of $TiO_2$ nanoparticles on the microstructure of P(VDF-TrFE-CTFE) matrix. As revealed in the DSC profile obtained in the cooling scan (Figure 11), the crystallization temperature ($T_c$) of the nanocomposites shifts by around 3 °C, from ~100 °C for P(VDF-TrFE-CTFE) to ~103 °C for the nanocomposite with 2.5 vol% $TiO_2$ nanoparticles. The glass transition temperatures ($T_g$) measured by DMA gradually increase from -27.6 °C in P(VDF-TrFE-CTFE) to -24.5 °C in the 2.5 vol%-$TiO_2$ nanocomposite. No further change was found as the concentration of $TiO_2$ increases, which indicates the effect of $TiO_2$ filler on the thermal transition is saturated at a loading of 2.5 vol%. The introduction of $TiO_2$ also results in an increase of the heat of fusion from ~18.3 J/g for the polymer to ~22 J/g for the nanocomposite containing 2.5 vol% $TiO_2$ nanoparticles, implying a raise of the degree of crystallinity from 21% in the polymer to 25.5% in the nanocomposite (*31*). Similarly, no noticeable change in the heat of fusion has been observed as the volume fraction of $TiO_2$ nanoparticle further increases.

The WAXD patterns of the nanocomposites display a main peak at a 2θ angle of 18.2° corresponding to the compound (020) and (002) diffractions from the α and γ phases in the polymer. (Figure 12) (*32*) The diffraction peaks at 27.4, 36.1, 41.3 and 44.0° are attributed to the rutile phase $TiO_2$, whose intensities are obviously pronounced as the concentration of the nanoparticle increases. The size of the crystalline domain was calculated by using Scherrer's formula, $t=\lambda/B\cos\theta$, where $t$ is the crystallite size, $\lambda$ is the wavelength (1.54 Å), $B$ is the normalized full width at half maximum (fwhm) of diffraction peak, and $\theta$ is the diffraction angle. The inclusion of $TiO_2$ nanoparticles significantly reduces the crystallite size from ~8 nm in the polymer to ~3.7 nm in the nanocomposites. This result is in agreement with the change of melting temperature ($T_m$) observed in DSC studies, in which $T_m$ decreases from 128 °C for the neat polymer to ~123 °C for the nanocomposites. The nanoparticle acts as a nucleating agent and improves the degree of crystallinity of the polymer matrix, consistent with other reports. ((*33*), (*34*)) On the other hand, the presence of the nanoparticles suppresses the recrystallization process and affords reduction in size of the crystalline domain in the polymer. Both of these effects induced by the nanoparticles are highly beneficial for large polarization at high electric fields. As the crystalline region in the polymer is responsible for polarization, an improved crystallinity would offer a high polarizability and an enhanced permittivity, whereas smaller crystalline domains suggest a low energy barrier in phase transition from disordered *trans-gauche* chain conformation (TGTG' and $T_3GT_3G'$ in the α and γ phases, respectively) to the polar β phase with all-*trans* conformation yielded from the orientation under an applied electric field. Consequently, polarization can be

Downloaded by PENNSYLVANIA STATE UNIV on June 21, 2012 | http://pubs.acs.org
Publication Date (Web): March 11, 2010 | doi: 10.1021/bk-2010-1034.ch004

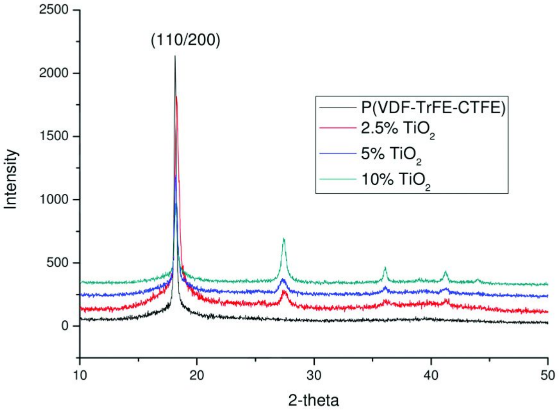

*Figure 12. WAXD spectra of P(VDF-CTFE-TrFE) and nanocomposites.*

induced to a high degree at lower electric fields in the nanocomposites compared to those in the neat polymer.

## Conclusion

In summary, nanocomposites based on the surface-functionalized $BaTiO_3$ and $TiO_2$ nanoparticles and ferroelectric polymers were prepared. The presence of organic surface layers on the particle affords excellent compatibility between the fillers and the polymer matrix and ensures uniform composite films even at higher filler concentrations. It was found that the presence of the nano-scale filler favors a higher degree of crystallinity in the polymer. The dielectric permittivity of the polymer matrix plays a dominant role in determining the energy density of the nanocomposite. On the other hand, substantial enhancements in electric displacement and energy density at high electric fields have been demonstrated in the nanocomposites. The interfacial region between the matrix and fillers is interpreted as the origin of enhanced dielectric displacement. This interfacial polarization phenomena and coupling effect will be further explored in the future.

## References

1. Jain, P.; Pymaszewski, E. J. *Thin Film Capacitors for Packaged Electronics*; Kluwer: Norwell, MA, 2003.
2. Cao, Y.; Irwin, P. C.; Younsi, K. *IEEE Trans. Dielect. Elect. Insul.* **2004**, *11*, 797.
3. Nalwa, H., Ed. *Handbook of Low and High Dielectric Constant Materials and Their Applications*; Academic Press: London, 1999.
4. Tanaka, T.; Montanari, G. C.; Mülhaupt, R. *IEEE Trans. Dielect. Elect. Insul.* **2004**, *11*, 763.
5. Li, J. Y.; Zhang, L.; Ducharme, S. *Appl. Phys. Lett.* **2007**, *90*, 132901.

Downloaded by PENNSYLVANIA STATE UNIV on June 21, 2012 | http://pubs.acs.org
Publication Date (Web): March 11, 2010 | doi: 10.1021/bk-2010-1034.ch004

6. Ma, D.; Hugener, T. A.; Siegel, R. W.; Christerson, A.; Mårtensson, E.; Önneby, C.; Schadler, L. S. *Nanotechnology* **2005**, *6*, 724.
7. Guo, N.; DiBenedetto, S. A.; Kwon, D.-K.; Wang, L.; Russell, M. T.; Lanagan, M. T.; Facchetti, A.; Marks, T. J. *J. Am. Chem. Soc.* **2007**, *129*, 766.
8. Gilbert, L. J.; Schuman, T. P.; Dogan, F. *Ceram. Trans.* **2006**, *179*, 17.
9. Slenes, K. M.; Winsor, P.; Scholz, T.; Hudis, M. *IEEE Trans. Magn.* **2001**, *37*, 324.
10. Dang, Z. M.; Lin, Y. H.; Nan, C. W. *Adv. Mater.* **2003**, *15*, 1625.
11. Wei, T.; Jin, C. Q.; Zhong, W.; Liu, J. M. *Appl. Phys. Lett.* **2007**, *91*, 222907.
12. Kim, P.; Jones, S. C.; Hotchkiss, P. J.; Haddock, J. N.; Kippelen, B.; Marder, S. R.; Perry, J. W. *Adv. Mater.* **2007**, *19*, 1001.
13. Chu, B.; Lin, M.; Neese, B.; Zhou, X.; Chen, Q.; Zhang, Q. M. *Appl. Phys. Lett.* **2007**, *91*, 122909.
14. Lovinger, A. J. *Science* **1983**, *220*, 1115.
15. An, L.; Boggs, S. A.; Calame, J. P. *IEEE Electr. Insul. Mag.* **2008**, *25*, 5.
16. Li, J. Y.; Zhang, L.; Ducharme, S. *Appl. Phys. Lett.* **2007**, *90*, 132901.
17. Lu, Y.; Claude, J.; Neese, B.; Zhang, Q. M.; Wang, Q. *J. Am. Chem. Soc.* **2006**, *128*, 8120.
18. Claude, J.; Lu, Y.; Li, K.; Wang, Q. *Chem. Mater.* **2008**, *20*, 2078.
19. Pramanik, N. C.; Seok, S. I.; Ahn, B. Y. *J. Alloys Compd.* **2008**, *449*, 77.
20. Ahn, B. Y.; Seok, S. I.; Pramanik, N. C.; Kim, H.; Hong, S. *J. Colloid Interface Sci.* **2006**, *297*, 138.
21. Lu, Y.; Claude, J.; Zhang, Q. M.; Wang, Q. *Macromolecules* **2006**, *39*.
22. Petrovsky, V.; Manohar, A.; Dogan, F. *J. Appl. Phys.* **2006**, *100*, 014102.
23. Claude, J.; Lu, Y.; Wang, Q. *Appl. Phys. Lett.* **2007**, *91*, 212904.
24. Rao, Y.; Qu, J. M.; Marinis, T.; Wong, C. P. *IEEE Trans. Compon., Packag. Technol.* **2000**, *23*, 680.
25. Smith, R. C.; Liang, C.; Landry, M.; Nelson, J. K.; Schadler, L. S. *IEEE Trans. Dielect. Elect. Insul.* **2008**, *15*, 187.
26. Kilaru, M. K.; Heikenfeld, J.; Lin, G.; Mark, J. E. *Appl. Phys. Lett.* **2007**, *90*, 212906.
27. Kim, K. M.; Park, N. G.; Ryu, K. S.; Chang, S. H. *Polymer* **2002**, *43*, 3951.
28. Pirc, R.; Blinc, R.; Kutnjak, Z. *Phys. Rev. B* **2002**, *65*, 214101.
29. Lunkenheimer, P.; Bobnar, V.; Pronin, A. V.; Ritus, A. I.; Volkov, A. A.; Loidl, A. *Phys. Rev. B* **2002**, *66*, 052105.
30. Nelson, J. K.; Fothergill, J. C. *Nanotechnology* **2004**, *15*, 586.
31. Nakagawa, K.; Ishida, Y. *J. Polym. Sci. Phys.* **1973**, *11*, 2153.
32. Lu, Y.; Claude, J.; Norena-Franco, L. E.; Wang, Q. J. *J. Phys. Chem.* **2008**, *112*, 10411.
33. Levi, N.; Czerw, R.; Xing, S.; Lyer, P.; Carroll, D. *Nano Lett.* **2004**, *4*, 1267.
34. Shah, D.; Maiti, P.; Gunn, E.; Schmidt, D. F.; Jiang, D. D.; Batt, C.; Giannelis, E. P. *Adv. Mater.* **2004**, *16*, 1173.

Downloaded by PENNSYLVANIA STATE UNIV on June 21, 2012 | http://pubs.acs.org
Publication Date (Web): March 11, 2010 | doi: 10.1021/bk-2010-1034.ch004

## Chapter 5

# Ultrafast IR Spectroscopic Study of Free Carrier Formation in OPV Polymer Blends

**Ryan D. Pensack, Kyle M. Banyas, and John B. Asbury***

**Department of Chemistry, Pennsylvania State University, University Park, PA 16802**
***jasbury@psu.edu**

Downloaded by DUKE UNIV on June 22, 2012 | http://pubs.acs.org
Publication Date (Web): March 11, 2010 | doi: 10.1021/bk-2010-1034.ch005

A new charge separation mechanism arising from interfacial dipolar fields at interfaces of organic photovoltaic materials has been identified using ultrafast infrared spectroscopy. This mechanism, termed electric field-assisted charge separation, is in part responsible for the surprisingly rapid and efficient charge separation that is observed in OPV materials. The dynamics of interfacial electron transfer and free carrier formation are examined through the carbonyl stretch of an electron accepting functionalized fullerene in a blend with an electron donating conjugated polymer. Free carrier formation following photoexcitation occurs on the 1 – 10 ps time scale, which suggests that the Coulombic binding energy is considerably smaller than the value predicted from the dielectric properties of the materials. The electric field that assists the separation of the charge carriers arises from interfacial dipoles that form due to spontaneous partial charge transfer from the polymer to the fullerene.

## Introduction

Organic solar cells based on organic photovoltaic (OPV) materials offer promising alternatives to large area solar modules because they can be processed from solution (*1–4*). OPV materials are excitonic in nature (*5–7*) which requires that electrons and holes be separated by electron transfer from electron donating to electron accepting materials. For electron transfer to occur, photogenerated

In Functional Polymer Nanocomposites for Energy Storage and Conversion; Wang, Q., et al.;
ACS Symposium Series; American Chemical Society: Washington, DC, 2010.

Downloaded by DUKE UNIV on June 22, 2012 | http://pubs.acs.org
Publication Date (Web): March 11, 2010 | doi: 10.1021/bk-2010-1034.ch005

excitations (principally excitons) must first diffuse to the donor/acceptor interfaces. Following interfacial electron transfer from the electron donor to the acceptor, the electron-hole pairs (biradical pairs) that form at the interfaces are bound to the interfaces by their mutual Coulombic attraction which can be several tenths on an electron-volt (eV) (*8*, *9*). This Coulombic attraction should not be misinterpreted as the exciton binding energy in the polymer (*10*). Given that free carrier formation in OPV materials requires that the biradical pairs escape these Coulombic potentials that are more than ten times greater than the thermal energy that is available at room temperature, it may seem surprising that free carriers form readily in these materials.

Conventional wisdom in the OPV community predicts that efficient free carrier formation can occur in OPV materials as long as free energy differences between the lowest unoccupied molecular orbital (LUMO) of the donor and the LUMO of the acceptor are in the 0.3 – 0.4 eV range (*6*, *11–13*). In contrast, the polymers that have been extensively studied in organic solar cells, poly(2-methoxy-5-(3,7-dimethyloctyloxy)-1,4-phenylenevinylene) and regioregular poly(3-hexylthiophene), referred to here and afterward as MDMO-PPV and RR-P3HT, respectively, have free energy differences compared with PCBM of about 1 eV (*5*, *6*). The structures of these materials are depicted in Fig. 1.

Considerable research has been undertaken to tune the energy levels of the materials in an effort to reduce the amount of energy that is 'wasted' in organic solar cells as a result of these large free energy differences (*12–27*). However, the Durrant group recently suggested that large free energy differences may be necessary to facilitate efficient free carrier formation (*9*). This group recently reported a correlation between the polymer-PCBM LUMO free energy difference and the efficiency of free carrier formation for a series of polythiophene variants blended with PCBM. The authors suggested that the excess vibrational energy which results from large free energy differences may be critical to the efficient escape of biradical pairs from their Coulombic potentials at the interfaces.

The uncertainty about the role of excess vibrational energy in the free carrier formation mechanism suggests that fundamental understanding of this process is incomplete. A more thorough understanding of this process may lead to novel approaches to tune the charge collection efficiency of OPV devices with the practical aim of developing more efficient organic solar cells. We have recently demonstrated that ultrafast vibrational spectroscopy offers the unique ability to directly examine the dynamics of free carrier formation in OPV materials (*28–32*). In this chapter, we describe our recent use of this technique to examine charge carrier dynamics in an OPV material composed of PCBM blended with the conjugated polymer, poly[2-methoxy-5-(2-ethylhexyloxy)-1,4-(1-cyanovinylene-1,4-phenylene)] (CN-MEH-PPV, see Fig. 2).

The frequency of the carbonyl (C=O) stretch of the methyl ester group of PCBM is sensitive to changes in the local charge distribution following electron transfer from CN-MEH-PPV (*28–32*). This sensitivity permits the dynamics of interfacial electron transfer to be measured through changes in the transient vibrational spectra of the carbonyl bond following optical excitation of

CN-MEH-PPV. The carbonyl bond stretch frequency also varies radially within the PCBM domains such that molecules at the interfaces with CN-MEH-PPV have higher frequency carbonyl stretch modes compared with molecules in the centers of the domains (*29*). This sensitivity results in part from the presence of electric fields arising from interfacial dipoles that form at the CN-MEH-PPV:PCBM junctions. The spatial dependence of these electric fields gives rise to variation of the carbonyl frequency with the radial position of PCBM molecules within the roughly spherical domains. This gradient in the vibrational frequency permits the direct measurement of the dynamics of free carrier formation by spatially resolving the separation of biradical pairs at the interfaces. Free carrier formation occurs surprisingly quickly – an observation that we explain through the influence of the electric fields arising from the interfacial dipoles. The resulting dipolar fields decrease the Coulombic binding energy of the biradical pairs at the interfaces – thus facilitating their rapid escape from the interfaces.

Downloaded by DUKE UNIV on June 22, 2012 | http://pubs.acs.org
Publication Date (Web): March 11, 2010 | doi: 10.1021/bk-2010-1034.ch005

## Experimental Procedures

The experimental procedures have been described in detail elsewhere (*29*, *30*). Briefly, the ultrafast IR spectroscopy instrumentation is based on a Ti:sapphire laser system which is used to pump two optical parametric amplifiers (OPAs). One OPA is used to generate mid-infrared (IR) pulses that serve as the probe source for all experiments and as the IR pump pulse for two-dimensional (2D) IR and polarization resolved IR pump-probe experiments. For the experiments reported here, the probe is tuned to the 5.8 μm region to probe the carbonyl stretch of PCBM. The second OPA is used to generate tunable visible pump pulses that can be adjusted to specifically excite CN-MEH-PPV at 550 nm.

A transmissive beam geometry is used for the visible pump-IR probe experiments in which the sample consists of a thin photovoltaic film deposited onto the front surface of a $CaF_2$ optical flat. A reflective beam geometry is utilized for the 2D IR and polarization resolved IR pump-probe experiments. Both geometries virtually eliminate non-resonant contributions to the transient signals. The polymer blends are deposited onto the appropriate substrates from chlorobenzene solutions. All experiments are conducted under inert nitrogen atmosphere.

## Interfacial Electron Transfer Dynamics

The primary events following photon absorption involve diffusion of the resulting excitons to interfaces between CN-MEH-PPV and PCBM with subsequent electron transfer on ultrafast time scales. In the polymer blends reported here, the electron transfer dynamics from the polymer to PCBM are examined by probing the carbonyl (C=O) stretch vibrational absorption of PCBM after selectively exciting the polymer at 550 nm. The linear IR absorption spectrum of a 1:1 blend (by mass) of CN-MEH-PPV with PCBM is displayed

Downloaded by DUKE UNIV on June 22, 2012 | http://pubs.acs.org
Publication Date (Web): March 11, 2010 | doi: 10.1021/bk-2010-1034.ch005

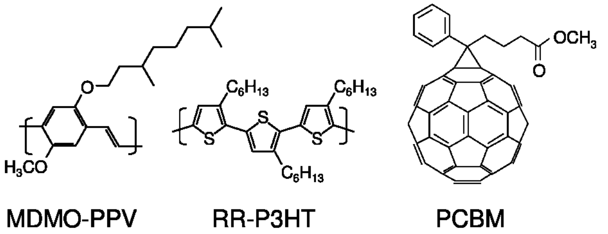

*Figure 1. Molecular structures of two polymeric electron donors, MDMO-PPV and RR-P3HT, and the electron accepting fullerene, PCBM, that have been studied in organic solar cells.*

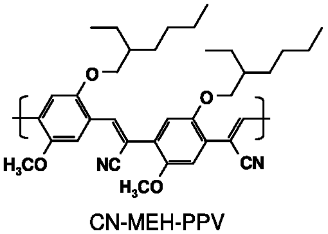

*Figure 2. Molecular structure of the conjugated polymer, CN-MEH-PPV, which was blended with PCBM and studied using ultrafast vibrational spectroscopy as reported here.*

in the lower panel of Fig. 3 along with a spectrum of pure CN-MEH-PPV for comparison. The spectra show that the carbonyl absorption of PCBM is spectrally isolated which facilitates unambiguous measurement of the electron transfer dynamics without interference from other species.

Transient IR spectra collected using visible pump-IR probe spectroscopy and centered on the carbonyl stretch of PCBM are depicted in the upper panel of Fig. 3 at several time delays following optical excitation of a 1:1 blend of the molecule with CN-MEH-PPV. The spectra at each time delay are characterized by a broad absorption that results from polarons in the polymer (*33–40*) and a reduced absorption of the ground to first excited state (0 → 1) vibrational transition of the carbonyl stretch (termed a bleach). The area of the carbonyl bleach in the transient spectra is proportional to the concentration of electrons that have transferred to the PCBM domains at the corresponding time delay. A fitting procedure was developed to quantitatively extract the bleach spectra from the transient vibrational spectra (*29*). Examples of the fitting results are visible as the smooth lines overlaying the data in the transient vibrational spectra displayed in Fig. 3.

The dynamics of interfacial electron transfer are obtained by integrating the bleach of the carbonyl stretch of PCBM at each time delay recorded in the experiment. The main panel of Fig. 4 displays the time evolution of the area of the PCBM carbonyl bleach. Following an initial rise, the bleach area decreases slightly due to back electron transfer from PCBM to the polymer.

Downloaded by DUKE UNIV on June 22, 2012 | http://pubs.acs.org
Publication Date (Web): March 11, 2010 | doi: 10.1021/bk-2010-1034.ch005

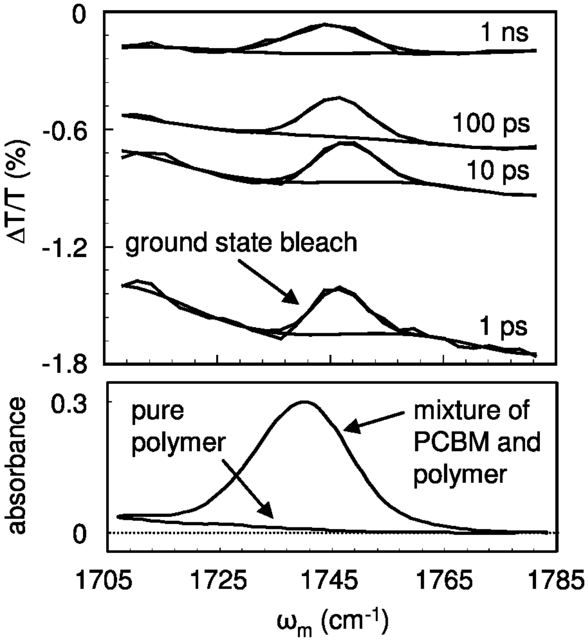

*Figure 3. Upper panel: Comparison of transient IR spectra of the 1:1 polymer blend following optical excitation at 550 nm with best fit spectra used to extract the C=O stretch bleach. Lower panel: Linear IR spectra of the 1:1 polymer blend compared with the pure polymer. The polymer does not have an IR-active vibrational mode at 1740 cm$^{-1}$. All transient vibrational features arise from transferring electrons to PCBM. (Reproduced from reference (30).)*

We have recently shown that the bleach area undergoes a second rise on the nanosecond time scale due to diffusion of excitations to the CN-MEH-PPV:PCBM interfaces (*30*). The time dependence of the second rise matches the excited state lifetime of the CN-MEH-PPV film, confirming that the second rise results from exciton diffusion. The inset of Fig. 4 represents the time evolution of the bleach area on a shorter time scale. A multi-exponential fit curve that is convolved with the 200 fs instrument response function is overlaid on the data. The fit curve represents an electron transfer process to PCBM that occurs on multiple time scales ranging from 90 fs (~ 30%) to 0.9 ps (~ 70%) (*30*). These dynamics are similar to previous measurements of electron transfer in conjugated polymer/fullerene blends (*41–46*). The biphasic dynamics indicate that electron transfer occurs from a distribution of distances and/or orientations of CN-MEH-PPV conjugated segments relative to PCBM molecules (*32*). The longer time scale electron transfer process may originate from conjugated segments that are displaced from PCBM molecules by one polymer layer or which present their 2-ethylhexyloxy side group to the fullerene acceptor.

Downloaded by DUKE UNIV on June 22, 2012 | http://pubs.acs.org
Publication Date (Web): March 11, 2010 | doi: 10.1021/bk-2010-1034.ch005

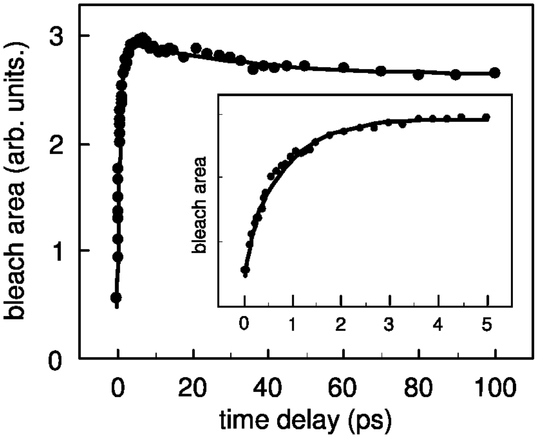

*Figure 4. Integrated area of the carbonyl bleach of PCBM versus the corresponding time delay for the 1:1 polymer blend plotted on a linear time axis. Inset) The first five picoseconds of the same data showing the gradual rise resulting from interfacial electron transfer on the 90 fs and 0.9 ps time scales.*

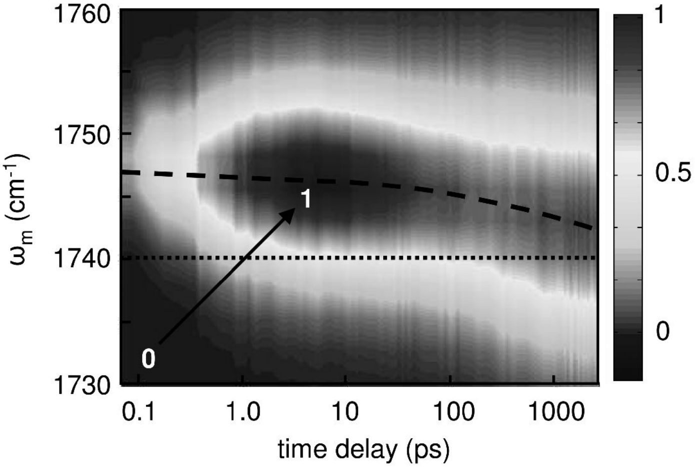

*Figure 5. Two-dimensional surface plot of the carbonyl bleach spectrum versus the corresponding time delay. The 0 and 1 markers indicate the regions of low and high amplitude. The bleach spectra shift toward the equilibrium center frequency of 1740 cm$^{-1}$ as electrons escape from the interfaces and move toward the interior regions of the domains. (Reproduced from reference (29).)*

## Radial Motion of Electrons

Interfacial electron transfer does not result directly in free carrier formation in excitonic materials (*47–49*). Instead, biradical pairs are generated that consist of a hole in the donor phase and an electron in the acceptor phase. These carriers are Coulombically bound to the interface by in many cases several tenths of an electron-volt (*8*, *9*). Free carrier formation requires that the charge carriers escape from this Coulombic potential and dissociate the biradical pair. The time dependence of this process is revealed through the time evolution of the carbonyl bleach spectra which are sensitive to the motion of electrons within the PCBM domains after the initial interfacial electron transfer step. The fitting procedure used to extract the carbonyl bleach spectra from the transient IR data displayed in Fig. 3 enable the time dependence of the bleach spectra to be carefully analyzed (*29*, *30*, *32*).

Figure 5 displays the carbonyl bleach spectra in a two-dimensional surface plot versus the corresponding time delay (horizontal axis). The axis has been plotted on a logarithmic scale to highlight the extended time dependence of the bleach spectra. The dashed curve is a guide to the eye showing the shift of the bleach spectrum toward the equilibrium center frequency at 1740 $cm^{-1}$ at longer time delays between the 550 nm optical excitation pulse and the IR probe pulse. The data indicate that the bleach of the carbonyl stretch of PCBM appears several wavenumbers higher in frequency in comparison to the equilibrium carbonyl stretch peak that is measured using linear IR spectroscopy. The subset of molecules that accept electrons from CN-MEH-PPV possess higher frequency carbonyl stretch modes in comparison to the ensemble of PCBM molecules in the polymer blend. Because electron transfer is highly distance dependent (*50*, *51*), the appearance of the bleach on the higher frequency side of the transition indicates that molecules at the interfaces of the PCBM domains have higher frequency carbonyl bonds because these are the molecules that accept electrons. By extension, PCBM molecules that do not accept electrons from the polymer have lower frequency carbonyl bonds. These molecules are interpreted as being buried within the PCBM domains and are therefore not available to be the primary electron accepting species in the ultrafast electron transfer reaction. Figure 6 illustrates these conclusions.

Further evidence for the shift of the carbonyl frequency with radial position has been obtained from composition dependent linear IR studies (*29*, *32*). As CN-MEH-PPV is added to films of pure PCBM, the carbonyl stretch shifts to higher frequency. Because the polymer has negligible absorption around 1740 $cm^{-1}$, the frequency shift results from a perturbation of the carbonyl stretch by the presence of the polymer. Since the interactions that cause this shift are concentrated at the polymer:PCBM interface, it stands to reason that PCBM molecules at the interface have higher frequency carbonyl bonds – consistent with the spectra of the carbonyl bleach immediately following interfacial electron transfer (Fig. 5).

Downloaded by DUKE UNIV on June 22, 2012 | http://pubs.acs.org
Publication Date (Web): March 11, 2010 | doi: 10.1021/bk-2010-1034.ch005

Downloaded by DUKE UNIV on June 22, 2012 | http://pubs.acs.org
Publication Date (Web): March 11, 2010 | doi: 10.1021/bk-2010-1034.ch005

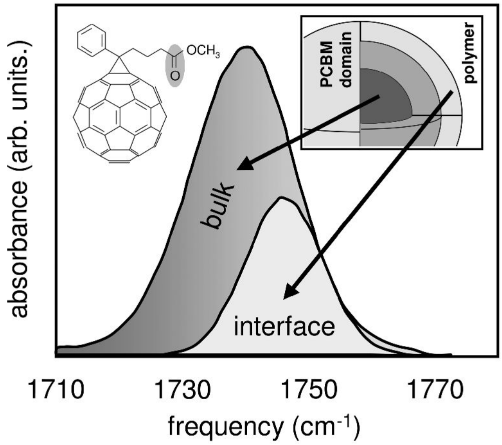

*Figure 6. Schematic illustration of the correlation of the carbonyl frequency with radial position in the PCBM domains. PCBM molecules near the CN-MEH-PPV:PCBM interfaces have higher frequency carbonyl stretch vibrations in comparison to molecules that reside in the bulk of the PCBM domains.*

## Origin of the Frequency Correlation with Radial Position

The shift of the carbonyl frequency with radial position in PCBM domains may be understood in terms of the vibrational Stark effect (*52–54*). The Stark shift of the carbonyl vibration of PCBM results from the formation of interfacial dipoles due to spontaneous charge transfer at the CN-MEH-PPV:PCBM junctions. Interfacial dipoles have been observed at numerous organic-organic electron donor/acceptor junctions with corresponding vacuum level shifts on the order of several tenths of an electron-volt (*55–64*). For example, a vacuum level shift of 0.25 eV was recently reported for interfaces between *p*-bis[(*p*-styryl)styryl]benzene and $C_{60}$ with a corresponding interfacial dipole of 4.7 Debye (*55*). A vacuum level shift of 0.6 eV has been reported for P3HT/$C_{60}$ interfaces (*64*). In both cases, the negative poles of the dipoles reside on the $C_{60}$ side. We hypothesize that similar interfacial dipoles form at the CN-MEH-PPV:PCBM interfaces because the ionization potential and electron affinity of the materials are quite different (*65*, *66*). On the basis of this hypothesis, an electric field is expected to form spontaneously as a result of interfacial dipoles at the CN-MEH-PPV:PCBM interfaces resulting in a vibrational Stark shift of the carbonyl bond. The electric field decreases rapidly with distance from the interface because the dipoles are centered on the junctions between the two materials. This radial variation in the electric field naturally gives rise to the correlation of the carbonyl frequency with radial position in CN-MEH-PPV:PCBM blends.

The validity of the hypothesis that interfacial dipoles give rise to the correlation of the carbonyl frequency with radial position can be tested by calculating the resulting electric field. As a starting point, the interfacial

In Functional Polymer Nanocomposites for Energy Storage and Conversion; Wang, Q., et al.;
ACS Symposium Series; American Chemical Society: Washington, DC, 2010.

Downloaded by DUKE UNIV on June 22, 2012 | http://pubs.acs.org
Publication Date (Web): March 11, 2010 | doi: 10.1021/bk-2010-1034.ch005

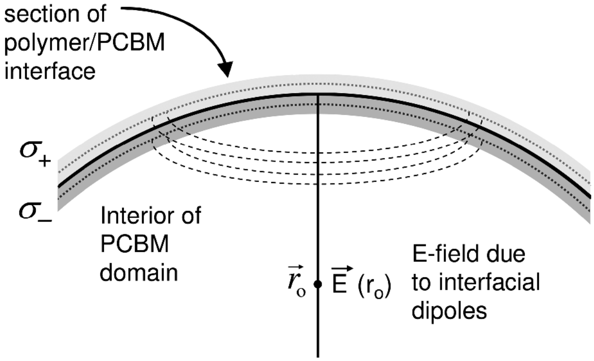

*Figure 7. Schematic illustration of a CN-MEH-PPV:PCBM interface showing spontaneous partial charge transfer from the polymer to PCBM that results in charge densities σ+ and σ− in the two layers, respectively. An electric field forms at the PCBM domain interfaces as a result of the interfacial dipoles. The PCBM domains are modeled as spheres surrounded by CN-MEH-PPV layers.*

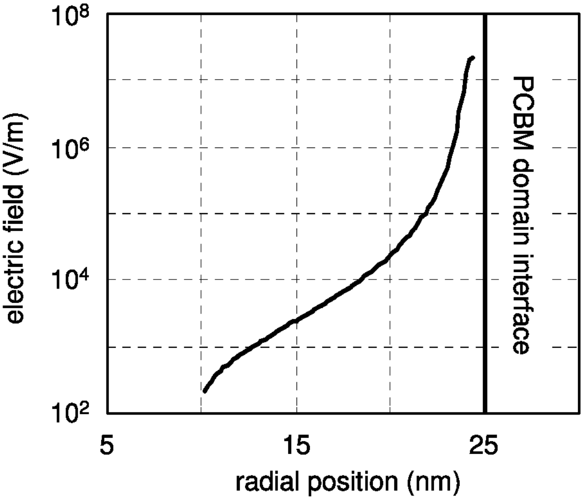

*Figure 8. Variation of electric field as a result of the collective addition of interfacial dipoles versus radial position within the PCBM domains. Surprisingly large electric fields form at the interfaces of the PCBM domains.*

dipoles can be estimated on the basis of the parameters for the interfacial dipole considered by Bässler and coworkers in which a partial charge of ~ 1.6 * $10^{-20}$ C (10% of an elementary charge) was estimated to transfer from *p*-bis[(*p*-styryl)styryl]benzene to $C_{60}$ at a 1 nm separation (*55*). Figure 7 represents a model of the CN-MEH-PPV:PCBM interface in which a shell of polymer in contact with a PCBM domain develops a positive charge density equal to σ+ due to partial charge redistribution. Each conjugated segment in direct contact with a PCBM domain is assumed to transfer about 10% of an elementary charge to the

Downloaded by DUKE UNIV on June 22, 2012 | http://pubs.acs.org
Publication Date (Web): March 11, 2010 | doi: 10.1021/bk-2010-1034.ch005

nearest PCBM molecule. This partial charge transfer results in a negative charge density in the outer shell of a PCBM domain equal to $\sigma_{-}$.

Figure 8 displays the variation of the electric field estimated at the CN-MEH-PPV:PCBM interfaces. The electric field at a particular distance along the interface normal, $r_0$, resulting from the collective addition of the charge densities at the interface was recently calculated (*32*). Surprisingly large fields on the order of $10^7 – 10^8$ V/m result from the formation of the interfacial dipoles. Electric fields are known to influence the frequency of molecular vibrations through the vibrational Stark effect. The influence of an electric field on a particular vibration of a molecule is described by the Stark tuning rate. Stark tuning rates have not been measured for the ester carbonyl stretch mode. Boxer and coworkers recently measured the tuning rate for acetone and methyl vinyl ketone at approximately 1 $\text{cm}^{-1}/(10^8$ V/m) (*52*). A vibrational Stark shift of a few tenths of a wavenumber is predicted on the basis of these results – which indicates that the vibrational Stark effect is partially responsible for the correlation of the carbonyl frequency of PCBM with radial position within the domains. Another influence that may affect the carbonyl stretch of PCBM is the difference in polarity between the CN-MEH-PPV phase and the PCBM phase. The polarity of the solvent environment is known to shift the frequency of carbonyl bonds several wavenumbers, and this effect may contribute to the radial variation of the carbonyl frequency.

## Free Carrier Formation Dynamics

The fitting procedure used to extract the bleach spectra from the transient IR data displayed in Fig. 3 allows the center frequency of the bleach peak to be precisely determined (*29*). Figure 9A displays the center frequency of the carbonyl bleach at each time delay recorded in the transient IR experiment on a logarithmic time axis. The data indicate that the carbonyl bleach shifts toward the equilibrium spectrum with increasing time delay between the pump and the probe pulses. For reference, the equilibrium center frequency of 1740 $\text{cm}^{-1}$ is represented by the dotted line. The transfer of electrons to PCBM molecules at the interfaces of the domains on ultrafast time scales results in the appearance of the ground state bleach of the PCBM carbonyl stretch on the higher frequency side of the transition. Following this initial interfacial electron transfer reaction, the center frequency of the carbonyl bleach proceeds to shift toward the equilibrium frequency on numerous time scales ranging from a few hundred femtoseconds to many nanoseconds.

The spectral evolution of the carbonyl bleach with increasing time delay could have numerous causes related to *i*) interference from the PCBM negative polaron, *ii*) thermal redistribution in the film, *iii*) vibrational spectral diffusion within the carbonyl transition, or *iv*) motion of electrons in the PCBM domains. The first three causes have been eliminated on the basis of the following experiments. *i*) transient IR spectra have been recorded over a broad frequency range centered on the 1740 $\text{cm}^{-1}$ region of the carbonyl bleach in an effort to locate the negative polaron absorption. On ultrafast time scales, the PCBM negative polaron does

Downloaded by DUKE UNIV on June 22, 2012 | http://pubs.acs.org
Publication Date (Web): March 11, 2010 | doi: 10.1021/bk-2010-1034.ch005

not absorb in this spectral region (*30*). As a result, the bleach spectrum is not influenced by dynamics of the PCBM negative polaron. *ii*) by examining the temperature dependence of the linear IR spectrum of the carbonyl absorption peak, it has been determined that the frequency of this mode is very insensitive to temperature (*29*) – thus the spectral evolution does not result from thermal redistribution. *iii*) spectral diffusion in the carbonyl transition was examined using 2D IR spectroscopy (*28*). The 2D IR experiments show that the carbonyl transition is inhomogeneously broadened such that the dynamically broadened line shape is much narrower than the inhomogeneous line shape (giving rise to diagonally elongated peaks). The dynamically broadened line shapes in the 2D IR spectra are time independent after a 1 ps time delay between the narrow-band IR pump pulse and the broad-band IR probe pulse – indicating that spectral diffusion does not occur in the carbonyl stretch mode on the 1 ps and longer time scales (*29*). The fast frequency evolution observed on the sub-picosecond time scale in Fig. 9A may result from spectral diffusion. The 2D IR spectra do not reveal spectral diffusion on this time scale because the self-heterodyned pump-probe experimental approach averages over the dynamics that occur while the ~ 1 ps IR pump pulse interacts with the sample (*67*).

After eliminating the first three explanations for the spectral evolution of the carbonyl bleach of PCBM on the 1 ps time scale and longer, the physical picture represented in Fig. 9B emerges (*32*). Interfacial electron transfer occurs on the sub-100 fs to sub-ps time scales following exciton diffusion to the CN-MEH-PPV:PCBM interfaces. Immediately after this process, electrons begin to escape their Coulombic potentials at the interfaces and dissociate the biradical pairs.

This initial motion represents the primary step in free carrier formation and results in the spectral evolution of the carbonyl bleach that appears on the 1 – 10 ps time scale in Fig. 9A. As the electrons diffuse or drift into the PCBM domains, they restore the neutral ground state absorption of the molecules at the interfaces and reduce the absorption of molecules that reside in more interior locations. This exchange of molecules with higher frequency carbonyl bonds for those with lower frequency bonds gives rise to the spectral shift to lower frequency that is observed in the data. The rapid time evolution of the carbonyl bleach frequency indicates that electrons are able to escape their Coulombic barriers surprisingly quickly in spite of the large activation energy of several tenths of an electron-volt that is expected (*8*, *9*). The continued evolution of the carbonyl bleach frequency on longer time scales results from diffusion or drift of electrons further into the PCBM domains (*29*).

Such fast escape of electrons from their biradical pairs is surprising considering the depth of the Coulombic potentials that bind them to the interfaces. The data suggest a rate $v$ for free carrier formation between $10^{12}$ and $10^{11}$ $s^{-1}$. A similar rate of charge separation has been observed in RR-P3HT:PCBM blends (*46*). To estimate the effective activation energy for free carrier formation, the Arrhenius picture of an activated process is adopted with a rate, $v = v_o \exp(-E^{\ddagger}/kT)$, that depends on the maximum attempt frequency, $v_o$, the activation energy, $E^{\ddagger}$, and the temperature, T. $k$ is Boltzmann's constant. The highest frequency Frank-Condon active vibrational modes of $C_{60}$ that are known to be involved in electron transfer are the $A_g(2)$ and $T_{1u}(4)$ modes around 1400 $cm^{-1}$ (*68*)(*69*).

Downloaded by DUKE UNIV on June 22, 2012 | http://pubs.acs.org
Publication Date (Web): March 11, 2010 | doi: 10.1021/bk-2010-1034.ch005

Adopting these modes for PCBM, the maximum electron transfer attempt frequency between PCBM molecules, $v_0 = 4 \cdot 10^{13}$ s$^{-1}$, can be estimated. Letting the temperature equal 300 K, the data suggest that electrons which transfer on the picosecond time scale experience an activation energy between 0.1 and 0.15 eV – considerably smaller than the expected Coulombic binding energy of the biradical pairs. The estimated activation energy would be even smaller if lower frequency vibrations are involved.

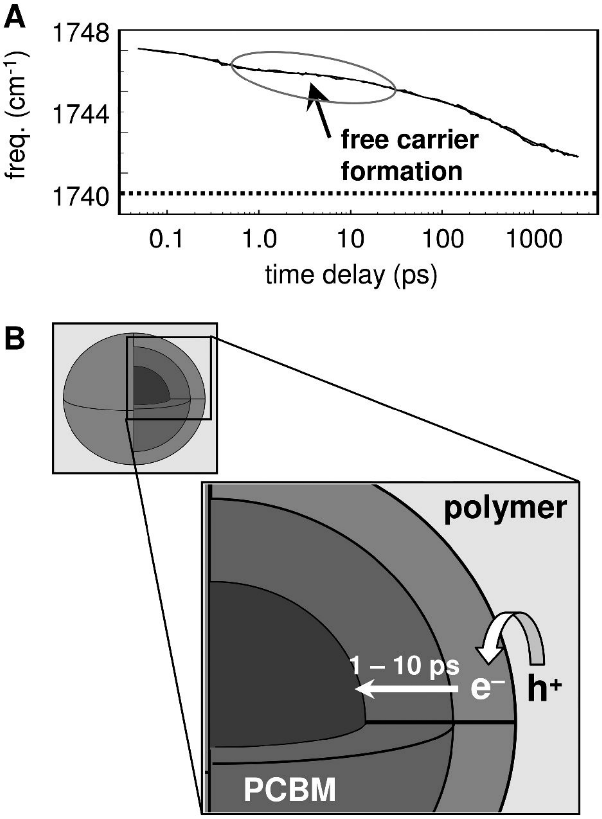

*Figure 9. A) Plot of the carbonyl bleach center frequency versus corresponding time delay. B) Schematic illustration of the CN-MEH-PPV:PCBM interface that summarizes the physical model by which we interpret the data. Following interfacial electron transfer from CN-MEH-PPV, electrons escape the Coulombic binding energy of the holes on the 1 – 10 ps time scale.*

## Field-Assisted Free Carrier Formation

Free carrier formation occurs quickly in organic photovoltaic materials due to a smaller than expected activation energy for escape from the biradical pairs that

Downloaded by DUKE UNIV on June 22, 2012 | http://pubs.acs.org
Publication Date (Web): March 11, 2010 | doi: 10.1021/bk-2010-1034.ch005

form following interfacial electron transfer (*32*). The effective activation energy is reduced as a result of the influence of the electric field that originates from interfacial dipoles. Because the negative ends of the dipoles lie in the acceptor phase, an electron that transfers to the acceptor is repelled by this charge while it is simultaneously attracted to the hole in the polymer phase. The net result is a reduction of the Coulombic binding energy of the biradical pair. This argument is similar to a model proposed by Bässler and coworkers (*55*).

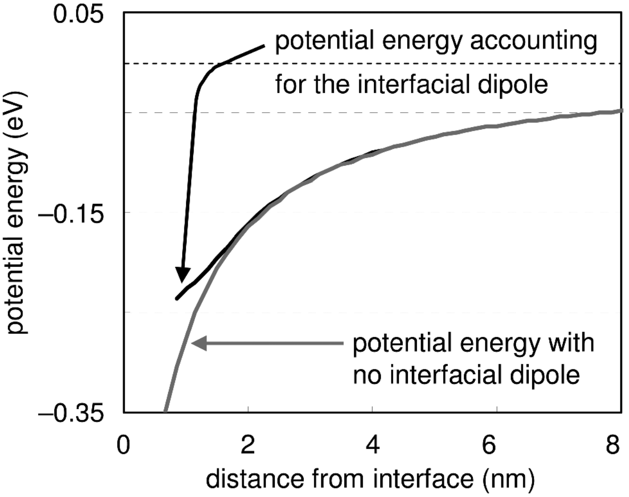

*Figure 10. Comparison of the potential energy versus electron-hole separation at CN-MEH-PPV:PCBM interfaces in the presence and absence of interfacial dipoles. The electric field arising from the interfacial dipoles reduces the effective Coulombic binding energy of the biradical pairs by nearly one tenth of an electron volt which significantly aids the escape of electrons from the interfaces on ultrafast time scales.*

The Coulombic attraction of an electron to a hole as a function of the separation of the electron from the interface was recently calculated in the presence and absence of an electric field arising from interfacial dipoles (*32*). The results of this calculation are represented in Fig. 10 in which the potential energy due to the Coulombic attraction of the electron and hole are plotted verses the separation of electrons from the PCBM domain interfaces. The calculations show that the Coulombic binding energy is reduced by about 0.1 eV – a significant fraction of the difference between the observed activation energy for free carrier formation and the activation energy predicted from the dielectric properties of the materials. Other factors may be important since the effect of the electric field may not completely account for the observed reduction of the activation energy.

A complementary explanation to the electric field-assisted free carrier formation mechanism described above was recently posited by the Durrant group (*9*). Examining a series of polythiophenes with various LUMO energy levels relative to PCBM, Durrant and coworkers discovered that the free carrier

Downloaded by DUKE UNIV on June 22, 2012 | http://pubs.acs.org
Publication Date (Web): March 11, 2010 | doi: 10.1021/bk-2010-1034.ch005

formation efficiency of OPV blends decreased as the free energy difference was reduced in the electron transfer reaction. The authors suggested that excess vibrational energy resulting from the electron transfer reaction facilitates the escape of electrons and holes from Coulombic potentials that hold the biradical pairs at the interfaces. Previous explanations along these lines suggested that the excess vibrational energy is transferred to the holes remaining in the polymer phase (*42*, *70*).

The experimental observations of the Durrant group are consistent with trends predicted by the interfacial dipolar field-assisted and the excess vibrational energy-assisted free carrier formation mechanisms (*9*). Polymer blends with greater free energy differences in the electron transfer reaction are more likely to have excess vibrational energy. Greater interfacial dipoles and associated electric fields due to spontaneous charge transfer are also expected in these polymer blends. It is likely that both explanations are important. However the electric field-assisted free carrier formation mechanism suggests a route toward OPV materials capable of efficient charge separation without the need for large free energy differences if molecular self-assembly of polar species can be used to form interfacial dipolar fields. This approach would enable efficient free carrier formation while minimizing the ‘wasted’ energy associated with large free energy differences between the polymer and acceptor LUMO levels.

## Summary and Outlook

This chapter describes our recent investigation of interfacial electron transfer and free carrier formation in an OPV polymer blend using ultrafast vibrational spectroscopy. Spontaneous charge transfer at junctions between CN-MEH-PPV and PCBM results in the formation of interfacial dipoles that induce a vibrational Stark shift in the carbonyl vibration of PCBM. This Stark shift enables the direct observation of the diffusion of charge carriers through the concomitant spectral evolution of the carbonyl (C=O) stretch frequency of the methyl ester group of PCBM. Free carrier formation in the CN-MEH-PPV:PCBM blend occurs on the few picosecond time scale - surprisingly quickly in view of the substantial Coulombic barriers arising from the mutual attraction of electrons and holes.

Calculations of the electric field originating from the interfacial dipoles show that the activation energy for free carrier formation is smaller than the expected Coulombic binding energy. The negative poles of the dipoles reside in the PCBM phase and repel electrons from the interfaces. The experimental observations suggest that the mechanism, field-assisted free carrier formation, may play an important role in facilitating efficient charge collection in organic solar cells. In current materials, the interfacial dipoles that produce the electric field arise from spontaneous charge transfer due to large free energy differences between the electron donating and accepting materials. However, the field-assisted free carrier formation mechanism appears to act through a simple electrostatic mechanism. Thus, a new design criterion is suggested for organic solar cells that may enable their open-circuit voltages to be maximized without loss of charge collection efficiency. In particular, if the electron donor:acceptor interface can be engineered to create substantial interfacial dipoles via molecular self-assembly of polar species, then the need for large free energy differences may be reduced. This approach would reduce the energy that is 'wasted' as heat per photon while still supporting efficient free carrier formation.

# References

1. Waldauf, C.; Schilinsky, P.; Hauch, J.; Brabec, C. J. *Thin Solid Films* **2004**, *451*, 503–507.
2. Brabec, C. J. *Sol. Energy Mater. Sol. Cells* **2004**, *83*, 273–292.
3. Krebs, F. C.; Alstrup, J.; Spanggaard, H.; Larsen, K.; Kold, E. *Sol. Energy Mater. Sol. Cells* **2004**, *83*, 293–300.
4. Brabec, C. J.; Hauch, J. A.; Schilinsky, P.; Waldauf, C. *Mater. Res. Soc. Bull.* **2005**, *30*, 50–52.
5. Gunes, S.; Neugebauer, H.; Sariciftci, N. S. *Chem. Rev.* **2007**, *107*, 1324–1338.
6. Thompson, B. C.; Frechet, J. M. J. *Angew. Chem., Int. Ed.* **2008**, *47*, 58–77.
7. Gregg, B. A. *Mat. Res. Soc. Bull.* **2005**, *30*, 20–22.
8. Gregg, B. A.; Chen, S.-G.; Cormier, R. A. *Chem. Mater.* **2004**, *16*, 4586–4599.
9. Ohkita, H.; Cook, S.; Astuti, Y.; Duffy, W.; Tierney, S.; Zhang, W.; Heeney, M.; McCulloch, I.; Nelson, J.; Bradley, D. D. C.; Durrant, J. R. *J. Am. Chem. Soc.* **2008**, *130*, 3030–3042.
10. Arkhipov, V. I.; Bassler, H. *Phys. Status Solidi A* **2004**, *201*, 1152–1187.
11. Bredas, J.-L.; Beljonne, D.; Coropceanu, V.; Cornil, J. *Chem. Rev.* **2004**, *104*, 4971–5003.
12. Brabec, C. J.; Winder, C.; Sariciftci, N. S.; Hummelen, J. C.; Dhanabalan, A.; Van Hal, P. A.; Jannsen, R. A. J. *Adv. Funct. Mater.* **2002**, *12*, 709–712.
13. Winder, C.; Matt, G.; Hummelen, J. C.; Janssen, R. A. J.; Sariciftci, N. S.; Brabec, C. J. *Thin Solid Films* **2002**, *403*, 373–379.
14. Koppe, M.; Scharber, M.; Brabec, C.; Duffy, W.; Heeney, M.; McCulloch, I. *Adv. Funct. Mater.* **2007**, *17*, 1371–1376.
15. Brabec, C. J.; Cravino, A.; Meissner, D.; Sariciftci, N. S.; Fromherz, T.; Rispens, M. T.; Sanchez, L.; Hummelen, J. C. *Adv. Funct. Mater.* **2001**, *11*, 374–380.
16. Muhlbacher, D.; Scharber, M.; Morana, M.; Zhu, Z.; Waller, D.; Gaudana, R.; Brabec, C. *Adv. Mater.* **2006**, *18*, 2884–2889.
17. Lee, S. K.; Cho, N. S.; Kwak, J. H.; Lim, K. S.; Shim, H.-K.; Hwang, D.-H.; Brabec, C. J. *Thin Solid Films* **2006**, *511*, 157–162.
18. Scharber, M.; Muhlbacher, D.; Koppe, M.; Denk, P.; Waldauf, C.; Heeger, A. J.; Brabec, C. J. *Adv. Mater.* **2006**, *18*, 789–794.
19. Xue, J.; Rand, B. P.; Forrest, S. R. *Proc. SPIE* **2006**, *6334*, 63340K.
20. Kooistra, F. B.; Knol, J.; Kastenberg, F.; Popescu, L. M.; Verhees, W. J. H.; Kroon, J. M.; Hummelen, J. C. *Org. Lett.* **2007**, *9*, 551–554.

Downloaded by DUKE UNIV on June 22, 2012 | http://pubs.acs.org
Publication Date (Web): March 11, 2010 | doi: 10.1021/bk-2010-1034.ch005

Downloaded by DUKE UNIV on June 22, 2012 | http://pubs.acs.org
Publication Date (Web): March 11, 2010 | doi: 10.1021/bk-2010-1034.ch005

21. Soci, C.; Hwang, I.-W.; Yang, C.; Moses, D.; Zhu, Z.; Waller, D.; Gaudiana, R.; Brabec, C. J.; Heeger, A. J. *Proc. SPIE* **2006**, *6334*, 63340D.
22. Thomas, C. A.; Zong, K.; Abboud, K. A.; Steel, P. J.; Reynolds, J. R. *J. Am. Chem. Soc.* **2004**, *126*, 16440–16450.
23. Kim, Y.-G.; Thompson, B. C.; Ananthakrishan, N.; Padmanaban, G.; Ramakrishnan, S.; Reynolds, J. R. *J. Mater. Res.* **2005**, *20*, 3188–3198.
24. Thompson, B. C.; Kim, Y.-G.; McCarley, T. D.; Reynolds, J. R. *J. Am. Chem. Soc.* **2006**, *128*, 12714–12725.
25. Galand, E. M.; Kim, Y.-G.; Mwaura, J. K.; Jones, A. G.; McCarley, T. D.; Shrotriya, V.; Yang, Y.; Reynolds, J. R. *Macromolecules* **2006**, *39*, 9132–9142.
26. Campos, L. M.; Tontcheva, A.; Gunes, S.; Sonmez, G.; Neugebauer, H.; Sariciftci, N. S.; Wudl, F. *Chem. Mater.* **2005**, *17*, 4031–4033.
27. Hadipour, A.; de Boer, B.; Blom, P. W. M. *J. Appl. Phys.* **2007**, *102*, 074506.
28. Barbour, L. W.; Hegadorn, M.; Asbury, J. B. *J. Phys. Chem. B* **2006**, *110*, 24281–24286.
29. Barbour, L. W.; Hegadorn, M.; Asbury, J. B. *J. Am. Chem. Soc.* **2007**, *129*, 15884–15894.
30. Barbour, L. W.; Pensack, R. D.; Hegadorn, M.; Arzhantsev, S.; Asbury, J. B. *J. Phys. Chem. C* **2008**, *112*, 3926–3934.
31. Pensack, R. D.; Banyas, K. M.; Barbour, L. W.; Asbury, J. B. *Proc. SPIE* **2008**, *7034*, 703403.
32. Pensack, R. D.; Banyas, K. M.; Barbour, L. W.; Hegadorn, M.; Asbury, J. B. *Phys. Chem. Chem. Phys.* **2009**, *11*, 2575–2591.
33. Jiang, X.-M.; Osterbacka, R.; Korovyanko, O.; An, C. P.; Horovitz, B.; Janssen, R. A. J.; Vardeny, Z. V. *Adv. Funct. Mater.* **2002**, *12*, 587–597.
34. Sheng, C.-X.; Tong, M.; Singh, S.; Vardeny, Z. V. *Phys. Rev. B* **2007**, *75*, 085206.
35. Lee, K.; Janssen, R. A. J.; Sariciftci, N. S.; Heeger, A. J. *Phys. Rev. B* **1994**, *49*, 5781–5784.
36. Miranda, P. B.; Moses, D.; Heeger, A. J. *Phys. Rev. B* **2001**, *64*, 081201(R).
37. Miranda, P. B.; Moses, D.; Heeger, A. J. *Syn. Metals* **2001**, *119*, 619–620.
38. Tong, M.; Sheng, C. X.; Yang, C.; Vardeny, Z. V.; Pang, Y. *Phys. Rev. B* **2004**, *69*, 155211.
39. Anderson, N. A.; Hao, E.; Ai, X.; Hastings, G.; Lian, T. *Chem. Phys. Lett.* **2001**, *347*, 304–310.
40. Dhoot, A. S.; Ginger, D. S.; Beljonne, D.; Shuai, Z.; Greenham, N. C. *Chem. Phys. Lett.* **2002**, *360*, 195–201.
41. Brabec, C. J.; Zerza, G.; Cerullo, G.; De Silvestri, S.; Luzzati, S.; Hummelen, J. C.; Sariciftci, N. S. *Chem. Phys. Lett.* **2001**, *340*, 232–236.
42. Hwang, I.-W.; Xu, Q.-H.; Soci, C.; Chen, B.; Jen, A. K.-Y.; Moses, D.; Heeger, A. J. *Adv. Funct. Mater.* **2007**, *17*, 563–568.
43. Haugeneder, A.; Neges, M.; Kallinger, C.; Spirkl, W.; Lemmer, U.; Feldmann, J.; Scherf, U.; Harth, E.; Gugel, A.; Mullen, K. *Phys. Rev. B* **1999**, *59*, 15346–15351.
44. Xu, Q.-H.; Moses, D.; Heeger, A. J. *Phys. Rev. B* **2003**, *67*, 245417.

45. Pacios, R.; Nelson, J.; Bradley, D. D. C.; Virgili, T.; Lanzani, G.; Brabec, C. J. *J. Phys. Condens. Matter* **2004**, *16*, 8105–8116.
46. Hwang, I.-W.; Moses, D.; Heeger, A. J. *J. Phys. Chem. C* **2008**, *112*, 4350–4354.
47. Fox, D.; Labes, M. M.; Weissberger, A. *Physics and Chemistry of the Organic Solid State*; Interscience: New York, 1963; Vol. 1.
48. Gutman, F.; Lyons, L. E. *Organic Semiconductors, Part A*; Krieger: Malabar, 1981.
49. Pope, M.; Swenberg, C. E. *Electronic Processes in Organic Crystals*; Clarendon Press: New York, 1982.
50. Barbara, P. F.; Meyer, T. J.; Ratner, M. A. *J. Phys. Chem.* **1996**, *100*, 13148–13168.
51. Gray, H. B.; Winkler, J. R. *Proc. Nat. Acad. Sci. U.S.A.* **2005**, *102*, 3534–3539.
52. Park, E. S.; Boxer, S. G. *J. Phys. Chem. B* **2002**, *106*, 5800–5806.
53. Suydam, I. T.; Boxer, S. G. *Biochemistry* **2003**, *42*, 12050–12055.
54. Cho, M. *J. Chem. Phys.* **2009**, *130*, 094505.
55. Arkhipov, V. I.; Heremans, P.; Bassler, H. *Appl. Phys. Lett.* **2003**, *82*, 4605–4607.
56. Rajagopal, A.; Kahn, A. *Adv. Mater.* **1998**, *10*, 140–144.
57. Rajagopal, A.; Wu, C. I.; Kahn, A. *J. Appl. Phys.* **1998**, *83*, 2649–2655.
58. Hill, I. G.; Kahn, A. *J. Appl. Phys.* **1998**, *84*, 5583–5586.
59. Hill, I. G.; Kahn, A. *J. Appl. Phys.* **1999**, *86*, 4515–4519.
60. Hill, I. G.; Milliron, D.; Schwartz, J.; Kahn, A. *Appl. Surf. Sci.* **2000**, *166*, 354–362.
61. Vazquez, H.; Gao, W.; Flores, F.; Kahn, A. *Phys. Rev. B* **2005**, *71*, 041306(R).
62. Schlaf, R.; Parkinson, B. A.; Lee, P. A.; Nebesny, K. W.; Armstrong, N. R. *J. Phys. Chem. B* **1999**, *103*, 2984–2992.
63. Schlettwein, D.; Hesse, K.; Gruhn, N. E.; Lee, P. A.; Nebesny, K. W.; Armstrong, N. R. *J. Phys. Chem. B* **2001**, *105*, 4791–4800.
64. Osikowicz, W.; de Jong, M. P.; Salaneck, W. R. *Adv. Mater.* **2007**, *19*, 4213–4217.
65. Li, Y.; Cao, Y.; Gao, J.; Wang, D.; Yu, G.; Heeger, A. J. *Syn. Metals* **1999**, *99*, 243–248.
66. Brabec, C.; Sariciftci, N. S.; Hummelen, J. C. *Adv. Funct. Mater.* **2001**, *11*, 15–26.
67. Hamm, P.; Lim, M.; DeGrado, W. F.; Hochstrasser, R. M. *J. Chem. Phys.* **2000**, *112*, 1907–1916.
68. Kuzmany, H.; Pfeiffer, R.; Hulman, M.; Kramberger, C. *Phil. Trans. R. Soc. London, Ser. A* **2004**, *362*, 2375–2406.
69. Wadayama, T.; Aoshima, K.; Kawano, S.; Hatta, A. *Appl. Spec.* **2004**, *58*, 299–303.
70. Rice, M. J.; Garstein, Y. N. *Phys. Rev. B* **1996**, *53*, 10764–10770.

Downloaded by DUKE UNIV on June 22, 2012 | http://pubs.acs.org
Publication Date (Web): March 11, 2010 | doi: 10.1021/bk-2010-1034.ch005

Downloaded by STANFORD UNIV GREEN LIBR on June 21, 2012 | http://pubs.acs.org
Publication Date (Web): March 11, 2010 | doi: 10.1021/bk-2010-1034.ch006

## Chapter 6

# Recent Progress on Highly Efficient Bulk Heterojunction Polymer Solar Cells

**Shengqiang Xiao,[1,2] Samuel C. Price,[1] Huaxing Zhou,[1] and Wei You*[,1]**

**[1]Department of Chemistry, the University of North Carolina at Chapel Hill, Chapel Hill, NC, 27599-3290**
**[2]State Key Lab of Advanced Technology for Materials Synthesis and Processing, Wuhan University of Technology, Wuhan, China 430070**
***wyou@unc.edu**

Bulk heterojunction polymer solar cells, based on thin films of polymer/fullerene blends, have progressed rapidly during the past few years. Efficiencies over 6% have been achieved in research labs. In this chapter, a brief review on recent progress was given by focusing on polymers over 3% efficiency in bulk heterojunction solar cells. Design rationales were summarized, as well as the general methods for morphology control.

## Introduction

In order to sustain the economic growth of the World, there has always been insatiable need for energy, 85% of which is provided by burning fossil fuels (such as coal, oil and natural gas). While these natural resources provide cheap and easily accessible energy sources, the large scale consumption of these present two serious problems to mankind. The first problem is the limited reserve of these natural resources – it is estimated that all the fossile fuels would be depleted as early as 2030. Moreover, the tremendous amount of released green house gases (e.g. $CO_2$) from the combustion of fossil fuels leads to the second and even more severe problem: global warming. In realizing these challenges, the scientific community has been looking for new energy sources, which should be environmentally benign and renewable. Currently as a small part of the renewable energy portfolio, harvesting energy directly from the Sun via photovoltaic (PV) technologies is increasingly being recognized as one of

In Functional Polymer Nanocomposites for Energy Storage and Conversion; Wang, Q., et al.;
ACS Symposium Series; American Chemical Society: Washington, DC, 2010.

Downloaded by STANFORD UNIV GREEN LIBR on June 21, 2012 | http://pubs.acs.org
Publication Date (Web): March 11, 2010 | doi: 10.1021/bk-2010-1034.ch006

the most promising long-term solutions – or maybe the ultimate solution – to a sustainable future. The past six decades witnessed a rapid development of the PV technologies, dominated by silicon-based inorganic semiconductors. These inorganic solar cells have been extensively studied and successfully used for pragmatic terrestrial applications. Though these cells are relatively efficient (12 ~ 15% in the PV modules), the high cost of both materials and manufacturing has hindered the widespread utilization of this technology. On the other hand, organic semiconductors, including small-molecule and conjugated polymers developed in the 1970s and 1980s, were envisaged as a possible alternative for PV applications over their inorganic counterparts due to their advantages such as low material and fabrication cost, light weight, and mechanical flexibility (*1*).

Apart from the PV effect in inorganic solar cells, in which light absorption leads to direct creation of free electron-hole pairs, organic solar cells operate under an excitonic mechanism (*2*, *3*). Upon photon absorption, organic materials first create neutral excitons, typically with diffusion length of 5 – 20 nm, which must migrate to a donor (D) – acceptor (A) heterojunction interface for excitons to dissociate into electrons and holes. Subsequently, these charge carriers can traverse the active layer (i.e. organic composite film) followed by charge collection at opposite electrodes (*4*). The most successful method to construct the active layer is to blend a donor material and an acceptor material in a bulk-heterojunction (BHJ) configuration to maximize the D-A interfaces. Specifically, BHJ solar cells based on conjugated polymer-fullerene blends in which fullerenes acting as electron acceptors, have attracted significant research interests in the past decades. One notable feature of these semiconducting polymers is that their physical properties (esp. optical and electrical) can be tailored by modifying their chemical structures, opening up an essentially limitless variety of opportunities for optimization. These "tunable" properties of semiconducting polymers include solubility, molecular weight, bandgap, molecular orbital energy levels, wetting properties, and structural properties such as rigidity, conjugation length, and molecule-to-molecule interactions.

The overall energy conversion efficiency ($\eta$) of any solar cell is given by: $\eta = V_{oc} \times J_{sc} \times FF / P_{in}$, where the $V_{\mathrm{oc}}$ is the open circuit voltage, $J_{\mathrm{sc}}$ is the short current density, *FF* stands for the fill factor, and $P_{in}$ is the incident light intensity. In polymer-fullerene BHJ solar cells, the $V_{\mathrm{oc}}$ of a device is essentially determined by the energy difference between the highest occupied molecular orbital (HOMO) of the donor polymer and the lowest unoccupied molecular orbital (LUMO) of the acceptor (fullerene) (*5*, *6*). The $J_{\mathrm{sc}}$ depends on the photon absorption of the blend layer, which is ultimately determined by the bandgap (the difference between LUMO and HOMO of a semiconductor) and the absorption coefficient of donor and acceptor semiconductors. Therefore, maximizing the overall energy conversion efficiency requires a delicate balance of the bandgap and energy levels of both donor and acceptor materials to collaboratively enhance the $V_{\mathrm{oc}}$ and the $J_{\mathrm{sc}}$. On the other hand, the nature of short exciton diffusion length (~ 10 nm) of conjugated polymers renders the morphology of a D-A blend critical on device properties and performances. It was hypothesized and experimentally proved that a nm-sized D-A bicontinuous interpenetrating network is the ideal morphology to

Downloaded by STANFORD UNIV GREEN LIBR on June 21, 2012 | http://pubs.acs.org
Publication Date (Web): March 11, 2010 | doi: 10.1021/bk-2010-1034.ch006

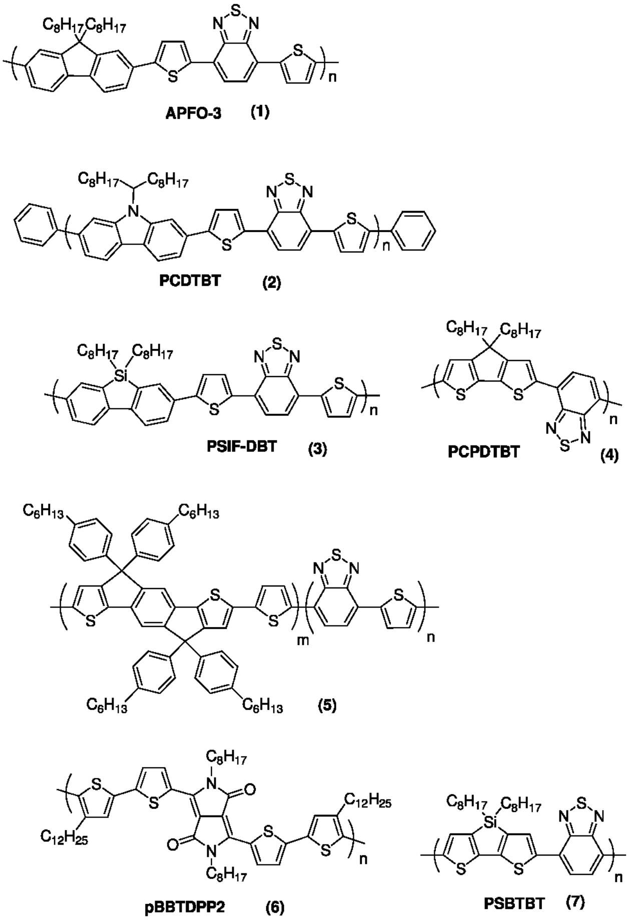

*Figure 1. Structures of donor-acceptor copolymers with high PV performances when blended with fullerene derivatives*

maximize device efficiencies. In retrospect, the short history of polymer-fullerene BHJ solar cells has witnessed various research efforts on topics mentioned above.

In the 1990s, poly(phenylene vinylene)s represented the most studied class of conjugated polymers in organic solar cells. A record high efficiency of 3.3% was attained by blending poly[2-methoxy-5-(3',7'-dimethyloctyloxy)-1,4-phenylene vinylene) (MDMO-PPV) with a soluble fullerene derivative, [6,6]-phenyl-$C_{61}$-butyric acid methyl ester (PCBM) (*7–9*). The next milestone was set by regioregular poly-(3-hexylthiophene) (RR-P3HT), which offered an impressive 5% efficiency when applied in a BHJ solar cell in conjugation with PCBM (*10–12*). However, the relative large bandgap (1.9 eV) and high HOMO (-5.1 eV) of P3HT limited further potential improvement on the efficiency. Therefore, in the past few years, the search for low bandgap polymers has taken center stage. The field has advanced very rapidly: numerous materials have been synthezied and their PV properties have been carefully studied. Not

Downloaded by STANFORD UNIV GREEN LIBR on June 21, 2012 | http://pubs.acs.org
Publication Date (Web): March 11, 2010 | doi: 10.1021/bk-2010-1034.ch006

surprisingly, a new record high efficiency of 6.1% (certified by NREL) was just reported by a BHJ solar cell of poly[*N*-9''-heptadecanyl-2,7-carbazole-*alt*-5,5-(4',7'-di-2-thienyl-2',1',3'-benzothiadiazole)] (PCDTBT) and a fullerene derivative, [6,6]-phenyl-C71-butyric acid methyl ester ($PC_{70}BM$) (*13*, *14*). More importantly, an internal quantum efficiency of near unity has been obtained at this particular case, which implied that 10% or even higher efficiency would be very likely achievable (*15*). In this chapter, we will present an updated report on recent research activities in polymer-PCBM BHJ solar cells. In order to make the discussion more fruitful and inspirational, we limit our selection to polymers that demonstrated > 3% efficiency in the optimized BHJ devies. In addition to new materials, there has been significant progress in morphology control via various processing techniques, which will also be briefly discussed.

## Semiconducting Polymers with Engineered Energy Levels towards High Device Efficiencies

The BHJ solar cell of RR-P3HT and PCBM has been investigated intensively in the past few years (*12*). Efficiencies of ~5% have been achieved in a number of labs for RR-P3HT based BHJ solar cells, largely due to its structural regularity, strong absorption coefficient, high charge carrier mobility and three-dimensional nanoscale organization in thin films. However, RR-P3HT/PCBM blend has almost reached the maximum attainable device performance upon exentive optimization. Further improvement on device efficiency of RR-P3HT/PCBM BHJ solar cell is very limited, mainly due to the large bandgap (1.9 eV) of RR-P3HT and its unmatched energy levels with PCBM.

The control of energy levels and bandgap of donor polymers has been one of the key issues to be addressed on pursuing new materials to achieve higher PV efficiency. Theoretical analyses of the optimum device performance as a function of materials energy levels and bandgap have been carried out, which serve a useful guidance to the design of new polymers other than P3HT (*15*). Two design strategies of donor polymers are commonly adopted by the polymer PV community in order to further enhance the PV performance. The first one is to maximum the open circuit voltage ($V_{oc}$) by lowering the HOMO value of donor polymers, while ensuring the difference between the LUMO of the donor and acceptor is large enough to facilitate exciton splitting. The second one is to improve light absorption via low bandgap polymers, which technically should help enhance the photocurrent ($J_{sc}$). Significant progress has been achieved by employing individual strategies; for example, $V_{oc}$ greater than 1 V and $J_{sc}$ larger than 15 mA/cm$^2$ have been obtained on different polymers. However, to further enhance the overall energy conversion efficiency, one has to create new synthetic approaches welding these two strategies together to comprehensively engineer energy levels and the bandgap of donor polymers, collaboratively improving both $V_{oc}$ and $J_{sc}$.

Continuously lowering the HOMO energy level would potentially lead to a higher $V_{oc}$, which, would diminish the $J_{sc}$ due to the enlarged bandgap. Therefore,

Downloaded by STANFORD UNIV GREEN LIBR on June 21, 2012 | http://pubs.acs.org
Publication Date (Web): March 11, 2010 | doi: 10.1021/bk-2010-1034.ch006

**Table 1. Donor-Acceptor copolymers with high PV performances when blended with $PC_{61}BM$**

| *Poly-mer* | *HOMO (eV)* | *LUMO (eV)* | *$E_g$(opt) (eV)* | *$V_{oc}$ (V)* | *$J_{sc}$ (mA)* | *FF(%)* | *$\eta$ (%)$^a$* | *Ref.* |
|---|---|---|---|---|---|---|---|---|
| (1) | -5.80 | -3.5 | – | 1.03 | 6.3 | 43.0 | 2.8 | (*22*, *23*) |
| (2) | -5.5 | -3.6 | 1.88 | 0.89 | 6.92 | 63.0 | 3.6 | (*13*, *24*) |
| (3) | -5.39 | – | 1.82 | 0.90 | 9.5 | 50.7 | 5.4 | (*25*) |
| (4) | -5.3 | -3.57 | 1.40 | 0.7 | 9<br>11 | 47.0 | 2.8<br>3.2 ($PC_{71}BM$) | (*26*, *27*) |
| (5) | -5.43 | -3.66 | 1.70 | 0.80<br>0.80 | 6.2<br>10.1 | 51.0<br>53.0 | 2.5<br>4.3 ($PC_{71}BM$) | (*28*) |
| (6) | -5.1 | -3.4 | 1.7 (film) | 0.66<br>0.61 | 9.4<br>11.3 | 47.0<br>58.0 | 2.9<br>4.0 ($PC_{71}BM$) | (*29*) |
| (7) | -5.05 | -3.27 | 1.45 | 0.68 | 12.7 | 55.0 | 5.1 ($PC_{71}BM$) | (*30*) |

[a] Indicated in the bracket is the blend of polymer with $PC_{71}BM$.

an optimal bandgap of 1.5 eV was proposed to compromise the balance of the output of $V_{oc}$ and $J_{sc}$. Moreover, it is generally believed that a minimum energy difference of 0.3 eV is required to overcome exciton binding energy for efficient electron transfer from donor polymers to PCBM (*16*), therefore the HOMO and LUMO energy levels of the "ideal" donor polymer for a polymer/PCBM BHJ solar cell are estimated to be around 3.9 eV and 5.4 eV, respectively (*17–19*). Since the energy levels and bandgap of a semiconducting polymer can be tuned and modified via tweaking parameters such as bond length alternation, aromticity, substitution, planarity and intermolecular interactions (*19–21*), a wide range of new donor polymers have been rationally designed and synthesized by adjusting one of these parameter or more often a synergistic combination (*19*). However, in regard to the polymer/PCBM photovoltaic applications, successful examples of an ideal combination of optimal low bandgap (~1.5 eV) and low-lying HOMO level (~5.3 eV or lower) on the donor polymers are still very limited.

## Donor-Acceptor Approach To Construct Low Bandgap Polymers

The most popular and successful method to tune the energy levels and bandgap of a semiconducting polymer is the D-A concept, by alternating electron rich monomers with electron poor monomers via copolymerization. The regular alternation of donor and acceptor groups leads to a broadening of the valence and conduction bands and stabilizing the quinoid form by increasing double bond character between aromatic repeating units, leading to a band gap reduction. Figure 1 listed the structures of D-A polymers that have demonstrated over 3% efficiency when they served as donors in polymer/PCBM BHJ solar cells. Table 1 summaried their energy levels, bandgap and their PV performance. A particularly notable feature is the almost exclusive use of benzothiadiazole as electron poor monomer, whereas a variety of electron rich monomers have been used, such as

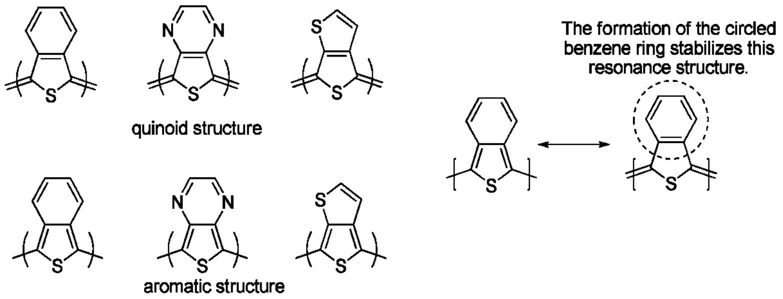
quinoid structure
aromatic structure
The formation of the circled benzene ring stabilizes this resonance structure.
S
N
N

*Figure 2. Aromatic and quinoid forms of poly(benzo[c]thiophene) (a), poly(thieno[3,4-b]pyrazine (b), and poly(thieno[3,4-b]-thiophene) (c).*

Downloaded by STANFORD UNIV GREEN LIBR on June 21, 2012 | http://pubs.acs.org
Publication Date (Web): March 11, 2010 | doi: 10.1021/bk-2010-1034.ch006

thiophene, fused bithiophene, carbozole or fluorene analogues. Closer inspection revealed that incorporation of benzene into the donor monomer usually lead to a lower HOMO energy level, resulting a higher $V_{\mathrm{oc}}$ in the related BHJ solar cells. On the other hand, more thiophenes in the conjugated system raise the HOMO energy level (and thereby smaller $V_{\mathrm{oc}}$); however, a smaller bandgap was generally obtained, offering a higher $J_{\mathrm{sc}}$.

It is worth to note that D-A polymers may have intrinsically low charge carrier mobility since charge carriers are likely to be tightly bound to either the donors or the acceptors, depending on whether holes or electrons are the major charge carriers. Low charge carrier mobility hinders the charge transport across the film, which usually dictates a very thin film (<100 nm) to be employed. Such a thin film cannot adequately absorb the light within the absorption range of the film. This is probably the reason why most of these polymers with alternating D-A structures failed to show expected PV performance, even after extensive optimization.

## Incorporation of Stabilized Quinoid Form To Achieve Low Bandgap

Incorporation of a stabilized quinoid form represents another effective method to tune the bandgap and energy level (to a lesser extent) of semiconducting polymers. Typically two aromatic units are fused in a particular geometry to take advantage of the larger value of resonance energy of benzene (1.56 eV) over thiophene (1.26 eV), so that the thiophene ring tends to de-aromatize to adopt a quinoid structure. Since the quinoid resonance form is lower in energy than the aromatic form, stabilizing the quinoid form will effectively reduce the bandgap of related conjugated polymers. A few successful examples are shown in Figure 2, including poly(benzo[*c*]thiophene) ($E_g$ = 1.1 eV) (*31*), poly(thieno[3,4-*b*]pyrazine ($E_g$ = 0.95 eV) (*32*), and poly(thieno[3,4-*b*]thiophene) ($E_g$ = 0.8-0.9 eV) (*33*, *34*). The major drawback of these fused systems lies in their relatively high-lying HOMO energy levels, which explains that low bandgap copolymers synthesized by alternating these pre-qunoid monomers with other aromatic rings such as thiophenes and fluorenes showed low $V_{\mathrm{oc}}$ in BHJ solar cells (*35–39*). Nevertheless, a series of copolymers by althernating thieno[3,4-*b*]thiophene and benzodithiophene showed improved $V_{oc}$ and very high $J_{sc}$ (Table 2). Energy conversion efficiency as high as 6% has been reported via exquisite chemical modifications to fine-tune energy levels and bandgaps of this series of polymers (Figure 3) (*40*, *41*).

## Morphology Control towards High Efficiencies

In parallel with significant research efforts on engineering energy levels and bandgaps of novel donor polymers for BHJ PV applications, various approaches to control the morphology of active D-A blends have also been attempted. The full potential of any donor polymers in a BHJ blend with PCBM can only be demonstrated via morphology control of the D-A blend, in order to achieve the desired nm-sized separated, however continuous two phases.

Downloaded by STANFORD UNIV GREEN LIBR on June 21, 2012 | http://pubs.acs.org
Publication Date (Web): March 11, 2010 | doi: 10.1021/bk-2010-1034.ch006

### Annealing and Additives

The effect of annealing is exemplied by RR-P3HT/PCBM BHJ solar cells, whose device efficiency had stalled at ~ 1-3% for a few years. However, the efficiency was much improved to 5% via either “solvent annealing” or “thermal annealing” of the finished device, partly because the semi-crystalline nature of RR-P3HT facilitated the formation of nm-sized D-A bi-continuous interpenetrating network upon annealing (*42*). Though different types of annealing work well with RR-P3HT/PCBM BHJ solar cells to improve the device performance, the “annealing” method rarely helped other polymer/PCBM BHJ systems, mainly due to the amorphous nature of most newly synthesized conjugated polymers. The rescue came from a rather serendipitous approach: adding a small amount of additives to the polymer/PCBM blend. It is believed that these additives (e.g. diiodooctane, octanedithiol) selectively dissolved PCBM (or $PC_{70}BM$), aggregating the fullerene acceptor into nm-sized n-type domains upon removal of additives, which helped approach the ideal morphology. Details are provided by two most recent review papers (*43*, *44*).

### TiO2 Interfacial Layer

The generally low hole mobility of donor polymers usually limits the thickness of active layers to be less than 100 nm. Such a thin film cannot absorb light efficiently, which is exacerbated by the optical interference between the incident light and the light reflected from the top metal electrode. In order to redistribute the light intensity in the active layer, a solution processible TiOx layer via sol gel chemistry was inserted between the top metal electrode and the active layer. This thin layer of TiOx (~10 nm) not only spatially redistributed the light to maximize the light absorption in the thin active layer, also served as a hole blocking layer whereas promoting electron transport. This strategy has been

Downloaded by STANFORD UNIV GREEN LIBR on June 21, 2012 | http://pubs.acs.org
Publication Date (Web): March 11, 2010 | doi: 10.1021/bk-2010-1034.ch006

**Table 2. Characteristic properties of polymers and solar cell devices when mixed with $PC_{61}BM$ (SOURCE: Reproduced from Reference (*41*). Copyright 2009 American Chemical Society.)**

| *Polymer* | *HOMO (eV)* | *LUMO (eV)* | *$E_g$(opt) (eV)* | *$V_{oc}$ (V)* | *$J_{sc}$ (mA)* | *FF(%)* | *η( % )* |
|---|---|---|---|---|---|---|---|
| PTB1 | -4.90 | -3.20 | 1.58 | 0.58 | 12.5 | 65.4 | 4.76 |
| | | | | 0.56 | 15.0 | 63.3 | 5.3 ($PC_{71}BM$)[a] |
| PTB2 | -4.94 | -3.22 | 1.59 | 0.60 | 12.8 | 66.3 | 5.10 |
| PTB3 | -5.04 | -3.29 | 1.60 | 0.74 | 13.1 | 56.8 | 5.53 |
| | | | | 0.72 | 13.9 | 58.5 | 5.85[b] |
| PTB4 | -5.12 | -3.31 | 1.63 | 0.76 | 9.20 | 44.5 | 3.10 |
| | | | | 0.74 | 13.0 | 61.4 | 5.90[b] |
| PTB5 | -5.01 | -3.24 | 1.62 | 0.68 | 10.3 | 43.1 | 3.02 |
| | | | | 0.66 | 10.7 | 58.0 | 4.10[b] |

[a] Indicated in the bracket is the blend of polymer with $PC_{71}BM$. [b] Devices fabricated from mixed solvents dichlorobenzene/diiodooctance (97/3, v/v).

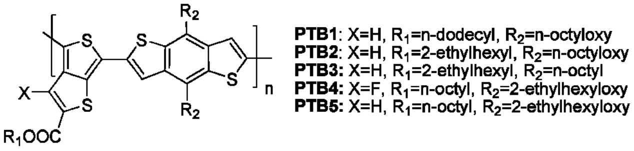
R2
S
S
S
S
X
R1OOC
R2
n
PTB1: X=H, R1=n-dodecyl, R2=n-octyloxy
PTB2: X=H, R1=2-ethylhexyl, R2=n-octyloxy
PTB3: X=H, R1=2-ethylhexyl, R2=n-octyl
PTB4: X=F, R1=n-octyl, R2=2-ethylhexyloxy
PTB5: X=H, R1=n-octyl, R2=2-ethylhexyloxy

*Figure 3. Molecular structures of the **PTB** polymers.*

successfully applied in a few examples; the most notable case was to improve the efficiency of PCDTBT (polymer 2 in Figure 1) based BHJ solar cell from 3.6% to an unprecedented 6.1% (*14*). In fact, an internal quantum efficiency of close to 100% was observed, which experimentally proved that it is possible to collect all the separated charge carriers in a typical BHJ solar cell.

## Summary

Since the inception of polymer/PCBM BHJ solar cell in 1995, tremendous research activities have been devoted to this particular field. Numerous new polymers have been synthesized and tested, though only a handful of donor polymers have demonstrated over 3% efficiency when blended with PCBM (or $PC_{70}BM$) in BHJ solar cells, one of which indeed set a new record high efficiency (6.1%). It is expected that 10% efficiency or greater will be reached in the next few years, if one can design and synthesize the "ideal" polymers and demonstrate their full potential through morphology control via either fine tuning chemical structures or other physical methods.

# References

1. McGehee, M. D.; Topinka, M. A. *Nat. Mater.* **2006**, *5*, 675–676.
2. Moliton, A.; Nunzi, J.-M. *Polym. Int.* **2006**, *55*, 583–600.
3. Nunzi, J. M. *Compt. Rend. Physique* **2002**, *3*, 523–542.
4. Tang, C. W. *Appl. Phys. Lett.* **1986**, *48*, 183–185.
5. Brabec, C. J.; Cravino, A.; Meissner, D.; Sariciftci, N. S.; Fromherz, T.; Rispens, M. T.; Sanchez, L.; Hummelen, J. C. *Adv. Funct. Mater.* **2001**, *11*, 374–380.
6. Koster, L. J. A.; Mihailetchi, V. D.; Ramaker, R.; Blom, P. W. M. *Appl. Phys. Lett.* **2005**, *86*, 123509.
7. Shaheen, S. E.; Brabec, C. J.; Sariciftci, N. S.; Padinger, F.; Fromherz, T.; Hummelen, J. C. *Appl. Phys. Lett.* **2001**, *78*, 841–843.
8. Gunes, S.; Neugebauer, H.; Sariciftci, N. S. *Chem. Rev.* **2007**, *107*, 1324–1338.
9. Brabec, C. J.; Shaheen, S. E.; Winder, C.; Sariciftci, N. S.; Denk, P. *Appl. Phys. Lett.* **2002**, *80*, 1288–1290.
10. Ma, W. L.; Yang, C. Y.; Gong, X.; Lee, K.; Heeger, A. J. *Adv. Funct. Mater.* **2005**, *15*, 1617–1622.
11. Li, G.; Shrotriya, V.; Huang, J. S.; Yao, Y.; Moriarty, T.; Emery, K.; Yang, Y. *Nat. Mater.* **2005**, *4*, 864–868.
12. Dennler, G.; Scharber, M. C.; Brabec, C. J. *Adv. Mater.* **2009**, *21*, 1323–1338.
13. Blouin, N.; Michaud, A.; Leclerc, M. *Adv. Mater.* **2007**, *19*, 2295–2300.
14. Park, S. H.; Roy, A.; Beaupre, S.; Cho, S.; Coates, N.; Moon, J. S.; Moses, D.; Leclerc, M.; Lee, K.; Heeger, A. J. *Nat. Photonics* **2009**, *3*, 297–302.
15. Scharber, M. C.; Mühlbacher, D.; Koppe, M.; Denk, P.; Waldauf, C.; Heeger, A. J.; Brabec, C. J. *Adv. Mater.* **2006**, *18*, 789–794.
16. Arkhipov, V. I.; Bassler, H. *Phys. Status Solidi A* **2004**, *201*, 1152–1187.
17. Bundgaard, E.; Krebs, F. C. *Sol. Energy Mater. Sol. Cells* **2007**, *91*, 954–985.
18. Thompson, B. C.; Fréchet, J. M. J. *Angew. Chem., Int. Ed.* **2008**, *47*, 58–77.
19. Kroon, R.; Lenes, M.; Hummelen, J. C.; Blom, P. W. M.; de Boer, B. *Polym. Rev.* **2008**, *48*, 531–582.
20. Roncali, J. *Chem. Rev.* **1997**, *97*, 173–205.
21. Roncali, J. *Macromol. Rapid Commun.* **2007**, *28*, 1761–1775.
22. Zhang, F.; Jespersen, K. G.; Björström, C.; Svensson, M.; Andersson, M. R.; Sundström, V.; Magnusson, K.; Moons, E.; Yartsev, A.; Inganäs, O. *Adv. Funct. Mater.* **2006**, *16*, 667–674.
23. Andersson, L. M.; Zhang, F.; Inganas, O. *Appl. Phys. Lett.* **2007**, *91*, 071108.
24. Blouin, N.; Michaud, A.; Gendron, D.; Wakim, S.; Blair, E.; Neagu-Plesu, R.; Belletete, M.; Durocher, G.; Tao, Y.; Leclerc, M. *J. Am. Chem. Soc.* **2008**, *130*, 732–742.
25. Wang, E.; Wang, L.; Lan, L. F.; Luo, C.; Zhuang, W. L.; Peng, J. B.; Cao, Y. *Appl. Phys. Lett.* **2008**, *92*, 033307.
26. Muhlbacher, D.; Scharber, M.; Morana, M.; Zhu, Z. G.; Waller, D.; Gaudiana, R.; Brabec, C. *Adv. Mater.* **2006**, *18*, 2884–2889.

Downloaded by STANFORD UNIV GREEN LIBR on June 21, 2012 | http://pubs.acs.org
Publication Date (Web): March 11, 2010 | doi: 10.1021/bk-2010-1034.ch006

27. Peet, J.; Kim, J. Y.; Coates, N. E.; Ma, W. L.; Moses, D.; Heeger, A. J.; Bazan, G. C. *Nat. Mater.* **2007**, *6*, 497–500.
28. Chen, C. P.; Chan, S. H.; Chao, T. C.; Ting, C.; Ko, B. T. *J. Am. Chem. Soc.* **2008**, *130*, 12828–12833.
29. Wienk, M. M.; Turbiez, M.; Gilot, J.; Janssen, R. A. J. *Adv. Mater.* **2008**, *20*, 2556–2560.
30. Hou, J.; Chen, H.-Y.; Zhang, S.; Li, G.; Yang, Y. *J. Am. Chem. Soc.* **2008**, *130*, 16144–16145.
31. Wudl, F.; Kobayashi, M.; Heeger, A. J. *J. Org. Chem.* **1984**, *49*, 3382–3384.
32. Pomerantz, M.; Chalonergill, B.; Harding, L. O.; Tseng, J. J.; Pomerantz, W. J. *J. Chem. Soc. Chem. Commun.* **1992**, 1672–1673.
33. Hong, S. Y.; Marynick, D. S. *Macromolecules* **1992**, *25*, 4652–4657.
34. Sotzing, G. A.; Lee, K. H. *Macromolecules* **2002**, *35*, 7281–7286.
35. Qin, Y.; Kim, J. Y.; Frisbie, C. D.; Hillmyer, M. A. *Macromolecules* **2008**, *41*, 5563–5570.
36. Hou, J. H.; Park, M. H.; Zhang, S. Q.; Yao, Y.; Chen, L. M.; Li, J. H.; Yang, Y. *Macromolecules* **2008**, *41*, 6012–6018.
37. Wienk, M. M.; Turbiez, M. G. R.; Struijk, M. P.; Fonrodona, M.; Janssen, R. A. J. *Appl. Phys. Lett.* **2006**, *88*, 153511.
38. Zhang, F.; Mammo, W.; Andersson, L. M.; Admassie, S.; Andersson, M. R.; Inganäs, O. *Adv. Mater.* **2006**, *18*, 2169–2173.
39. Liang, Y. Y.; Xiao, S. Q.; Feng, D. Q.; Yu, L. P. *J. Phys. Chem. C* **2008**, *112*, 7866–7871.
40. Liang, Y.; Wu, Y.; Feng, D.; Tsai, S.-T.; Son, H.-J.; Li, G.; Yu, L. *J. Am. Chem. Soc.* **2009**, *131*, 56–57.
41. Liang, Y.; Feng, D.; Wu, Y.; Tsai, S.-T.; Li, G.; Ray, C.; Yu, L. *J. Am. Chem. Soc.* **2009**, *131*, 7792–7799.
42. Moon, J. S.; Lee, J. K.; Cho, S.; Byun, J.; Heeger, A. J. *Nano Lett.* **2009**, *9*, 230–234.
43. Peet, J.; Senatore, M. L.; Heeger, A. J.; Bazan, G. C. *Adv. Mater.* **2009**, *21*, 1521–1527.
44. Chen, L.-M.; Hong, Z.; Li, G.; Yang, Y. *Adv. Mater.* **2009**, *21*, 1434–1449.

Downloaded by STANFORD UNIV GREEN LIBR on June 21, 2012 | http://pubs.acs.org
Publication Date (Web): March 11, 2010 | doi: 10.1021/bk-2010-1034.ch006

Downloaded by CORNELL UNIV on June 22, 2012 | http://pubs.acs.org
Publication Date (Web): March 11, 2010 | doi: 10.1021/bk-2010-1034.ch007

## Chapter 7

# Two Scale Roughness, Self-Cleaning, and Low Reflectivity Silicon Surface for Solar Cell Applications

**Yonghao Xiu,[1,2] Yan Liu,[2] and C. P. Wong [*,2]**

**[1]School of Chemical and Biomolecular Engineering, 311 Ferst Drive, Atlanta, GA 30332, U.S.A.**
**[2]School of Materials Science and Engineering, 771 Ferst Drive, Atlanta, GA 30332, U.S.A.**
**[*]cp.wong@mse.gatech.edu**

Si surface modification is of great significance for a variety of applications, such as hydrophobic treatment, surface passivation of photovoltaic devices, and microelectronic devices. In this study, a facile way of forming superhydrophobic surfaces is reported that uses Au assisted HF/$H_2O_2$ etching of silicon wafers. The Au layer was deposited onto a silicon wafer via e-beam evaporation. By controlling the evaporation and etching times, the micro/nano scale roughness can be manipulated and superhydrophobic surfaces with reduced hysteresis can be generated. Light reflection on the as prepared black surfaces was measured to assess the efficiency for low cost solar cell applications. The two scale roughnes surface showed a much reduced reflectance compared to that of pyramid textured silicon surfaces which are commonly employed in high efficiency solar cells. This approach offers a new way both to theoretically study the surface roughness effect and to investigate engineering applications of self-cleaning surfaces in solar cells.

## Introduction

Over the last decade, much attention has been directed to semiconductor materials with surface micro/nano structures, primarily due to potential

In Functional Polymer Nanocomposites for Energy Storage and Conversion; Wang, Q., et al.;
ACS Symposium Series; American Chemical Society: Washington, DC, 2010.

applications in opto-electronics, chemical and biochemical sensing and the possibility of creating material properties not readily obtained in the corresponding crystalline materials (*1*). The surface micro/nano structures of semiconductors can be produced by anodic etching, where the semiconductor is biased positively in a conductive electrolyte to facilitate oxidation and subsequent removal of surface atoms. The magnitude of the applied voltage and current and the electrolyte composition are used to control etch rate and, thus, morphology and properties. This approach is hampered by the need for a conducting substrate that is stable under the electrochemical etching conditions and the need to explore the relatively large parameter space to identify the optimum etching conditions. To circumvent these problems, an efficient chemical etching method to produce Si surface structures that requires no external bias was developed recently (*2*, *3*). In this process, a discontinuous layer of Pt or Au (20 - 200 Å thick) is deposited on the silicon surface before immersing it in HF/$H_2O_2$. Reduction of the oxidant ($H_2O_2$) injects holes into the valence band of the semiconductor material, which then participate in oxidative etching of the semiconductor surface.

Superhydrophobic self-cleaning surfaces are of interest for a variety of applications such as self-cleaning, water repellency and anticorrosion (*4*, *5*) properties. Numerous approaches to generate superhydrophobic surfaces have been proposed (*6–11*). In these studies, high contact angles and reduced contact angle hysteresis were intensively investigated (*12–18*). In our study, we invoked a surface etching technique for the preparation of multi-functional (self-cleaning, non-reflecting, water repellent) surface micro/nano structures for potential photovoltaic applications. It is expected that by controlled manipulation of surface structures via the etching process, multifunctional silicon surfaces can be achieved and cost-effective photovoltaics may be possible (*19*).

## Experimental

p-type silicon (100) wafers with a resistivity of 1-10 Ω cm were used in all experiments. KOH etching was performed in a solution of KOH (2-3 wt %), water, and isopropyl alcohol (20% by volume) at 80-85 °C for 20-30 min to create pyramidal structures (2-4 μm in height). To form nanostructures,, a thin discontinuous layer of Au (2-10nm diameter) was deposited by e-beam evaporation. Etching was then performed for various times in an HF/$H_2O_2$ solution (49%HF, 30%$H_2O_2$ and isopropyl alcohol with a volume ratio of 1:2:1 was used in etching nanostructures only, and 49% HF, 30% H2O2, and H2O with a volume ratio of 1:5:10 was used in etching two scale structures). Subsequently, the Au layer was removed by immersing the samples in KI/I2 (100 g KI and 25g I2 per 1L $H_2O$) for 60 seconds.

Contact angle measurements were performed with a Rame-Hart goniometer that has a CCD camera equipped for image capture. Scanning Electron Microscopy (SEM) was used to investigate the surface morphology. After fabrication of the surface structures, surface fluorination was performed by treatment with fluoroalkylsilane. Ten millimolar solutions of perfluorooctyl

Downloaded by CORNELL UNIV on June 22, 2012 | http://pubs.acs.org
Publication Date (Web): March 11, 2010 | doi: 10.1021/bk-2010-1034.ch007

Downloaded by CORNELL UNIV on June 22, 2012 | http://pubs.acs.org
Publication Date (Web): March 11, 2010 | doi: 10.1021/bk-2010-1034.ch007

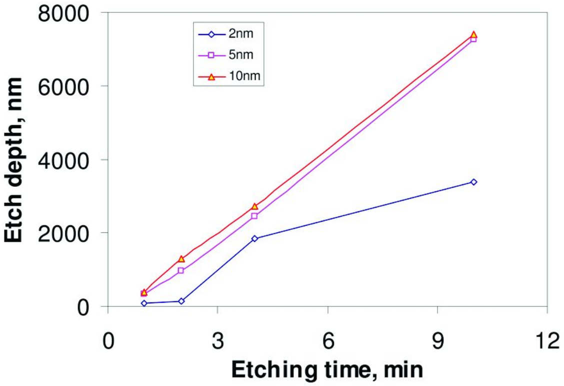

*Figure 1. Etching depth of Au assisted etching of Si in HF/$H_2O_2$.*

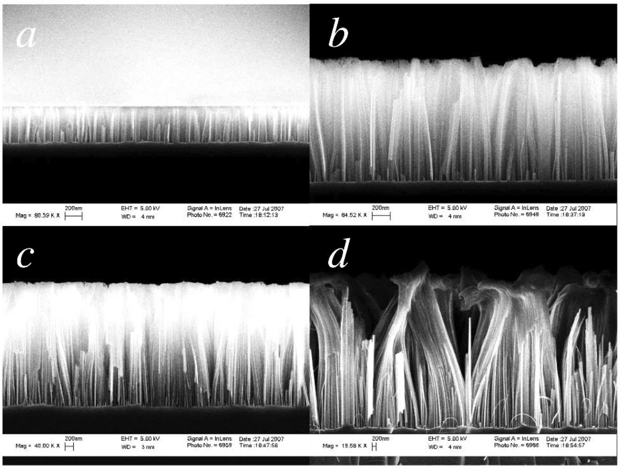
a
b
c
d
Mag = 80.39 K X
200nm
EHT = 5.00 kV
WD = 4 mm
Signal A = InLens
Photo No. = 6922
Date :27 Jul 2007
Time :18:12:13
Mag = 84.52 K X
200nm
EHT = 5.00 kV
WD = 4 mm
Signal A = InLens
Photo No. = 6948
Date :27 Jul 2007
Time :18:37:19
Mag = 40.00 K X
200nm
EHT = 5.00 kV
WD = 3 mm
Signal A = InLens
Photo No. = 6959
Date :27 Jul 2007
Time :18:47:56
Mag = 19.58 K X
200nm
EHT = 5.00 kV
WD = 4 mm
Signal A = InLens
Photo No. = 6966
Date :27 Jul 2007
Time :18:54:57

*Figure 2. Cross-sections of 10nm Au layer assisted Si etching for etch times, (a) 1min, (b) 2min, (c) 4 min, and (d) 10 min.*

trichlorosilane (PFOS) were prepared in hexane. For the specific treatment, the structured silicon wafer was soaked in the solutions for 30 min followed by a heat treatment at 150°C in air for 1 hour, to complete the hydrophobic surface modification. The nanostructured surface was characterized by diffuse reflectivity measurements to establish reflectivity. The weighted reflectance (WR) was calculated by normalizing the hemispherical reflectance spectrum (350-1100 nm) by the AM (air mass) 1.5 spectrum.

## Results and Discussion

Metal assisted etching of Si surfaces is used in the preparation of black non reflecting surfaces (*2*). This process may have considerable promise for light

Downloaded by CORNELL UNIV on June 22, 2012 | http://pubs.acs.org
Publication Date (Web): March 11, 2010 | doi: 10.1021/bk-2010-1034.ch007

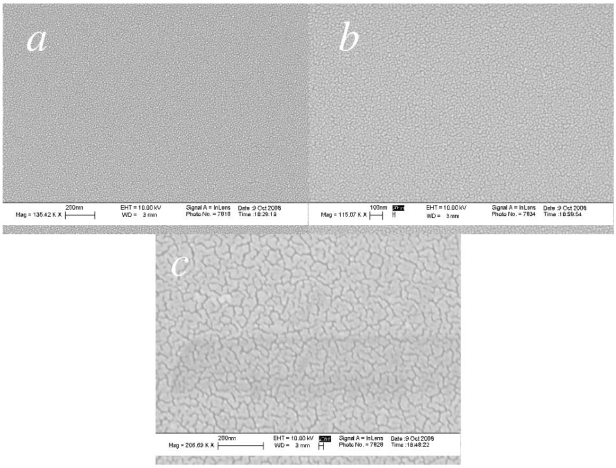

*Figure 3. Silicon surface with Au layers of thickness of, 2 nm, 5 nm and 10 nm respectively.*

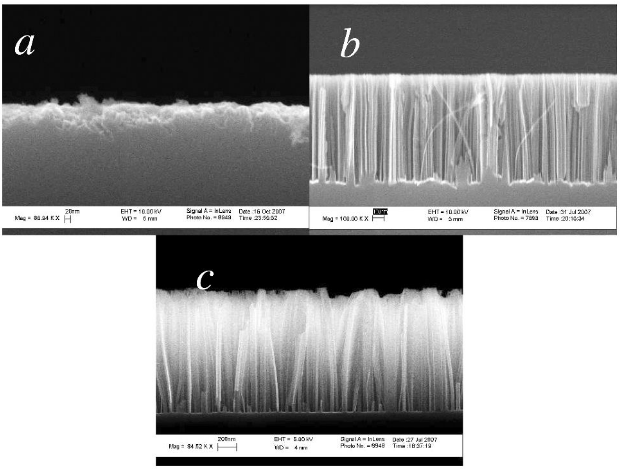

*Figure 4. Cross-section of silicon etched for 2 min: 2 nm; 5 nm, 10 nm.*

trapping in high efficiency solar cells. In this study, we investigate the application of this technique for the generation of superhydrophobicity for which structured surfaces are necessary. Au was used in our study for the metal layer on a silicon surface.

## Etching Time

To achieve superhydrophobicity, hydrophobic surface modification, density of surface structures, and height and diameter of the asperities must be controlled; only then will the hydrophobic surface shows a high contact angle. The density

Downloaded by CORNELL UNIV on June 22, 2012 | http://pubs.acs.org
Publication Date (Web): March 11, 2010 | doi: 10.1021/bk-2010-1034.ch007

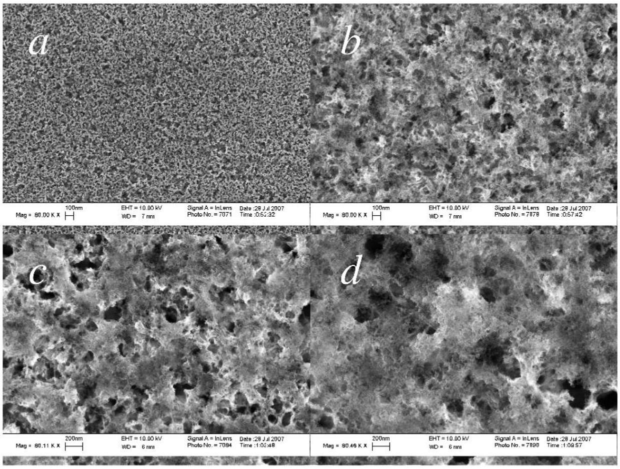

*Figure 5. 2 nm Au assisted etching of Si for different times, (a) 1 min, (b) 2 min, (c) 4 min, and (d) 10 min.*

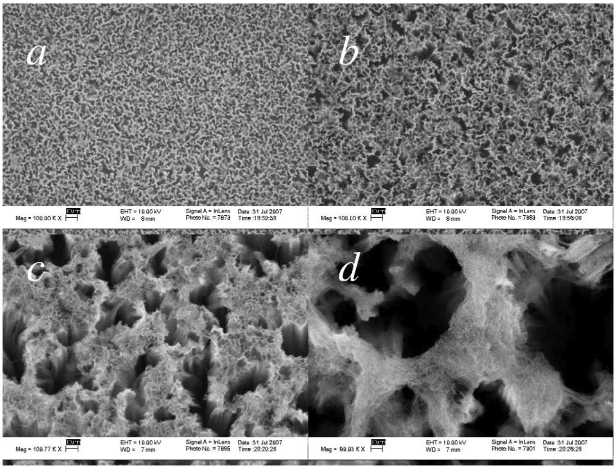

*Figure 6. 5nm Au assisted etching of Si for different times, (a) 1 min, (b) 2 min, (c) 4 min, and (d) 10 min.*

of the surface structures can be represented by the micro three phase contact line density which yields the necessary surface forces to suspend the liquid against the forces of gravity. The topographic features must be tall enough so that the liquid does not reach the underlying surface. Also, the diameter of individual feature needs to be small enough to reduce the solid/liquid contact area so that a higher apparent contact angle results. When the etching time is increased, the etching depth of the silicon surface increases. The depth of the surface structures is important in achieving better dewetting properties. The time effect on the etch depth is shown in Figure 1. With time, the etching depth increased at different rates for different thickness of Au layers. For 10 nm Au layers on silicon, the

SEM cross-section images of surfaces etched at different time are shown in Figure 2.

## Thickness of the Au Layer

The thickness of the Au layer is also very important in achieving the desired surface structures. We prepared Au layers of three different thicknesses on silicon surfaces: 2 nm, 5 nm and 10 nm as shown in Figure 3. The effect of the Au layer on etching is shown in Figure 4. As the Au layer thickness increases, the surface etched structures also increase in height. This corresponds to the difference in the etching rate shown in Figure 1. For a 2 nm Au layer (low particle density on silicon surface), the etch rate is much lower than that for 5 nm and 10 nm Au layers. This observation may be due to the low density of Au particles. However, for 5 nm and 10 nm Au layers on silicon surfaces which have a higher density than 2 nm Au, the higher density of Au particles may cause the etching to proceed at a higher speed. The etching rate for the 5 nm and 10 nm Au coated silicon surfaces is similar and the etching rate is also not dependent on the etching depth for thicker Au films on silicon surface. However, for 2 nm Au on silicon surface, the etching is slowed down when the etching proceeds. This also suggests a depth dependent diffusion effect on the etching process.

Downloaded by CORNELL UNIV on June 22, 2012 | http://pubs.acs.org
Publication Date (Web): March 11, 2010 | doi: 10.1021/bk-2010-1034.ch007

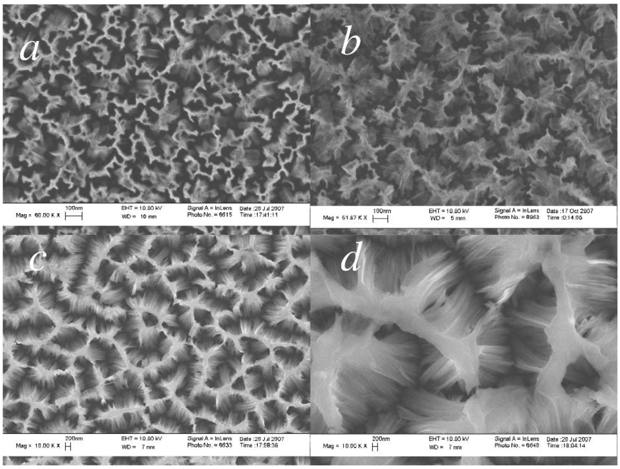
a
b
c
d
Mag = 60.00 K X
100nm
EHT = 10.00 kV
WD = 10 mm
Signal A = InLens
Photo No. = 6615
Date :20 Jul 2007
Time :17:41:11
Mag = 51.67 K X
100nm
EHT = 10.00 kV
WD = 5 mm
Signal A = InLens
Photo No. = 8963
Date :17 Oct 2007
Time :0:14:06
Mag = 10.00 K X
200nm
EHT = 10.00 kV
WD = 7 mm
Signal A = InLens
Photo No. = 6633
Date :20 Jul 2007
Time :17:58:36
Mag = 10.00 K X
200nm
EHT = 10.00 kV
WD = 7 mm
Signal A = InLens
Photo No. = 6640
Date :20 Jul 2007
Time :18:04:14

*Figure 7. 10nm Au assisted etching of Si for different times, (a) 1min, (b) 2 min, and (c) 4 min and (d) 10 min.*

## Effect of Au Layer on the Etching Morphology

The etched silicon surfaces are shown in Figures 5, 6 and 7 for different etching times with different Au layers on top. As shown from the figures, the surface morphology size scale increased from nano scale when etched for a shorter time with thinner Au layer to submicron scale when etched at longer time with thicker Au layers. Clearly, the surface morphology can be manipulated over quite a large scale range.

We know that for anodic silicon etching, the voltage and current are critical. In our process electroless etching is used. The hydrogen peroxide affects the injection of holes from Au particles into silicon substrate; therefore, the particle size as well as the Au particle density may play an important role on the etching reaction since both affect the hole injection process. As a result, it is expected that for small Au particles (e.g., 2 nm), the increase in the particle size will result in an increase in the number of holes injected into silicon, while for large Au particles (5-10 nm) the size effect vanishes.

According to Wenzel and Cassie, rough surfaces facilitate the enhancement of contact angles which cannot be achieved on a flat surface even with the most hydrophobic surface coatings available. The rough silicon surfaces obtained from the metal assisted etching process were therefore treated with fluoroalkyl silane (PFOS) to render the surface hydrophobic to investigate the surface roughness effect in achieving superhydrophobicity. Contact angle and contact angle hysteresis data are shown in Figures 8 and 9. With increasing etching time, the contact angles increased. All surfaces showed contact angles greater than 140° while for a flat silicon surface treated with the same silane, the contact angle is only ~115°. In addition, the contact angle hysteresis of all samples decreased with etching time, which suggests an enhanced surface roughness with longer etching times. The effect of the thickness of Au layers is also shown in Figures 8 and 9. With thicker layers, contact angles were higher and hysteresis was much reduced relative to that of thinner Au layers. For 10 nm Au layers, the silicon surface etched for 10 min showed a contact angle of 167.7° and a hysteresis of 12.4°.

Downloaded by CORNELL UNIV on June 22, 2012 | http://pubs.acs.org
Publication Date (Web): March 11, 2010 | doi: 10.1021/bk-2010-1034.ch007

## Two-Scale Surface Structures

The above data have demonstrated that the surface nanostructures formed from Au-assisted etching in HF/H2O2/H2O do not result in roll-off superhydrophobicity within a short (<4 min) etch time.Onlotus leaf surfaces, two-scale roughness generates superhydrophobic and selfcleaning micron-sized silicon pyramids can be formed using KOHetching and nanostructures can be fabricated readily using Au-assisted etching. It may be possible to form a hierarchical structure that allows a biomimetic superhydrophobic surface to be realized in silicon. Indeed, by first etching Si pyramids, followed by deposition of a 5 nm Au layer and subsequent Au-assisted etching, microsized pyramids with attendant nanostructures can be generated by the two-step etching process. The pyramid Si surfaces alone cannot generate a superhydrophobic state (with a contact angle of ~140° after hydrophobization with PFOS). The nanostructure is critical on top of the pyramid surfaces to achieve both a high contact angle and low hysteresis after surface hydrophobization.

Downloaded by CORNELL UNIV on June 22, 2012 | http://pubs.acs.org
Publication Date (Web): March 11, 2010 | doi: 10.1021/bk-2010-1034.ch007

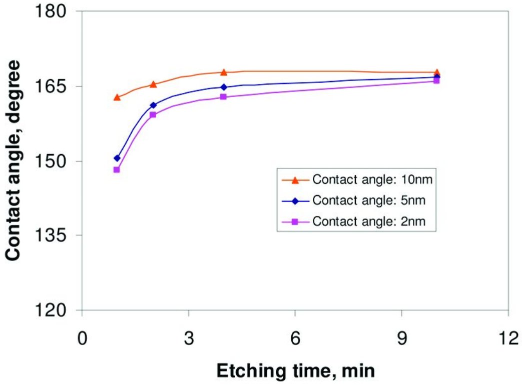

*Figure 8. Stactic Contact angles for etched silicon samples.*

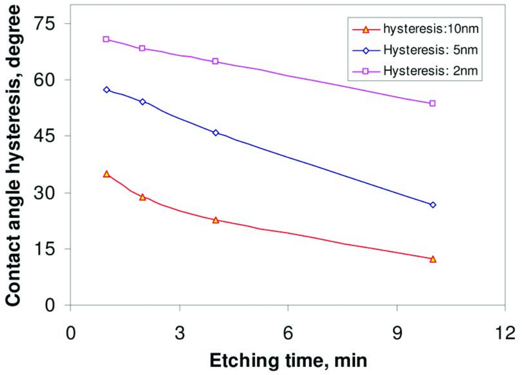

*Figure 9. Contact angle hysteresis for etched silicon samples.*

As shown in Figure 10, after Au-assisted etching of the silicon pyramid morphology, the surface became hierarchically rough. Treatment of the surface with PFOS to hydrophobize the surface yielded high contact angles and low hysteresis, as shown in the inset of Figure 11. The existence of the two roughness scales resulted in a roll-off superhydrophobic surface due to the reduced liquid contact area fraction. Figure 12 indicates that, with increased etch time, the contact angle hysteresis first decreased then increased after 2 min of Au-assisted etching. The hysteresis reduction is due to the generation of nanoscale roughness superimposed on the microscale roughness; the subsequent hysteresis increase can be attributed to a reduction of the size of the silicon pyramids due to the prolonged Au-assisted etching and the loss of the nanostructures. These effects are clearly shown in Figure 12, which displays cross-sections of the etched pyramid surfaces. Despite the changes in receding contact angle, the advancing contact angles remained nearly constant.

Downloaded by CORNELL UNIV on June 22, 2012 | http://pubs.acs.org
Publication Date (Web): March 11, 2010 | doi: 10.1021/bk-2010-1034.ch007

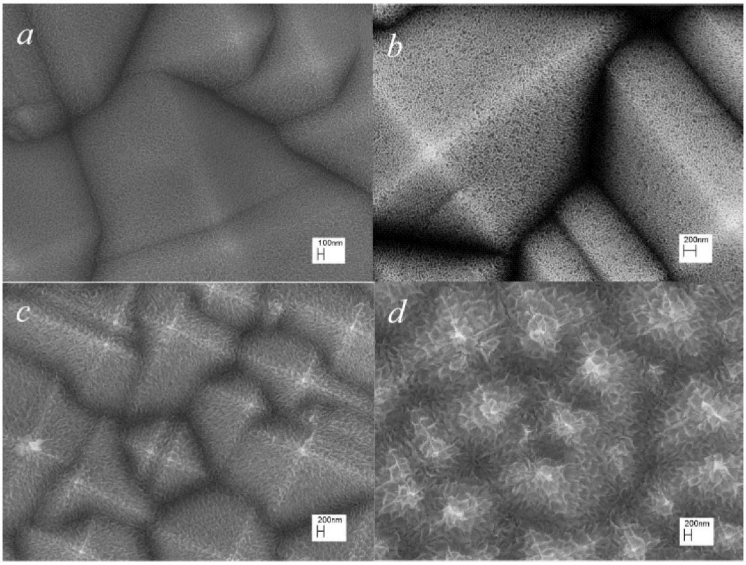

*Figure 10. Si pyramid surface etched by Au-assisted etching in HF/H2O2/H2O (v/v/v 1:5:10) for (a) 30 s, (b) 1 min, (c) 2 min, and (d) 4 min. Au layer thickness was 5 nm.*

## Light Reflection Measurement

The Au assisted etching of silicon surfaces can generate 'black' low-reflectance surfaces as shown in Figure 13, where a weighted surface reflectance of 6.4% resulted after a 2 min etch. Because of the presence of surface nanostructures, the surface absorbs most of the incident light, thus reducing reflection, especially in the 300-1000 nm wavelength regime. The nano-textured surface may also increase the path length of light as it travels through the cell, which allows thinner solar cells with reduced cost; furthermore, the surface may trap the weakly absorbed light reflected from the back surface by total internal reflection at the front surface/air interface. Pyramid textured silicon surfaces are already employed for high efficiency solar cell applications to increase light absorption by silicon surfaces (*20*). Therefore, when combined with the pyramid textures on silicon surfaces, the micro/nano structured surfaces can optimize light absorption, and also establish self-cleaning properties if the surface is treated with fluoroalkylsilanes or other hydrophobic material. On the micro/nano two scale structured surfaces, the weighted light reflectance is further reduced to 3.8% as shown in Figure 13 and Table 1. Longer wavelength light is reduced more. Such surface modifications should result in lowered maintenance costs and higher efficiencies due to reduction of dust/contamination build-up on solar cell surfaces.

Downloaded by CORNELL UNIV on June 22, 2012 | http://pubs.acs.org
Publication Date (Web): March 11, 2010 | doi: 10.1021/bk-2010-1034.ch007

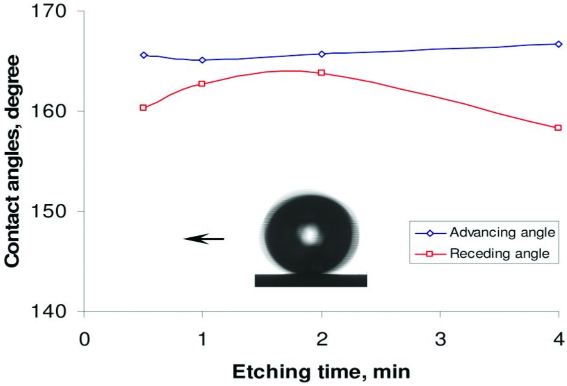

*Figure 11. Contact angle and contact angle hysteresis on two-scale etched Si surfaces. (Inset) The dynamic water droplet moving on the superhydrophobic surfaces with two-scale structures (Au-assisted etching for 2 min on micropyramid surfaces). the droplet edge is blurred due to the fast movement of the water droplet.*

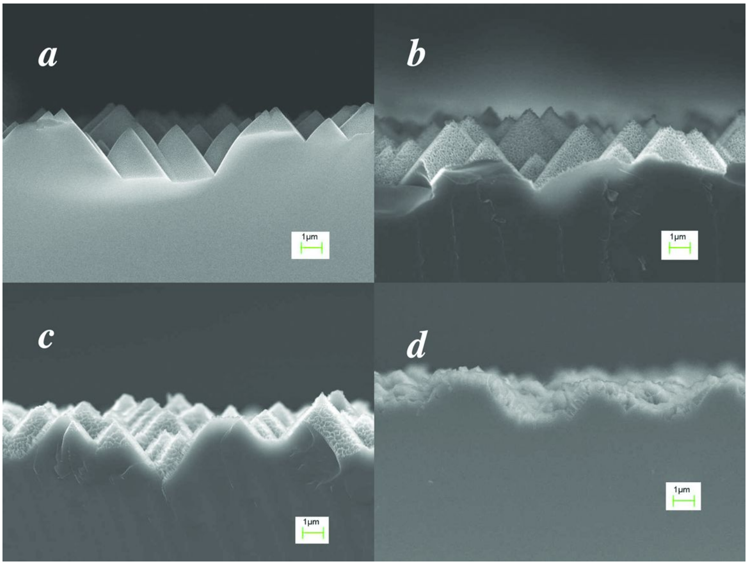

*Figure 12. Cross sections of Si pyramid surfaces etched by Au-assisted etching in HF/H2O2/H2O (v/v/v 1:5:10) for (a) 30 s, (b) 1 min, (c) 2 min, and (d) 4 min. Au layer thickness was 5 nm.*

Downloaded by CORNELL UNIV on June 22, 2012 | http://pubs.acs.org
Publication Date (Web): March 11, 2010 | doi: 10.1021/bk-2010-1034.ch007

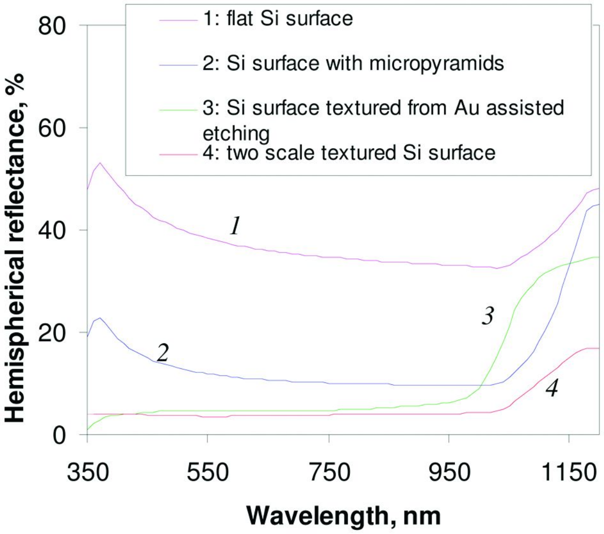

*Figure 13. Light reflection on silicon nano-textured surfaces generated by Au assisted etching. Au (5 nm thickness) assisted etching in HF:H2O2:H2O of 1:5:10 (v/v/v) for 2 min.*

**Table 1. Weighted Reflectance on Different Textured Surfaces**

| *Sample* | *Weighted reflectance %* |
|---|---|
| Flat Si surface | 37.3 |
| Pyramid textured surface | 12.3 |
| Nano-textured surface (Au assisted etching) | 6.4 |
| Two scale textured surface | 3.8 |

## Conclusions

The Au assisted etching of silicon surfaces with Au layers of 2 nm, 5 nm and 10 nm was investigated. Increased etching time resulted in surface structures with greater depths. The etching rate for thicker Au layer coated silicon was constant while for a 2 nm Au layer coated silicon surface, the etching rate was dependent on etch depth which suggested a diffusion-controlled etching process. The surface morphologies changed from small nanostructures at shorter times to large submicron structures at longer etching times. When the etched surfaces were treated with PFOS, the surfaces all showed high contact angles (superhydrophobicity). An increase in etching time resulted in a higher contact angle and a reduced hysteresis. With increased thickness of the Au layer, analogous trends were observed. The appropriate combination of the two-scale structures is effective in achieving roll-off superhydrophobicity. Reflectance measurements showed that the etched surface showed a much reduced reflectance compared to that of pyramid textured silicon surfaces which are commonly employed in high efficiency solar cells. This shows that the surfaces prepared using Au assisted etching technique is promising for light absorption for photovoltaic applications.

## Acknowledgments

We would like to acknowledge financial support from the National Science Foundation (NSF CMMI #0422553) and the National Electric Energy Testing Research and Applications Center (NEETRAC) at Georgia Institute of Technology. We also would like to thank Dr. Vijay Yelunder for the help on the reflectance measurement

Downloaded by CORNELL UNIV on June 22, 2012 | http://pubs.acs.org
Publication Date (Web): March 11, 2010 | doi: 10.1021/bk-2010-1034.ch007

## References

1. Kolasinski, K. W. *Curr. Opin. Solid State Mater. Sci.* **2005**, *9*, 73.
2. Koynov, S.; Brandt, M. S.; Stutzmann, M. *Appl. Phys. Lett.* **2006**, *88*, 203.
3. Li, X.; Bohn, P. W. *Appl. Phys. Lett.* **2000**, *77*, 2572.
4. Zhang, F. Z.; Zhao, L. L.; Chen, H. Y.; Xu, S. L.; Evans, D. G.; Duan, X. *Angew. Chem., Int. Ed.* **2008**, *47*, 2466.
5. Neinhuis, C.; Barthlott, W. *Ann. Bot.* **1997**, *79*, 667.
6. Artus, G. R. J.; Jung, S.; Zimmermann, J.; Gautschi, H. P.; Marquardt, K.; Seeger, S. *Adv. Mater.* **2006**, *18*, 2758.
7. Jisr, R. M.; Rmaile, H. H.; Schlenoff, J. B. *Angew. Chem., Int. Ed.* **2005**, *44*, 782.
8. Tung, P. H.; Kuo, S. W.; Jeong, K. U.; Cheng, S. Z. D.; Huang, C. F.; Chang, F. C. *Macromol. Rapid Commun.* **2007**, *28*, 271.
9. Ahuja, A.; Taylor, J. A.; Lifton, V.; Sidorenko, A. A.; Salamon, T. R.; Lobaton, E. J.; Kolodner, P.; Krupenkin, T. N. *Langmuir* **2008**, *24*, 9.
10. Baldacchini, T.; Carey, J. E.; Zhou, M.; Mazur, E. *Langmuir* **2006**, *22*, 4917.
11. Wang, M. F.; Raghunathan, N.; Ziaie, B. *Langmuir* **2007**, *23*, 2300.
12. Extrand, C. W. *Langmuir* **2002**, *18*, 7991.
13. Chen, W.; Fadeev, A. Y.; Hsieh, M. C.; Oner, D.; Youngblood, J.; McCarthy, T. J. *Langmuir* **1999**, *15*, 3395.
14. McHale, G.; Shirtcliffe, N. J.; Newton, M. I. *Langmuir* **2004**, *20*, 10146.
15. Krasovitski, B.; Marmur, A. *Langmuir* **2005**, *21*, 3881.
16. Anantharaju, N.; Panchagnula, M. V.; Vedantam, S.; Neti, S.; Tatic-Lucic, S. *Langmuir* **2007**, *23*, 11673.
17. Oner, D.; McCarthy, T. J. *Langmuir* **2000**, *16*, 7777.
18. Cao, L. L.; Price, T. P.; Weiss, M.; Gao, D. *Langmuir* **2008**, *24*, 1640.

19. Koynov, S.; Brandt, M. S.; Stutzmann, M. *Phys. Status Solidi: Rapid Res. Lett.* **2007**, *1*, R53.
20. Green, M. A. *Solar Cells: Operating Principles, Technology, and System Applications*; University of New South Wales: Kensington, NSW, 1998.

Downloaded by CORNELL UNIV on June 22, 2012 | http://pubs.acs.org
Publication Date (Web): March 11, 2010 | doi: 10.1021/bk-2010-1034.ch007

Downloaded by OHIO STATE UNIV LIBRARIES on June 21, 2012 | http://pubs.acs.org
Publication Date (Web): March 11, 2010 | doi: 10.1021/bk-2010-1034.ch008

## Chapter 8

# Dispersing and Functionalizing Carbon Nanotubes Using Conjugated Block Copolymers

**Jianhua Zou, Jianhua Liu, and Lei Zhai***

**NanoScience Technology Center and Department of Chemistry, University of Central Florida, Orlando, FL 32826**
***lzhai@mail.ucf.edu**

Conjugated block copolymers have been used to disperse and functionalize pristine carbon nanotubes (CNTs). Upon a simple sonication, the conjugated polymer block such as polythiophenes can form strong π-π interactions with CNT walls, while the non-conjugated polymer block provides the de-bundled CNTs with a good solubility and stability in a wide range of organic solvents and host polymer matrices. Various block copolymers have been utilized to fabricate CNT nanocomposites with unique mechanical and electrical properties. The conductive block copolymers not only provide a universal system to disperse CNTs but also introduce other interesting properties into the system. Such non-invasive approach generates promising CNT composites for energy conversion and storage applications.

## Introduction

Carbon nanotubes (CNTs) and conjugated polymers have demonstrated great potential for energy conversion and storage applications due to their intriguing electrical and optoelectrical properties. In theory, the electrical conductivity of metallic single wall carbon nanotubes (SWCNTs) can be 1000 times higher than that of silver and copper, and the tensile strength of a multi-wall CNT (MWCNT) is expected to be in the range of 10-100 GPa. The applications of CNTs extend from nanoelectronics, to sensors, energy conversion

In Functional Polymer Nanocomposites for Energy Storage and Conversion; Wang, Q., et al.;
ACS Symposium Series; American Chemical Society: Washington, DC, 2010.

and storage devices (fuel cells, photovoltaics, batteries, and supercapacitors), thermal management, and conductive nanocomposite (*1–11*). On the other hand, conjugated polymers have been extensively investigated as promising materials for organic photovoltaics (OPVs) and supercapacitors. For example, poly(3-hexylthiophene)s (P3HTs) have been widely used in OPVs due to their high charge mobility (*12–19*). CNTs have also been investigated as promising functional materials in OPVs (*20–22*). MWCNTs have been used in OPVs with P3HT and 1-(3-methoxycarbonyl)propyl-1-phenyl[6,6]-methanofullerenes (PCBMs) for exciton dissociating and charge collecting (*20–22*). In these OPV devices, high current density was obtained due to the efficient hole collection associated with the work function of MWCNT (4.5-6.0 eV) (*23*). Conjugated polymers have demonstrated great potential as supercapacitor electrode materials with high energy density and high pulse power due to their good electrical conductivity and large pseudo capacitance (*24–29*). The most commonly used conjugated polymers include polyaniline (PANI), polypyrrole (PPy), and poly(3,4-ethylenedioxythiopene) (PEDOT). Conjugated polymers show high capacitance close to ruthenium oxides like 775 F/g for PANI (*27*), 480 F/g for PPy (*28*) and 210 F/g for PEDOT (*29*).

Apart from their promising capabilities, CNTs and conjugated polymers are facing several challenges to realize their applications. For example, conjugated polymers, as supercapacitor electrode materials, suffer from low mechanical stability due to repeated intercalation and depletion of ions during charging and discharging. The effective utilization of CNTs in composites and devices depends strongly on the ability to disperse nanotubes homogeneously in solvents and the matrix, and to functionalize the CNT surfaces with target functional groups. However, it is challenging to achieve stable CNT dispersions in different solvent media and the functionalization of CNTs surfaces. The as-produced CNTs bundle together due to strong van der Waals interactions between the nanotubes. Whether the ultimate use is for single nanotube devices, or for polymer composites, the CNTs need to be debundled and dispersed uniformly in solvents or polymer matrices in order to achieve a good reproducibility in material fabrication and device function. With the promising applications of CNT and conjugated polymers in energy conversion and storage applications, it is highly desirable to develop CNT/conjugated polymer composites with well dispersed CNTs to overcome previous mentioned challenges. Although enormous effort has been invested in this field, and nanocomposites with excellent combined mechanical and electrical properties have been reported from research labs, the commercial application of CNTs is still extremely limited, mainly due to the incompatibility between CNT and conjugated polymers. Currently, there are three major approaches to disperse CNTs and each has its own advantages and disadvantages:

(1) Mechanical exfoliation: The CNTs are dispersed in solutions or polymer matrices by mechanical force such as shear-intensive mechanical stirring or ultrasonication (*6*, *7*, *30*, *31*). This is one of the most convenient methods to achieve CNT dispersion, however, the dispersion quality is often unsatisfactory. This method is mostly applicable for nanocomposite fabrication, but not suitable

Downloaded by OHIO STATE UNIV LIBRARIES on June 21, 2012 | http://pubs.acs.org
Publication Date (Web): March 11, 2010 | doi: 10.1021/bk-2010-1034.ch008

for applications requiring a stable CNT dispersion in solution and CNT surface functionalization.

(2) Chemical surface modification: This is one of the most widely used methods to achieve a stable CNT dispersion in solvents, especially in aqueous solutions. CNTs are treated with strong oxidation reagents such as $HNO_3$ or $KMnO_4/H_2SO_4$ (*32*, *33*). Such treatment leaves oxygenated functional groups such as carboxylic acids, ketones, and alcohols on the nanotube walls, ends and defect sites of the CNTs (*34*). These functional groups may be further reacted, leading to CNTs functionalized with esters, amides, zwitterions or grafts of polymer chains (*11*, *35–41*). The covalent functionalization allows purification and solubilization of CNTs. However, the oxidative treatment tends to disrupt the conjugated electronic structure, shortens the CNTs, and deteriorates the electrical and mechanical properties of CNTs.

(3) Third component-assisted dispersion. In this approach, a third component chemical is used as dispersant. CNTs are mechanically de-bundled and stabilized by the third component chemicals through sonication or other methods, where dispersant attaches to CNT surfaces to prevent them from aggregating. Many chemicals have been used as the third component, such as surfactants (*42*, *43*), polymer electrolytes (*44*, *45*), proteins (*46*, *47*), DNAs (*48*), conjugated polymers (*49–66*), and block copolymers (*67–73*). So far, the third component approach has shown the most promising potential for CNT dispersion. The main reason is that these chemicals stabilize the CNTs through non-covalent interactions, therefore, avoiding the destruction of the chemical structures, electronic and mechanical properties of the CNTs.

Recently, there are two types of materials that have shown particularly promising potential for third component-assisted CNT dispersion. One of these materials is the conjugated polymers (*49*, *53*, *57–66*). Conjugated polymers stabilize CNTs by attaching to CNT surfaces through strong π-π stack interactions. However, the conjugated homopolymer itself suffers solubility and miscibility issues. Due to the strong π-π interactions of conjugated polymers in solid state, most conjugated polymers have poor solubility in organic and aqueous solvents. Poly(3-hexylthiophene) (P3HT) is one of a few conjugated polymers that have relatively better solubility, and has been reported as a third component for CNT dispersion (*49*, *53*). Other conjugated polymers, such as polypyrrole and polyphenylene, form stable dispersions with CNTs through in-situ polymerization of monomers in the presence of mechanically exfoliated CNTs. A second family of interesting materials with potential for third component-assisted CNT dispersion are the block copolymers (*67–73*). In general, the block copolymer is designed in such a way that one block of the polymer will form a close interaction with the CNT surfaces, while the other block(s) will render the solubility to the exfoliated nanotubes by providing a steric barrier or repulsion interaction between polymer-wrapped nanotubes. So far, a number of block copolymers such as poly(ethylene oxide) (PEO) with poly(propylene oxide) (PPO) (PEO-PPO-PEO) (*73*), polystyrene (PS) with poly(t-butylacrylate) (PBA) or poly(vinyl pyridine) (PVP) (*72*) have been reported for CNT dispersion. However, among all the block copolymers being studied, they do not contain conjugated polymers as part of the block copolymer structure. Although non-conjugated polymers such as

Downloaded by OHIO STATE UNIV LIBRARIES on June 21, 2012 | http://pubs.acs.org
Publication Date (Web): March 11, 2010 | doi: 10.1021/bk-2010-1034.ch008

Downloaded by OHIO STATE UNIV LIBRARIES on June 21, 2012 | http://pubs.acs.org
Publication Date (Web): March 11, 2010 | doi: 10.1021/bk-2010-1034.ch008

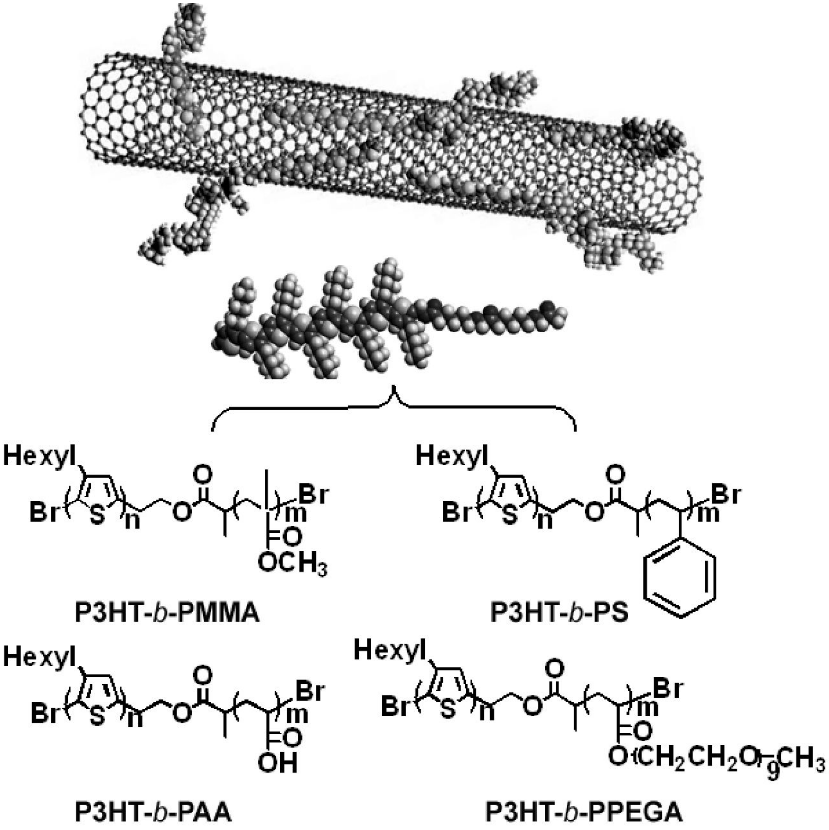

*Scheme 1. Schematic illustration of dispersing CNTs using P3HT block copolymers*

polystyrene are known to form non-covalent interactions with CNTs (*72*), the interactions between conjugated polymers and CNTs are the strongest, according to a recent theoretical modeling study (*74*).

It is reasonable to hypothesize that a conjugated block copolymer, a copolymer with a conjugated polymer block and a non-conjugated polymer block, should be an excellent dispersant for CNT dispersion/stabilization. The conjugated polymer block such as P3HT can form strong π-π interactions with CNT walls, while the non-conjugated polymer block will provide the de-bundled CNTs with a good solubility and stability in a wide range of organic solvents and host polymer matrices. Additionally, non-conjugated block can also introduce various functional groups onto CNT surfaces, providing a non-invasive approach to functionalize CNTs. In this chapter, we present recent progress in dispersing and functionalizing CNTs using poly(3-hexylthiophene) (P3HT) block copolymers (*75–77*) and fabricating P3HT supramolecular structures on dispersed CNTs (*78*) (Scheme 1).

Downloaded by OHIO STATE UNIV LIBRARIES on June 21, 2012 | http://pubs.acs.org
Publication Date (Web): March 11, 2010 | doi: 10.1021/bk-2010-1034.ch008

## Experimental

### Synthesizing P3HT Block Copolymers and Dispersing CNTs

The P3HT block copolymers were synthesized from P3HT macroinitiator via atom transfer radical polymerization (ATRP). P3HT macroinitiator was synthesized according to the reported procedure (Scheme 2.) (*79*, *80*).

**P3HT-*b*-PS** was synthesized in toluene (75 vol %) at 95°C. The molar ratio of the reactants is [polystyrene (PS)]: [P3HT]: [CuBr]: [pentamethyldiethylenetriamine (PMDETA)] = 300:1:1:2. The block copolymer is readily soluble in chloroform, toluene, and tetrahydrofuran (THF). Gel permeation chromatography (GPC) measurement using polystyrene as a standard indicates a number average molecular weight $M_n$ of 23000 dalton with a polydispersity of $M_w/M_n$=1.3. The composition of P3HT-*b*-PS was estimated by $^1$H NMR spectral analysis to contain 34.1% and 65.9% (weight percentage) of P3HT and PS, respectively.

**P3HT-*b*-PMMA** was synthesized through the ATRP of methyl methacrylate (MMA) in toluene (75 vol%) at 95°C for 10 hours. The molar ratio of the reactants is [MMA]: [P3HT]: [CuBr]: [PMDETA] = 400:1:1:2. The molar ration of P3HT: PMMA was determined to be 1: 2.49 by the $^1$H NMR analysis.

**P3HT-*b*-PAA** was synthesized through the hydrolysis of its precursor, P3HT-*b*-poly (tert-butyl acrylate) (P3HT-*b*-PtBA), which was synthesized by ATRP. The reaction was performed in toluene (50 vol%) at 105 °C for 20 hours. The molar ratio of the reactants is [tBA]: [P3HT]: [CuBr]: [PMDETA ]=600:1:1:2.

To hydrolyze P3HT-b-PtBA, 32 mg of the polymer was dissolved in 10 mL $CH_2Cl_2$, and 0.5mL of trifluoroacetic acid (TFA) was added. The reaction was then conducted at room temperature with shaking for 24 hours. The product P3HT-*b*-PAA was collected as a precipitate and washed three times with $CH_2Cl_2$, and then dried under vacuum. The P3HT-b-PAA is not soluble in chloroform, but well dissolved in THF, methanol, and NaOH aqueous solutions.

**P3HT-*b*-PPEGA** was synthesized by ATRP performed in toluene (60%) at 100 °C for 10 hours, the molar ratio of [poly (ethylene glycol) methyl ether acrylate (MW=452, Sigma Aldrich)]: [P3HT]: [CuBr]: [PMDETA]=150:1:1:2. The molar ratio of P3HT: PPEGA in P3HT-*b*-PPEGA was determined to be 1.28:1 from the $^1$H NMR spectrum of P3HT-*b*-PPEGA. P3HT-*b*-PPEGA was soluble in a variety of solvents, such as chloroform, toluene, THF, DMF, acetonitrile, methanol, ethanol, and water.

HiPco SWCNTs were purchased from Carbon Nanotechnologies with a diameter of 0.8-1.2 nm and a length of 100-1000 nm. The purity was declared to be above 65%. MWCNTs were purchased from Nanolab with a diameter of 10-20 nm and a length of 5-20 μm, with the purity above 95%. The as-received CNTs were used directly in the experiments without further purification or chemical modification throughout the study.

All the dispersing of CNTs by conjugated block copolymers used chloroform as the solvent except the P3HT-*b*-PAA/MWCNT dispersion which was dispersed in THF. The concentration of CNTs and the weight ratio between CNTs and conjugated block copolymers was tuned to investigate the effect of these factors

Downloaded by OHIO STATE UNIV LIBRARIES on June 21, 2012 | http://pubs.acs.org
Publication Date (Web): March 11, 2010 | doi: 10.1021/bk-2010-1034.ch008

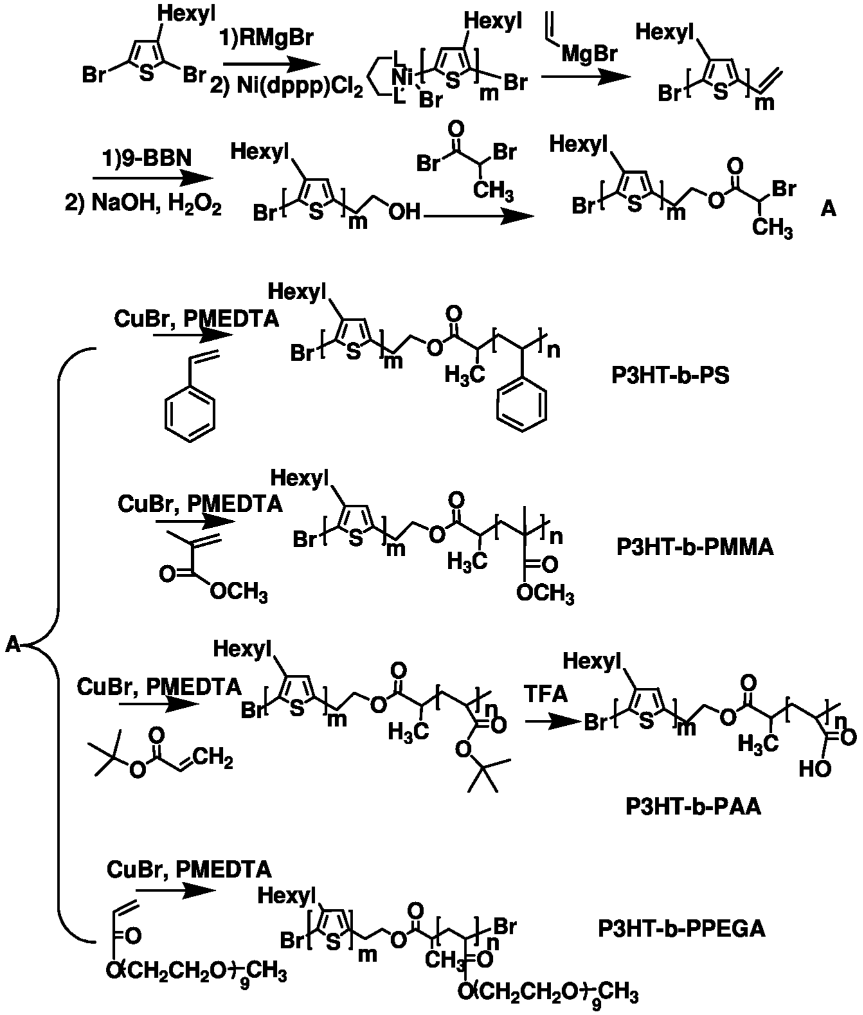

*Scheme 2. The synthetic scheme of P3HT block copolymers*

on the stability of CNT dispersion. After mixing the copolymers and CNTs in solvent, 30 minutes sonication was applied to obtain the CNT dispersion.

**Fabrication of P3HT supramolecular structures on CNTs:** P3HT (0.2 mg) was dissolved into anisole (4.0 mL) by heating to 70 °C. 42.0 µL as-prepared MWCNT dispersion was added (P3HT/MWCNTs mass ratio = 7), and then the mixture was cooled to room temperature in few minutes. The solution was kept at room temperature for 12 hours. To prepare P3HT/SWCNT supramolecular structures, 15.0 µL SWCNT dispersion was added to 4.0 ml P3HT anisole hot solution, which gives the P3HT/SWCNT mass ratio of 40. The mixture was cooled to room temperature in few minutes and kept at room temperature for 12 hours. The obtained deep purple dispersions were stable for months at room temperature.

Downloaded by OHIO STATE UNIV LIBRARIES on June 21, 2012 | http://pubs.acs.org
Publication Date (Web): March 11, 2010 | doi: 10.1021/bk-2010-1034.ch008

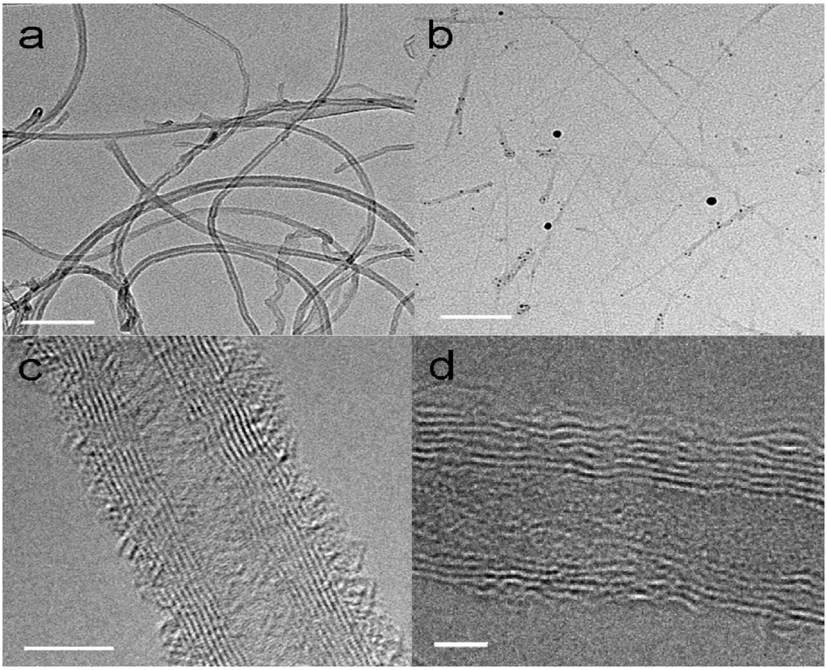

*Figure 1. (a) TEM image of P3HT-b-PS/MWCNT (1:1, mass ratio); (b) TEM image of P3HT-b-PS/SWCNT (3:1); (c) HRTEM image of a single MWCNT covered by a thin layer of P3HT-b-PS; (d) HRTEM image of pristine MWCNT. The scale bars in a, b, c, and d represent 100, 100, 5, and 2 nm respectively.*

# Results and Discussion

## Dispersing CNTs Using P3HT-*b*-PS and the Properties of the Composites

P3HT-*b*-PS block copolymers have been used to disperse both SWCNTs and MWCNTs in chloroform by sonication. The minimum P3HT-*b*-PS to CNTs mass ratio to achieve a good CNT dispersion is 0.6 and 0.5 for SWCNTs and MWCNTs, respectively, suggesting the high efficiency of P3HT-*b*-PS in dispersing CNTs. The stable CNT dispersions contain as much as 2.5 mg/mL SWCNTs (using 2:1 polymer to SWCNTs mass ratio) and 3.0 mg/mL MWCNTs (using 1:1 polymer to MWCNTs mass ratio). The CNT concentration is significantly higher than most reported CNT dispersions (*58*). A good dispersion of CNTs was also obtained in toluene and tetrahydrofuran (THF) using P3HT-*b*-PS with comparable solubility to that in chloroform. The as-dispersed CNTs are very stable, no precipitation was found even after one year of standing at room temperature. The efficient dispersion and stability of the suspension is attributed to the good solubility of the PS block in these solvents. The stability of the P3HT-*b*-PS dispersed CNT suspensions was also examined through a centrifugation test at 13200 rpm for 30

Downloaded by OHIO STATE UNIV LIBRARIES on June 21, 2012 | http://pubs.acs.org
Publication Date (Web): March 11, 2010 | doi: 10.1021/bk-2010-1034.ch008

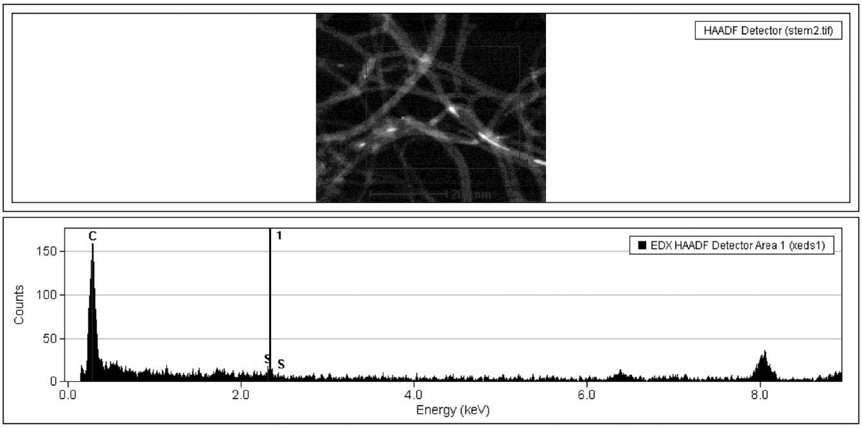

*Figure 2. Dark field TEM image of dispersed MWCNTs by P3HT-b-PS and EDX spectrum from the area of TEM image marked by red rectangle.*

min. After centrifuging, most SWCNTs remained in solution, while MWCNTs precipitated out due to their much larger dimensions. The MWCNTs collected after multiple centrifugation and re-dispersion cycles could be readily re-dispersed in chloroform, toluene and THF without adding more P3HT-*b*-PS. This result suggests that P3HT-*b*-PS strongly attaches to CNT walls through a strong and stable molecular interaction, most likely π-π stacking interactions between the copolymers and CNTs. MWCNTs dispersed by P3HT-*b*-PS (1:1 mass ratio) were purified by three cycles of centrifuge and re-dispersion to remove the free P3HT-*b*-PS and were examined using transmission electron microscopy (TEM) and energy dispersive X-ray (EDX) analysis. As shown in Figure 1a, the majority of MWCNTs are de-bundled into individual tubes. A high resolution TEM image of a MWCNT segment (Figure 1c) clearly revealed the presence of a thin layer of amorphous coating with the thickness around 2 nm on the surface of CNT wall, while the pristine nanotube shows a clean surface (Figure 1d). The thin layer coating is believed to be P3HT-*b*-PS copolymer self-assembled on the nanotube surface.

EDX spectrum in Figure 2 clearly shows the sulfur signal, which arises from the P3HT-*b*-PS polymer attached on the surface of CNTs.

Two groups of nanotube structures were observed in SWCNT dispersions, one with an average diameter around 5-6 nm and another group with an average diameter around 10-15 nm (Figure 1b). The first group, also the major component of the dispersion, is believed to be the completely de-bundled individual SWCNTs coated with the conjugated copolymer since the diameter of the polymer-wrapped SWCNTs corresponds very well to the thickness of the copolymer coating (about 2 nm) and the diameter of the individual SWCNTs (0.8-1.2 nm). The second group is believed to be SWCNT bundles that are not completely dispersed. The P3HT-*b*-PS dispersed SWCNTs were also examined by an atomic force microscope (AFM). The AFM image and the height analysis clearly suggest that most SWCNTs were dispersed into individual nanotube level (Figure 3).

Downloaded by OHIO STATE UNIV LIBRARIES on June 21, 2012 | http://pubs.acs.org
Publication Date (Web): March 11, 2010 | doi: 10.1021/bk-2010-1034.ch008

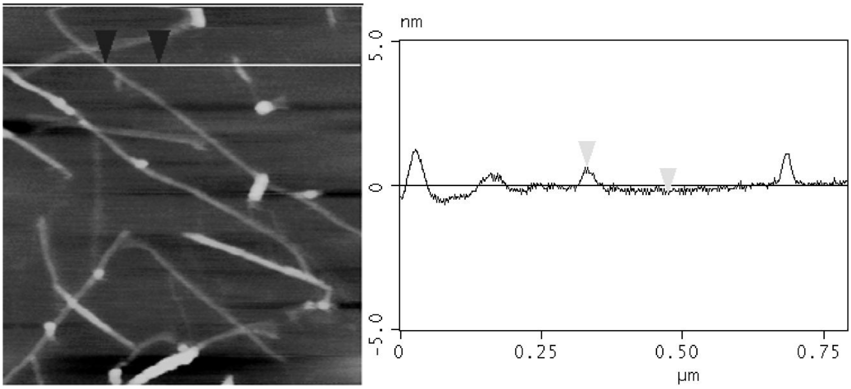

*Figure 3. An AFM image of P3HT-b-PS dispersed SWCNTs with the section analysis (The size of the AFM image is 1 micron.).*

In order to reveal the assembly structure of P3HT-*b*-PS on CNTs, the P3HT-*b*-PS/CNT dispersion was studied by UV-Vis absorption spectroscopy, and compared with P3HT-*b*-PS chloroform solution. In a dilute chloroform solution, P3HT-*b*-PS exhibits an absorption band centered at 454 nm (Figure 4a), revealing the regioregular nature of the P3HT blocks in copolymer (*81*). The UV-Vis absorption band of a solid state P3HT-*b*-PS film shifted to longer wavelength, and split into three peaks (513, 560, and 604 nm) (Figure 4a), suggesting a π-π stacking of P3HT chains in the solid state (*81*, *82*). The UV-Vis absorption spectrum of P3HT-*b*-PS/SWCNT dispersion in chloroform exhibits three main absorption peaks at 513, 560, and 604 nm (Figure 4b), similar to the spectrum of solid state P3HT-*b*-PS. This interesting result indicates that the P3HT block in P3HT-*b*-PS copolymer form a π-π stacked structure on CNT surfaces. The UV-Vis spectrum of a solid thin film formed from P3HT-*b*-PS/SWCNT dispersion by solvent-casting did not show much difference from that of in solution, suggesting that the interaction of P3HT blocks with SWCNTs is not disrupted during solvent drying process. Because of the strong interaction between conjugated block copolymer with CNTs, the dispersed CNT solution can be purified, dried and easily re-dispersed back to solution.

Fluorescence spectroscopy has been used to study the interaction between the P3HT-*b*-PS block copolymers and CNTs. P3HT-*b*-PS block copolymer in chloroform exhibits a strong fluorescence emission at 575 nm (Figure 5a). In contrast, the fluorescence emission of P3HT-*b*-PS with the same concentration shows 97% quench when dispersed SWCNT suspension (Mass ratio of P3HT-*b*-PS/SWCNTs is 2/1.). Such fluorescence quenching is probably due to electron transfer and/or energy transfer between P3HT-*b*-PS and CNTs (*83*). This observation clearly indicates a strong molecular interaction between conjugated block copolymers and CNTs.

Downloaded by OHIO STATE UNIV LIBRARIES on June 21, 2012 | http://pubs.acs.org
Publication Date (Web): March 11, 2010 | doi: 10.1021/bk-2010-1034.ch008

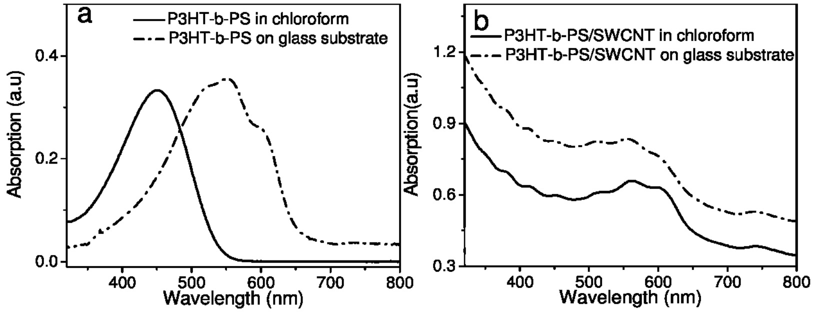

*Figure 4. UV-Vis spectra of (a) P3HT-b-PS in chloroform and a cast film on a glass substrate; (b) P3HT-b-PS/SWCNT (2:1) in chloroform and a cast film on a glass substrate.*

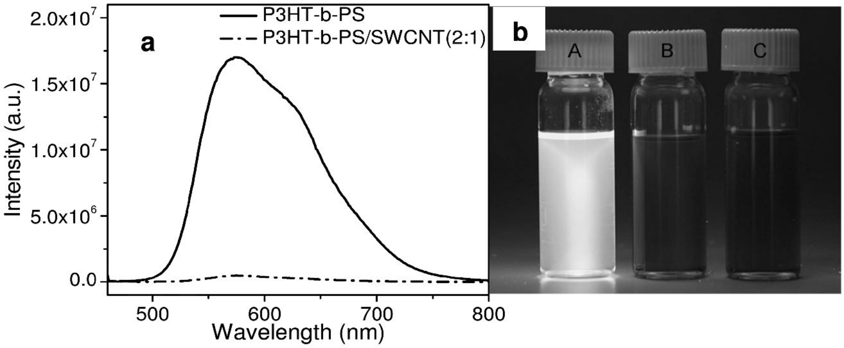

*Figure 5. The fluorescence spectra of pure P3HT-b-PS and P3HT-b-PS/SWCNTs (2:1) dispersion in chloroform(a) and pictures of P3HT-b-PS (A), P3HT-b-PS/SWCNT (2:1) (B), and P3HT-b-PS/MWCNT (1:1) (C) solution in chloroform. under UV light irradiation.*

The electronic properties of SWCNTs before and after interacting with P3HT-*b*-PS were investigated using Raman spectroscopy. As shown in Figure 6, the tangential vibrational mode (G band) of SWCNTs shifts significantly to higher frequency from 1579.9 (pristine SWCNT) to 1595.6 cm$^{-1}$ when dispersed with P3HT-*b*-PS, while the radical breathing modes (RBM) shift slightly from 179.8 to 181.7 cm$^{-1}$. Previous study indicated that the G band and RBM band of SWCNTs shifted to higher frequency with the loss electrons (*84*). The observed band shift associated with the CNT dispersion suggests that a molecular-level interaction between CNTs and the block copolymers.

Downloaded by OHIO STATE UNIV LIBRARIES on June 21, 2012 | http://pubs.acs.org
Publication Date (Web): March 11, 2010 | doi: 10.1021/bk-2010-1034.ch008

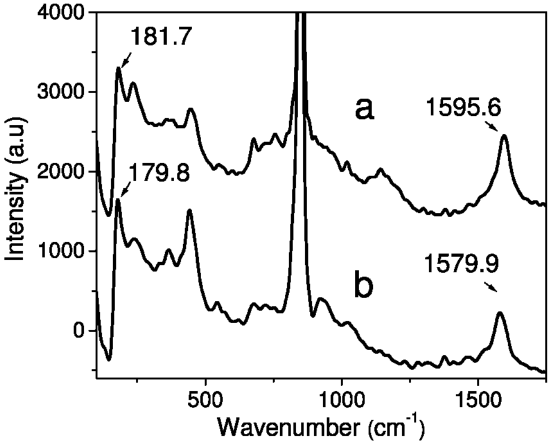

*Figure 6. Raman scattering spectra of a) SWCNTs dispersed by P3HT-b-PS, and b) pristine SWCNTs.*

Previous results clearly demonstrate that P3HT in P3HT-*b*-PS make good contact with CNT surfaces while non-conjugated blocks (PS) provide CNTs with a good solubility in organic solvents. Additionally, non-conjugated block is expected to provide excellent miscibility in a compatible polymer matrix, offering a versatile approach to fabricate uniform CNT/polymer nanocomposites. On the other hand, if the non-conjugated block is not compatible with the polymer matrix, the stability of CNT in the polymer matrix will be greatly reduced. To understand the advantage of conjugated block copolymer in dispersing CNTs and the effect of non-conjugated block on the stability of dispersed CNTs in different polymer matrices, two sets of experiments were performed using P3HT-*b*-PS, P3HT-*b*-PMMA, and P3HT. In the first experiment, P3HT-*b*-PS and P3HT was used to disperse CNTs in PS matrix to examine the advantage of P3HT-*b*-PS over P3HT. In the second experiment, the stability of CNTs dispersed by P3HT-*b*-PMMA, P3HT-*b*-PS and P3HT in CNT-PMMA composites was compared to investigate the effect of non-conjugated block on the stability of dispersed CNT in polymer matrix. Properties including percolation threshold determined by conductivity and the CNT aggregation upon thermal annealing of each CNT-PMMA composite produced using P3HT-*b*-PMMA, P3HT-*b*-PS and P3HT were examined.

In order to examine the advantage of the P3HT-*b*-PS over P3HT homopolymers in dispersing CNTs in PS matrix, P3HT-*b*-PS/SWCNT (2/1, mass ratio) dispersions and P3HT/SWCNT dispersions with the same P3HT to SWCNT ratio were mixed with polystyrene chloroform solutions. In both cases, the SWCNTs were first dispersed in the P3HT or P3HT-*b*-PS chloroform solution. Then same amount of SWCNT dispersions were added to two same volume 10 wt. % polystyrene chloroform solutions. The mixtures were stirred for half an hour and the stability of the dispersions was examined. P3HT-*b*-PS dispersed SWCNTs were stable in polystyrene chloroform solution after several months of standing, while P3HT dispersed SWCNTs precipitated out from the PS solution within one day, suggesting that P3HT-*b*-PS is more efficient than P3HT in stabilizing CNTs in polystyrene solutions. The quality of CNT dispersion in PS matrix was evaluated using the percolation thresholds of the solid films. Percolation threshold means the lowest filler loading ratio to obtain a significant conductivity increase, and has been used as an indicator of nanotube dispersion quality in polymer matrices (*85*). Solid CNT/PS nanocomposite films with the thickness around 30 μm were fabricated by casting the CNT dispersions in PS solutions on a glass substrate using a drawdown bar. The electrical conductivity of the nanocomposite thin films was measured a Keithley 2400 instrument by a four-probe method. Percolation thresholds were obtained from the plots of conductivity versus the SWCNT concentration in polystyrene (Figure 7). The percolation threshold obtained from P3HT-*b*-PS dispersed SWCNTs nanocomposite is 0.03 wt% SWCNTs, which is significantly lower than that of 0.12 wt% for P3HT dispersed SWCNTs nanocomposite. These results suggest that P3HT-*b*-PS block copolymer is more efficient in dispersing CNTs in PS matrix that P3HT homopolymer due to the compatibility of PS block with PS matrix. We also observed that when the loading amount of CNTs in the nanocomposite was higher than 0.3 wt%, the conductivity of the P3HT homopolymer composite is higher than that of P3HT-*b*-PS composite, attributed to the PS on CNT surface that decreases the conductivity of the CNTs.

Similarly, the CNT dispersing capability of P3HT-*b*-PMMA in PMMA is compared with that of P3HT. The percolation threshold of CNT in CNT-PMMA composite using P3HT-*b*-PMMA as the dispersant is in the range of 0.12-0.16 %, while the percolation threshold is in the range of 0.16-0.20 % for the CNT-PMMA composite using P3HT as the dispersant. The lower percolation threshold of CNT in P3HT-*b*-PMMA/CNT/PMMA than that in P3HT/CNT/PMMA indicates that P3HT-*b*-PMMA disperses CNTs more homogenously in PMMA than P3HT. This result is attributed to the PMMA block in P3HT-*b*-PMMA which creates a well-defined interface between CNT and PMMA (Figure 8). In contrast, when P3HT-*b*-PS was used to disperse CNT in PMMA matrix, the percolation threshold is in the range of 0.20-0.25 % which is even higher than that of P3HT/CNT. The increased percolation threshold is due to the incompatibility between the PS block in P3HT-*b*-PS and the PMMA matrix. These results suggest that the compatibility of non-conjugated block with the host polymer matrix significantly affects the CNT dispersion quality in polymer composites.

The compatibility of the non-conjugated block with the host polymer matrix also determines the long term stability of CNTs in the polymer matrix. In our studies, the stability of CNTs dispersed by P3HT-*b*-PMMA and P3HT in CNT-PMMA composites was compared. The CNT/PMMA composite films (1 wt % SWCNT in PMMA) with a thickness of 30 μm were annealed at 140°C under vacuum for 10 hours to model the long term stability of CNTs in PMMA matrix. Under the anneal temperature above the $T_g$ of PMMA, CNTs can move freely to form aggregates unless they are uniformly dispersed. The optical images of the composite film before and after annealing were presented in Figure 9. After annealing, P3HT-*b*-PMMA/CNT-PMMA composite film remained transparent, and was comparable with the as-prepared sample. In contrast, the P3HT dispersed

Downloaded by OHIO STATE UNIV LIBRARIES on June 21, 2012 | http://pubs.acs.org
Publication Date (Web): March 11, 2010 | doi: 10.1021/bk-2010-1034.ch008

Downloaded by OHIO STATE UNIV LIBRARIES on June 21, 2012 | http://pubs.acs.org
Publication Date (Web): March 11, 2010 | doi: 10.1021/bk-2010-1034.ch008

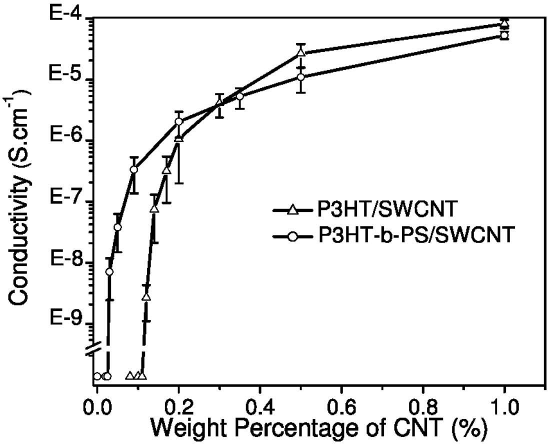

*Figure 7. The conductivity of SWCNT/PS nanocomposites prepared from SWCNTs dispersed in P3HT-b-PS and P3HT*

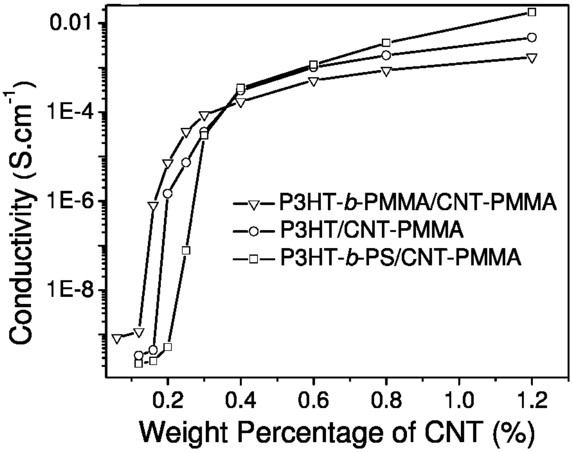

*Figure 8. The conductivity of CNT-PMMA nanocomposites with the CNT dispersed by P3HT-b-PMMA, P3HT, and P3HT-b-PS, respectively.*

SWCNT/PMMA composite film exhibited a significant CNT aggregation after annealing. As indicated in Figure 9 c and d, the composite film became translucent due to the aggregation. This study suggests that P3HT-*b*-PMMA dispersed CNTs have long term stability in the CNT-PMMA composite than P3HT dispersed CNTs, and further proves that the compatibility of the non-conjugated block in conjugated block copolymers with the host polymer matrix is crucial to obtain uniform CNT polymer composites. It is worthy to note that various types of non-conjugated block can be introduced into conjugated block copolymers through well establish synthetic routes to provide versatile dispersants of CNT for different polymer matrices.

Downloaded by OHIO STATE UNIV LIBRARIES on June 21, 2012 | http://pubs.acs.org
Publication Date (Web): March 11, 2010 | doi: 10.1021/bk-2010-1034.ch008

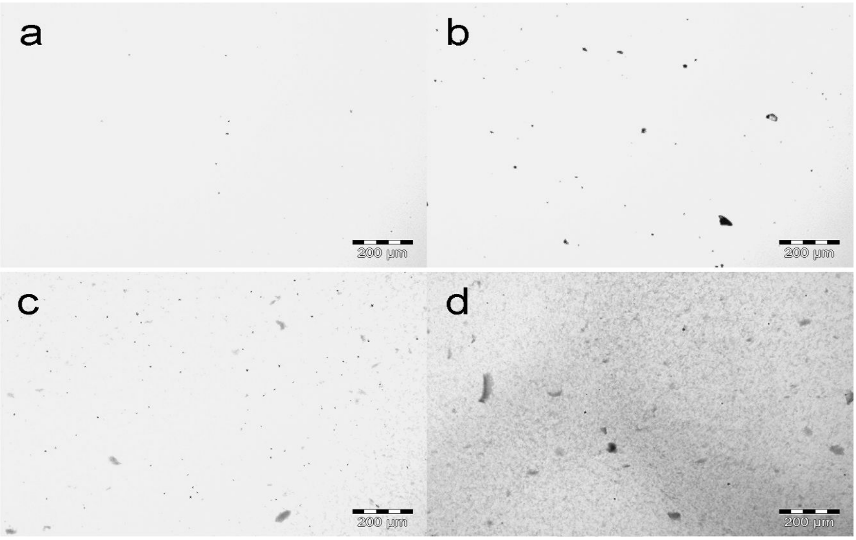

*Figure 9. Optical images of P3HT-b-PMMA/SWCNT-PMMA composite film a) before and b) after annealing, P3HT /SWCNT-PMMA composite film c) before and d) after annealing.*

The rod-coil characteristics of P3HT-*b*-PS also cause the formation of honeycomb-like surface structures when a P3HT-*b*-PS/MWCNT chloroform dispersion is cast on a substrate. As the chloroform evaporates, small water droplets with the size of microns condensed on the surfaces due to the cooling of the surface, leaving micron size dimples on the surface. The scanning electron microscope (SEM) study of the morphology of a P3HT-*b*-PS/MWCNT film on a glass substrate revealed honeycomb like structures with the diameter of the honeycomb pore ranging from 2 to 15 μm (Figure 10a). The height of the honeycomb ridges ranges from 200 to 500 nm as determined by a profilometer. A magnified SEM image (Figure 10b) shows different morphology and compositions of the ridge and the base of the honeycomb structure. The ridge is mainly composed of P3HT-*b*-PS polymers with a small amount of MWCNTs, while the main component in the base is entangled CNTs with nano-scale porosity (Figure 10b). The honeycomb morphology of the superhydrophobic film was also observed under a fluorescence microscope (Figure 10c). Because the honeycomb ridge is mainly composed of P3HT-*b*-PS, a fluorescent conjugated polymer, the ridge appears in a bright green color. As to the base area, MWCNTs is the main component, and the fluorescence of the block copolymer is quenched by MWCNTs through electron and/or charge transfer process (*83*), the base area appears to be dark under the fluorescence microscope. The combination of micro-scale roughness, nano-scale roughness and the hydrophobic surface chemistry (polystyrene block) also generate a superhydrophobic coating (water contact angle = 154° ~ 160°, sliding angle < 5°) from the P3HT-*b*-PS/WMCNT composite (Figure 10d). With the conductivity in the range of 30-100 S/cm, such conductive superhydrophobic coating is of particular interest due to their capability of removing the static charges accumulated on the surfaces, and has potential applications as electromagnetic interference (EMI) shielding materials and corrosion protecting coatings.

The unique properties of P3HT-*b*-PS/CNT composite including large surface area associated with MWCNTs and superhydrophobicity made it a promising material for gas sensing. Conjugated polymers, with their interesting electrical properties, have significant advantages over traditional semiconductor gas sensors with respect to design flexibility and room temperature operation (*86–89*). However, such application is limited by low sensitivity, long response time (tens of seconds to minutes (*83*)) and interference of moisture. The low sensitivity and long response time is mainly caused by the slow penetration of gas into the conjugated polymers. Improvement in both sensitivity and response time can be achieved by using nano-scale structured conjugated polymer with large surface area (*89*). The interference of moisture is due to the influence of moisture on the interface between conducting polymers and substrates which leads to a cooperative sensing response of both analyte and moisture. Such interference can be eliminated by keeping the moisture out of the interface. For example, the moisture interference can be reduced by making the substrate surface hydrophobic before the deposition of conjugated polymer (*90*). The conductive superhydrophobic P3HT-*b*-PS/MWCNT composite can improve the sensitivity and response time (micro- and nanostructures with large surface area), as well as to eliminate the interference of moisture (superhydrophobicity) in the gas sensing application.

Superhydrophobic P3HT-*b*-PS/MWCNT composite films were exposed to various organic vapors to evaluate their gas sensing properties. The resistance change of the films with exposure time was monitored to examine the responding rate. As shown in Figure 11, the film shows a quick response to toluene, chloroform and tetrahydrofuran (THF) with the resistance change saturating within 5 seconds after the exposure. The resistance of the film recovered quickly when the vapor was removed. Multiple cycles of exposure and removal of the vapor induced similar decrease and increase of the film resistance, suggesting a good stability and sensitivity of the sensors. On the other hand, the film had no response to polar organic solvents such as methanol, ethanol, acetic acid and acetone, due to a low solubility of P3HT in these solvents. Above all, the P3HT-*b*-PS/MWCNT composite film is completely inert to moisture (Figure 11). The gas sensing response of the film towards moisture-rich organic vapors of toluene, chloroform, and THF was exactly the same as what was observed from the pure organic vapors.

Downloaded by OHIO STATE UNIV LIBRARIES on June 21, 2012 | http://pubs.acs.org
Publication Date (Web): March 11, 2010 | doi: 10.1021/bk-2010-1034.ch008

## Non-Invasive Functionalization of CNTs

P3HT block copolymers can also non-invasively functionalize CNTs by using functional non-conjugated block. Two P3HT block copolymers P3HT-*b*-PAA and P3HT-*b*-PPEGA were synthesized and used to introduce acid groups on pristine CNTs, and obtain good solubility of CNTs in polar and non-polar solvents, respectively.

Downloaded by OHIO STATE UNIV LIBRARIES on June 21, 2012 | http://pubs.acs.org
Publication Date (Web): March 11, 2010 | doi: 10.1021/bk-2010-1034.ch008

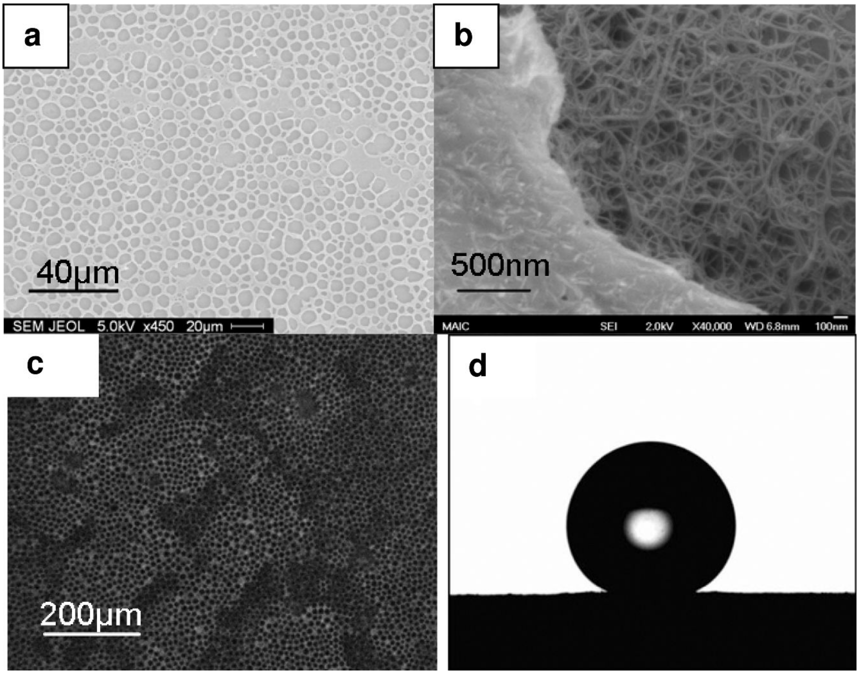

*Figure 10. SEM image of the honeycomb structures formed by solvent casting of P3HT-b-PS/MWCNT dispersions. d) Magnified view of the honeycomb structure showing P3HT-b-PS-rich ridge and MWCNT-rich base. e) Fluorescence image of the honeycomb structure. f) A digital photo image of a 10 μL water droplet on superhydrophobic surface with a contact angle of 159.6°.*

### *Carboxylate Group Functionalized CNTs*

Carboxylate groups functionalized CNTs (CNTs-$COO^-$) are important and versatile precursors for CNTs composites with metal, metal oxide or semiconductive nanoparticles, which have potential applications for energy conversion and storage. For example, ruthenium oxide nanoparticles were attached on carboxylated CNTs as supercapacitor electrode materials (*91*). Platinum nanoparticles on acid functionalized CNTs demonstrated high electrocatalytic activity for methanol oxidation, which is crucial for efficient fuel cells (*92*). Although CNTs-$COO^-$ can be obtained by a well established approach of treating CNTs with $HNO_3/H_2SO_4$ (*9*), the resultant functionalized CNTs were shortened down to 1μm with decreased electrical and mechanical properties. Additionally, carboxylate groups are not uniformly distributed on CNTs, and mainly located at the defect of CNT fragments without the control of the carboxylate group density. In our studies, P3HT-*b*-PAA was used to disperse and functionalize MWCNTs in THF. According to our proposed mechanism, P3HT blocks attach to the surface of MWCNT through π-π interactions, while the PAA blocks locate at the surface of CNTs and functionalize MWCNT with carboxylate groups. The TEM characterization of the obtained MWCNT-COO$^-$ shows that MWCNTs were dispersed into individual tube level with large aspect ratio (Figure 12a). Since P3HT-*b*-PAA block copolymers bond with CNTs through non-covalent π-π interactions, and a short time sonication was applied for the dispersing process, the chemical structure, electric and mechanical properties were maintained.

The high resolution TEM image of MWCNT-COOH (Figure 12b) reveals that the CNT is covered homogenously by an amorphous thin layer of the block copolymers. The homogenous and non-specific binding of P3HT-*b*-PAA on CNT surfaces allows a uniform distribution of carboxylic groups. Additionally, the carboxylic group density on CNT surfaces can be controlled by tuning the composition of P3HT-*b*-PAA. The P3HT-*b*-PAA block copolymers with longer PAA block will lead to higher density of acid groups on CNT surfaces. In order to investigate the relationship between block copolymer composition and acid group density on CNTs. P3HT-*b*-PAAs with P3HT to PAA ratio of 1:6.8 and 1:0.9 were synthesized by the hydrolysis of corresponding P3HT-*b*-PtBA. MWCNTs were dispersed by these two types of P3HT-*b*-PAA in THF with the same P3HT to MWCNT weight ratio (0.5:1). The dispersion was purified by three cycles of centrifugation and re-dispersing to remove free P3HT-*b*-PAA. The dispersion was finally collected by centrifugation and dried in vacuum. The weight ratio between P3HT-*b*-PAA and MWCNTs of the obtained MWCNT-COOH was characterized by thermogravimetric analysis (TGA) (*66*) to be 1.72:1 and 0.63:1 for 1:6.8 and 1:0.9 P3HT-*b*-PAA, respectively. 1:6.8 P3HT-*b*-PAA leads to much higher polymer content in the MWCNT-COOH indicating denser carboxylic acid group on MWCNT surface. The carboxylic group density on the obtained CNT-COOH was characterized by the titration with NaOH ($10^{-3}$M) (*93*), and was determined to be 7.5 and 1.2 mmol/g for the P3HT-*b*-PAA with the P3HT to PAA ratio of 1:6.8 and 1:0.9, respectively. Therefore, P3HT-*b*-PAA block copolymers can not only introduce carboxylic groups onto CNT surfaces while retaining their structure and properties, but also provide uniform distribution of carboxylic groups on CNT surfaces with controlled density.

Downloaded by OHIO STATE UNIV LIBRARIES on June 21, 2012 | http://pubs.acs.org
Publication Date (Web): March 11, 2010 | doi: 10.1021/bk-2010-1034.ch008

### *Manipulating Solubility of CNTs in Various Solvents*

CNTs with good solubility in a variety of solvents are desirable for different applications. Base on our previous results, we believe that such CNTs can be obtained by surface modification with conjugated block polymers with non-conjugated amphiphilic blocks which are soluble in both polar and non-polar solvents. The amphiphilic blocks anchored on CNT surfaces endow CNTs with the solubility in various solvents. To verify the speculation, a conjugated block copolymer with an amphiphilic block- poly(3-hexylthiophene)-*b*-poly (poly (ethylene glycol) methyl ether acrylate) (P3HT-*b*-PPEGA) was synthesized.

MWCNTs were first dispersed by P3HT-*b*-PPEGA in chloroform, and the solvent was removed to obtain a solid product. The solubility of the P3HT-*b*-PPEGA dispersed MWCNT was tested by re-dispersing the solid product

Downloaded by OHIO STATE UNIV LIBRARIES on June 21, 2012 | http://pubs.acs.org
Publication Date (Web): March 11, 2010 | doi: 10.1021/bk-2010-1034.ch008

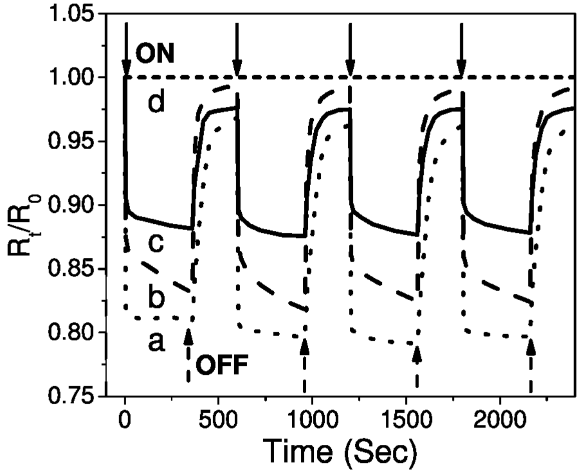

*Figure 11. The normalized resistance of the superhydrophobic film exposed to organic vapor: a) toluene; b) chloroform; c) tetrahydrofuran; d) moisture. Solid arrows and dash arrows indicate the moment that the sample was exposed to and removed from the vapor, respectively.*

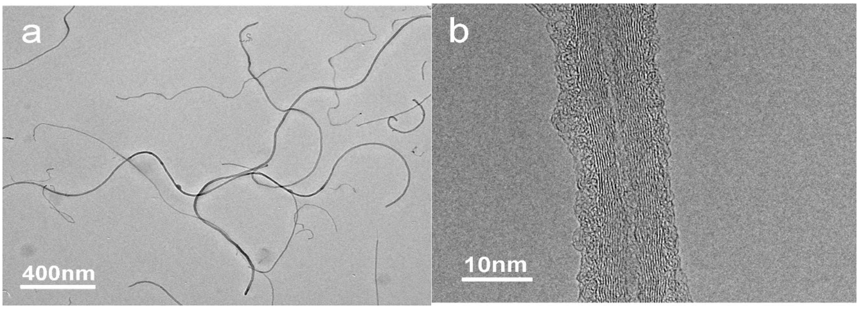

*Figure 12. a) A TEM image of MWCNT dispersed by P3HT-b-PAA, b) A HRTEM image indicating homogenous coverage of CNT by P3HT-b-PAA.*

in various solvents. In comparison, the solubility of P3HT dispersed MWCNTs was also tested. The P3HT dispersed MWCNT is soluble in chloroform, but not soluble in toluene, methanol, ethanol, dimethylformamide (DMF), acetonitrile, or water. In contrast, P3HT-*b*-PPEGA dispersed MWCNTs are soluble in various solvents including chloroform, toluene, methanol, ethanol, DMF, and acetonitrile. All these solvents are good solvents for the PPEGA block, indicating that the solubility of CNTs can be manipulated by the PPEGA block. The photographs in Figure 13 show that P3HT-b-PPEGA can disperse MWCNT in different solvents.

Downloaded by OHIO STATE UNIV LIBRARIES on June 21, 2012 | http://pubs.acs.org
Publication Date (Web): March 11, 2010 | doi: 10.1021/bk-2010-1034.ch008

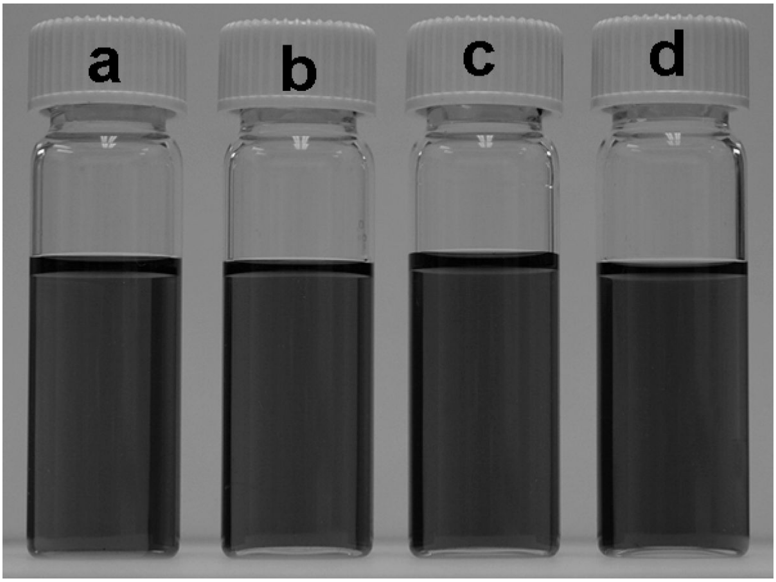

*Figure 13. The photographs of P3HT-b-PPEGA dispersed MWCNT in a) chloroform, b) toluene, c) methanol, d) DMF.*

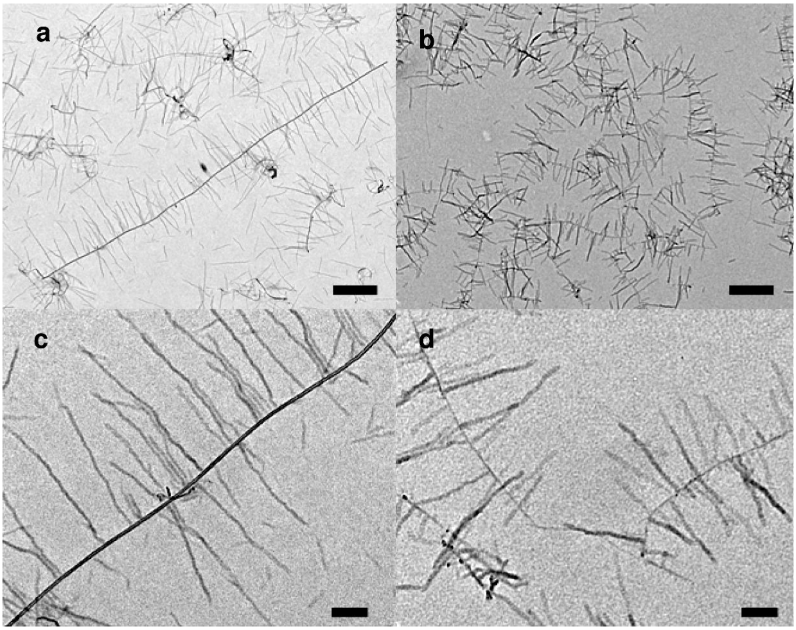

*Figure 14. TEM images of P3HT supramolecular structures on MWCNTs (a and c, P3HT/MWCNT mass ratio = 7) and SWCNTs b and d, P3HT/SWCNT mass ratio = 22). The width of the nanowhiskers is about 12~15 nm. (Scale bar: a, b = 500 nm, c, d = 100 nm)*

## Poly(3-hexylthiophene) Supramolecular Structures on Dispersed CNTs

As mentioned previously, P3HT and CNTs are promising materials for organic photovoltaics (*12–23*). Studies of the relationship between the P3HT film morphology and its charge mobility clearly suggested that more ordered structure led to higher charge mobilities (*17*, *94*). Un-ordered crystalline domains in P3HT creates a tortuous charge transport path that in turn lowers the effective charge mobility and increases the charge recombination. To achieve long-range ordered P3HT structures, P3HT nanowhiskers (with high aspect ratio) were fabricated by dissolving P3HT in their hot marginal solvents followed by a slow cooling process (*95*, *96*). The resulted P3HT nanowhiskers have ordered crystalline structures with high charge mobility, leading to better performances in OPV devices (*95*, *96*). Based on previous reports about CNT induced crystallization of semicrystalline polymers (*97–99*) and our recent work of dispersing CNTs using regioregular poly(3-hexylthiophene) (P3HT) and P3HT block copolymers (*75*, *76*), we have utilized CNTs to induce the crystallization of P3HT to form ordered "centipede-like" P3HT supramolecular structures on CNTs.

To fabricate P3HT supramolecular structures on CNT surfaces, P3HT dispersed CNTs (SWCNTs or MWCNTs) were added to a hot P3HT anisole solution. The solution was then quickly cooled down to room temperature and stood overnight for crystallization. Due to the low solubility of P3HT in anisole at room temperature, P3HT precipitated from the supersaturated solution, and formed supramolecular structures (nanowhiskers) on CNT surfaces. The resulted dark purple suspension was stable at room temperature for months, and the obtained supramolecular structures were examined by transmission electron microscopy (TEM) and atomic force microscopy (AFM). As shown in Figure 14, ordered P3HT nanowhiskers grow perpendicularly from both MWCNT and SWCNT surfaces, generating "centipede-like" supramolecular structures. The width of the nanowhiskers is almost the same as that of the free P3HT nanowhiskers prepared without CNTs. The TEM images also show that the diameter of SWCNTs (5-7 nm) is larger than that of bare SWCNTs (0.8-1.2 nm). Moreover, Figure 14a clearly show that the obtained supramolecular structures on MWCNTs are affected by the nanotube diameter and surface curvature. Generally, MWCNTs with large diameter and less surface curvature have a higher density of nanowhiskers. In contrast, the nanowhiskers on SWCNTs (Figure 14b) are more uniform because SWCNTs are straight with uniform diameters.

The AFM height images (Figure 15) show the same P3HT supramolecular structures on CNT surfaces as those observed by TEM. From the AFM cross section analysis (bottom panel in Figure 15), the height of the P3HT nanowhiskers is around 3-5 nm on both MWCNTs and SWCNTs, which is approximately 2 or 3 times of the lattice dimension of the P3HT unit cell (1.68 nm). The height of MWCNTs and SWCNTs is about 17 nm and 1 nm, respectively. The width of the P3HT nanowhiskers is around 28-32 nm determined by AFM. The deviation from the values given by the TEM (12~15 nm) may be caused by the AFM tips (*100*, *101*).

The formation of the "centipede-like" P3HT supramolecular structures is believed to be through the CNT enhanced crystallization of P3HT, where the

Downloaded by OHIO STATE UNIV LIBRARIES on June 21, 2012 | http://pubs.acs.org
Publication Date (Web): March 11, 2010 | doi: 10.1021/bk-2010-1034.ch008

Downloaded by OHIO STATE UNIV LIBRARIES on June 21, 2012 | http://pubs.acs.org
Publication Date (Web): March 11, 2010 | doi: 10.1021/bk-2010-1034.ch008

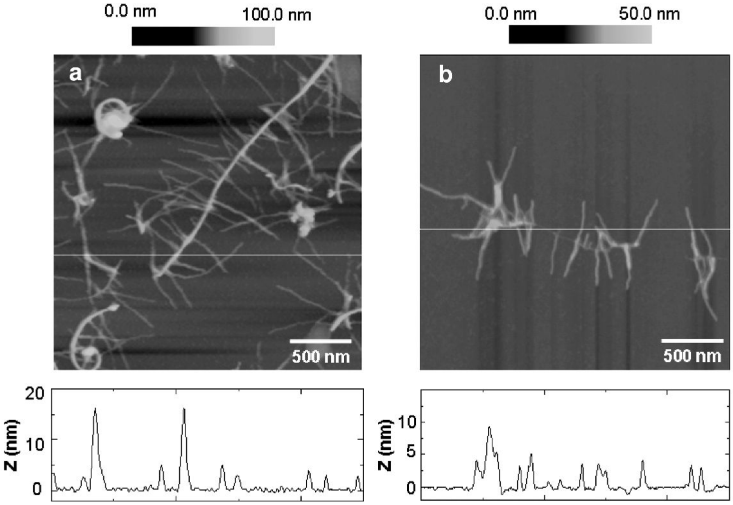

*Figure 15. Tapping-mode AFM height images (top) and their cross sections of the line trace (bottom) of P3HT supramolecular structures on MWCNTs (a, P3HT/MWCNT mass ratio = 7) and SWCNTs (b, P3HT/SWCNT mass ratio = 22) on silicon wafers ($SiO_2$/Si substrates) by drop casting.*

dispersed CNTs function as the nucleation seeds to grow P3HT nanowhiskers (Figure 16a). The P3HT (0.05mg/mL) isothermal crystallization processes in anisole with (Figure 16b) and without CNTs were studied by in-situ UV-Vis spectroscopy (Figure 16c). The evolution of UV-Vis absorption of P3HT in anisole with MWCNTs during the crystallization process is presented in Figure16a. The intensity of the absorption at 455 nm attributed to individual or isolated P3HT chain in solution decreases, while the low-energy absorption bands at 510, 550, and 600 nm increased. These low-energy peaks were explained as a combination of a π-π* electronic transition and a strong lattice vibration in P3HT crystalline domains (*102*). The absorbance in these fine structural peaks can be employed as a quantitative method to evaluate the amount of the crystallized P3HT in the dispersion. Therefore, the crystallization process in anisole with and without MWCNTs could be investigated by plotting the change of the UV-Vis absorbance at 600 nm versus time (Figure 16d). It is obvious that MWCNTs can greatly accelerate the crystallization of P3HT. The crystallization of P3HT completes in less than 3 hours with the presence of MWCNTs (squares), while it takes more than 24 hours for free P3HT to finish the crystallization (circles) (Figure 16d). The presence of an obvious isosbestic point at 481 nm in the UV-Vis spectra suggests a direct transformation from dissolved individual polymer chains to ordered nanowhiskers without any intermediate state (*103*). Our studies show that the isothermal P3HT crystallization processes follow the first-ordered kinetics.

Downloaded by OHIO STATE UNIV LIBRARIES on June 21, 2012 | http://pubs.acs.org
Publication Date (Web): March 11, 2010 | doi: 10.1021/bk-2010-1034.ch008

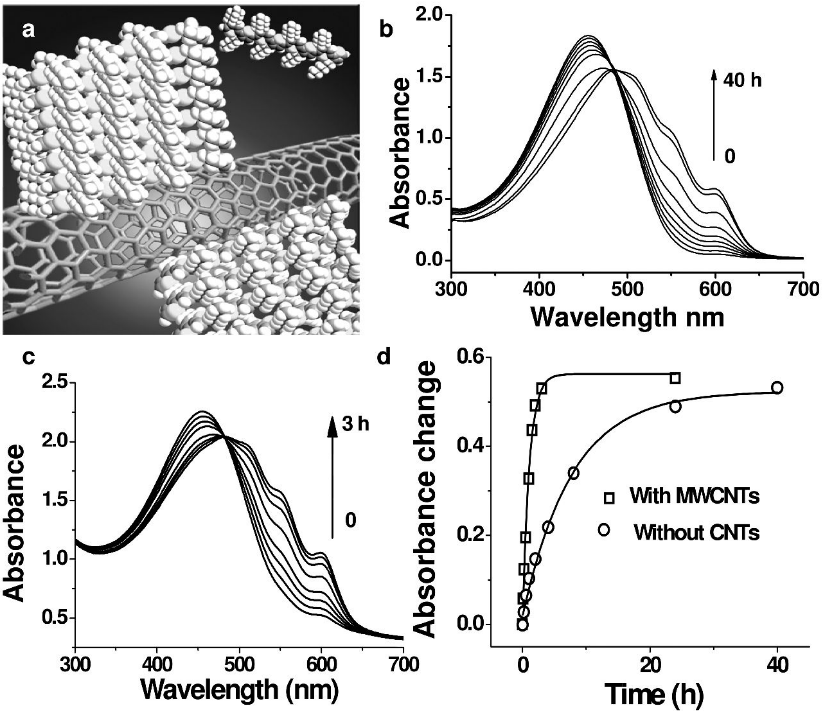

*Figure 16. (a) A schematic illustration of CNT induced crystallization of P3HT. (b)The crystallization process of P3HT on MWCNTs monitored by in situ UV-Vis spectroscopy at room temperature. ([P3HT] = 0.05 mg/mL, P3HT/MWCNT mass ratio = 7, collecting time of the curves (from bottom to top at 600 nm): 0 min, 5 min, 15 min, 30 min, 1 h, 1.5 h, 2 h and 3 h)(c) In situ UV-Vis absorption spectra of P3HT isothermal crystallization process at room temperature in anisole. ([P3HT] = 0.05 mg/mL, collecting time of the curves (from bottom to top at 600 nm): 0 min, 10 min, 30 min, 1 h, 2 h, 4 h, 8 h, 24 h and 40 h ) (d) UV-Vis absorbance change at 600 nm of the P3HT suspension with (squares) and without (circles) CNTs during the crystallization process. Solid lines are the fitted first-ordered kinetics curves.*

## Conclusions

In this chapter, we have demonstrated a non-invasive approach to disperse and functionalize CNTs using conjugated block copolymers. In contrast to traditional chemical CNT functionalization, conjugated block copolymers disperse and introduce functionalities through π-π interaction, preserving the mechanical and electrical properties of pristine CNTs. Additionally, conjugated polymer and block copolymers allow bottom-up fabrication of supramolecular nano-structures on CNTs and CNT/conjugated polymer composites. These materials have intriguing properties for energy conversion and storage. For example, CNT aerogels with large surface area have been developed in our group that can be used to support metal oxide nanoparticles for supercapacitors. The ordered P3HT supramolecular structures on CNT surfaces are investigated to achieve high charge mobility in organic photovoltaic devices. We believe that it is a general approach to build functional CNT composites that will lead to numerous applications in energy conversion and storage applications.

## Acknowledgments

The financial supports from National Science Foundation (CAREER Award DMR 0746499 and CBET 0608870) are greatly appreciated.

## References

1. *Carbon Nanotubes: Properties and Applications*; Connell, O., Michael, J., Eds.; CRC Press and Taylor & Francis Group: Boca Raton, FL, 2006.
2. Endo, M.; Ijima, S.; Dresselhaus, M.S. *Carbon Nanotubes*; Elsevier: 1997.
3. Reich, S.; Thomson, C.; Maultzsch, J. *Carbon Nanotubes: Basic Concepts and Physical Properties*; Wiley-VCH: 2004.
4. *Carbon Nanotechnology*; Dai, L., Ed.; Elsevier: Amsterdam, 2006.
5. Ijima, S. *Nature* **1991**, *363*, 56–58.
6. Sandler, J. K. W.; Kirk, J. E.; Kinloch, I. A.; Shaffer, M. S. P.; Windle, A. H. *Polymer* **2003**, *44*, 5893–5899.
7. Sandler, J.; Shaffer, M. S. P.; Prasse, T.; Bauhofer, W.; Schulte, K.; Windle, A. H. *Polymer* **1999**, *40*, 5967–5971.
8. Dujardin, E.; Ebbesen, T. W.; Krishnan, A. E.; Treacy, M. M. J. *Adv. Mater.* **1998**, *10*, 611–613.
9. Liu, J.; Rinzler, A. G.; Dai, H.; Hafner, J. H.; Bradley, R. K.; Boul, P. J.; Lu, A.; Iverson, T.; Shelimov, K.; Huffman, C. B.; Rodriguez-Macias, F.; Shon, Y. S.; Lee, T. R.; Colbert, D. T.; Smalley, R. E. *Science* **1998**, *280*, 1253–1256.
10. Hiura, H.; Ebbesen, T. W.; Tanigaki, K. *Adv. Mater.* **1995**, *7*, 275–276.
11. Hamon, M. A.; Hui, H.; Bhowmik, P.; Itkis, H. M. E.; Haddon, R. C. *Appl. Phys. A* **2002**, *74*, 333–338.
12. Kim, Y.; Cook, S.; Tuladhar, S. M.; Choulis, S. A.; Nelson, J.; Durrant, J. R.; Bradley, D. D. C.; Giles, M.; McCulloch, I.; Ha, C. S.; Ree, M. *Nat. Mater.* **2006**, *5*, 197–203.
13. Yu, G.; Gao, J.; Hummelen, J. C.; Wudl, F.; Heeger, A. J. *Science* **1995**, *270*, 1789–1791.
14. Ma, W.; Yang, C.; Gong, X.; Lee, K.; Heeger, A. J. *Adv. Funct. Mater.* **2005**, *15*, 1617–1622.
15. Li, G.; Shorotriya, V.; Huang, J.; Yao, Y.; Moriatry, T.; Emery, K.; Yang, Y. *Nat. Mater.* **2005**, *4*, 864–868.

Downloaded by OHIO STATE UNIV LIBRARIES on June 21, 2012 | http://pubs.acs.org
Publication Date (Web): March 11, 2010 | doi: 10.1021/bk-2010-1034.ch008

16. Reyes-Reyes, M.; Kim, K.; Dewald, J.; Lopez-Sandoval, R.; Avadhanula, A.; Curran, S.; Carrol, D. L. *Org. Lett.* **2005**, *7*, 5749–5752.
17. Bao, Z.; Dodabalapur, A.; Lovinger, A. J. *Appl. Phys. Lett.* **1996**, *69*, 4108–4110.
18. Lan, Y.-K.; Huang, C.-I. *J. Phys. Chem. B* **2008**, *112*, 14857–14862.
19. *Organic Photovoltaics: Mechanisms, Materials, and Device*; Sun, S.–S., Sariciftci, N. S., Eds.; CRC Press Taylor & Francis Group: London, 2005.
20. Miller, A. J.; Haton, R. A.; Chen, G. Y.; Silva, S. R. P. *Appl. Phys. Lett.* **2007**, *90*, 023105, 01–03.
21. Pradhan, B.; Batabyal, S. K.; Pal, A. *Appl. Phys. Lett.* **2006**, *88*, 093106, 01–03.
22. Berson, S.; de Bettignies, R.; Bailly, S.; Guillerez, S.; Jousselme, B. *Adv. Funct. Mater.* **2007**, *17*, 3363–3370.
23. Zhao, J.; Han, J.; Lu, J. P. *Phys. Rev. B.* **2002**, *66*, 193401, 1–4.
24. Boara, G.; Sparpaglione, M. *Synth. Met* **1995**, *72*, 135–140.
25. Noh, K. A.; Kim, D.W.; Jin, C. S.; Kyung, H. S.; Kim, J. H.; Ko, J. M. J *J. Power Sources* **2003**, *124*, 593–595.
26. Sivakumar, S. R.; Ko, J. M.; Kim, D. Y.; Kim, B. C.; Wallace, G.G. *Electrochim. Acta* **2007**, *52*, 7377–7385.
27. Gupta, V.; Miura, N. H *Mater. Lett.* **2006**, *60*, 1466–1469.
28. Fan, L. Z.; Maier, J. *Electrochem. Commun.* **2006**, *8*, 937–940.
29. Xu, Y.; Wang, J.; Sun, W.; Wang, S. *J. Power Sources* **2006**, *159*, 370–373.
30. Yang, D.-Q.; Rochette, J.-F.; Sacher, E. *J. Phys. Chem. B* **2005**, *109*, 7788–7796.
31. Curtzwiler, G.; Singh, J.; Miltz, J.; Doi, J.; Vorst, K. *J. Appl. Polym. Sci.* **2008**, *109*, 218–225.
32. Osorio, A. G.; Silverira, I. C. L.; Bueno, V. L.; Bergmann, C. P. *Appl. Surf. Sci.* **2008**, *25*, 2485–2489.
33. Kim, M.; Hong, C. K.; Choe, S.; Shim, S. E. *J. Polym. Sci., Part A: Polym. Chem.* **2007**, *45*, 4413–4420.
34. Monthioux, M.; Smith, B. W.; Burteaux, B.; Claye, A.; Fischer, J. E.; Luzzi, D. E. *Carbon* **2001**, *39*, 1251–1272.
35. Alvaro, M.; Atienzar, P.; de la Cruz, P.; Delgado, J. L.; Garcia, H.; Langa, F. *Chem. Phys. Lett.* **2004**, *386*, 342–347.
36. Sun, Y. P.; Huang, W.; Lin, Y.; Fu, K.; Kitaygorodskiy, A.; Riddle, L. A.; Yu, Y. J.; Carroll, D. L. *Chem. Mater.* **2001**, *13*, 2864–2869.
37. Chattopadhyay, D.; Lastella, S.; Kim, S.; Papadimitrakopoulos, F. *J. Am. Chem. Soc.* **2002**, *124*, 728–729.
38. Sung, J. H.; Kim, H. S.; Jin, H. J.; Choi, H. J.; Chin, I. J. *Macromolecules* **2004**, *37*, 9899–9902.
39. Shaffer, M. S. P.; Koziol, K. *Chem. Commun.* **2002**, 2074–2075.
40. Lin, Y.; Meziani, M. J.; Sun, Y. *J. Mater. Chem.* **2007**, *17*, 1143–1148.
41. Tasis, D.; Tagmatarchis, N.; Bianco, A.; Prato, M. *Chem. Rev.* **2006**, *106*, 1105–1136.
42. Barraza, H. J.; Pompeo, F.; O'Rear, E. A.; Resasco, D. E. *Nano Lett.* **2002**, *2*, 797–802.

Downloaded by OHIO STATE UNIV LIBRARIES on June 21, 2012 | http://pubs.acs.org
Publication Date (Web): March 11, 2010 | doi: 10.1021/bk-2010-1034.ch008

43. Islam, M. F.; Rojas, E.; Bergey, D. M.; Johnson, A. T.; Yodh, A. G. *Nano Lett.* **2003**, *3*, 269–273.
44. Bandhyopadhyaya, R.; Nativ-Roth, E.; Regev, O.; Yerushalmi-Rozen, R. *Nano Lett.* **2002**, *2*, 25–28.
45. Grunlan, J. C.; Liu, L.; Kim, Y. S. *Nano Lett.* **2006**, *6*, 911–915.
46. Nepal, D.; Geckeler, K. E. *Small* **2007**, *3*, 1259.
47. Karajanagi, S. S.; Yang, H.; Asuri, P.; Sellitto, E.; Dordick, J. S.; Kane, R. S. *Langmuir* **2006**, *22*, 1392–1395.
48. Zheng, M.; Jagota, A.; Semke, E. D.; Diner, B. A.; Mclean, R. S.; Lustig, S. R.; Richardson, R. E.; Tassi, N. G. *Nat. Mater.* **2003**, *2*, 338–342.
49. Barbarac, M.; Gomez-Romero, P. *J. Nanosci. Nanotechnol.* **2006**, *6*, 289–302.
50. Peng, C.; Snook, G. A.; Fray, D. J.; Shaffer, M. S. P.; Chen, G. Z. *Chem. Commun.* **2006**, 4629–4631.
51. An, K. H.; Jeon, K. K.; Heo, J. K.; Lim, S. C.; Bae, D. J.; Lee, Y. H. *J. Electrochem. Soc.* **2002**, *149*, A1058–A1062.
52. Philip, B.; Xie, J.; Chandrasekhar, A.; Abraham, J.; Varadan, V. K. *Smart Mater. Struct.* **2004**, *13*, 295–298.
53. Kuila, B. K.; Malik, S.; Batabyal, S. K.; Nandi, A. K. *Macromolecules* **2007**, *40*, 278–287.
54. Bell, J. M.; Goh, R. G. S.; Motta, N.; Musumeci, A.; Waclawik, E. R. *Proc. SPIE* **2006**, *6325*, 632503–632507.
55. Coleman, J. N.; Dalton, A. B.; Curran, S.; Rubio, A.; Davey, A. P.; Drury, A.; McCarthy, B.; Lahr, B.; Ajayan, P. M.; Roth, S.; Barklie, R. C.; Blau, W. J. *Adv. Mater.* **2000**, *12*, 213–216.
56. Murphy, R.; Coleman, J. N.; Cadek, M.; McCarthy, B.; Bent, M.; Drury, A.; Barklie, R. C.; Blau, W. J. *J. Phys. Chem. B* **2002**, *106*, 3087–3091.
57. McCarthy, B.; Coleman, J. N.; Czerw, R.; Dalton, A. B.; Panhuis, M.; Maiti, A.; Drury, A.; Bernier, P.; Nagy, J. B.; Lahr, B.; Byrne, H. J.; Carroll, D. L.; Blau, W. J. *J. Phys. Chem. B* **2002**, *106*, 2210–2216.
58. Chen, J.; Liu, H.; Weimer, W. A.; Halls, M. D.; Waldeck, D. H.; Walker, G. C. *J. Am. Chem. Soc.* **2002**, *124*, 9034–9035.
59. Baibarac, M.; Baltog, I.; Lefrant, S.; Mevellec, J. Y.; Chauvet, O. *Chem. Mater.* **2003**, *15*, 4149–4156.
60. Zengin, H.; Zhou, W.; Jin, J.; Czerw, R.; Smith, D. W.; Echegoyen, L.; Carroll, D. L.; Foulger, S. H.; Ballato, J. *Adv. Mater.* **2002**, *14*, 1480–1483.
61. Curran, S. A.; Ajayan, P. M.; Blau, W. J.; Carroll, D. G.; Coleman, J. N.; Dalton, A. B.; Davery, A.; Drury, A.; McCarthy, B.; Maier, S.; Strevens, A. *Adv. Mater.* **1998**, *10*, 1091–1093.
62. Star, A.; Stoddart, J. F.; Steuerman, D.; Diehl, M.; Boukai, A.; Wong, E. W.; Yang, X.; Chung, S. W.; Choi, H.; Heath, J. R. *Angew. Chem., Int. Ed.* **2001**, *40*, 1721–1725.
63. Tang, B. Z.; Xu, H. Y. *Macromolecules* **1999**, *32*, 2569–2576.
64. Chen, J.; Ramasubramaniam, R.; Xue, C.; Liu, H. Y. *Adv. Funct. Mater.* **2006**, *16*, 114–119.
65. Rice, N. A.; Soper, K.; Zhou, N.; Merschrod, E.; Zhao, Y. *Chem. Commun.* **2006**, 4937–4939.

Downloaded by OHIO STATE UNIV LIBRARIES on June 21, 2012 | http://pubs.acs.org
Publication Date (Web): March 11, 2010 | doi: 10.1021/bk-2010-1034.ch008

Downloaded by OHIO STATE UNIV LIBRARIES on June 21, 2012 | http://pubs.acs.org
Publication Date (Web): March 11, 2010 | doi: 10.1021/bk-2010-1034.ch008

66. Cheng, F.; Imin, P.; Maunders, C.; Botton, G.; Adronov, A. *Macromolecules* **2008**, *41*, 2304–2308.
67. Shin, H.; Min, B. G.; Jeong, W.; Park, C. *Macromol. Rapid Commun.* **2005**, *26*, 1451–1457.
68. Shvartzman-Cohen, R.; Levi-Kalisman, Y.; Nativ-Roth, E.; Yerushalmi-Rozen, R. *Langmuir* **2004**, *20*, 6085–6088.
69. Nativ-Roth, E.; Shvartzman-Cohen, R.; Bounioux, C.; Florent, M.; Zhang, D.; Szleifer, I.; Yerushalmi-Rozen, R. *Macromolecules* **2007**, *40*, 3676–3685.
70. Park, I.; Lee, W.; Kim, J.; Park, M.; Lee, H. *Sens. Actuators, B* **2007**, *126*, 301–305.
71. Mountrichas, G.; Tagmatarchis, N.; Pispas, S. *J. Phys. Chem. B* **2007**, *111*, 8369–8372.
72. Cotiuga, I.; Picchioni, F.; Agarwal, U. S.; Wouters, D.; Loos, J.; Lemstra, P. J. *Macromol. Rapid Commun.* **2006**, *27*, 1073–1078.
73. Sinani, V. A.; Gheith, M. K.; Yaroslavov, A. A.; Rakhnyanskaya, A. A.; Sun, K.; Mamedov, A. A.; Wicksted, J. P.; Kotov, N. A. *J. Am. Chem. Soc.* **2005**, *127*, 3463–3472.
74. Yang, M.; Koutsos, V.; Zaiser, M. *J. Phys. Chem. B* **2005**, *109*, 10009.
75. Zou, J.; Liu, L.; Chen, H.; Khondaker, S. I.; McCullough, R. D.; Huo, Q.; Zhai, L. *Adv. Mater.* **2008**, *20*, 2055–2060.
76. Zou, J.; Chen, H.; Chunder, A.; Yu, Y.; Huo, Q.; Zhai, L. *Adv. Mater.* **2008**, *20*, 3337–3341.
77. Zou, J.; Khondaker, S. I.; Huo, Q.; Zhai, L. *Adv. Funct. Mater.* **2009**, *19*, 479–483.
78. Liu, J.; Zou, J.; Zhai, L. *Macromol. Rapid Commun.* 2009, DOI: 10.1002/marc.200900225.
79. Jeffries-EL, M.; Sauvé, G.; McCullough, R. D. *Adv. Mater.* **2004**, *16*, 1017–1019.
80. Iovu, M. C.; Jeffries-EL, M.; Sheina, E. E.; Cooper, J. R.; McCullough, R. D. *Macromolecules* **2005**, *46*, 8582–8586.
81. Chen, T.; Wu, X.; Rieke, R. D. *J. Am. Chem. Soc.* **1995**, *117*, 233–234.
82. Ai, X.; Anderson, N.; Guo, J.; Kowalik, J.; Tolbert, L. M.; Lian, T. *J. Phys. Chem. B* **2006**, *110*, 25496–25503.
83. Fan, C.; Wang, S.; Hong, J. W.; Bazan, G. C.; Plaxco, K. W.; A. Heeger, J. *PNAS* **2003**, *100*, 6297–6301.
84. Rao, A. M.; Eklund, P. C.; Bandow, S.; Thess, A.; Smalley, R. E. *Nature* **1997**, *388*, 257–259.
85. Grossiord, N.; Loos, J.; Regev, O.; Koning, C. E. *Chem. Mater.* **2006**, *18*, 1089–1099.
86. McQuade, D. T.; Pullen, A. E.; Swager, T. M. *Chem. Rev.* **2000**, *100*, 2537–2574.
87. Janata, J.; Josowicz, M. *Nat. Mater.* **2002**, *2*, 19–24.
88. Li, B.; Sauvé, G.; Lovu, M. C.; Jeffries-EL, M.; Zhang, R.; Cooper, J.; Santhanam, S.; Schulz, L.; Revelli, J. C.; Kusne, A. G.; Kowalewski, T.; Snyder, J. L.; Weiss, L. E.; Fedder, G. K.; McCullough, R. D.; Lambeth, D. N. *Nano Lett.* **2006**, *6*, 1598–1602.

89. Virji, S.; Huang, J.; Kaner, R. B.; Weiller, B. H. *Nano Lett.* **2004**, *4*, 491–496.
90. Wang, P-C.; Huang, Z.; MacDiarmid, A. G. *Synth. Met.* **1999**, *101*, 852–853.
91. Kim, Y.-T.; Tadai, K.; Mitani, T. *J. Mater. Chem.* **2005**, *15*, 4914–4921.
92. Halder, A.; Sharma, S.; Hegde, M. S.; Ravishankar, N. *J. Phys. Chem. C* **2009**, *113*, 1466–1473.
93. Eitan, A.; Jiang, K.; Dukes, D.; Andrews, R.; Schadler, L. S. *Chem. Mater.* **2003**, *15*, 3198–3201.
94. Sirringhaus, H.; Brown, P. J.; Friend, R. H.; Nielsen, M. M.; Bechgaard, K.; Langeveld-Voss, B. M. W.; Spiering, A. J. H.; Janssen, R. A. J.; Meijer, E. W.; Herwig, P.; de Leeuw, D. M. *Nature* **1999**, *401*, 685–688.
95. Xin, H.; Kim, F. S.; Jenekhe, S. A. *J. Am. Chem. Soc.* **2008**, *130*, 5424–5425.
96. Berson, S.; Gettignies, R. D.; Bailly, S.; Guillerez, S. *Adv. Funct. Mater.* **2007**, *17*, 1377.
97. Li, L.; Li, C. Y.; Ni, C. *J. Am. Chem. Soc.* **2006**, *128*, 1692–1699.
98. Lu, K.; Grossiord, N.; Koning, C. E.; Miltner, H. E.; van Mele, B.; Loos, J. *Macromolecules* **2008**, *41*, 8081–8085.
99. Li, L.; Yang, Y.; Yang, G.; Chen, X.; Hsiao, B. S.; Chu, B.; Spanier, J. E.; Li, C. Y. *Nano Lett.* **2006**, *6*, 1007–1012.
100. Wong, S. S.; Harper, J. D.; Lansbury, P. T.; Lieber, C. M. *J. Am. Chem. Soc.* **1998**, *120*, 603–604.
101. Kline, R. J.; McGehee, M. D.; Kadnikova, E. N.; Liu, J.; Fréchet, J. M. J.; Toney, M. F. *Macromolecules* **2005**, *38*, 3312–3319.
102. Yamamoto, T.; Komarudin, D.; Arai, M.; Lee, B.-L.; Suganuma, H.; Asakawa, N.; Inoue, Y.; Kubota, K.; Sasaki, S.; Fukuda, T.; Matsuda, H. *J. Am. Chem. Soc.* **1998**, *120*, 2047–2058.
103. Mårdalen, J.; Samuelsen, E. M.; Pedersen, A. Ø. *Synth. Met.* **1993**, *55*, 378–383.

Downloaded by OHIO STATE UNIV LIBRARIES on June 21, 2012 | http://pubs.acs.org
Publication Date (Web): March 11, 2010 | doi: 10.1021/bk-2010-1034.ch008

Downloaded by UNIV OF DELAWARE MORRIS LIB on June 22, 2012 | http://pubs.acs.org
Publication Date (Web): March 11, 2010 | doi: 10.1021/bk-2010-1034.ch009

## Chapter 9

# Tailoring the Morphology of the Poly(3-hexylthiophene)/$C_{60}$ Films and Charge Carrier Mobility

**Weili Liu, Ruigang Liu,[*] and Yong Huang[*]**

**State Key Laboratory of Polymer Physics and Chemistry, Beijing National Laboratory for Molecular Sciences, Institute of Chemistry, Chinese Academy of Sciences, Beijing 100190, China**
**[*]Correspondence to R. Liu (rgliu@iccas.ac.cn) and Y. Huang (yhuang@mail.ipc.ac.cn). Tel: +86-10-82618573.**

We used solvent-vapor treatment method to tailor the nanoscale phase-seperation and thus tailor the charge mobility of the poly(3-hexylthiophene)/fullerene (P3HT/$C_{60}$) blend films. The nanowires obtained by chloroform vapor treatment are rich in $C_{60}$, whereas the nanowires obtained by DCB vapor treatment are rich in P3HT. The treated blends offers far superior hole transport than the untreated blends, which is attributed to the nanoscale phase-segregation and a 3-D network contained either $C_{60}$ or P3HT nanowires. Meanwhile, the electrically bicontinous nanoscale morphology realized by controlling the crystallinity of P3HT and $C_{60}$ using different solvents vapor results in enhanced absorption in visible light without further heat-treatment or preparation in both cases. Solar cells fabricating from the films after treatment show several-fold improvements in power conversion efficiency compared to devices having films without treatment.

## 1. Introduction

Polymer solar cells based on a thin-film bulk heterojunction of electron-donating conjugated polymers and electron-accepting fullerene ($C_{60}$) derivatives have been attracted much attention in recent years for their potential applications

In Functional Polymer Nanocomposites for Energy Storage and Conversion; Wang, Q., et al.;
ACS Symposium Series; American Chemical Society: Washington, DC, 2010.

as a low cost approach to solar energy conversion (*1*). The blends of regioregular poly(3-hexylthiophene) (P3HT) and $C_{60}$ derivatives are the most promising candidates for these solar cells. The power conversion efficiency of photovoltaic devices based on P3HT/$C_{60}$ derivatives has reached 4.4%-6.5% (*2*, *3*). The recent progress in improving the performance of the polymer/fullerene solar cells has come from the synthesis of new low band-gap polymer (*4–6*), controlling the blend nanoscale morphology (*7*, *8*), and improving the device fabrication and architectures (*3*).

The main factors that limit the performance of polymer solar cells are the poor charge carrier transport (*9*) and the narrow absorption in the visible range of solar spectrum of the active layer (*10*, *11*). Generally, the bicontinuous nanoscale morphology is desirable for the donor and acceptor junctions and high crystallinity in the donor and acceptor phases is also required for the better transportation ability of the charge carrier. However, the ideal bicontinuous two-phase nanoscale morphology is difficult to be obtained due to the poor solubility of fullerene and the improper phase separation during film cast process. Many protocols to control the two-phase nanoscale morphology have been proposed, including both deposition and post-deposition procedures, such as varying the solvents (*5*, *12*, *13*), thermal annealing (*14*, *15*), drying rate (*2*, *16*), melting of bilayers (*17*), etc. More recently, several works have been reported on creating nanorods or nanowires of P3HT or $C_{60}$ to form three dimension interpenetrating network, such as the formation of fullerene nanorods with different sizes by solvent vapor treatment at different vapor pressure (*18*), the P3HT nanowires/PCBM prepared from the mixture of P3HT nanowires suspension with PCBM (*19*), and the formation of the fibrillar P3HT in P3HT/PCBM blends (*14*). These approaches provide the promising new protocols for morphology manipulation of conjugated polymer/$C_{60}$ for solar cells to obtain better charge carrier mobility and increase the absorption of solar energy. The $C_{60}$ derivative [6.6]-phenyl $C_{61}$-butyric acid methyl ester (PCBM) was mainly used in the published works, which is due to its good solubility. However, $C_{60}$ is much cheaper than PCBM. The morphology fabrication of P3HT/$C_{60}$ blends remains a fundamental challenge in the field of conjugated polymer/$C_{60}$ solar cells (*18*, *20*).

New facile approaches to tailor the morphology are attracting the increasing interest for the ease producing, low cost, high efficiency, and mass production of polymeric solar cells, especially the facile and efficient method for the selected controlling of the nanoscale crystallinity of the components in the active film of polymer solar cells. In this paper, the morphology in nanoscale of the P3HT/$C_{60}$ blend film was tailored by the solvent vapor of chloroform and 1,2-dichlorobenzene (DCB). The hole transport properties was investigated by space charge limited current (SCLC) measurements (*21*). The correlation between the morphology and the hole transport properties was investigated. Consequently, solar cells were fabricated from the films after treatment and without treatment.

Downloaded by UNIV OF DELAWARE MORRIS LIB on June 22, 2012 | http://pubs.acs.org
Publication Date (Web): March 11, 2010 | doi: 10.1021/bk-2010-1034.ch009

Downloaded by UNIV OF DELAWARE MORRIS LIB on June 22, 2012 | http://pubs.acs.org
Publication Date (Web): March 11, 2010 | doi: 10.1021/bk-2010-1034.ch009

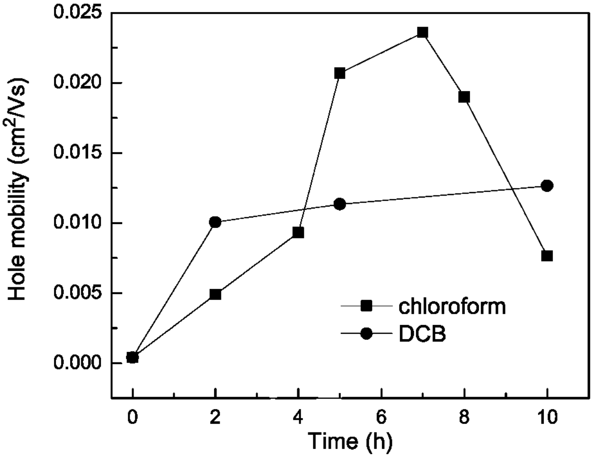

*Figure 1. The hole mobility of P3HT/$C_{60}$ films as a function of time treated in chloroform and DCB vapors at 25 °C.*

## 2. Experimental Section

### 2.1. Materials and Sample Preparation

P3HT (regioregular, $M_n$ = 34,500 g/mol, $M_w/M_n$ = 1.9, Alfa Aesar) and $C_{60}$ (>99.9%, Alfa Aecar) were used as received. All the solvents were analytical grade and used as received.

For the preparation of the mixed solution (15mg/mL) that had a P3HT:C60 ratio of 1:1 by weight in DCB (> 99%, GC grade, Fluka) was stirred in glove box at 50 °C and then spin-coated to produce a 110 nm thick active layer after being slowly cooled to room temperature on the pre-cleaned glass (for WAXD, SEM and AFM), quartz (for UV-vis absorption), KBr (for TEM) or ITO/PEDOT: PSS substrates (for the solar cells and hole mobility measurements). Subsequently, the samples were transferred into a sealed jar filled with saturated chloroform or DCB vapor and stayed for different time at 25°C and 40°C. The saturation vapor pressures of chloroform and DCB are 26.2 and 0.180 kPa (*22*), respectively, at 25°C and 47.6 and 0.445 kPa, respectively, at 40°C. The resulting samples were dried in a vacuum box for 24 hr before measurements. Solar cells with 4 mm2 area were fabricated from P3HT/C60 blend films and tested in air under AM 1.5 illuminations. For the device fabrication, the ITO substrates first underwent a routine cleaning procedure, which included sonication in detergent followed by repeated rinsing in deionized water, acetone, and isopropyl alcohol, and finally treatment with ultraviolet (UV) ozone. Poly(3,4-ethylenedioxythiophene): polystyrenesulfonate (PEDOT:PSS, Baytron-P 4083) was first spin-cast onto an ITO/glass substrate at a spin speed of 2500 rpm, which corresponds to a thickness of 25 nm, and baked at 150°C for 10 min. After spin casting the polymer film, Aluminium electrodes (100 nm thick) were deposited for solar cells testing. Here the hole mobility was determined from the space-charge-limited current (SCLC) model with a device structure of ITO/PEDOT:PSS/P3HT:C60 /Au (*21*).

### 2.2. Characterization

The morphology of P3HT/$C_{60}$ nanocomposite films was investigated by transmission electron microscopy (TEM, JEOL JEM-2200FS Japan) at an accelerating voltage of 200 kV, scan electron microscopy (SEM, JEOL 6700F Japan) at an accelerating voltage of 5 kV and atomic force microscopy (AFM, NanoScope III Multimode, Digital Instrument) in its tapping mode. A solar light simulator (Oriel, 91192) was used as the white light source to give AM 1.5 illumination on the surface of the solar cells. Current density-Voltage (I-V) characteristics were measured by a computer-controlled Keithley 236 source measurement unit in air and under dark or calibrated simulated solar illumination (AM 1.5).

## 3. Results and Discussion

Charge mobility is a key factor for the efficient collection photo-generated charges in solar cells (*23–25*). Generally, the mobility of the donor material is lower than the mobility of the acceptor material which causes a mismatch resulting in asymmetric carrier extraction (*26*). The hole mobility of P3HT/$C_{60}$ blend films was generally estimated by the SCLC measurements (*21*). Figure 1 shows that the hole mobility of the P3HT/$C_{60}$ blend films increases obviously with the treatments of both chloroform and dichloride benzene (DCB) vapors. When the P3HT/$C_{60}$ films were treated with chloroform vapor, the hole mobility increases markedly and then decreases with treating time. The maximum value of the hole mobility is about $2.4 \times 10^{-2}$ $cm^2/V \cdot s$, which is a relatively higher value for poly(3-alkylthiophene)/$C_{60}$ derivatives blends in literatures (*21*, *24*, *27*), when the film was treated for about 7 hrs. Whereas when the P3HT/$C_{60}$ film was treated with DCB, the hole mobility increases markedly within 2 hrs and then increasing slowly with the treatment time (Figure 1). The higher hole mobility may attribute to the enhancement on the balance between the electron and hole transport, which reduces the space-charge accumulation (*27*).

The hole mobility is a function of morphological variables such as the degree of crystallinity, crystallite size, phase domain size, etc. (*23–25*). In this work, it was found that the enhancement of the hole mobility is correlated to the morphology of the P3HT/ $C_{60}$ films. The typical morphology of the P3HT/$C_{60}$ films treated with chloroform and DCB vapors are shown in Figure 2 and 3, respectively, as a function of the treating time. The results show that the morphology development behavior is different when the P3HT/$C_{60}$ films are treated with chloroform or DCB. In the case of treating the film with chloroform, granular structure appeared first (Figure 2b), then nanowire formed when the film was treated for about 5 hrs (Figure 2c). The nanowire developed with time (Figure 2d) and then new granular structure appeared (Figure 2e). When the P3HT/$C_{60}$ film was treated with chloroform vapor at 25°C for 20 hrs, the nanowire disappeared completely and large granular formed (Figure 2f). The morphology of the P3HT/$C_{60}$ film correlates to the hole mobility of the film.

Downloaded by UNIV OF DELAWARE MORRIS LIB on June 22, 2012 | http://pubs.acs.org
Publication Date (Web): March 11, 2010 | doi: 10.1021/bk-2010-1034.ch009

Downloaded by UNIV OF DELAWARE MORRIS LIB on June 22, 2012 | http://pubs.acs.org
Publication Date (Web): March 11, 2010 | doi: 10.1021/bk-2010-1034.ch009

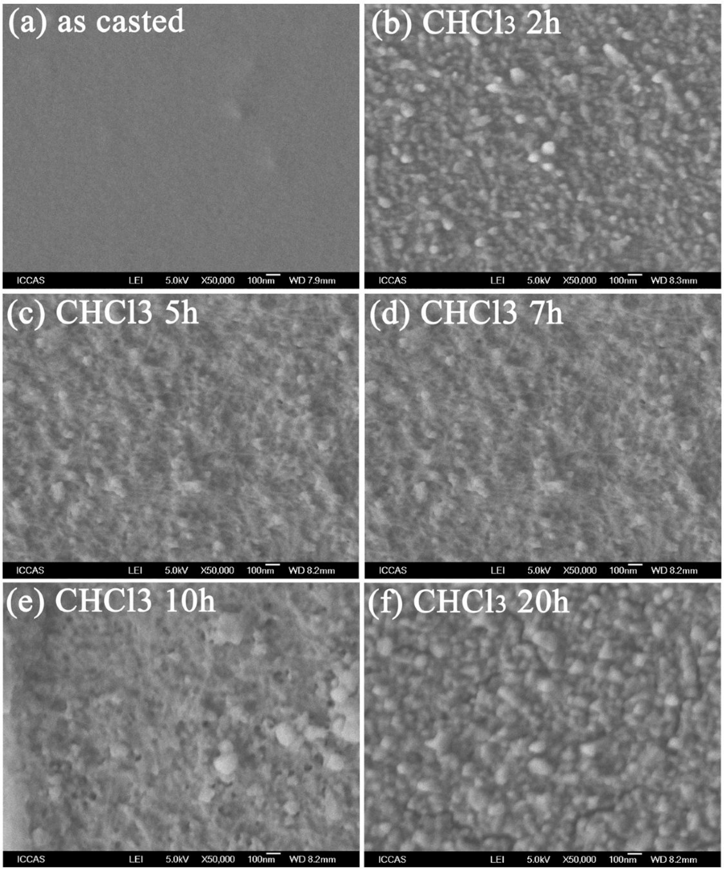
(a) as casted
(b) CHCl3 2h
(c) CHCl3 5h
(d) CHCl3 7h
(e) CHCl3 10h
(f) CHCl3 20h
ICCAS LEI 5.0kV X50,000 100nm WD 7.9mm
ICCAS LEI 5.0kV X50,000 100nm WD 8.3mm
ICCAS LEI 5.0kV X50,000 100nm WD 8.2mm
ICCAS LEI 5.0kV X50,000 100nm WD 8.2mm
ICCAS LEI 5.0kV X50,000 100nm WD 8.2mm
ICCAS LEI 5.0kV X50,000 100nm WD 8.2mm

*Figure 2. The typical SEM images of the composite films s a function of time treated in chloroform vapor at 25 °C.*

The appearance of the nanowire corresponds to the increase in the hole mobility, whereas the granular morphology relates to the decrease in the hole mobility. The optimum treating time by chloroform is around 7 hrs when the films are treated with chloroform vapor at 25°C (Figure 1).

When the P3HT/$C_{60}$ film was treated with DCB vapor at 25°C, the nanowire morphology appeared at about 2 hrs (Figure 3b). The nanowires morphology developed during the whole treating procedure (Figure 2c and 2d) and resulted the increase in hole mobility (Figure 1). The above results indicate that the morphology changes in the P3HT/$C_{60}$ films are different when treated with chloroform and DCB vapors and the formation of the nanowire morphology in the P3HT/$C_{60}$ film promotes the increase of the hole mobility. However, a question arises from the above results. The maximum value of the hole mobility of films treated with chloroform vapor is higher than that of the films treated with DCB vapor (Figure 1), even though similar morphology were observed in the films obtained in both cases.

Downloaded by UNIV OF DELAWARE MORRIS LIB on June 22, 2012 | http://pubs.acs.org
Publication Date (Web): March 11, 2010 | doi: 10.1021/bk-2010-1034.ch009

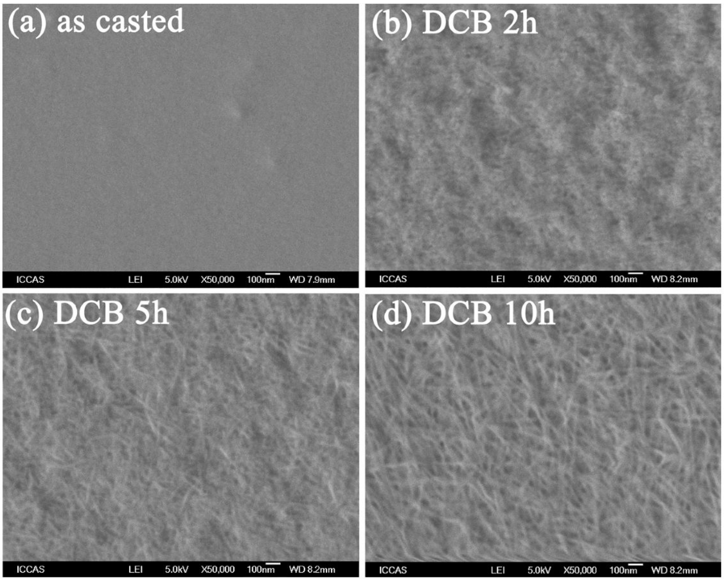
(a) as casted
(b) DCB 2h
(c) DCB 5h
(d) DCB 10h
ICCAS LEI 5.0kV X50,000 100nm WD 7.9mm
ICCAS LEI 5.0kV X50,000 100nm WD 8.2mm
ICCAS LEI 5.0kV X50,000 100nm WD 8.2mm
ICCAS LEI 5.0kV X50,000 100nm WD 8.2mm

*Figure 3. The typical SEM images of the composite films s a function of time treated in DCB vapor at 25 °C.*

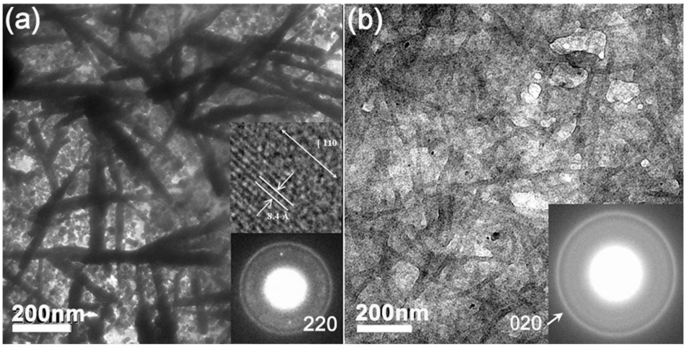
(a)
(b)
[110]
3.4 Å
200nm
220
200nm
020

*Figure 4. TEM images of P3HT/$C_{60}$ films treated in chloroform (a) and DCB (b) vapors for 5 h at 25 °C. Inset: typical high-resolution TEM (HRTEM) image of an individual wire and SAED pattern. HRTEM shows the growing direction of these $C_{60}$ wires is along the crystallographic [110] axis.*

It is known that P3HT has the good solubility in both chloroform and DCB. However, the solubility of $C_{60}$ in chloroform and DCB is $10^{-4.8}$ and $10^{-2.4}$ (g/g), respectively (*28*), which may contribute to the different morphologies during the treatment of the P3HT/C60 films with chloroform and DCB vapors. Figure 4 shows the TEM images of the nanowires obtained by chloroform and DCB vapor treatment. The results show that the nanowires formed by chloroform vapor treatments are typically 20–40 nm in diameter and 0.5–1 µm in length (Figure

Downloaded by UNIV OF DELAWARE MORRIS LIB on June 22, 2012 | http://pubs.acs.org
Publication Date (Web): March 11, 2010 | doi: 10.1021/bk-2010-1034.ch009

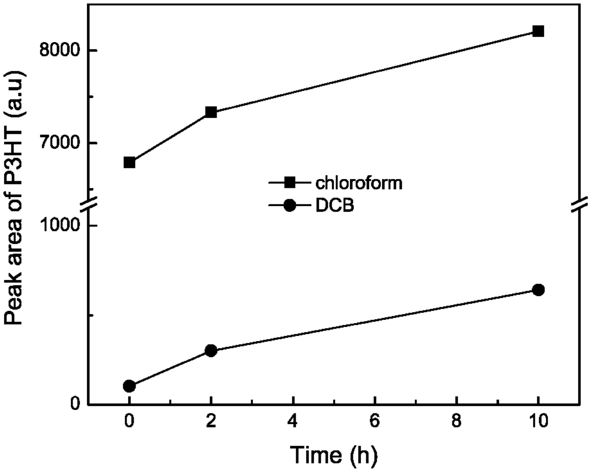

*Figure 5. P3HT relative crystallinity calculated from WXRD curves of the P3HT/$C_{60}$ (1/1 wt ratio) films with the time of treatment time in choloroform and DCB vapors at 25°C. Same film were used for each serial treatment.*

4a). The selective area electron diffraction (down insert, Figure 4a) shows the characteristic polymorphous diffraction spots of $C_{60}$ crystallites (*29*) and one discernible diffraction ring of P3HT (*30*, *31*). The high resolution TEM image (up insert, Figure 4a) shows the typical crystal lattice of $C_{60}$ nanowire whose growing direction is along the crystallographic [110] axis. Moreover, EDX results indicates that the C:S ratio in the nanowire regions is about 14:1 (w:w), whereas the C:S ratio in the region between two nanowires is about 6:1 (w:w). The theoretical C:S ratio of the bulk P3HT/$C_{60}$ blend film is 8.875:1 (w:w), whereas the experimental C:S ratio of the bulk film is about 13:1. The results indicate that the EDX experiments cannot determine the C:S ratio precisely in present work. However, we can estimate the relative content of carbon and sulfur elements in the different parts of the P3HT/$C_{60}$ blend film by EDX experimental results. The above results indicate that the nanowires obtained by the chloroform treatment are the $C_{60}$-rich domain. The $C_{60}$-rich nanowires connect each other and form the non-woven like network in the semi-crystallized P3HT matrix. In the case of the nanowires obtained by the DCB vapor treatment, their diameter is 10–20 nm and the length is more than 1 µm (Figure 4b). Moreover, one discernible diffraction ring can be observed in the SAED pattern without the appearance of the $C_{60}$ crystal diffraction pattern (insert, Figure 4b), corresponding to characteristic diffraction of P3HT crystals. EDX results show that the C:S ratio is about 7:1 and 12:1 (w:w) in the nanowires region and in the matrix region, respectively, which indicates that the nanowires formed by DCB vapor treatment are rich in P3HT.

Wide-angle X-ray diffraction (WAXD) experiments indicate that the crystalline peak of P3HT increases with the chloroform and DCB-vapor treatments. The peak area of the P3HT is shown in Figure 5 as a function of the time that the blends films were treated by chloroform and DCB vapors. The results show that the crystalline peak area of P3HT of the same thin film increase

Downloaded by UNIV OF DELAWARE MORRIS LIB on June 22, 2012 | http://pubs.acs.org
Publication Date (Web): March 11, 2010 | doi: 10.1021/bk-2010-1034.ch009

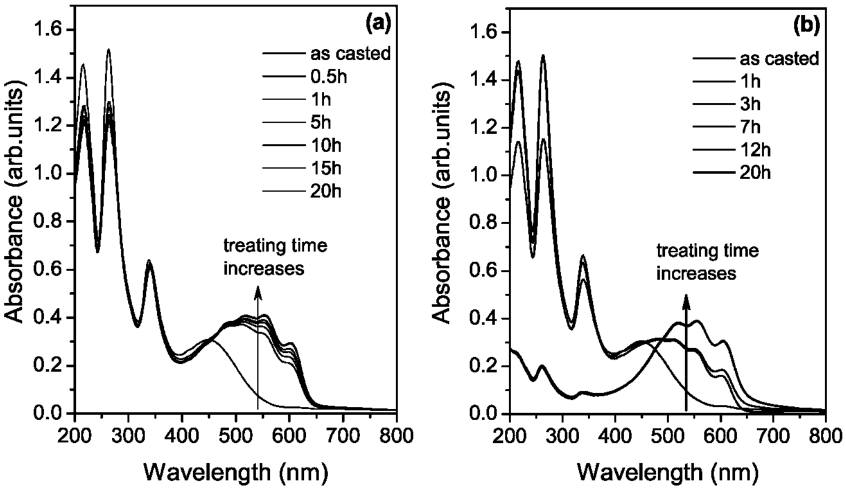

*Figure 6. UV-vis absorption spectra of the P3HT/$C_{60}$ films treated in chloroform vapor (a) and DCB vapor (b) at 25 °C.*

with the time treated with both chloroform and DCB vapors (Figure 5), indicates the crystallinity of P3HT increases with vapor treatment.

The different nanowires formed by chloroform and DCB vapor treatments can be depicted as follows. During the chloroform vapor treatment, the solvent molecules penetrate into the P3HT matrix and increase the mobility of polymer chain as a plasticizer. Simultaneously, the dispersed $C_{60}$ molecules acquired the increased mobility due to that P3HT was partially dissolved. Therefore, P3HT chains self-organized into more ordered structure and $C_{60}$ molecules aggregated into crystals simultaneously (*32*). During the DCB vapor treatment, P3HT self-organized into more ordered and nanowire-like crystallite due to that P3HT has a much better solubility in DCB than that in chloroform. Moreover, since $C_{60}$ can well dissolved in DCB, the DCB molecules penetrate into the $C_{60}$ aggregates which leads to the isotropic phase of $C_{60}$ as that in the solution. When the film is dried in vacuum after DCB vapor solvent treatment, the $C_{60}$ molecules in the blend film were quenched in the P3HT matrix due to the fast evaporation of DCB. As a result, no crystallite of $C_{60}$ was formed when the P3HT/$C_{60}$ films were treated by DCB vapor. Another additional reason for the different results obtained by chloroform-vapor and DCB-vapor treatment might be that because the chloroform molecule is much smaller than DCB, the former can be easily trapped in $C_{60}$ crystal due to its large molecule size (~0.8 nm in diameter) and so assists the nucleation and crystallization process of $C_{60}$. The above results indicate that both chloroform and DCB vapor treatment lead to the self-organization of polymer chains, whereas the crystallizability of $C_{60}$ is different due to the different interactions between $C_{60}$ and solvents molecule.

The above results and discussion may answer the question why the films treated with chloroform vapor have a higher hole mobility than that treated with DCB vapor (Figure 1). In the films treated with chloroform vapor, the $C_{60}$ crystallized into nanowire. The transport properties of charge carriers in

Downloaded by UNIV OF DELAWARE MORRIS LIB on June 22, 2012 | http://pubs.acs.org
Publication Date (Web): March 11, 2010 | doi: 10.1021/bk-2010-1034.ch009

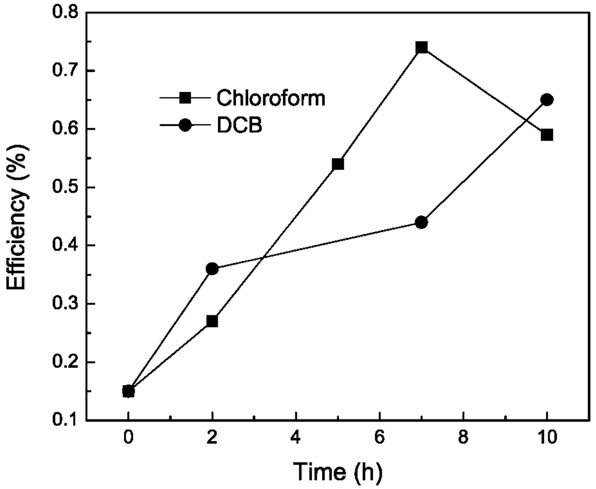

*Figure 7. Power conversion efficiency under AM 1.5 full sunlight irradiation intensities of P3HT/$C_{60}$ solar cells as a function of the time treated in solvent vapor at 25°C.*

the $C_{60}$ single crystals has been investigated by time-of-flight technique and the absolute values of the mobility of the holes and electrons in $C_{60}$ single crystals are 1.7±0.2 $cm^2/V{\cdot}s$ and 0.5±0.2 $cm^{-2}/V{\cdot}s$), respectively (*33*). Therefore, in the case of P3HT/$C_{60}$ films treated with chloroform, both the holes and electrons can transport in the induced $C_{60}$ crystals in the films, which resulted the higher hole mobility than that of the film without $C_{60}$ crystal treated with DCB vapor. Previous studies have shown that the addition of PCBM into PPV (*34*), MDMO-PPV (*35*), and a red polyfluorene (*36*) improves not only electron mobility but also hole mobility, which also indicated that the holes can transport in both the conducting polymer and PCBM phases. The decreases of the hole mobility of the films treated with chloroform vapor for more than 7 hrs (Figure 1) is due to that the $C_{60}$ large aggregates are formed and the the intersurface between the P3HT and $C_{60}$ is decreased. The results suggest that the crystallinity of both conducting polymer and $C_{60}$ as well as the phase size are essential to improve the efficiency for organic solar cells.

It has been noted that the color of the P3HT/$C_{60}$ film treated by chloroform and DCB vapors are also different. In the case of films treated by chloroform, the orange as-cast films changed gradually into brown red. Whereas the films treated by DCB changed gradually into purple. Figure 6 shows the UV-vis spectra of the P3HT/$C_{60}$ blend films treated with chloroform and DCB vapor for different time. The results show that the intensity of the vibronic absorption peaks at $\lambda$ = 600, 550, 510 nm (*37*), which come from the more ordered structure of P3HT (*32*), increases obviously with the time treated by solvent vapors. Similar phenomena have been found when the blend films were treated by thermal annealing (*14*). Whereas the absorption peaks of $C_{60}$ at $\lambda$ = 215, 262, and 340 nm decrease rapidly when the films were treated by DCB vapors for 5 hrs, which is probably attributed to two aspects as follows. (i) The reduced reflectivity derived from the increased

Downloaded by UNIV OF DELAWARE MORRIS LIB on June 22, 2012 | http://pubs.acs.org
Publication Date (Web): March 11, 2010 | doi: 10.1021/bk-2010-1034.ch009

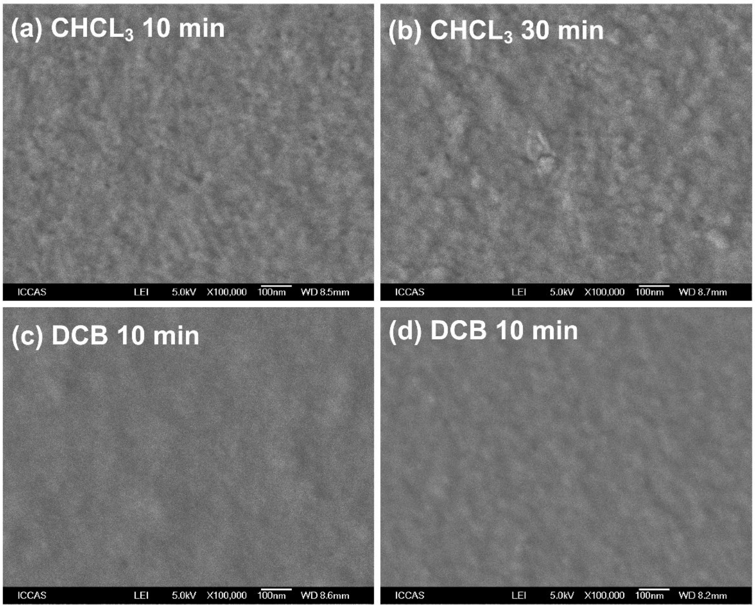
(a) CHCL3 10 min
ICCAS LEI 5.0kV X100,000 100nm WD 8.5mm
(b) CHCL3 30 min
ICCAS LEI 5.0kV X100,000 100nm WD 8.7mm
(c) DCB 10 min
ICCAS LEI 5.0kV X100,000 100nm WD 8.6mm
(d) DCB 10 min
ICCAS LEI 5.0kV X100,000 100nm WD 8.2mm

*Figure 8. SEM images of P3HT/$C_{60}$ (1/1 wt ratio) films treated with chloroform and DCB vapors at 40°C.*

roughness of the blends film after the DCB vapor treatment. The formation of P3HT nanowire gives a much rougher surface than the untreated film. (ii) The strength of the $C_{60}$ molecular transition assigned to 215, 262, and 340 nm was lower resulting from decrease of π-π interaction between P3HT and $C_{60}$ because of the phase separation of the two components. The above results indicate that the structure and morphology of the P3HT/$C_{60}$ blend films can be tailored by the treatment in different solvent vapors. The increased absorption in the range of 500-700nm could help to improve the harvesting of solar energy, which will lead to the higher photocurrent output.

Figure 7 shows a comparison of power conversion efficiency of as-cast and solvent-vapor treated solar cells. The devices efficiency increased markedly after both chloroform and DCB vapor treatment. When the P3HT/$C_{60}$ films were treated with chloroform vapor, the device efficiency first increases obviously with the treating time. The device efficiency reaches its maximum value at about 7 hrs and then decreases with treating time. Whereas when the P3HT/$C_{60}$ film was treated with DCB, the device efficiency increases with the treating time. Obviously, the interpenetration two-phase morphology enabled by P3HT or $C_{60}$ nanowires offers much better device performance resulting from far superior hole transport and increased light absorption. The dependence of the device efficiency on the treating time is similar to that of the hole mobility.

The influence of vapor treatment temperature on the morphology control of P3HT/$C_{60}$ film is also investigated under the vapor treatments by chloroform and DCB and the results are given in the supporting information. The results shows that in both cases the phase separation of the P3HT/$C_{60}$ film blend film

Downloaded by UNIV OF DELAWARE MORRIS LIB on June 22, 2012 | http://pubs.acs.org
Publication Date (Web): March 11, 2010 | doi: 10.1021/bk-2010-1034.ch009

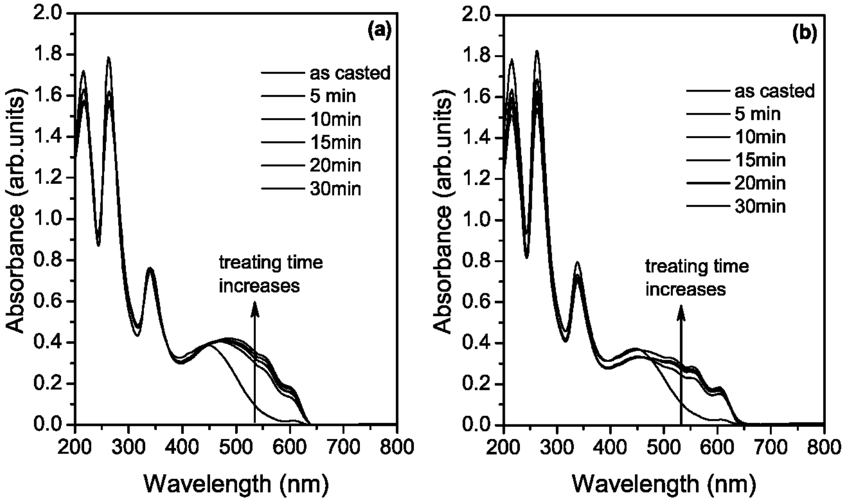

*Figure 9. UV-vis absorption spectra of the P3HT/$C_{60}$ films treated in chloroform vapor (a) and DCB (b) vapor at 40°C.*

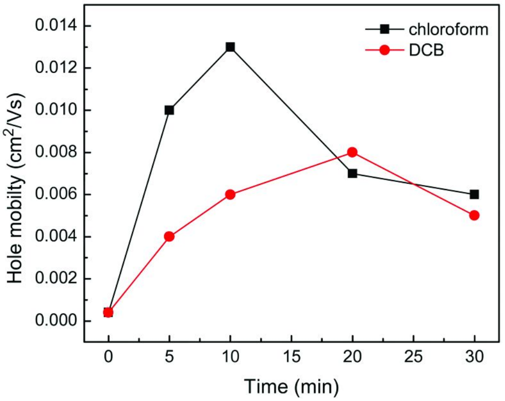

*Figure 10. The hole mobility of P3HT/$C_{60}$ films as a function of time treated in the chloroform and DCB vapor at 40°C.*

at 40°C is faster than that at 25°C, which leads to the less ordered morphology in the blend film (Figure 8). No nanowire structure is observed which maybe attribute to that the phase separation and aggregation of P3HT and $C_{60}$ are too fast to form dedicated crystalline nanowire structure at 40°C. Whereas the UV-Vis absorption spectra also show the similar results as those treated at 25°C due to the increased crystallinity and ordered structure of P3HT in the blend films (Figure 9). Moreover, both of the hole mobility of the blend films (Figure 10) and the device efficiency (Figure 11) first increase obviously with the treating time as that treated at 25°C. However, the hole mobility of the blend films and the device efficiency then decrease due to reduced intersurface caused by the formation of

Downloaded by UNIV OF DELAWARE MORRIS LIB on June 22, 2012 | http://pubs.acs.org
Publication Date (Web): March 11, 2010 | doi: 10.1021/bk-2010-1034.ch009

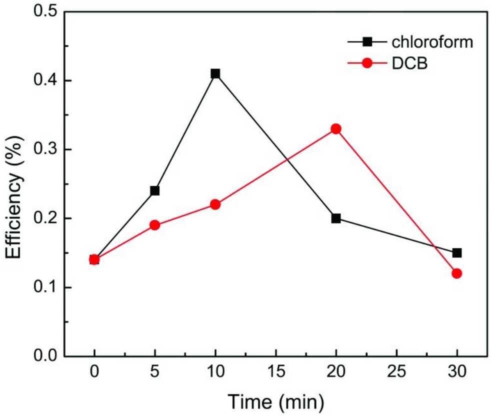

*Figure 11. Power conversion efficiency under AM 1.5 full sunlight irradiation intensities of P3HT/$C_{60}$ solar cells as a function of the time treated in solvent vapors at 40°C.*

large aggregates. These results indicate that lower treating temperature benefits the morphology control of P3HT/$C_{60}$ film.

## 4. Conclusions

Phase separation of P3HT/$C_{60}$ blend films were tailored by solvent vapor treatments and the hole mobility of the films was improved remarkably. When the films were treated with chloroform vapor, $C_{60}$ aggregates into crystalline nanowires and formed interconnect network in the P3HT matrix. Whereas P3HT nanowires interconnect network was formed without forming $C_{60}$ crystals when the films were treated with DCB vapor treatment. Both chloroform and DCB treatment resulted the obvious increase in charge mobility of the films and the absorption of the P3HT/$C_{60}$ films at 500-700nm. The hole mobility of the films treated with chloroform vapor is higher than that of the film treated with DCB vapor due to the ambipolar charge transport of $C_{60}$ crystals. The several-fold enhancement of device efficiency after solvent-vapor treatment is attributed to the better charge transport enabled by the nanowire network and increased light absorption resulting from crystalline of P3HT and $C_{60}$. The demonstrated ability to control the crystallinity of P3HT and $C_{60}$ using different solvent-vapor treatment opens a new route to obtain proper phase separating and 3-D network in P3HT/$C_{60}$ blends and better charge mobility to help improve efficiency of photovoltaic devices.

## Acknowledgments

Financial support of National Natural Scientific Foundation of China (NSFC Grant No. 50821062).

# References

1. Sivula, K.; Ball, Z. T.; Watanabe, N.; Frechet, J. M. J. *Adv. Mater.* **2006**, *18*, 206–210.
2. Li, G.; Shrotriya, V.; Huang, J. S.; Yao, Y.; Moriarty, T.; Emery, K.; Yang, Y. *Nat. Mater.* **2005**, *4*, 864–868.
3. Kim, J. Y.; Lee, K.; Coates, N. E.; Moses, D.; Nguyen, T. Q.; Dante, M.; Heeger, A. J. *Science* **2007**, *317*, 222–225.
4. Svensson, M.; Zhang, F. L.; Veenstra, S. C.; Verhees, W. J. H.; Hummelen, J. C.; Kroon, J. M.; Inganas, O.; Andersson, M. R. *Adv. Mater.* **2003**, *15*, 988–991.
5. Peet, J.; Kim, J. Y.; Coates, N. E.; Ma, W. L.; Moses, D.; Heeger, A. J.; Bazan, G. C. *Nat. Mater.* **2007**, *6*, 497–500.
6. Hou, J. H.; Tan, Z. A.; Yan, Y.; He, Y. J.; Yang, C. H.; Li, Y. F. *J. Am. Chem. Soc.* **2006**, *128*, 4911–4916.
7. Campoy-Quiles, M.; Ferenczi, T.; Agostinelli, T.; Etchegoin, P. G.; Kim, Y.; Anthopoulos, T. D.; Stavrinou, P. N.; Bradley, D. D. C.; Nelson, J. *Nat. Mater.* **2008**, *7*, 158–164.
8. Yang, X.; Loos, J. *Macromolecules* **2007**, *40*, 1353–1362.
9. Wang, W. L.; Wu, H. B.; Yang, C. Y.; Luo, C.; Zhang, Y.; Chen, J. W.; Cao, Y. *Appl. Phys. Lett.* **2007**, *90*.
10. Loi, M. A.; Toffanin, S.; Muccini, M.; Forster, M.; Scherf, U.; Scharber, M. *Adv. Funct. Mater.* **2007**, *17*, 2111–2116.
11. Chen, C. P.; Chan, S. H.; Chao, T. C.; Ting, C.; Ko, B. T. *J. Am. Chem. Soc.* **2008**, *130*, 12828–12833.
12. Shaheen, S. E.; Brabec, C. J.; Sariciftci, N. S.; Padinger, F.; Fromherz, T.; Hummelen, J. C. *Appl. Phys. Lett.* **2001**, *78*, 841–843.
13. Li, L. G.; Lu, G. H.; Yang, X. N. *J. Mater. Chem.* **2008**, *18*, 1984–1990.
14. Yang, X. N.; Loos, J.; Veenstra, S. C.; Verhees, W. J. H.; Wienk, M. M.; Kroon, J. M.; Michels, M. A. J.; Janssen, R. A. J. *Nano Lett.* **2005**, *5*, 579–583.
15. Yu, G.; Gao, J.; Hummelen, J. C.; Wudl, F.; Heeger, A. J. *Science* **1995**, *270*, 1789–1791.
16. Mihailetchi, V. D.; Xie, H. X.; de Boer, B.; Popescu, L. M.; Hummelen, J. C.; Blom, P. W. M.; Koster, L. J. A. *Appl. Phys. Lett.* **2006**, *89*, 012107.
17. Kim, K.; Liu, J. W.; Carroll, D. L. *Appl. Phys. Lett.* **2006**, *88*, 181911.
18. Lu, G.; Li, L.; Yang, X. *Small* **2008**, *4*, 601–606.
19. Berson, S.; De Bettignies, R.; Bailly, S.; Guillerez, S. *Adv. Funct. Mater.* **2007**, *17*, 1377–1384.
20. Yang, X. N.; Lu, G. H.; Li, L. G.; Zhou, E. L. *Small* **2007**, *3*, 611–615.
21. Zhou, E. J.; Tan, Z.; Yang, Y.; Huo, L. J.; Zou, Y. P.; Yang, C. H.; Li, Y. F. *Macromolecules* **2007**, *40*, 1831–1837.
22. Lide, D. R.; Frederikse, H. P. R. *CRC Handbook of Chemistry and Physics*; 76th ed.; CRC Press, Inc.: New York, 1995.
23. Tu, G.; Bilge, A.; Adamczyk, S.; Forster, M.; Heiderhoff, R.; Balk, L. J.; Muhlbacher, D.; Morana, M.; Koppe, M.; Scharber, M. C.; Choulis, S. A.; Brabec, C. J.; Scherf, U. *Macromol. Rapid Commun.* **2007**, *28*, 1781–1785.

Downloaded by UNIV OF DELAWARE MORRIS LIB on June 22, 2012 | http://pubs.acs.org
Publication Date (Web): March 11, 2010 | doi: 10.1021/bk-2010-1034.ch009

24. Xin, H.; Kim, F. S.; Jenekhe, S. A. *J. Am. Chem. Soc.* **2008**, *130*, 5424–5425.
25. Dante, M.; Peet, J.; Nguyen, T. Q. *J. Phys. Chem. C* **2008**, *112*, 7241–7249.
26. Parmer, J. E.; Mayer, A. C.; Hardin, B. E.; Scully, S. R.; McGehee, M. D.; Heeney, M.; McCulloch, I. *Appl. Phys. Lett.* **2008**, *92*, 113309.
27. Li, G.; Shrotriya, V.; Yao, Y.; Huang, J. S.; Yang, Y. *J. Mater. Chem.* **2007**, *17*, 3126–3140.
28. Kiss, I. Z.; Mandi, G.; Beck, M. T. *J. Phys. Chem. A* **2000**, *104*, 8081–8088.
29. Miyazawa, K.; Kuwasaki, Y.; Obayashi, A.; Kuwabara, M. *J. Mater. Res.* **2002**, *17*, 83–88.
30. Lu, G. H.; Li, L. G.; Yang, X. N. *Adv. Mater.* **2007**, *19*, 3594–3598.
31. Lu, G. H.; Li, L. G.; Yang, X. N. *Macromolecules* **2008**, *41*, 2062–2070.
32. Zhao, Y.; Xie, Z. Y.; Qu, Y.; Geng, Y. H.; Wang, L. X. *Appl. Phys. Lett.* **2007**, *90*, 043504.
33. Frankevich, E.; Maruyama, Y.; Ogata, H. *Chem. Phys. Lett.* **1993**, *214*, 39–44.
34. Mihailetchi, V. D.; Koster, L. J. A.; Blom, P. W. M.; Melzer, C.; de Boer, B.; van Duren, J. K. J.; Janssen, R. A. J. *Adv. Funct. Mater.* **2005**, *15*, 795–801.
35. Tuladhar, S. M.; Poplavskyy, D.; Choulis, S. A.; Durrant, J. R.; Bradley, D. D. C.; Nelson, J. *Adv. Funct. Mater.* **2005**, *15*, 1171–1182.
36. Pacios, R.; Bradley, D. D. C.; Nelson, J.; Brabec, C. J. *Synth. Met.* **2003**, *137*, 1469–1470.
37. Moule, A. J.; Meerholz, K. *Adv. Mater.* **2008**, *20*, 240–245.

Downloaded by UNIV OF DELAWARE MORRIS LIB on June 22, 2012 | http://pubs.acs.org
Publication Date (Web): March 11, 2010 | doi: 10.1021/bk-2010-1034.ch009

Downloaded by PENNSYLVANIA STATE UNIV on June 22, 2012 | http://pubs.acs.org
Publication Date (Web): March 11, 2010 | doi: 10.1021/bk-2010-1034.ch010

## Chapter 10

# Quantum Dots in Polymer Films for Light Selectivity

**William Z. Xu and Paul A. Charpentier***

**Department of Chemical and Biochemical Engineering, Faculty of Engineering, University of Western Ontario, London, Ontario, Canada N6A 5B9**
***pcharpentier@eng.uwo.ca**

By taking advantage of the spectral properties of quantum dots (QDs), QD-poly(ethylene-co-vinyl acetate) (PEVA) nanocomposites were synthesized using supercritical carbon dioxide (sc$CO_2$). As a very promising copolymer, PEVA has been widely applied in various fields including photovoltaic encapsulation. In order to effectively apply sc$CO_2$ for the synthesis of QD-PEVA nanocomposite films, the reactivity ratios of ethylene and vinyl acetate were determined using in situ FTIR. For the QD synthesis, both CdS and CdS-ZnS core-shell QDs were synthesized by means of the pyrolysis of single molecular precursors, then functionalized with a methoxysilane group, which were subsequent attached to PEVA chains in sc$CO_2$ using sol-gel chemistry. The synthesized QD-PEVA nanofilms displayed significant absorption in the UV and violet regions of the electromagnetic spectrum, while providing a characteristic emission in the region from orange to red light. These QD-polymer nanofilms have potential applications in sunlight conversion.

## Introduction

Converting higher-energy UV irradiation from solar light into desirable lower-energy light is of significant scientific and industrial interest (*1*). Potentially, polymer films can be tailored for various applications such as in energy

In Functional Polymer Nanocomposites for Energy Storage and Conversion; Wang, Q., et al.;
ACS Symposium Series; American Chemical Society: Washington, DC, 2010.

Downloaded by PENNSYLVANIA STATE UNIV on June 22, 2012 | http://pubs.acs.org
Publication Date (Web): March 11, 2010 | doi: 10.1021/bk-2010-1034.ch010

conversion processes such as solar cell coatings, window coatings, or greenhouses for heat and sunlight control. Semiconducting nanocrystalline quantum dots (QDs) provide this ability and are being explored in a variety of fields such as nanobiotechnology (*2*, *3*) and solar cell technology (*4*). When the QDs are irradiated by light from an excitation source to reach their respective excited states, they emit photons corresponding to their respective energy band gaps. The advantages of QDs over conventional organic fluorescent dyes include large absorption bands, narrow spectral emission bands, and photochemical stability (*5*). Furthermore, the band gaps of quantum dots can be tailored by changing the type of QDs, e.g., CdS, CdSe and CdTe, and/or the size, which are tunable by controlling the reaction conditions such as time and temperature (*6–8*). By incorporation of QDs into a polymer matrix, one can potentially synthesize light-selective polymeric nanofilms.

Due to their nanosize dimensions, the colloidal QDs must be stabilized by an outer layer of organic ligands. These ligands dictate the surface chemistry of the QDs, and therefore play a key role in the miscibility within a polymer (*9*). As the high-temperature synthesis of QDs is not compatible with most organic functional groups, ligand exchange is often required for the introduction of surface functionality to the QDs. Ligand exchange with various thiol ligands has been extensively studied (*10–13*). Compatible organic ligands with polymer matrices, such as bifunctional molecules containing a coordination "head" and a polymerizable "tail", enable the applications of QDs in polymer composites (*14*). Bawendi *et al* (*9*) reported a family of oligomeric phosphine ligands allowing tunable compatibility in diverse environments and flexibility for further chemistry. In their study, tris(hydroxypropyl)phosphine (THPP) was reacted with diisocyanatohexane (DIH) to produce oligomerized THPP that was further functionalized with molecules containing an isocyanate group and an additional functional group such as methacrylate group which enabled copolymerization of QDs with many monomers.

Several polymers are of interest for solar applications including conductive melt processible polymers for energy transport and optically transparent polymers for films and coatings (*15*, *16*). Poly(ethylene-co-vinyl acetate) (PEVA) is a polyolefin copolymer which resembles polyethylene but has considerably increased flexibility, with lower crystallinity suitable for transparent films. PEVA copolymers containing 2~18% VAc are well-recognized materials in the film industry and are widely used as an encapsulating resin for silicon based photovoltaic (PV) devices providing mechanical support, electrical isolation, and protection against environmental exposure (*17*). Some of the grades are also used for hot-melt adhesive applications that are of significant interest for solar applications.

The physical and mechanical properties of PEVA depend primarily on the vinyl acetate (VAc) content and the polymerization process. The VAc content has a significant effect on the crystallinity, flexibility, and elastomeric properties of the copolymer with increasing VAc content leading to the PEVA copolymer becoming softer and more transparent. Although the reactivity ratios of copolymerization of ethylene and vinyl acetate were previously studied under various reaction conditions (*18*), they have not been examined in the green

Downloaded by PENNSYLVANIA STATE UNIV on June 22, 2012 | http://pubs.acs.org
Publication Date (Web): March 11, 2010 | doi: 10.1021/bk-2010-1034.ch010

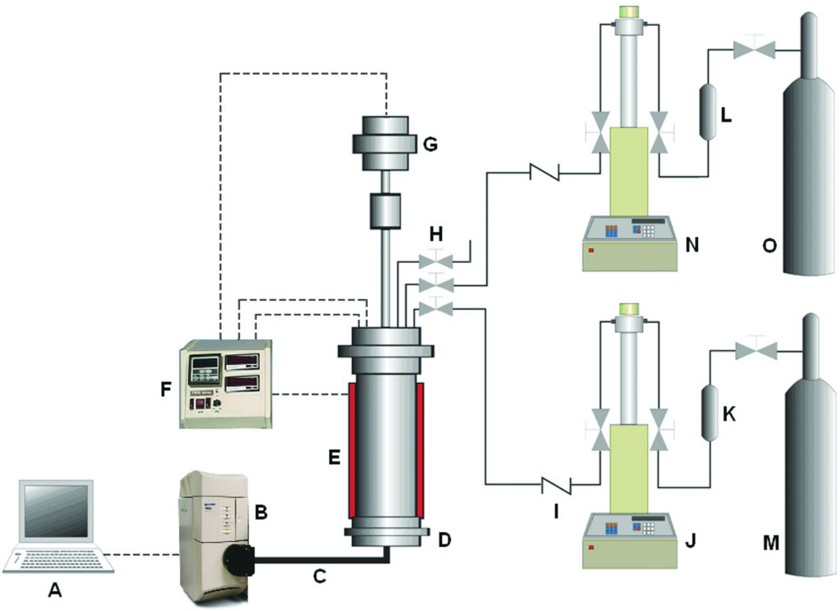

*Figure 1. Schematic diagram of experimental setup. (A) Computer; (B) FTIR; (C) K4 conduit; (D) 100-mL stainless steel autoclave equipped with IR probe; (E) heating mantle; (F) Parr 4842 temperature and stirring speed controller with pressure display; (G) stirrer; (H) needle valve; (I) check valve; (J) ISCO 260D syringe pump; (K) & (L) purification columns; (M) $CO_2$ cylinder; (N) ISCO 100DX syringe pump; (O) ethylene cylinder.*

solvent, supercritical carbon dioxide ($scCO_2$). $ScCO_2$ has emerged as a viable "green" alternative to organic solvents (*19*, *20*) as $CO_2$ is inexpensive, non-toxic, non-flammable, and environmentally benign (*21*). In the supercritical state ($T_c$= 31.1 °C, $P_c$ = 7.38 MPa), it can have unique properties such as a liquid-like density, gas-like diffusivity, and "zero surface tension" with these properties "tunable" by varying the pressure and/or temperature (*22*). DeSimone and coworkers have shown that $scCO_2$ is a promising alternative medium for free-radical, cationic, and step-growth polymerizations, and continuous processes (*21*, *23*, *24*). In addition, polymerization in $scCO_2$ provides the ability to produce new desirable properties in the polymer, including enhanced free volume for increased loading of nanoparticles (*25*).

The goal of this research was to explore the possibility of synthesis of PEVA and PEVA-based nanocomposites containing QDs using $scCO_2$. Particularly, by incorporating QDs into a PEVA matrix, it was expected to synthesize light-selective PEVA films, expanding the application of PEVA to new areas for light and heat selective films. In order to effectively control and tailor the copolymers with desired composition, the reactivity ratios of ethylene and vinyl acetate in $scCO_2$ were measured by means of in situ FTIR. To make light-selective PEVA films, CdS-ZnS core-shell QDs and CdS QDs were synthesized at a relatively low temperature, functionalized with a methoxysilane group, and then

Downloaded by PENNSYLVANIA STATE UNIV on June 22, 2012 | http://pubs.acs.org
Publication Date (Web): March 11, 2010 | doi: 10.1021/bk-2010-1034.ch010

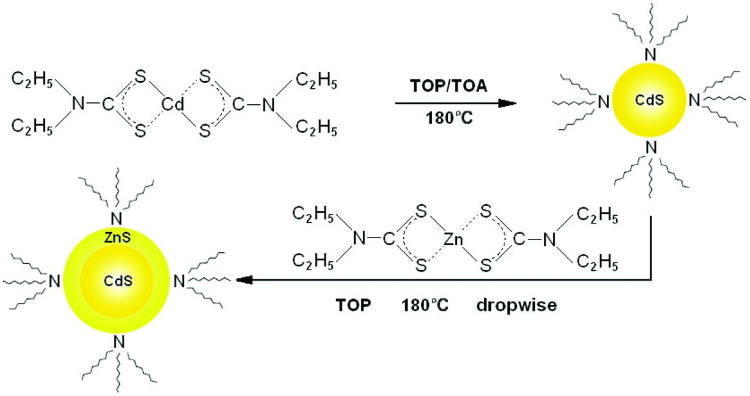

*Scheme 1. Synthesis of CdS-ZnS core-shell QDs*

incorporated into poly(vinyl acetate) (PVAc) and PEVA matrices by means of hydrolysis/condensation in $scCO_2$.

# Experimental

## Materials

Instrument grade $CO_2$ (99.99% purity from Praxair Canada Inc., with dip-tube), polymer grade ethylene (99.9% purity, Praxair), and ultra high-purity $N_2$ (99.99%, Praxair) were further purified by passing through columns filled with 5 Å molecular sieves and reduced 20% copper oxide/$Al_2O_3$ to remove the moisture and oxygen, respectively. Argon (99.999% purity, Praxair) was used without further purification. Vinyl acetate (VAc) (>99%) purchased from Sigma-Aldrich Canada was further purified by passing through an inhibitor removal column (Aldrich) to remove hydroquinone. 1,2,4-Trichlorobenzene (TCB) (>99%), (3-mercaptopropyl)trimethoxysilane (MPTMO), tetrahydrofuran (THF) (≥99.9%) (CHROMASOLV® Plus), tetraethyl orthosilicate (TEOS) (98%), tetramethyl orthosilicate (TMOS) (98%), vinyltrimethoxysilane (VTMO) (97%), pentane (≥99%) (DriSolv®), zinc diethyldithiocarbamate (98%), glacial acetic acid (≥99.99%), trioctylamine (TOA) (≥99.0%) (Fluka), trioctylphosphine (TOP) (≥90%) (Fluka), anhydrous methanol (99.8%), and toluene (≥99.9%) (CHROMASOLV® Plus) were purchased from Sigma-Aldrich Canada and used as received. Anhydrous ethyl alcohol was purchased from Commercial Alcohols, Inc., Canada and used as received. Bis(diethyldithiocarbamato) cadmium (II), and the initiator diethyl peroxydicarbonate (DEPDC) were synthesized as previously described (*26*, *27*).

Downloaded by PENNSYLVANIA STATE UNIV on June 22, 2012 | http://pubs.acs.org
Publication Date (Web): March 11, 2010 | doi: 10.1021/bk-2010-1034.ch010

## Experimental Setup

Figure 1 displays the experimental setup, comprising a 100-mL high-pressure stainless steel autoclave coupled with a digital pressure transducer and a temperature controller. The stirring speed was controlled at 300 rpm. In situ FTIR was mounted at the bottom of the autoclave to monitor the reactions using a high-pressure immersion probe (Sentinel-Mettler Toledo AutoChem). The DiComp ATR probe consists of a diamond wafer, a gold seal, a ZnSe support/focusing element, housed in alloy C-276. The probe was attached to an FTIR spectrometer (Mettler Toledo AutoChem ReactIR 4000) via a mirrored optical conduit, connected to a computer, supported by ReactIR 2.21 software (MTAC). Spectra were recorded at a resolution of 2 $cm^{-1}$ and the absorption spectra were the results of 32 scans.

## Copolymerization of Ethylene and Vinyl Acetate

The copolymerizations were carried out at 50±1 or 72±1 °C, and 27.6±0.3 or 13.8±0.3 MPa in the 100-mL autoclave. Vinyl acetate and initiator DEPDC were charged into the reactor, purged with a flow of argon, then ethylene and $CO_2$ were pumped into the autoclave by means of syringe pumps (Isco 100DX and Isco 260D, respectively). The amount of ethylene and $CO_2$ injected into the reactor was determined by measuring the pressure and volume dispensed from the syringe pumps, with the density obtained from equations of state (*28*, *29*).

## Preparation of CdS-ZnS and CdS QDs

Synthesis of CdS-ZnS core-shell QDs were carried out as shown in Scheme 1. 25 mL TOA and a magnetic stirring bar were placed in a 100-mL three-neck flask under nitrogen equipped with a reflux condenser, a thermometer, and a thermocouple for automatic temperature control. When the temperature was stable at 180 °C, a solution of 0.5 g $Cd[S_2CN(C_2H_5)_2]_2$ in 9 mL TOP was rapidly injected into the flask. After 5 min reaction, a solution of 0.2 g $Zn[S_2CN(C_2H_5)_2]_2$ in 3 mL TOP was slowly added dropwise. 5 min after the completion of addition of the zinc diethyldithiocarbamate solution, the heater was removed to cool down the reaction mixture. When the temperature dropped to ca. 75 °C, a large excess of methanol/ethyl alcohol was added followed by separation of the quantum dots through centrifugation. The QDs were washed with methanol, and then dispersed into toluene. The mixture of QDs in toluene was further filtered under vacuum to remove any insoluble material (poorly capped and large particles).

For the synthesis of CdS QDs, the procedure was carried out in the same manner as the synthesis of CdS-ZnS core-shell QDs described above, except a higher temperature (235 °C), longer reaction time (30 min), and no addition of $Zn[S_2CN(C_2H_5)_2]_2$ were utilized.

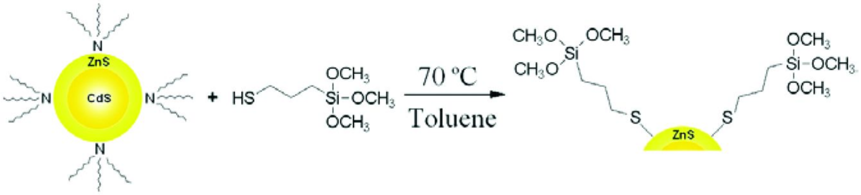

Scheme 2. *Ligand exchange of CdS-ZnS core-shell QDs*

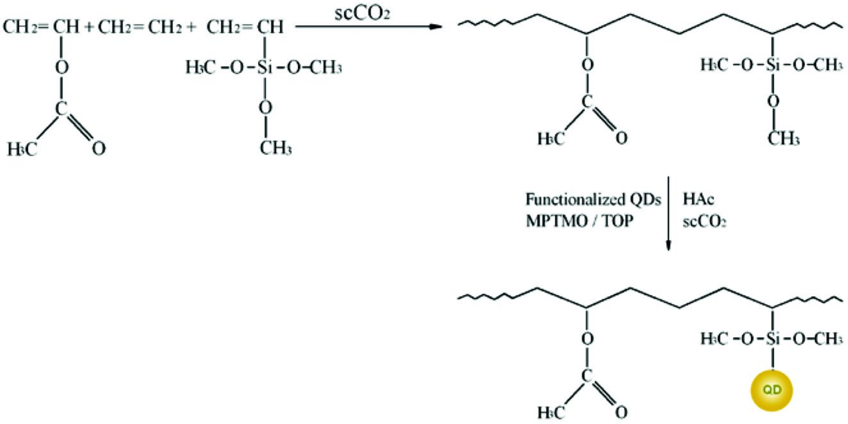

Scheme 3. *2-step synthesis of QD-PEVA nanofilm in scCO₂*

Downloaded by PENNSYLVANIA STATE UNIV on June 22, 2012 | http://pubs.acs.org
Publication Date (Web): March 11, 2010 | doi: 10.1021/bk-2010-1034.ch010

## Ligand Exchange of QDs

The synthesized QDs were subsequently ligand exchanged with 5 mM MPTMO with stirring at 70 °C for 24 hours under a nitrogen flow, as shown in Scheme 2. After the reaction, the reaction mixture was cooled to ambient temperature. Then a large excess of pentane was added into the mixture followed by separation of the QDs through centrifugation. The separated quantum dots were re-dispersed into 40 mL of toluene, and then 5 mM MPTMO was added. The mixture was refluxed with stirring under a nitrogen flow at 70 °C for 24 hours. This procedure was repeated several times. After centrifugation, the surface-displaced QDs were dispersed in toluene.

## Synthesis of QD-PEVA Nanofilms

The synthesis of QD-PEVA nanofilms was carried out using a two-step method (Scheme 3). A poly(ethylene-vinyl acetate-VTMO) terpolymer (1 g), QD solution (1 g 0.39 wt% in toluene), HAc(0.005 mol), toluene (2.2 g), and MPTMO (0.04 g) were introduced into the 100-mL autoclave, with TOP(0.06

Downloaded by PENNSYLVANIA STATE UNIV on June 22, 2012 | http://pubs.acs.org
Publication Date (Web): March 11, 2010 | doi: 10.1021/bk-2010-1034.ch010

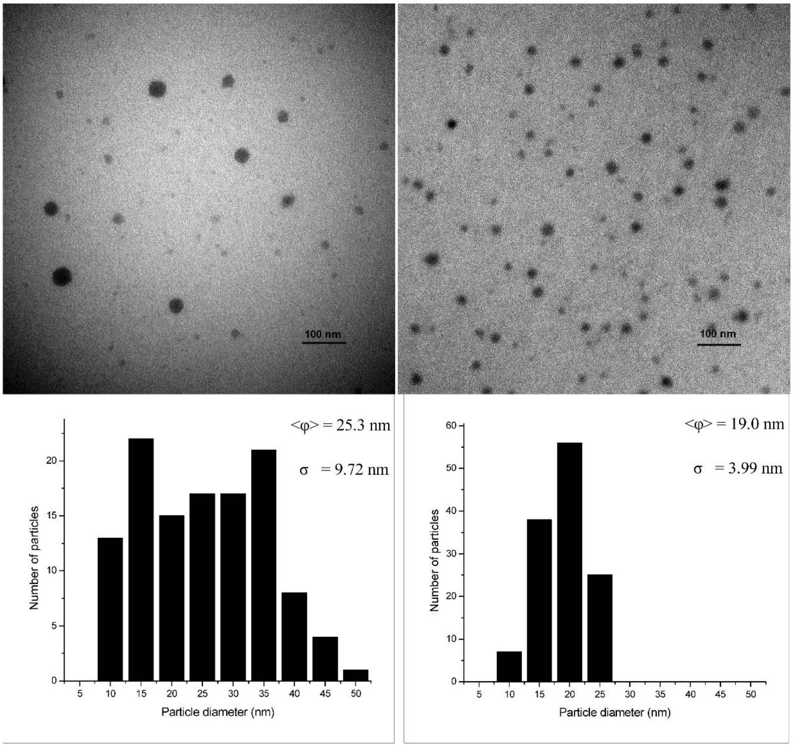

*Figure 2. TEM images and particle size distribution histograms of the $SiO_2$-PVAc nanocomposites from the one-pot synthesis in $scCO_2$ using TMOS (left) / TEOS (right) (the experimental conditions: T = 60 °C, P = 16.8 MPa, molar ratio: VAc : VTMO : HAc : TMOS : DEPDC = 40 : 1 : 43 : 10 : 1). (Reproduced with permission from reference (25). Copyright 2007 The Royal Society of Chemistry.)*

g) being optionally added, followed by pumping $CO_2$ into the autoclave by the syringe pump (Isco 260D). The reaction was carried out at 50 or 80 °C under 27.6 MPa for 2 or 20 hours for the synthesis of CdS-ZnS QD-PEVA nanofilms and at 50 °C under 27.6 MPa for 2 hours for the synthesis of CdS QD-PEVA nanofilms. After the reaction, $CO_2$ was carefully vented leaving the formed sample in the autoclave. The solid product was collected from the reactor and subsequently dried under vacuum at 60 °C overnight.

## Characterization

Photoluminescence (PL) spectra were recorded on a Photon Technology International QuantaMaster™. UV-Vis absorption spectra were measured on a Cary Varian UV-VIS spectrophotometer or a Shimadzu UV-3600 UV-VIS-NIR spectrophotometer. Transmission electron microscopy (TEM) images were recorded using a Philips CM10 transmission electron microscope operated at 80 kV. The specimens were previously dissolved in toluene or THF, and then

Downloaded by PENNSYLVANIA STATE UNIV on June 22, 2012 | http://pubs.acs.org
Publication Date (Web): March 11, 2010 | doi: 10.1021/bk-2010-1034.ch010

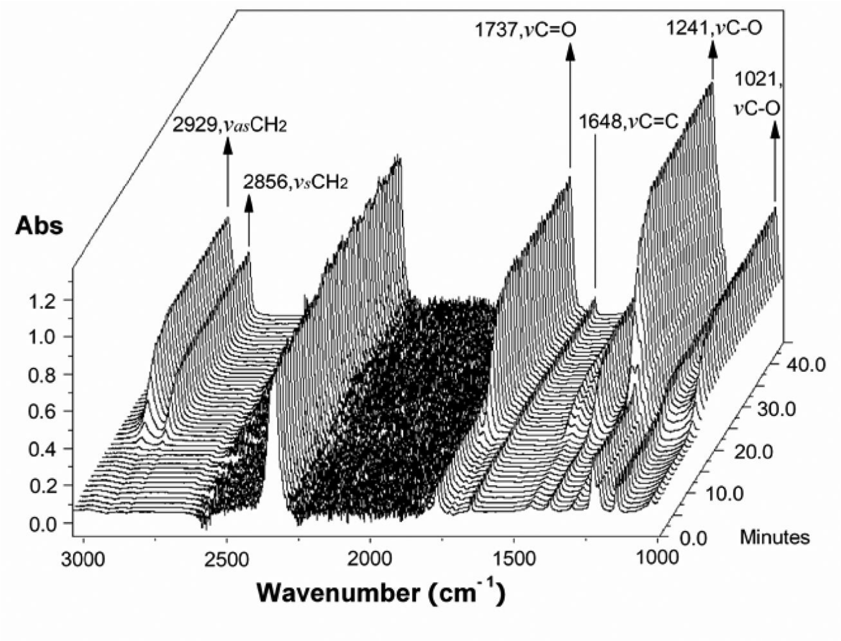

*Figure 3. In situ FTIR waterfall plot of the copolymerization of ethylene and VAc in scCO$_2$ (the experimental conditions: T=50°C, P=27.6MPa, ethylene mole fraction in feed: 0.887).*

placed on a copper grid covered with carbon film. High resolution transmission electron microscopy (HRTEM) images were recorded using a JEOL 2010F FEG TEM/STEM operated at 200 kV. The images were taken with the Gatan Tridium spectrometer with a 2048 × 2048 CCD array. The in situ ATR-FTIR was applied to monitor the various chemistries studied including: (1) the copolymerization of ethylene and VAc in scCO$_2$, (2) the CdS-ZnS QDs before and after ligand exchange, and (3) the synthesis of QD-polymer nanofilms.

## Results and Discussion

### Polymer Nanocomposite Synthesis Using ScCO$_2$

In addition to being a green solvent, supercritical carbon dioxide (scCO$_2$) is also an enabling agent for the synthesis of nanoparticles and polymer nanocomposites (*25*). Initial proof-of-concept experiments examined parallel reactions of free-radical polymerization chemistry along with sol-gel chemistry. Figure 2 shows TEM images of the resulting SiO$_2$-poly(vinyl acetate) (PVAc) nanocomposites formed from a one-pot synthesis in scCO$_2$ using TMOS and TEOS, respectively, where copolymerization of VAc and VTMO and hydrolysis of TMOS or TEOS took place simultaneously. One significant advantage of scCO$_2$ in this synthesis of polymer nanocomposites is the uniform dispersion of nano-$SiO_2$ into the PVAc matrices. $SiO_2$ is transparent as described below, although can have excellent heat transfer capabilities (high R value) due to its aerogel structure (*30*).

## Copolymerization of Ethylene and VAc in $ScCO_2$

As described in the introduction, PEVA is a flexible polymer utilized as a photovoltaic encapsulant. In order to synthesize PEVA-based nanocomposites of quantum dots using $scCO_2$, it is firstly necessary to obtain the reactivity ratios for the copolymerization of ethylene and VAc under similar experimental conditions. These reactivity ratios provide how much of the monomers ethylene and vinyl acetate are integrated into the PEVA copolymer, influencing both the transparency and the polymers glass transition temperature ($T_g$). In situ FTIR was utilized for this determination of the reactivity ratios under the high-pressure experimental conditions. Figure 3 displays a typical in situ FTIR waterfall plot of the copolymerization of ethylene and VAc in $scCO_2$ at the early stages of the copolymerization. Normally, while performing kinetic analysis on copolymerizations, the consumption of the monomers is monitored. However, while following this copolymerization in $scCO_2$, the consumption of ethylene could not be monitored due to its infrared-inactive $\nu$C=C peak. Although the consumption of VAc could be followed from the characteristic $\nu$C=C peak (1648 $cm^{-1}$), this peak was rather small. By analyzing the spectra, the absorbance intensities increased quickly during the first several minutes at 2929, 2856, 1737, 1241 and 1021 $cm^{-1}$, which are attributed to the formation of copolymers. The growing PEVA peaks provide useful and reliable information on the composition of the formed copolymers at low conversions, from which the reactivity ratios can be determined.

By using the Mayo-Lewis equation, the reactivity ratios were calculated using both the non-linear least-square and the Kelen-Tudos (*31*) methods. The reactivity ratios of both ethylene and VAc decrease slightly with increasing temperature from 50 to 72 °C and increase with pressure (*32*). As the reactivity ratios of both ethylene and VAc change in the same direction when varing the reaction temperature and pressure, the copolymer composition for the same monomer feed composition varies only slightly under the experimental conditions, as seen in Figure 4.

The small degree of dependence of reactivity ratios on temperature/pressure that was experimentally observed might be due in part to the variation of solvent nature with these variables, as reflected by the changing density (0.854, 0.756, and 0.665 g/ml at 50 °C 27.6 MPa, 72 °C 27.6 MPa, and 50 °C 13.8 MPa, respectively (*29*)). The effect of solvent on the copolymerization of ethylene and vinyl acetate was studied by Van der Meer *et al* (*33*) at 62 °C and 3.4 MPa who found that solvents of higher polarity or stronger interaction with VAc resulted in higher $r_{ethylene}$ and lower $r_{VAc}$ values. Our experimental results are in good agreement with this finding, with lower $r_{ethylene}$ and higher $r_{VAc}$ values being observed when the non-polar $scCO_2$ was used as solvent in the present study. Supercritical $CO_2$ is well known to be a good solvent for most low molar mass non-polar and some polar

Downloaded by PENNSYLVANIA STATE UNIV on June 22, 2012 | http://pubs.acs.org
Publication Date (Web): March 11, 2010 | doi: 10.1021/bk-2010-1034.ch010

molecules (i.e. our monomers and initiator) (*34*), but it is a poor solvent for most high molar mass polymers under mild conditions (*21*). With a good understanding of the monomer reactivity in the copolymerization in scCO$_2$, subsequent efforts were devoted to the synthesis of QD-PEVA nanofilms using scCO$_2$.

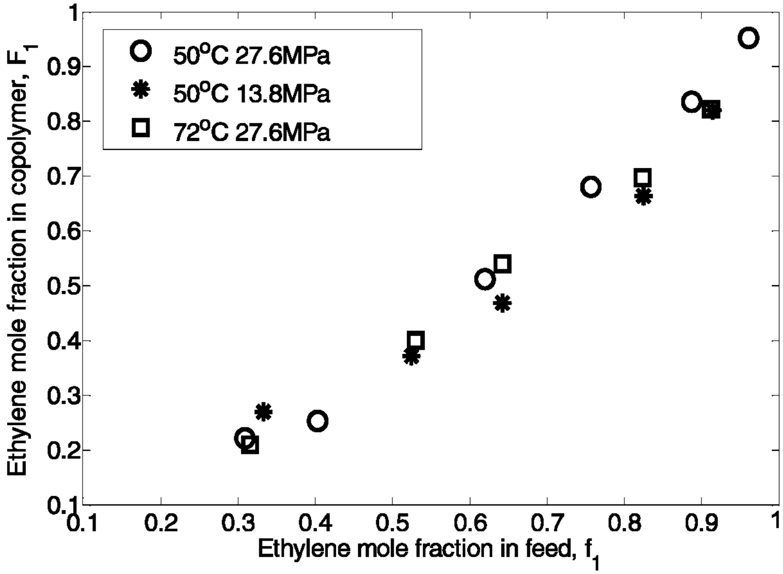

*Figure 4. Copolymer composition versus feed composition for different reaction temperature and pressure conditions in scCO$_2$. (Reproduced with permission from reference (32). Copyright 2009 American Chemical Society.)*

## Synthesis of QD-PEVA Nanofilms

There were three steps involved for the synthesis of QD-PEVA nanofilms, including synthesis of QDs, ligand exchange of QDs, and incorporation of functionalized QDs into PEVA matrix.

### *Synthesis of Quantum Dots (QDs)*

Core-shell QDs (CdS-ZnS) were synthesized by pyrolysis of the single-molecular precursor bis(diethyldithiocarbamato) cadmium (II) and zinc diethyldithiocarbamate, as described earlier in Scheme 1. Figure 5 displays the TEM images of both the synthesized core-shell CdS-ZnS and "bare" CdS QDs, where nanoparticles are clearly observed. HRTEM was also used for the characterization of both the core-shell CdS-ZnS and CdS QDs (*26*). It was found that both the "bare" and core-shell QDs presented nanocrystal structure, with a clear difference between the two types of QDs. The nanocrystal structure of the CdS QDs appears to be more uniform and regular than that of the CdS-ZnS

Downloaded by PENNSYLVANIA STATE UNIV on June 22, 2012 | http://pubs.acs.org
Publication Date (Web): March 11, 2010 | doi: 10.1021/bk-2010-1034.ch010

Downloaded by PENNSYLVANIA STATE UNIV on June 22, 2012 | http://pubs.acs.org
Publication Date (Web): March 11, 2010 | doi: 10.1021/bk-2010-1034.ch010

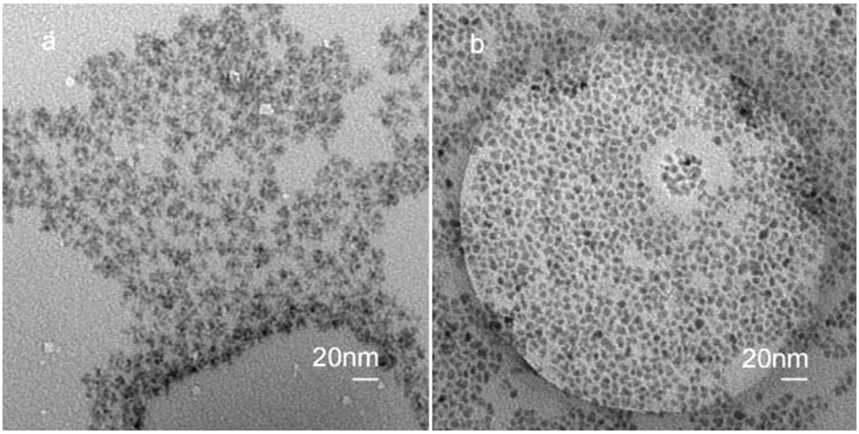

*Figure 5. TEM images of the synthesized QDs. (a) CdS-ZnS QDs, (b) CdS QDs. (The experimental conditions are: for CdS-ZnS core-shell QDs, 180 °C, 5 min for core growth; for CdS QDs, 235 °C, 30 min).*

QDs. The d-spacing of the CdS QDs was measured to be approximately 4.5 Å while the CdS-ZnS QDs have a d-spacing value of approximately 3.5 Å (*26*). The slight "bending" of the lattice fringes of some CdS-ZnS QDs suggests that strain exists in the core-shell structure, as also observed by Bawendi and coworkers for CdSe-ZnS QDs (*35*).

### *Ligand Exchange of QDs*

In order to chemically link the QDs to the polymer chains, the surrounding alkyl group of the QDs has to be modified. MPTMO was chosen for the ligand exchange of the synthesized QDs as it has the required functionality with a thiol head that can coordinate with zinc or cadmium to stabilize the QDs, while the methoxysilane tail can be used for subsequent reaction to attach the QDs to the polymer chains (see Scheme 2).

To examine if the ligand exchange proceeded successfully, the QDs before and after ligand exchange were characterized by several techniques including EDX elemental analysis, HRTEM, FTIR, and solubility testing. As an example, the FTIR spectra of the CdS-ZnS QDs before and after the ligand exchange were collected and displayed in Figure 6. From the spectra, the dominant peaks from the TOA alkyl groups observed at 2954 ($v_{as}CH_3$), 2923($v_{as}CH_2$), 2871($v_sCH_3$), 2853($v_sCH_2$), 1466($\delta_sCH_2$ & $\delta_{as}CH_3$), and 723 cm$^{-1}$ ($\rho CH_2$) disappear after the ligand exchange, while new peaks are formed from the ligand exchange at 2926($v_{as}CH_2$ & $v_{as}CH_3$), 2842($v_sCH_2$ & $v_sCH_3$), 1191($\rho CH_3$), 1087($v_{as}$Si-O-C), and 813 cm$^{-1}$($v_s$Si-O-C) (*36*). This FTIR data shows clearly that ligand exchange occurred.

Downloaded by PENNSYLVANIA STATE UNIV on June 22, 2012 | http://pubs.acs.org
Publication Date (Web): March 11, 2010 | doi: 10.1021/bk-2010-1034.ch010

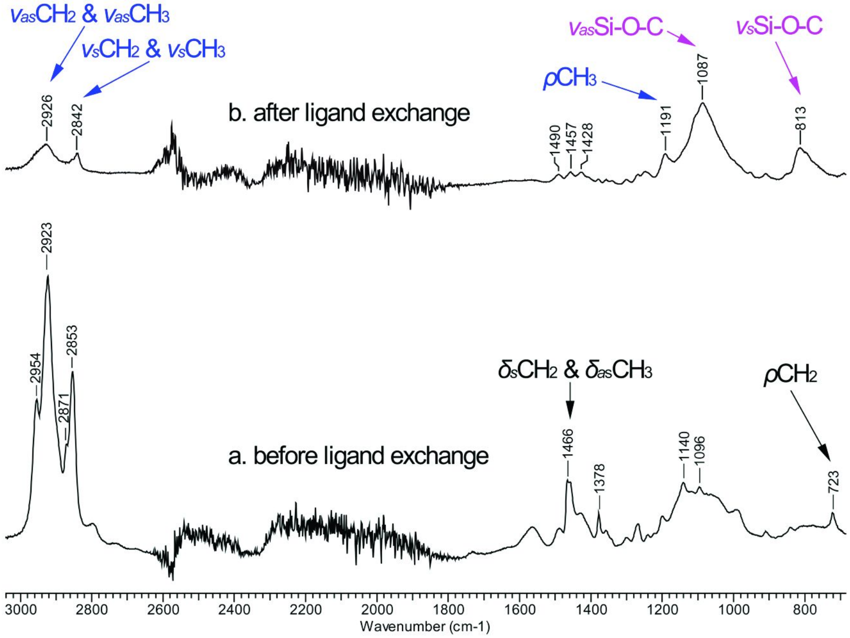

*Figure 6. FTIR spectra of the CdS-ZnS QDs before and after ligand exchange. (Reproduced with permission from reference (26). Copyright 2009 American Chemical Society.)*

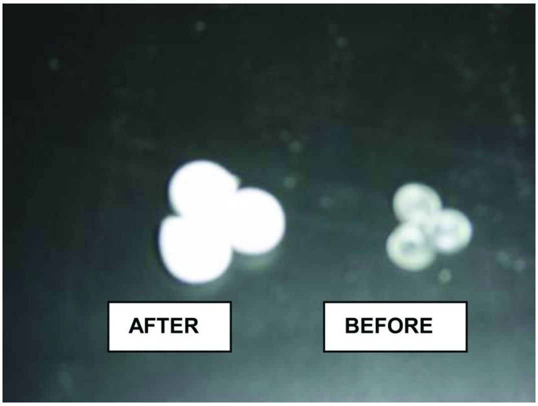

*Figure 7. Commercial PEVA sample treated to scCO$_2$ P=27.6 MPa, T=40 °C for 10 min.*

### *Synthesis of QD-PEVA Nanofilms*

By modification of the QDs to give a Si-O-CH$_3$ functional group, the new ligand can be utilized for linking the QDs to the PEVA polymer matrix

Downloaded by PENNSYLVANIA STATE UNIV on June 22, 2012 | http://pubs.acs.org
Publication Date (Web): March 11, 2010 | doi: 10.1021/bk-2010-1034.ch010

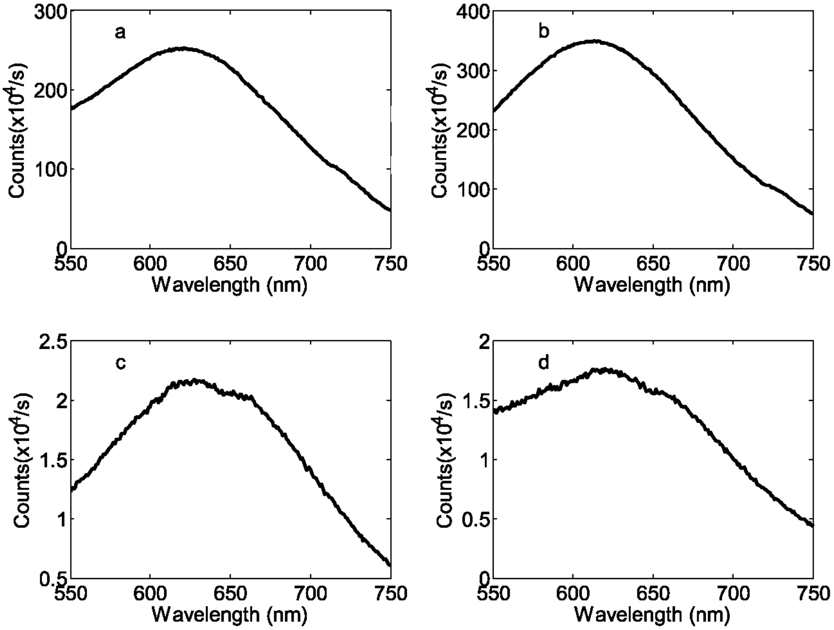

*Figure 8. Photoluminescence emission spectra of CdS-ZnS QD-PEVA nanofilms prepared in different reaction conditions (under 27.6MPa in scCO$_2$. (a) 50°C 2 hours without TOP; (b) 50°C 2 hours with TOP; (c) 50°C 20 hours with TOP; (d) 80°C 2 hours with TOP). (Reproduced with permission from reference (26). Copyright 2009 American Chemical Society.)*

using scCO$_2$, which acts as both a reaction medium and drying agent for the sol-gel chemistry. As described previously, the in situ FTIR measurements show that the polymerization and the hydrolysis/condensation reactions proceeded simultaneously, which was also found to occur with the functionalized QDs. In order to both stabilize the QDs during the process of synthesizing the QD-PEVA nanofilms and maintaining a low crosslink density during synthesis, a small amount of the ligand MPTMO was added to the QD solution before the synthesis of nanofilms. A one-pot method including polymerization and hydrolysis was tested but did not give high molecular weight polymer with resulting poor performance attributed to the high chain transfer capability of the thiol group in the ligand MPTMO. Hence, a two-step method was subsequently developed for the synthesis including: (1) terpolymerization of ethylene, vinyl acetate, and VTMO, and (2) hydrolysis of the ligand and VTMO in the terpolymer chains with HAc (see Scheme 3). ScCO$_2$ was used as the reaction medium for both steps as it can effectively swell and plasticize the amorphous region of polymer to help incorporate nanoparticles into the polymer matrix (*37*), along with facilitating both the polymerization and sol-gel chemistry steps (*38*). To illustrate the effect of scCO$_2$ on commercial PEVA beads, Figure 7 shows these beads both before and after treatment of scCO$_2$, illulstrating that mild treatment significantly swells this polymer, facilitating nanoparticle penetration.

Downloaded by PENNSYLVANIA STATE UNIV on June 22, 2012 | http://pubs.acs.org
Publication Date (Web): March 11, 2010 | doi: 10.1021/bk-2010-1034.ch010

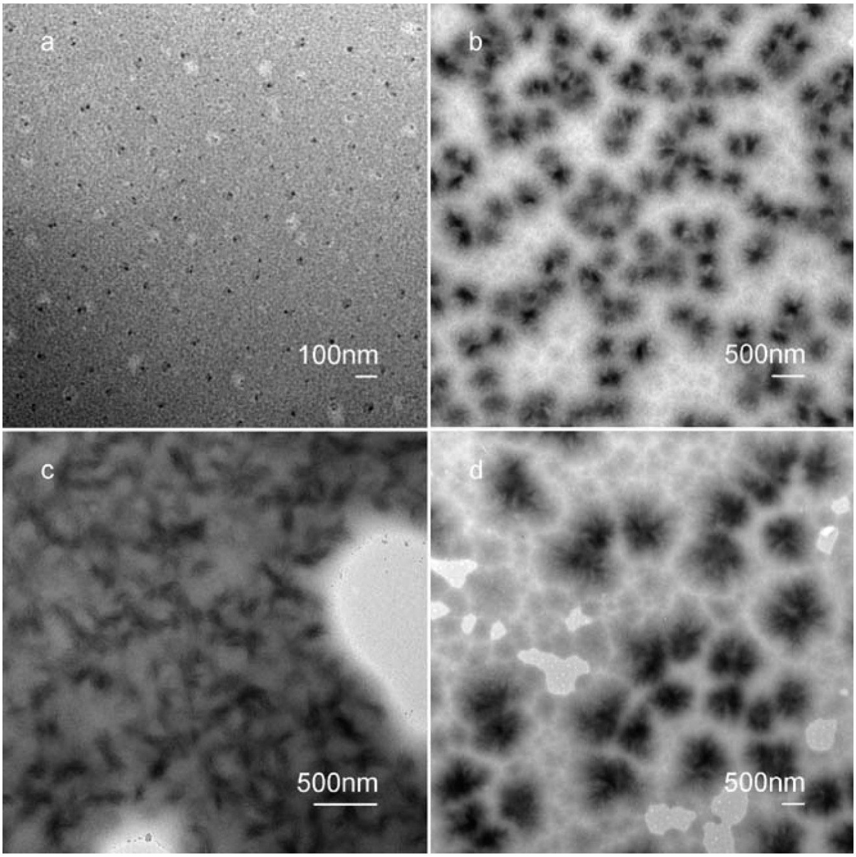

*Figure 9. TEM images of (a) functionalized CdS-ZnS QDs, and CdS-ZnS QD-PEVA nanofilms prepared in different reaction conditions (under 27.6MPa in scCO$_2$ with TOP). (b) 50°C 2 hours; (c) 50°C 20 hours; (d) 80°C 2 hours. (Reproduced with permission from reference (26). Copyright 2009 American Chemical Society.)*

After 2 hours hydrolysis at 50 °C under 27.6 MPa in scCO$_2$, the synthesized CdS-ZnS QD-PEVA nanofilms stabilized by MPTMO with/without TOP retained the characteristic emission peak of the CdS-ZnS QDs at ca. 620 nm (see Figure 8a and 8b). Extra TOP was added to examine if it would help to stabilize the QDs from agglomerating in the PEVA matrix. The absorbance maximum is slightly increased when adding extra TOP, while the peak position is not changed. In order to examine the effect of reaction temperature and time on the optical properties of PEVA nanofilms, the hydrolysis was also carried out at (1) 50 °C for 20 hours and (2) 80 °C for 2 hours. The resulting photoluminescence emission spectra are displayed in Figure 8c and 8d which show that the characteristic peak of the QDs was still maintained in these synthesized PEVA nanofilms. However, the emission intensity decreased significantly with both the extended reaction time from 2 to 20 hours at 50 °C and the increased reaction temperature from 50 to 80 °C for

Downloaded by PENNSYLVANIA STATE UNIV on June 22, 2012 | http://pubs.acs.org
Publication Date (Web): March 11, 2010 | doi: 10.1021/bk-2010-1034.ch010

2 hours. All the three film samples were examined by TGA up to 700 °C and found to contain 0.6~1.4 wt% QDs/$SiO_2$. The decrease in emission intensity was attributed to a change in the microstructures, as evidenced by TEM and STEM. By incorporation of the functionalized CdS-ZnS QDs of less than 10 nm (Figure 9a) into the PEVA matrix at 50 °C for 2 hours, QDs/$SiO_2$ particles of 100~200 nm (Figure 9b) were formed and well dispersed. When the reaction time was extended from 2 to 20 hours at the same temperature of 50 °C, a network of particles was formed (Figure 9c) while increased reaction temperature from 50 to 80 °C for the same reaction time of 2 hours resulted in larger particle size of ca. 500 nm (Figure 9d).

To examine the stability of the synthesized QD-PEVA nanofilms, these samples were then exposed to light irradiation using a solar simulator. Figure 10 compares the UV-Vis and photoluminescence spectra of the sample hydrolyzed at 50 °C for 2 hours before and after light irradiation. After being irradiated at 3 W/$cm^2$ for 5 hours, the sample showed weakened absorbance and enhanced emission intensity, accompanied by a blue shift of ca. 35 nm in the emission peak. These phenomena were also previously observed and reported in the literature (*39*, *40*). The reason for these changes may be due to the formation of smoother surfaces of QDs induced by the photooxidation and photocorrosion process (*41*). Further irradiation at the same intensity for another 5 hours did not result in a significant change in the absorbance, a wavelength shift in the emission peak, or an increase in the emission intensity, as shown in Figure 10b.

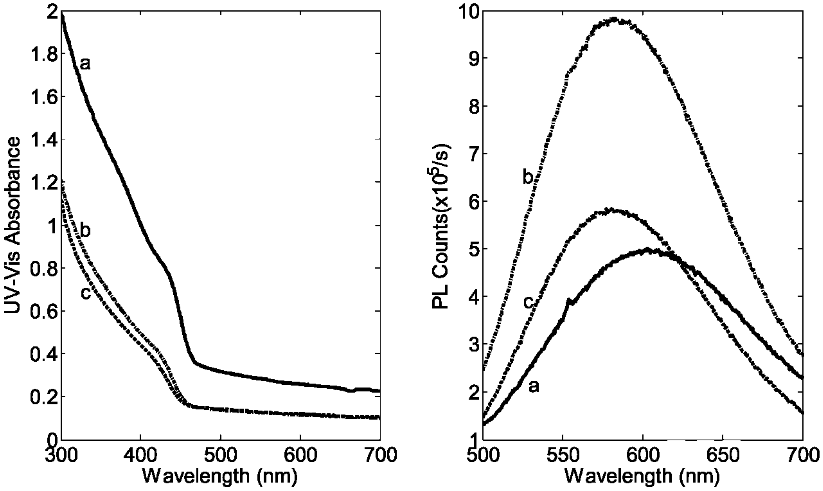

*Figure 10. UV-Vis (left) and photoluminescence emission (right) spectra of CdS-ZnS QD-PEVA nanofilm prepared at 50 °C under 27.6 MPa for 2 hours with TOP (a) before irradiation; (b) after 5 hours irradiation at 3 W/$cm^2$; (c) after further irradiation at 3 W/$cm^2$ for another 5 hours. (Reproduced with permission from reference (26). Copyright 2009 American Chemical Society.)*

Downloaded by PENNSYLVANIA STATE UNIV on June 22, 2012 | http://pubs.acs.org
Publication Date (Web): March 11, 2010 | doi: 10.1021/bk-2010-1034.ch010

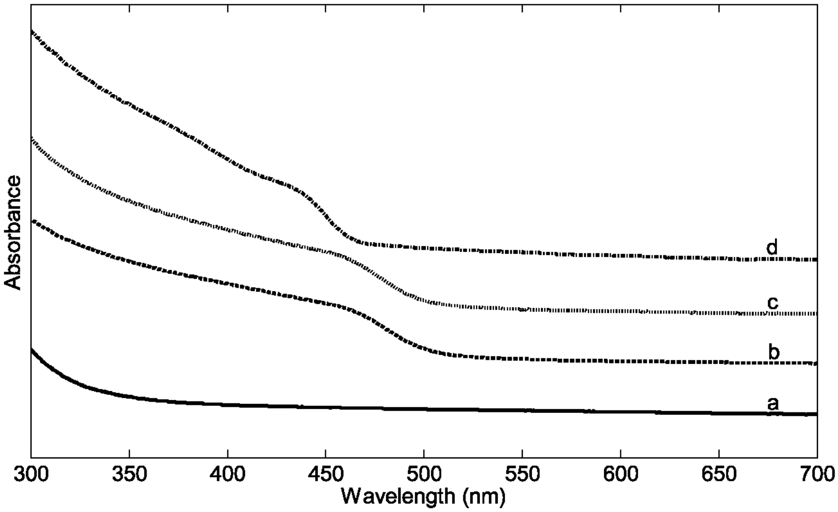

*Figure 11. UV-Vis spectra of PEVA and PEVA nanofilms. (a) PEVA; (b) CdS QD-PEVA without TOP; (c) CdS QD-PEVA with OP; (d) CdS-ZnS QD-PEVA with TOP. (Reproduced with permission from reference (26). Copyright 2009 American Chemical Society.)*

Figure 11 compares the UV-Vis absorption spectra of a series of synthesized PEVA films both with and without incorporation of QDs of both CdS and CdS-ZnS. It is obvious that these synthesized nanofilms by incorporating QDs demonstrate much stronger absorbance in the low wavelength region than the PEVA film. Along with the characteristic emission properties, these results imply potential applications of the QD-polymer nanocomposites in UV protection films and light-selective films for applications in window coatings, solar cells, greenhouses, etc.

## Conclusions

By incorporating QDs into a PEVA matrix, light-selective QD-PEVA nanofilms were produced that have the ability for energy conversion. CdS and CdS-ZnS core-shell QDs were synthesized by using single-molecular precursors and functionalized via ligand exchange with MPTMO which enabled chemical bonding to chemically link the QDs to te PEVA chains. Stabilization of the QDs to the polymer matrix was found to be extremely important for the successful synthesis of light-selective QD-polymer nanofilms. Using an excessive amount of ligands and controlling a low crosslink density can effectively stabilize the QDs. The synthesized QD-PEVA nanofilms showed excellent optical properties of selective absorbance and emission. With this technique, QD-polymer nanofilms with various optical properties can be synthesized by tuning the band gap of the QDs.

## Acknowledgments

This work was financially supported by the Canadian Natural Science and Engineering Research Council (NSERC), the Ontario Centres of Excellence (OCE) (through the EMK program), and the Canadian Foundation for Innovation (CFI). We thank Fred Pearson of the Brockhouse Institute, McMaster University for his assistance on HRTEM, Mr. X.Li for PEVA picture taking, Dr. Richard B. Gardiner and Ronald Smith of the Department of Biology, UWO, for TEM, Mark C. Biesinger of Surface Science Western, UWO for EDX elemental analysis, Dr. Nadine Merkley of the Department of Chemistry, UWO, for NMR analysis, Ms Lee-Ann Briere of the Schulich School of Medicine & Dentistry, UWO, and Dr. Alex Siemiarczuk of Photon Technology International for photoluminescence, and Jeff Gribbon, UWO for TGA. Special thanks go to the late Dr. Alex Henderson of AT Plastics for fruitful discussions.

Downloaded by PENNSYLVANIA STATE UNIV on June 22, 2012 | http://pubs.acs.org
Publication Date (Web): March 11, 2010 | doi: 10.1021/bk-2010-1034.ch010

## References

1. Richards, B. S. *Sol. Energy Mater. Sol. Cells* **2006**, *90*, 1189–1207.
2. Gopalakrishnan, G.; Danelon, C.; Izewska, P.; Prummer, M.; Bolinger, P.-Y.; Geissbuhler, I.; Demurtas, D.; Dubochet, J.; Vogel, H. *Angew. Chem., Int. Ed.* **2006**, *45*, 5478–5483.
3. Yao, H.; Zhang, Y.; Xiao, F.; Xia, Z.; Rao, J. *Angew. Chem., Int. Ed.* **2007**, *46*, 4346–4349.
4. Kukimoto, H. *J. Cryst. Growth* **1990**, *101*, 953–957.
5. Yang, H.; Holloway, P. H.; Santra, S. *J. Chem. Phys.* **2004**, *121*, 7421–7426.
6. Murray, C. B.; Norris, D. J.; Bawendi, M. G. *J. Am. Chem. Soc.* **1993**, *115*, 8706–8715.
7. Peng, X.; Wickham, J.; Alivisatos, A. P. *J. Am. Chem. Soc.* **1998**, *120*, 5343–5344.
8. Yang, C. S.; Awschalom, D. D.; Stucky, G. D. *Chem. Mater.* **2001**, *13*, 594–598.
9. Kim, S.; Bawendi, M. G. *J. Am. Chem. Soc.* **2003**, *125*, 14652–14653.
10. Chan, W. C. W.; Nie, S. *Science* **1998**, *281*, 2016–2018.
11. Mattoussi, H.; Mauro, J. M.; Goldman, E. R.; Anderson, G. P.; Sundar, V. C.; Mikulec, F. V.; Bawendi, M. G. *J. Am. Chem. Soc.* **2000**, *122*, 12142–12150.
12. Wang, Y. A.; Li, J. J.; Chen, H.; Peng, X. *J. Am. Chem. Soc.* **2002**, *124*, 2293–2298.
13. Huang, B.; Tomalia, D. A. *J. Lumin.* **2005**, *111*, 215–223.
14. Skaff, H.; Ilker, M. F.; Coughlin, E. B.; Emrick, T. *J. Am. Chem. Soc.* **2002**, *124*, 5729–5733.
15. Chen, C.-P.; Chan, S.-H.; Chao, T.-C.; Ting, C.; Ko, B.-T. *J. Am. Chem. Soc.* **2008**, *130*, 12828–12833.
16. Wallner, G. M.; Weigl, C.; Leitgeb, R.; Lang, R. W. *Polym. Degrad. Stab.* **2004**, *85*, 1065–1070.
17. Gast, M.; Koentges, M.; Brendel, R. *Prog. Photovoltaics* **2008**, *16*, 151–157.

18. Greenley, R. Z. Free Radical Copolymerization Reactivity Ratios. In *Polymer Handbook*, 4th ed.; Brandrup, J., Immergut, E. H., Grulke, E. A., Eds.; Wiley: New York, 1999; pp II/181−308.
19. Poliakoff, M.; Fitzpatrick, M.; Farren, T. R.; Anastas, P. *Science* **2002**, *297*, 807–810.
20. Leitner, W. *Science* **1999**, *284*, 1780–1781.
21. Kendall, J. L.; Canelas, D. A.; Young, J. L.; DeSimone, J. M. *Chem. Rev.* **1999**, *99*, 543–563.
22. McHugh, M. A.; Krukonis, V. J. *Supercritical Fluid Extraction: Principles and Practice*, 2nd ed.; Butterworth-Heinemann: Boston, MA, 1994.
23. Young, J. L.; DeSimone, J. M. Synthesis and Characterization of Polymers: From Polymeric Micelles to Step-Growth Polymerizations. In *Green Chemistry Using Liquid and Supercritical Carbon Dioxide*; DeSimone, J. M., Tumas, W., Eds.; Oxford University Press: Oxford, England, 2003; pp 149−163.
24. Charpentier, P. A.; Kennedy, K.; DeSimone, J. M.; Roberts, G. W. *Macromolecules* **1999**, *32*, 5973–5975.
25. Charpentier, P. A.; Xu, W. Z.; Li, X. *Green Chem.* **2007**, *9*, 768–776.
26. Xu, W. Z.; Charpentier, P. A. *J. Phys. Chem. C* **2009**, *113*, 6859–6870.
27. Xu, W. Z.; Li, X.; Charpentier, P. A. *Polymer* **2007**, *48*, 1219–1228.
28. Smukala, J.; Span, R.; Wagner, W. *J. Phys. Chem. Ref. Data* **2000**, *29*, 1053–1121.
29. Span, R.; Wagner, W. *J. Phys. Chem. Ref. Data* **1996**, *25*, 1509–1596.
30. Reim, M.; Reichenauer, G.; Koerner, W.; Manara, J.; Arduini-Schuster, M.; Korder, S.; Beck, A.; Fricke, J. *J. Non-Cryst. Solids* **2004**, *350*, 358–363.
31. Kelen, T.; Tudos, F. *J. Macromol. Sci., Chem.* **1975**, *A9*, 1–27.
32. Xu, W. Z.; Charpentier, P. A. *Ind. Eng. Chem. Res.* **2009**, *48*, 1384–1390.
33. Van der Meer, R.; Aarts, M. W. A. M.; German, A. L. *J. Polym. Sci.: Polym. Chem. Ed.* **1980**, *18*, 1347–1357.
34. Hyatt, J. A. *J. Org. Chem.* **1984**, *49*, 5097–5101.
35. Dabbousi, B. O.; Rodriguez-Viejo, J.; Mikulec, F. V.; Heine, J. R.; Mattoussi, H.; Ober, R.; Jensen, K. F.; Bawendi, M. G. *J. Phys. Chem. B* **1997**, *101*, 9463–9475.
36. Socrates, G. *Infrared and Raman Characteristic Group Frequencies: Tables and Charts*, 3rd ed.; John Wiley & Sons Ltd.: Chichester, England, 2001; p 347.
37. Sun, D.; Zhang, R.; Liu, Z.; Huang, Y.; Wang, Y.; He, J.; Han, B.; Yang, G. *Macromolecules* **2005**, *38*, 5617–5624.
38. Sui, R.; Rizkalla, A. S.; Charpentier, P. A. *Cryst. Growth Des.* **2008**, *8*, 3024–3031.
39. Wang, M.; Felorzabihi, N.; Guerin, G.; Haley, J. C.; Scholes, G. D.; Winnik, M. A. *Macromolecules* **2007**, *40*, 6377–6384.
40. Rene-Boisneuf, L.; Scaiano, J. C. *Chem. Mater.* **2008**, *20*, 6638–6642.
41. Wang, Y.; Tang, Z.; Correa-Duarte, M. A.; Pastoriza-Santos, I.; Giersig, M.; Kotov, N. A.; Liz-Marzan, L. M. *J. Phys. Chem. B* **2004**, *108*, 15461–15469.

Downloaded by PENNSYLVANIA STATE UNIV on June 22, 2012 | http://pubs.acs.org
Publication Date (Web): March 11, 2010 | doi: 10.1021/bk-2010-1034.ch010

## Chapter 11

# Proton Exchange Membrane Nanocomposites

**Michael A. Hickner***

**Department of Materials Science and Engineering, The Pennsylvania State University, University Park, PA 16802**
***mah49@mail.psu.edu**

Downloaded by UNIV OF GUELPH LIBRARY on June 22, 2012 | http://pubs.acs.org
Publication Date (Web): March 11, 2010 | doi: 10.1021/bk-2010-1034.ch011

Organic-inorganic nanocomposite proton conducting membranes have been an important thrust in the search for novel materials that outperform the state-of-the-art all-polymer membranes in fuel cells. Nanocomposite proton exchange membranes may provide routes to increased conductivity at low relative humidity, decreased methanol permeability without a conductivity penalty, enhanced mechanical properties, and long-term durability. A variety of nanocomposite architectures have been explored for fuel cell membranes including polymers of varying chemical compositions including Nafion, inert polymer supports, inorganic additives that serve as desiccants, proton conducting inorganic additives, and additives that are primarily designed to impeded methanol transport. This review highlights recent advances in the understanding of the unique properties of nanocomposite proton exchange membranes and how the coupling between the organic and inorganic phases can enhance the properties a nanocomposite material for targeted application in fuel cells. Original data is also presented in terms of understanding how inorganic phases influence the binding of water within the polymer and thus the transport properties of the nanocomposite.

## Introduction and Review

Fuel cells are environmentally friendly and efficient electrochemical energy conversion devices and are sought as enabling components of next-generation energy technology. While large markets may exist in automotive and portable

In Functional Polymer Nanocomposites for Energy Storage and Conversion; Wang, Q., et al.;
ACS Symposium Series; American Chemical Society: Washington, DC, 2010.

power for microelectronics, fuel cells are making inroads today in applications such as indoor forklifts, backup power for buildings and telecommunications sites, auxiliary power units for larger vehicles, and home cogeneration. As fuel cells become useful over a wide range of environments, new materials are sought that enable high performance outside of traditional operating windows, increase efficiency of chemical to electrical conversion, prolong lifetime of the devices, and cost less.

The proton exchange membrane, which serves as the supporting component for the electrodes, separates the reactant gases, and conducts protons from anode to cathode, is one of the critical components of the fuel cell. The proton conductivity and other transport properties of the membrane have a direct influence on the performance of the fuel cell and the physical and chemical durability of the membrane is a chief concern in the overall longevity of the device. Researchers seek to optimize the critical properties of the membrane including water transport, mechanical properties such as modulus and creep resistance, and reactant permeability, e.g. methanol permeability or hydrogen crossover, to affect the appropriate balance of properties for a specific application.

Organic-inorganic nanocomposite membrane architectures can impact all of the critical properties mentioned above and the multicomponent nature of the nanocomposites are desirable because both the organic and inorganic phases can be optimized to achieve the desired mix of properties. There are various approaches to forming proton conducting nanocomposite membranes as outlined in Table I. One approach, discussed here briefly, is to use an inert polymer binder and a functional inorganic phase. Another, more common, approach is to rely mostly on the polymeric phase for conductivity, while employing an inorganic phase that does not contribute greatly to ion conduction, but has other desirable attributes of mechanical reinforcement and the lowering of reactant permeability. These types of composites are typified by Nafion-metal oxide nanocomposites and will be discussed at length here. Finally, successful examples of employing both a functional polymer and a functional inorganic phase that each participate in the conduction of protons have been demonstrated in a variety of formats. These types of functional nanocomposites where each phase contributes desirable transport properties are some of the best-performing examples of proton exchange membranes incorporating both organic and inorganic components, but there is still much room for optimization and improvement of these materials and the nature of the coupling between the organic and inorganic phases is not yet well understood. This chapter will review the state-of-the-art materials that yield high performance proton exchange membranes and discuss fundamental understanding of their properties. Data will also be presented on the water binding and diffusion in two different types of organic-inorganic nanocomposites based on sulfonated poly(sulfone) that contains heteropolyacid or zirconium hydrogen phosphate. These two types of nanocomposites provide an interesting contrast in understanding how the state of water influences the transport properties in these types of materials.

Downloaded by UNIV OF GUELPH LIBRARY on June 22, 2012 | http://pubs.acs.org
Publication Date (Web): March 11, 2010 | doi: 10.1021/bk-2010-1034.ch011

**Table I. Types of Proton Exchange Membrane Nanocomposites**

| | *Example* | *Advantages* | *Disadvantages* | *Prospects* |
|---|---|---|---|---|
| Inert polymer/ functional inorganic | PVDF w/ heteropolyacid | Low water swelling, water-free conduction in the inorganic phase | Difficult to couple polymer and inorganic phases | One route to high temperature membranes based on conduction in the inorganic phase |
| Inert polymer/ functional polymer | Porous PTFE w/ sulfonated polymer | Highly processable, can promote strong organic/organic coupling, possible to go to high ion high exchange capacity | Most examples still based on sulfonated polymers | Current commercial materials, e.g. Gore |
| Functional polymer/inert filler | Sulfonated polymer w/ silica | Easy to fabricate, good mechanical properties, low methanol permeability, many literature examples | Conductivity can be depressed compare to pure sulfonated polymer | Possible applications in direct methanol fuel cells |
| Functional polymer/ functional filler | Sulfonated polymer w/ sulfonated silica | Synergistic conductivity enhancement between functional phases | Functional inorganic phase may be water soluble | Ideal nanocomposites for high conductivity in low water environment |

Multiple studies have shown it difficult to achieve high performance proton exchange membranes with a polymeric phase that does not contribute to water uptake or conductivity (*1*, *2*). Both zeolite-laden polymer membranes and phosphotungstic acid incorporated at high loading in an inert matrix achieved conductivities on the order of $10^{-2}$ - $10^{-3}$ S $cm^{-1}$, which is still too low compared to the benchmark of $10^{-1}$ S $cm^{-1}$ for a high performance proton exchange membrane. Additionally, membranes with a high loading of inorganic phase can suffer from brittleness and problems with low open circuit voltage due to pinholes. Despite these challenges, some recent progress has been made in the basic properties of membranes that use an inert supporting polymer and a functional inorganic phase. Herring et al. (*3*) employed Keggin, Wells–Dawson and elongated Wells–Dawson heteropolyacid structures to good effect in working fuel cells as pressed pellets and in thin membranes with poly(vinylidenefluoride-hexafluoropropylene) inert binder. This rational comparison of solid acid pellets versus polymer-supported membranes demonstrated that high limiting current densities, greater than 1 A

Downloaded by UNIV OF GUELPH LIBRARY on June 22, 2012 | http://pubs.acs.org
Publication Date (Web): March 11, 2010 | doi: 10.1021/bk-2010-1034.ch011

cm$^{-2}$, could be achieved with inorganic functional phases in proton conducting fuel cells. However, the water generated in the oxygen reduction reaction at these high currents tended to degrade the membrane due to the dissolution of the heteropolyacid from the membrane. Improvements were made to the heteropolyacid concept by tethering a lacunary heteropolyacid to a vinyl monomer for incorporation into a copolymer (*4*). A membrane with 75 wt % lacunary heteropolyacid exhibited reasonable fuel cell performance over multiple days with 75% RH gas feeds demonstrating that robust tethering of the inorganic to the polymer was achieved. While these tethered systems show interesting properties at high relative humidity, their performance at low humidity is yet to be optimized.

There are significant advantages to employing functional inorganic particles in an inert polymer matrix, such as high mechanical strength and solid-state proton conduction, but serious problems still exist with membranes that are composed of high fractions of inorganic material. Often, these materials contain significant defects and thus have low open circuit voltages in fuel cells. Additionally, some inorganic materials require moderate amounts of water to achieve desirable conductivity. The bulk of the research on proton exchange membrane nanocomposites has been conducted with Nafion as the organic matrix and a metal oxide filler (most often silica or titania). Nafion is a natural choice for the polymeric phase since it is the archetypical proton conducting polymer and is widely available in a variety of membrane, pellet, and dispersion forms. Silica and titania are attractive inorganic components to be incorporated into Nafion due to their ease of synthesis by a variety of methods and their well-studied properties in pure form. These types of composites can be prepared by forming the inorganic phase in-situ in a preformed membrane or by solution casing of a precurso sol and a Nafion polymer dispersion and subsequently completing the metal oxide condensation and Nafion annealing as the membrane is dried and heated. The most outstanding properties of Nafion-metal oxide composites are their increase in mechanical properties (*5*) and decrease in methanol permeability (*6*) and many examples of these type of composites have found use as proton exchange membranes in direct methanol fuel cells.

Bocarsly, et al., (*7*) explored a range of nanocomposites incorporating $SiO_2$, $TiO_2$, $Al_2O_3$, and $ZrO_2$ into a Nafion matrix. While these authors confirmed that the Nafion-metal oxide composites had similar or lower conductivity than the pure Nafion polymer due to the inert nature of the inorganic phase towards proton conductivity, they hypothesized that the increase in mechanical properties of the nanocomposites was caused by an increase in the glass transition temperature of the polymer upon addition of the inorganic phase. This increase in the glass transition temperature of the nanocomposite would allow the material to perform at higher temperatures where the phase-separated structure of the membrane, which is responsible for proton conductivity, could persist beyond where the pure polymer membrane loses its conductivity, presumably by an order-disorder transition of the ionic phase. The authors hypothesized three different sites for interaction between the metal oxide and the polymer which could lead to the higher glass transition temperature: a hydrogen-bonding site where M-OH exists on the surface of the inorganic phase, a ligation site for coordination of an unsaturated metal bond to sulfonate on the polymer, and nonspecific

Downloaded by UNIV OF GUELPH LIBRARY on June 22, 2012 | http://pubs.acs.org
Publication Date (Web): March 11, 2010 | doi: 10.1021/bk-2010-1034.ch011

Downloaded by UNIV OF GUELPH LIBRARY on June 22, 2012 | http://pubs.acs.org
Publication Date (Web): March 11, 2010 | doi: 10.1021/bk-2010-1034.ch011

physisorption involving van der Waals interactions between the polymer chain and the metal oxide surface. Using dehydration and thermal decomposition analysis, the authors support that the strongest interactions are between the metal oxide and the sulfonate moieties on the polymer. Improved water retention at elevated temperatures of Nafion-silicon oxide nanocomposite membranes with an excess of hydroxide and ethoxide functional groups on the silicon oxide phase was shown to increase membrane performance in fuel cell testing up to 130 - 140 °C (*8*). The moderate desiccating effect of the inorganic phase and its mechanical reinforcement of the polymeric phase, and by extension the proton conducting domains, renders these types of materials useful for applications where water retention at high temperature and robust mechanical properties are important. The durability of the membranes in a fuel cell device can be enhanced by the mechanical strengthening of the nanocomposite (*9*).

Polymer-metal oxide nanocomposites have also shown utility as proton exchange membranes for direct methanol fuel cells. Both Nafion (*10*) and sulfonated poly(aromatic) membranes (*11*) have been employed for liquid-fed fuel cells. It has been shown that generally the inorganic phase lowers the methanol permeability of the membrane without a large impact on conductivity. This lowering of the permeability, in turn, increases the electrochemical selectivity of the membrane for proton conduction over methanol permeation and thus gives an indication that the nanocomposite membranes may perform as well or better than Nafion in the device. The increased performance in the nanocomposites with higher electrochemical selectivity as compared to Nafion is often realized for well-designed membrane electrode assemblies. The decrease in methanol permeability in these types of composites is reasonable due to simple blockage of the methanol molecules by an excluding phase. Through tuning of the nanocomposite composition, researchers have found conditions where the decrease in methanol permeability does not accompany a correspondingly large decrease in proton conductivity, but the fundamental origins of why the electrochemical selectivity changes how it can be tuned precisely are still unknown. Physically impeding methanol transport has been attempted using exfoliated clays and other particles with high aspect ratios, very often with plate-like geometries like layered double hydroxides (*12*) or montmorillonite (*13*). These high aspect ratio particles can further decrease the methanol permeability as compared to randomly formed inorganic phases, but their extended structures can also begin to cut off the proton conducting pathways.

To increase the conductivity contribution of the inorganic component in Nafion-based nanocomposites, sulfonated variants of metal oxides, clays, and other minority component phases have been employed as the inorganic phase in proton exchange membrane nanocomposites. Sulfonated silica (*14*), sulfonated titania (*15*), sulfonated poly(phenylsilsesquioxane) (*16*), and sulfonated montmorillonite (*17*) improve the conductivity of nanocomposite proton exchange membranes by increasing the ion exchange capacity of the material. The additional ions in the membrane imparted by the inorganic, therefore, tend to give higher conductivity. The trade-off between conductivity and methanol permeability in these sulfonated systems is less understood than in cases where the inorganic phase does not participate in conductivity. There have been various mechanisms proposed for how the organic and inorganic phases function together to conduct protons, but there is still fundamental insight that needs to be developed and better experimental probes of the role of each component should be sought.

Giuver, et al. (*14*) observed a decrease in water uptake of a sulfonated poly(phthalazinone ether ketone) upon the addition of silica functionalized with sulfonated glycidyl phenyl ether. The decreased water uptake lowered the methanol permeability of the nanocomposite. These authors observed more bound water in the membrane by calorimetry due to the increase of the hydrogen bonding interactions with the water and additional sulfonate groups. Also, thermogravimetric stability studies of the nanocomposites lead the authors to propose sulfonate/sulfonate interactions between the organic and inorganic phases, which lead to greater stability of the material. The proper balance of the volume fraction of the organic and inorganic phases is important to give the maximum coupling between the two components and to prevent aggregation of the inorganic phase.

Another functional inorganic phase that has shown significant promise in sulfonated polymers are heteropolyacids (*18–20*). Solid acid compounds are potentially attractive as a high conductivity, solid-state electrolyte. On their own, solid acids are brittle materials and fabricating thin membranes from them is difficult. Inert polymeric binders have been used to facilitate membrane formation as described above, however, the largest benefits of incorporating heteropolyacids into proton exchange membrane nanocomposites have resulted from making use of sulfonated polymers as a majority phase. To combat the solubility of the heteropolyacids, silica and clay supports have been used to stabilize water-soluble additives and many examples of robust membranes have been reported. The conductivity mechanism and synergism between the heteropolyacid and polymer phases is still under intense study. Both heteropolyacids and sulfonated inorganic additives have strong hydrogen bonding sites and/or free protons as shown in Figure 1. Silica and other metal oxides with hydroxyl surface groups do provide some interaction with water, and these additives act as a desiccant especially at high temperature, but the exchange of the silanol or similar groups with the surrounding aqueous media is limited compared to other chemical moieties with strongly acidic protons. Interactions between sulfonate groups on a functional polymer and heteropolyacids or other sulfonated inorganic additives provides additional sites for strong hydrogen bonding and/or fast exchange of protons, which serves to increase the proton conductivity of the nanocomposite.

Alberti (*21*) has pioneered research into proton conducting composites based on inorganic layered zirconium hydrogen phosphate compounds and proton conducting polymers such as sulfonated poly(etheretherketone). The class of compounds known as zirconium sulfoarylphosphonates are themselves proton conductors as the previously mentioned heteropolyacids. However, there is one major difference; the heteropolyacids are water soluble and the zirconium systems are not. This may afford some additional stability advantage for the latter composites because the leaching of the inorganic from the copolymer may not be as severe as with some heteropolyacid composites. Alberti et al. (*22*) have extended this research to incorporating titanium phosphate sulfophenylphosphonate

Downloaded by UNIV OF GUELPH LIBRARY on June 22, 2012 | http://pubs.acs.org
Publication Date (Web): March 11, 2010 | doi: 10.1021/bk-2010-1034.ch011

Downloaded by UNIV OF GUELPH LIBRARY on June 22, 2012 | http://pubs.acs.org
Publication Date (Web): March 11, 2010 | doi: 10.1021/bk-2010-1034.ch011

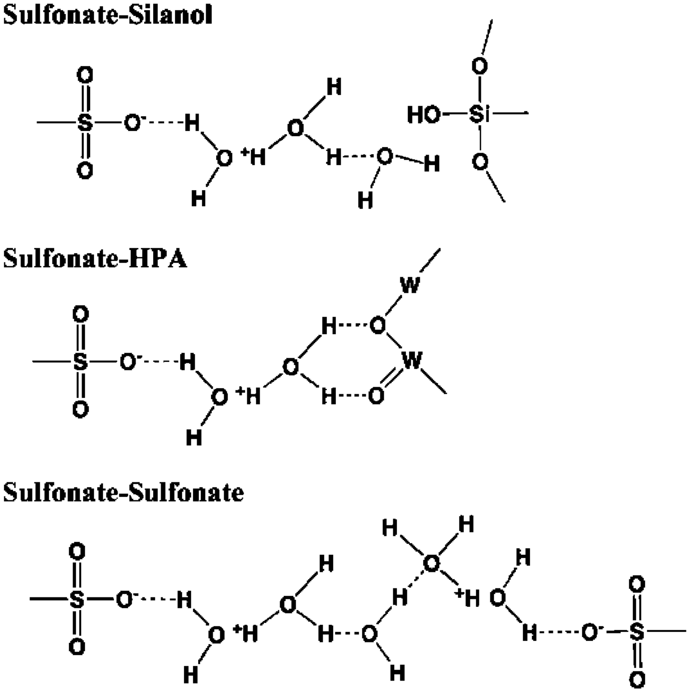

Sulfonate-Silanol

Sulfonate-HPA

Sulfonate-Sulfonate

*Figure 1. Interactions between different organic-inorganic moieties in proton exchange membrane nanocomposites*

into Nafion membranes. Titanium phosphate sulfophenylphosphonate was investigated because it has shown the greatest conductivity of the layered metal sulfonates. Composite membranes showed good conductivity up to 20 wt % filler, where the membranes started to become heterogeneous and brittle. This indicates poor coordination between the inorganic and organic phases. Nafion is very difficult to blend with fillers because it is so sensitive to solvent and thermal processing. Other types of proton conducting polymers such as sulfonated poly(arylene ethers) could prove to be more advantageous in this type of composite.

Most research dealing with organic/inorganic composites has focused on characterizing the proton exchange membrane properties that are important to fuel cell performance, namely protonic conductivity and methanol permeability. Insufficient information has been presented on the other transport properties of these composite membranes, e.g. electro-osmotic drag, and little data has been presented to justify the mechanism of how these inorganic compounds influence the transport within a proton exchange membrane. The aim of this work is to provide a framework for how the transport properties of a composite proton exchange membrane with either phosphotungstic acid (*18*) or zirconium hydrogen phosphate (*22*) differs from a pure sulfonated copolymer.

Downloaded by UNIV OF GUELPH LIBRARY on June 22, 2012 | http://pubs.acs.org
Publication Date (Web): March 11, 2010 | doi: 10.1021/bk-2010-1034.ch011

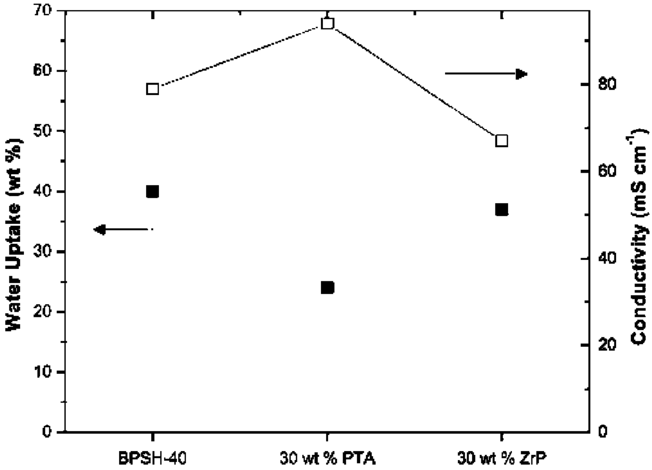

*Figure 2. Water uptake (■) and conductivity (□) of BPSH 40-based nanocomposites with phosphotunstic acid or zirconium hydrogen phosphate inorganic phases.*

# Experimental

## Materials

All reagents were purchased from commercial sources and used without further purification. Directly copolymerized sulfonated poly(arylene ether sulfone) based on biphenol (BPSH) was synthesized as described previously (*23*). BPSH/phosphotungstic acid composite membranes were cast from acid form copolymer. Once the acid form copolymer was dissolved in N,N'-dimethylacetamide (5% wt./vol.) to form a clear solution, the desired amount of phosphotungstic acid was added to the polymer/DMAc solution and the solution allowed to stir for another 24 h. The casting and reacidification conversion procedure to ensure the acid form of the polymer was obtained remained as previously reported (*18*).

BPSH/zirconium hydrogen phosphate membranes were prepared from an already cast and converted acid form BPSH membrane using an optimized procedure from the literature (*24*). To form the zirconium hydrogen phosphate composite, the acid form BPSH membrane was immersed in boiling water for 1 h, then immediately transferred to an 80°C zirconyl chloride ($ZrOCl_2$) solution of desired $ZrOCl_2$ concentration. The $ZrOCl_2$ solutions were prepared by diluting a stock $ZrOCl_2$ solution (30 % $ZrOCl_2$ in HCl from Aldrich) with DI water. The concentration of $ZrOCl_2$ determined the final zirconium hydrogen phosphate content of the composite. The membranes were removed from the $ZrOCl_2$ solution after 6 h, quickly rinsed with DI $H_2O$ to remove any surface $ZrOCl_2$, then immersed in 1.5 M phosphoric acid ($H_3Po4$) (a large excess for reaction with the

$ZrOCl_2$) for 24 h at room temperature. The $H_3PO_4$ diffused into the membrane and reacted with the $ZrOCl_2$ imbibed in the membrane to form zirconium hydrogen phosphate, $Zr(HPO_4)_2$ (and its associated waters of hydration), according to:

$$ZrOCl_2 + 2\, H_3PO_4 \rightarrow Zr(HPO_4)_2 \cdot x\, H_2O + 2\, HCl$$

After immersion for 24 h in 1.5 M $H_3PO_4$, the membranes were then rinsed well with DI water and boiled in DI water for 2 h to remove any residual reactants. The composite membranes were then re-acidified according to the method above to ensure full conversion to the acid form. All membranes were stored in DI water for at least 1 week before testing.

Downloaded by UNIV OF GUELPH LIBRARY on June 22, 2012 | http://pubs.acs.org
Publication Date (Web): March 11, 2010 | doi: 10.1021/bk-2010-1034.ch011

### Characterization

The water uptake, conductivity, and methanol permeability were measured as previously described (*25*, *26*). Electro-osmotic drag was measured in a fuel cell configuration where the water flux from anode to cathode was monitored. The water flux was then corrected for the cell current and the electro-osmotic drag was computed (*27*). Pulsed-field gradient NMR measurements were performed using a stimulated-echo pulsed-field gradient sequence on fully hydrated membranes as detailed in Ref. (*28*). Fuel cell membrane electrode assemblies were fabricated using LANL-standard procedures for thin-film DMFC electrodes (*29*). Electrochemical selectivity was determined using the framework proposed in Ref. (*30*).

## Results and Discussion

All membrane nanocomposites in this work were transparent, ductile films (*31*). The transparency of the materials, without any signs of cloudiness or drastic change in color after nanocomposite formation as compared to the pure polymers, was a good indication that the additives were incorporated into the film on a nanometer scale. Additionally, for the nanocomposites with 30 wt % and lower inorganic phase, robust mechanical properties were observed which signals, along with the transparency, that there was high dispersion of the inorganic material. The water uptake and conductivity of representative nanocomposite samples are shown in Figure 2.

The presence of the phosphotungstic acid (PTA) filler enhanced conductivity and decreased water uptake when solution blended and cast with BPSH 40. The presence of zirconium phosphate (ZrP) formed in-situ in a cast BPSH 40 membrane did not affect water uptake greatly, but decreased the observed conductivity somewhat.

The methanol permeability of the nanocomposites as a function of temperature is shown in Figure 3.

Downloaded by UNIV OF GUELPH LIBRARY on June 22, 2012 | http://pubs.acs.org
Publication Date (Web): March 11, 2010 | doi: 10.1021/bk-2010-1034.ch011

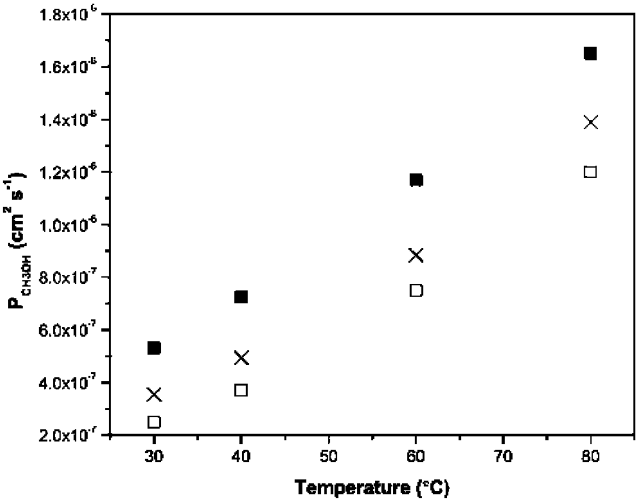

*Figure 3. Methanol permeability of proton exchange membrane nanocomposites as a function of temperature; (×) BPSH 35, (■) BPSH 35 w/30 wt % PTA, (□) BPSH 35 w/30 wt % ZrP.*

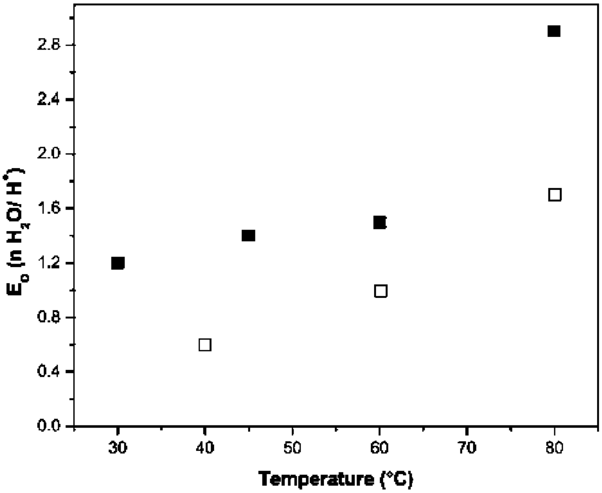

*Figure 4. Electro-osmotic drag coefficients of the nanocomposites as a function of temperature; (■) BPSH 40 w/30 wt % PTA, (□) BPSH 40 w/22 wt% ZrP.*

Similar to conductivity, the presence of phosphotunstic acid increased the transport of methanol across the membrane compared to the pure membrane, while the zirconium phosphate filler decreased methanol transport. This trend for both conductivity and methanol permeability is interesting in light of the water uptake of the materials. Generally, a lower water uptake for a given family of materials leads to decreased transport. However incorporation of phosphotunstic acid lowered the

Downloaded by UNIV OF GUELPH LIBRARY on June 22, 2012 | http://pubs.acs.org
Publication Date (Web): March 11, 2010 | doi: 10.1021/bk-2010-1034.ch011

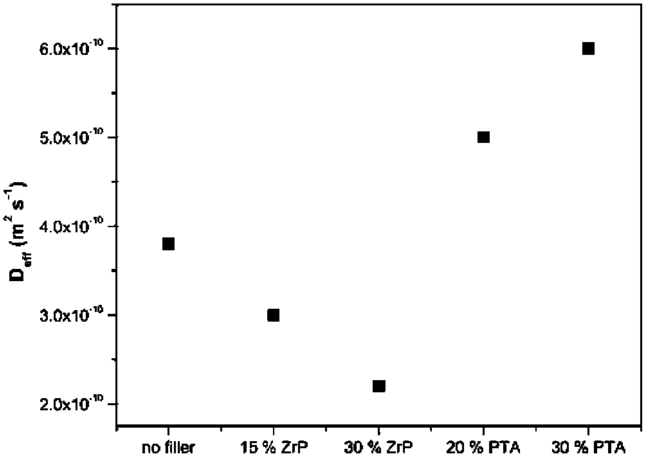

*Figure 5. Effective water self-diffusion coefficients in nanocomposite membranes with BPSH 35 as the base membrane. Nafion $D_{eff} = 7.5x10^{-10}$ $m^2$ $s^{-1}$, liquid water $D_{eff} = 2.3x10^{-9}$ $m^2$ $s^{-1}$.*

bulk water uptake, but the phosphotunstic acid increased the observed transport properties, both in the case of proton conductivity and methanol permeability. On the other hand, zirconium hydrogen phosphate shows a more expected trend of decreased transport and slightly lower water uptake. The heteropolyacid and zirconium phosphate are functioning differently in this case, which is likely due to the functionality of the heteropolyacid as described in the opening section of this chapter.

Electro-osmotic drag experiments showed similar trends in the ordering of transport properties where the phosphotungstic acid composite had increased electro-osmotic transport as compared to the zirconium phosphate nanocomposite – see Figure 4.

It is striking to see the connections between conductivity, methanol permeability, and electro-osmotic drag across the range of nanocomposite materials. It is the usual case that the methanol permeability and electro-osmotic drag coefficients for many membranes scale with the bulk water uptake within a single class of polymers. Additionally, polymers with a larger fraction of loosely bound water as determined by their chemical composition and morphology tend to have higher transport properties for a given water uptake than membranes with more tightly bound water. For instance, Nafion has high conductivity, methanol permeability, and electro-osmotic drag, while a poly(aromatic membrane) with similar water uptake shows lower conductivity, permeability, and water transport (*32*). The overriding factor in the difference between these two types of membranes is that the water within Nafion is less tightly associated with the polymer, e.g. a higher water self-diffusion coefficient and calorimetric signature, and therefore the more rapid dynamics of water lead to higher transport rates. By monitoring the water binding and diffusion within a membrane, one may obtain an accurate picture of what the resulting transport properties of that material.

Downloaded by UNIV OF GUELPH LIBRARY on June 22, 2012 | http://pubs.acs.org
Publication Date (Web): March 11, 2010 | doi: 10.1021/bk-2010-1034.ch011

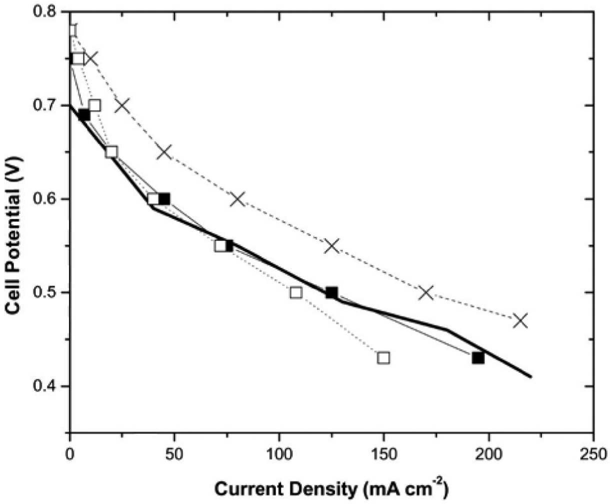

*Figure 6. Direct methanol polarization curves for Nafion (heavy line), BPSH 50 w/33 % ZrP (□), BPSH 30 w/30 % PTA (■), and BPSH 30 (×). Conditions were 80 °C cell temperature, 1 mL min$^{-1}$ 0.5 M $CH_3OH$ flow on anode, 200 std. mL min.$^{-1}$ air flow on cathode with dew point of 80 °C.*

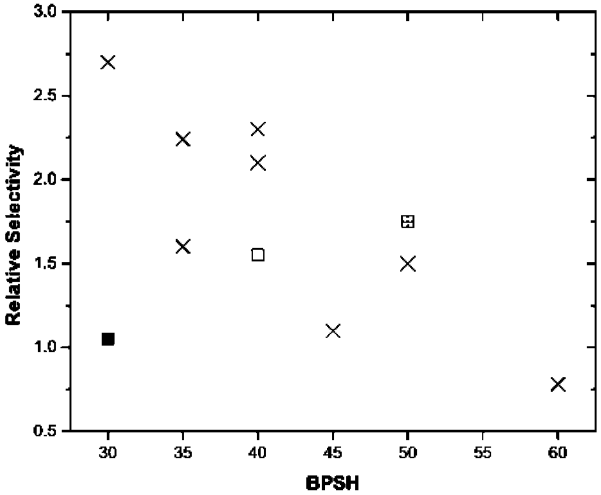

*Figure 7. Relative selectivity of BPSH membranes (×) compared to BPSH 30 w/30 % PTA (■), BPSH 40 w/22 wt % ZrP and BPSH 50 w/33 wt % ZrP (⊞).*

To probe the fundamental effect of nanocomposite fillers, the water diffusion in the membranes was measured using pulsed-field gradient nuclear magnetic resonance, Figure 5. The effective self-diffusion coefficient of water ($D_{eff}$) within the membrane structure serves as an important indicator of the mobility of transported species (ion, methanol, water) within the hydrated domains of the polymer membrane.

The figure shows that as ZrP is incorporated into the membrane, the water self-diffusion coefficient decreases, a signal that both the conductivity and methanol permeability may decrease in the resulting membranes. For PTA incorporation, the water self-diffusion coefficient increases, which will tend to promote an increase in the proton conductivity, methanol permeability, and electro-osmotic drag coefficient. By measuring the water-self diffusion coefficients in the nanocomposites, their resulting transport properties can be understood by considering the interactions of the material with water.

The changes in material properties with different nanocomposite fillers are caused by a change in the water binding within the membrane induced by the interaction of the filler with the polymer and the absorbed water. It was shown previously that phosphotungstic acid has specific interactions with BPSH as observed with FTIR (*18*). These interactions, in addition to phosphotungstic acid's native acidity, are most likely responsible for the enhanced fraction of loosely bound water and thus greater transport in these membranes. Zirconium phosphate, because it was formed in-situ in a cast membrane, acts as a physical barrier in the transport pathways within the membrane and due to its non-functional nature in terms of proton transport. The knowledge of the chemical and physical interactions of the inorganic phase within the polymer membrane and the connections of the water binding to the transport properties observed across a range of nanocomposite materials can be used to design new materials which break the traditional tradeoffs of proton, water, and small molecule transport.

The direct methanol fuel cell performance of a few examples of BPSH nanocomposites is shown in Figure 6. All of the nanocomposites show higher open circuit voltages than Nafion 117, which is indicative of their lower methanol permeability. The performance of the BPSH 30 w/30 wt % PTA nanocomposite membrane is much less than the pure BPSH 30 sample. As described above, adding PTA to the membrane increases the loosely bound water content and thus increases its methanol permeability, which causes a drop in performance under methanol fuel cell conditions. When a BPSH 50 w/33 wt % ZrP nanocomposite was tested, its performance was comparable to that of Nafion, even though BPSH 50 in its native form is a highly swelling polymer. The methanol fuel cell results show that high swelling membranes can still be useful in direct methanol fuel cells when employed in a nanocomposite that decreases the methanol permeability of the membrane.

The relative selectivity of proton conductivity to methanol permeability as compared to Nafion (RS=1) for various BPSH membranes and BPSH-based nanocomposites is shown in Figure 7. The figure shows that the relative selectivity of BPSH 30 is drastically decreased when PTA is added to the membrane, which supports the observed decline in fuel cell performance. Given the decline in selectivity, the methanol permeability of the membrane was increased in larger proportion as compared to the proton conductivity. Adding zirconium phosphate to BPSH 40 or BPSH 50 had somewhat opposite effects on the relative selectivity of the polymer. BPSH 40 has a reasonable relative selectivity of about 2.1 - 2.3. Adding ZrP decreases both its methanol permeability and

Downloaded by UNIV OF GUELPH LIBRARY on June 22, 2012 | http://pubs.acs.org
Publication Date (Web): March 11, 2010 | doi: 10.1021/bk-2010-1034.ch011

conductivity, but because the methanol permeability is already rather low, the conductivity decreases to a greater extent than the permeability, and therefore the nanocomposite has lower relative selectivity. For the more conductive and permeable BPSH 50 membrane, adding zirconium phosphate increased the relative selectivity by decreasing methanol permeability and not impacting proton conductivity to a large extent, thus raising the selectivity somewhat. Therefore, taking into account the data in Figure 7, the positive or negative effects of nanocomposite fillers can depend on the exact balance of properties and the water swelling of the base polymer.

## Conclusions

Nanocomposite proton exchange membranes enable unique functionality and may provide a route to properties that are not accessible with pure polymer membranes. Inorganic nanocomposite fillers can enhance proton conductivity, increase mechanical properties, and impede reactant transport. Silica and titania fillers have been employed to good effect to increase the mechanical integrity of proton exchange membranes, but so far these types of fillers have not proven extremely useful for enhancing conductivity. Heteropolyacids are recognized as some of the most promising additives for enhancing the proton conductivity of nanocomposite membranes, but there are still barriers to creating robust membranes from these water-soluble additives. Sulfonated metal oxides and other sulfonated insoluble fillers that greatly enhance the ion exchange capacity of the membrane, yet do not cause drastic increases in water swelling and are thus a promising route to organic/inorganic nanocomposites where both phases contribute to the ion transport of the membrane. Other types of proton exchange membrane nanocomposites have been demonstrated with self-humidifying functionality (*33*) and degradation tolerace (*34*) and the field remains open for creating materials with properties that are not accessible using only polymers.

Nanocomposites of sulfonated poly(sulfone) and phosphotungstic acid or zirconium phosphate were investigated for their transport properties and interactions with water. Phophotungstic acid fillers tended to enhance transport as opposed to zirconium phosphate. The difference in water binding properties as measured using pulsed-field gradient nuclear magnetic resonance were shown to account for the transport properties in each case. The idea of the absorbed water behavior in the membrane controlling the transport phenomena gives researchers a frame of reference in the design of new membranes with specific properties. Through the use of nanocomposites, both the physical pathways for transport through the membrane and the water-material interactions can be modified, which will facilitate new materials with novel properties were the proton, water, and reactant transport can be decoupled.

Downloaded by UNIV OF GUELPH LIBRARY on June 22, 2012 | http://pubs.acs.org
Publication Date (Web): March 11, 2010 | doi: 10.1021/bk-2010-1034.ch011

## Acknowledgments

The author thanks James E. McGrath and his research group at Virginia Tech and the Electronic and Electrochemical Materials and Devices, MST-11 at Los Alamos National Laboratory with Bryan Pivovar where a significant amount of the data shown here was collected during the author's PhD studies. The Penn State Materials Research Institute and Penn State Institutes of Energy and the Environment are also acknowledged for their support.

## References

1. Staiti, P.; Minutoli, M.; Hocevar, S. *J. Power Sources* **2000**, *90*, 231–235.
2. Poltarzewski, Z.; Wieczorek, W.; Przyhuski, J.; Antonucci, V. *Solid State Ionics* **1999**, *119*, 301–304.
3. Malers, J. L; Sweikart, M.-A.; Horan, J. L.; Turner, J. A.; Herring, A. M. *J. Power Sources* **2007**, *172*, 83–88.
4. Horan, J. L.; Genupur, A.; Ren, H.; Sikora, B. J.; Kuo, M.-C.; Meng, F.; Dec, S. F.; Haugen, G. M.; Yandrasits, M. A.; Hamrock, S. J.; Frey, M. H.; Herring, A. M. *ChemSusChem* **2009**, *2*, 226–229.
5. Satterfield, M. B.; Majsztrik, P. W.; Ota, H.; Benziger, J. B.; Bocarsly, A. B. *J. Polym. Sci., Part B: Polym. Phys.* **2006**, *44*, 2327–2345.
6. Miyake, N.; Wainright, J. S.; Savinell, R. F. *J. Electrochem. Soc.* **2001**, *148* (8), A905–A909.
7. Adjemian, K. T.; Dominey, R.; Krishnan, L.; Ota, H.; Majsztrik, P.; Zhang, T.; Mann, J.; Kirby, B.; Gatto, L.; Velo-Simpson, M.; Leahy, J.; Srinivasan, S.; Benziger, J. B; Bocarsly, A. B. *Chem. Mater.* **2006**, *18*, 2238–2248.
8. Adjemian, K. T.; Lee, S. J.; Srinivasan, S.; Benziger, J.; Bocarsly, A. B. *J. Electrochem. Soc.* **2002**, *149* (3), A256–A261.
9. Patil, Y.; Mauritz, K. A. *J. Appl. Polym. Sci.* **2009**, *113*, 3269–3278.
10. Ruichun, J.; Kunz, H. R.; Fenton, J. M. *J. Membrane Sci.* **2006**, *272* (1-2), 116–124.
11. Lee, C. H.; Min, K. A.; Park, H. B.; Hong, Y. T.; Jung, B. O.; Lee, Y. M. *J. Membr. Sci.* **2007**, *303*, 258–266.
12. Lee, K.; Nam, J.-H.; Lee, J. H.; Lee, Y.; Cho, S.M.; Jung, C.H.; Choi, H. G.; Chang, Y.-Y.; Kwon, Y.-U.; Nam, J.-D. *Electrochem. Commun.* **2005**, *7*, 113–118.
13. Jung, D. H.; Cho, S. Y.; Peck, D. H.; Shin, D. R.; Kim, J. S. *J. Power Sources* **2003**, *118*, 205–211.
14. Su, Y.-H.; Liu, Y.-L.; Sun, Y.-M.; Lai, J.-Y.; Wang, D.-M.; Gao, Y.; Liu, B.; Guiver, M. D. *J. Membr. Sci.* **2007**, *296*, 21–28.
15. Rhee, C. H.; Kim, Y.; Lee, J. S.; Kim, H. K.; Chang, H. *J. Power Sources* **2006**, *159*, 1015–1024.
16. Nam, S.-E.; Kim, S.-O.; Kang, Y.; Lee, J. W.; Lee, K.-H. *J. Membrane Sci.* **2008**, *322*, 466–474.

Downloaded by UNIV OF GUELPH LIBRARY on June 22, 2012 | http://pubs.acs.org
Publication Date (Web): March 11, 2010 | doi: 10.1021/bk-2010-1034.ch011

17. Gosalawit, R.; Chirachanchai, S.; Shishatskiy, S.; Nunes, S. P. *J. Membr. Sci.* **2008**, *323* (2), 337–346.
18. Kim, Y. S.; Wang, F.; Hickner, M.; Zawodzinski, T. A.; McGrath, J. E. *J. Membr. Sci.* **2003**, *212* (1-2), 263–282.
19. Ramani, V.; Kunz, H. R.; Fenton, J. M. *J. Membr. Sci.* **2004**, *232* (1-2), 31–44.
20. Vernon, D. R.; Meng, F.; Dec, S. F.; Williamson, D. L.; Turner, J. A.; Herring, A. M. *J. Power Sources* **2005**, *139* (1-2), 141–151.
21. Alberti, G.; Casciola, M.; Palombari, R. *J. Membr. Sci.* **2000**, *172*, 233–239.
22. Alberti, G.; Constantino, U.; Casciola, M.; Ferroni, S.; Massinelli, L.; Staiti, P. *Solid State Ionics* **2001**, *145*, 249–255.
23. Wang, F.; Hickner, M.; Kim, Y.; Zawodzinski, T.; McGrath, J. E. *J. Membr. Sci.* **2002**, *197*, 231–242.
24. Grot, W. G.; Rajendran, G. U.S. Patent 5,919,583 to E.I. du Pont de Nemours and Company, 1999.
25. Fujimoto, C. H.; Hickner, M. A.; Cornelius, C. J.; Loy, D. A. *Macromolecules* **2005**, *38* (12), 5010–5016.
26. Hickner, M. A.; Fujimoto, C. H.; Cornelius, C. J. *Polymer* **2006**, *47* (11), 4238–4244.
27. Ren, X. M.; Henderson, W.; Gottesfeld, S. *J. Electrochem. Soc.* **1997**, *144* (9), L267–L270.
28. Hibbs, M. R.; Hickner, M. A.; Alam, T. M.; McIntyre, S. K.; Fujimoto, C. H.; Cornelius, C.J. *Chem. Mater.* **2008**, *20* (7), 2566–2573.
29. Ren, X.; Springer, T. E.; Gottesfeld, S. *J. Electrochem. Soc.* **2000**, *147* (1), 92–98.
30. Pivovar, B. S.; Wang, Y.; Cussler, E. L. *J. Membrane Sci.* **1999**, *154* (2), 155–162.
31. Hickner, M. A.; Kim, Y.; Wang, F.; McGrath, J. E.; Zawodzinski, T. A. *Proc. Am. Soc. Compos. Tech., Conf.* **2001**, 323–336.
32. Hickner, M. A.; Pivovar, B. *Fuel Cells* **2005**, *5* (2), 213–229.
33. Watanabe, M.; Uchida, H.; Emori, M. *J. Phys. Chem. B* **1998**, *102* (17), 3129–3137.
34. Trogadas, P.; Parrondo, J.; Ramani, V. *ECS Trans.* **2008**, *16* (2), 1725–1733.

Downloaded by UNIV OF GUELPH LIBRARY on June 22, 2012 | http://pubs.acs.org
Publication Date (Web): March 11, 2010 | doi: 10.1021/bk-2010-1034.ch011

Downloaded by CORNELL UNIV on June 22, 2012 | http://pubs.acs.org
Publication Date (Web): March 11, 2010 | doi: 10.1021/bk-2010-1034.ch012

## Chapter 12

# Nanohybrid Nafion Membranes for Fuel Cells

**Antonios Kelarakis, Rafael Herrera Alonso, Huiqin Lian,
Engin Burgaz, Luiz Estevez, and Emmanuel P. Giannelis***

**Materials Science and Engineering, Cornell University, Ithaca, NY 14853
*epg2@cornell.edu**

We review strategies to produce Nafion nanohybrid membranes with improved properties based on functionalized silica and clay nanoparticles. Two distinct approaches are presented here: a) the use of $H^+$-exchanged clay platelets to act as physical barriers to methanol diffusion, while having high levels of ionic mobility and b) the application of depletion forces to construct a compact microstructure based on the assembly of clay platelets. Both classes of hybrids exhibit significantly improved selectivity (ratio of ionic conductivity over methanol permeability) and dramatically enhanced thermomechanical properties. Those characteristics are highly desirable for fuel cell applications and strongly depend on the morphological features of the membranes.

## Introduction

Sustainability is widely recognized as a right and an obligation of modern societies. Mayor environmental concerns coupled with a projected decline of fossil fuel sources point to the realization that global energy policies and practices should respond to the growing demand for alternative sustainable energy sources. In this respect, polymer electrolyte membrane (PEM) fuel cells and direct methanol fuel cells (DMFCs) are considered viable energy generators for a number of portable and stationary applications, where both high power efficiency and light weight are required at a minimal environmental cost (*1–4*). DMFCs offer several advantages over hydrogen-fed fuel cells: higher energy density per unit volume, existing infrastructure for fuel management, and the ability to produce methanol from biomass or natural gas (*5–7*). Prototypes of

In Functional Polymer Nanocomposites for Energy Storage and Conversion; Wang, Q., et al.;
ACS Symposium Series; American Chemical Society: Washington, DC, 2010.

several electronic devices that rely exclusively on DMFCs sources have been demonstrated by a number of companies, while an increasing amount of effort is directed towards further research and development of DMFCs.

An integral part of a fuel cell is the electrolyte, that ideally must be stable towards oxidation, reduction, hydrolysis and other degradation mechanisms over a broad temperature and humidity range, while maintaining high levels of ionic conductivity, low levels of parasitic energy losses and almost zero electronic conductivity.

However, the development of polymer electrolytes membranes (PEM) that endures the aggressive fuel cell environment for a long period of time remains a critical challenge for advancing fuel cell technology. It is generally recognized that a number of issues must be overcome before DMFCs become a competing alternative to internal combustions engines and meet the standards of commercialization. One major drawback in DMFCs is the low oxidation kinetics of methanol at temperatures below 100°C, which leads to lower efficiency (*8*, *9*). Increasing the device operation temperature would increase the electro-oxidation kinetics and improve the performance of DMFCs. Nevertheless, even the state-of-the-art electrolytes can only operate in a narrow temperature window, showing a loss of performance at elevated temperatures due to softening of the polymeric backbone as well as decreased conductivity due to dehydration (*10*, *11*). The second major drawback in conventional DMFC membranes is the high methanol crossover, which leads to depolarization of the cathode and conversion losses (*12*, *13*).

Fuel cells based on perfluorosulfonic acid (PFSA) polymer membranes are currently the workhorse of the industry and serve as the benchmark for future development (*14–16*). PFSA polymers have a Teflon-like molecular backbone with perfluoroether side chains bearing sulfonic acid terminal groups. This molecular design imparts morphological stability and excellent long-term durability in both oxidative and reductive environments, rarely seen in other macromolecules (*3*). The combination of an extremely hydrophobic perfluorinated backbone with the extremely hydrophilic sulfonic acid functional groups gives rise to nanometer scale hydrophobic/hydrophilic domains (*17*). The interconnectivity between the ionic clusters facilitates the transportation of ions and polar molecules.

To date different approaches have been used to improve the performance of polymer membranes used in DMFCs. These approaches can be classified into two main strategies: 1) synthetic routes to produce polymers with modified chemical structure such as alternative sulfonate polymers (e.g. sulfonated polyaromatics and polyheterocyclic) or acid-base polymers (e.g. phosphoric acid-doped polybenzimidazole (PBI)) (*18*, *19*) and 2) design and preparation of hybrid materials based on existing polyelectrolytes, mainly by embedding nanoparticles to the polymeric matrix.

In this chapter we focus mainly on Nafion/nanohybrid membranes based on silicate nanoparticles (*20*, *21*). The swelling and hydration efficacy of clays largely depends on their cation-exchange capacity, which typically falls within the range 0.65 to 1.50 meq/g (*22*).When fully hydrated, clay particles posses high proton conductivity ($0.6\times10^{-2}$ S/cm) (*23*). The water is strongly adsorbed and

Downloaded by CORNELL UNIV on June 22, 2012 | http://pubs.acs.org
Publication Date (Web): March 11, 2010 | doi: 10.1021/bk-2010-1034.ch012

can only be fully removed at temperatures in excess of 130 °C. Moreover, it is now well established that clay based polymer nanocomposites exhibit enhanced barrier properties due to the presence of impermeable, high aspect ratio inorganic particles (*24*). At the same time, pronounced structural changes in the polymer can be induced by clay platelets (*25*, *26*). A number of papers describe the synthesis and characterization of Nafion membranes based on sulfonated (*27–32*), fluoro-modified (*33*, *34*) conventional organo-modified (*35–37*) or native clays (*37*). Other approaches for synthesizing Nafion-clay hybrids have also been explored (*38*, *39*).

We review here recent work in our group to produce nanohybrids membranes (*40*, *41*). Our goal is not to present a complete literature review in the topic. We refer interested readers to a number of recent reports that provide a comprehensive synopsis of the substantial body of work published in this field (*7*, *16*, *18*, *42*). We emphasize, however, that a comparison between different performance characteristics reported in the literature is not always straightforward. Significant variations in processing protocols, membrane activation treatments, various device and techniques used to evaluate macroscopic properties can lead to pronounced discrepancies, making a meaningful comparison challenging. Nevertheless, careful consideration of the work reported can identify promising approaches and lead to the design of a new generation of fuel cells with improved performance.

Downloaded by CORNELL UNIV on June 22, 2012 | http://pubs.acs.org
Publication Date (Web): March 11, 2010 | doi: 10.1021/bk-2010-1034.ch012

## Morphology and Structural Characteristics of Nanohybrids

### 1. Dispersion Medium and Casting Process

The crystallinity of Nafion and the state of dispersion of nanoclays critically depend on the processing protocol followed for the preparation of hybrid materials. By optimizing the dispersion medium and the overall processing conditions, we were able to synthesize homogenous and mechanically robust free-standing membranes. Very poor dispersion of clay was obtained for membranes casted from high-boiling solvents, otherwise widely used for neat Nafion membranes, such as dimethylformamide (DMF), n-methylformamide (NMF), dimethyl sulfoxide ($Me_2SO$) (*43*). In fact, in those Nafion-solvent combinations the nanoparticles were clearly seen to phase separate and flocculate. Casting from water-alcohol mixtures also resulted in insufficient clay dispersion and was not considered further.

In contrast, homogeneous and well-dispersed Nafion nanohybrid membranes were prepared by casting at elevated temperatures (>160 °C) under pressure (15 psi) using aqueous precursor solutions. Casting at lower temperature leads to significantly lower crystallinity that has an adverse effect on the mechanical properties of the membranes. When the cast temperature is higher than the α relaxation of Nafion, there is sufficient mobility to allow for refolding of the polymer chain to crystallize (*44*). The morphological characteristics of the nanohybrid membranes are presented in the following sections. Unless otherwise stated, membranes were cast at T > 160 °C at 15 psi for 6h followed by acid post-treatment. In all cases studied here, deconvolution of the diffraction peaks of Nafion into a crystalline and an amorphous component indicates that the insertion of nanoparticles does not affect the crystallinity of Nafion.

## 2. MMT-$H^+$/Nafion Membranes

Prior to mixing with Nafion, the counterions of pristine sodium montmorillonite (MMT-$Na^+$) were replaced by $H^+$, through a facile ion exchange procedure, with the goal of minimizing any adverse effects on ionic conductivity induced by the clay particles. MMT-$H^+$/Nafion membranes were obtained from water dispersions cast at 180 °C, 15 psi for 6h.

The featureless X-Ray Diffraction (XRD) patterns at low scattering vectors (q) suggest that the structural registry of clay tactoids is destroyed in the nanohybrids. We note that the picture emerging from XRD patterns is essentially the mosaic of various local dispersion levels, while TEM imaging can provide crucial insights about the organization of clay platelets in a more localized scale. A representative Transmission Electron Microscopy (TEM) image shown in Figure 1 confirms an intercalated/exfoliated structure for 10wt% MMT-$H^+$/Nafion hybrid.

Interpretation of the scattering peaks at lower q values remains a subject of open debate (*45*). In this respect, numerous models have been proposed following the early approach of a spheroidal cluster-channel suggested from Gierke (*46*). Alternative approaches have recently emerged in literature that depict Nafion as a percolated network of bundles of elongated polymeric aggregates (*47*) or as a network of parallel ionic nanochannels inside cylindrical inverted micelles stabilized by the rigid polymeric backbone (*48*). Regardless of the exact nature of morphological features adopted from the several models proposed for Nafion, the recognition of two characteristic scattering maxima in the Small Angle X-ray Scattering (SAXS) region is unambiguous.

First the characteristic ionomer peak at ca. q=1-2 $nm^{-1}$ has been attributed to ionic clustering due to polar-non polar separation. Second, the matrix knee peak at ca. q= 0.4-0.5 $nm^{-1}$ has been originally assigned to the interlamelar long spacing in the crystalline region of the polymer, although recent investigations suggest that the repeat is orthogonal to the polymer chain axis (*48*, *49*). In addition, a sharp upturn of the scattering curve at very low q values (q<1 $nm^{-1}$) has been related to higher-order electron density fluctuations (*47*, *50*, *51*).

SAXS data on fully hydrated membranes were collected in two orthogonal directions; the *normal* plane, parallel to the membrane surface and the *transverse* plane which is orthogonal to the membrane surface (Figure 2). Both SAXS profiles of pure Nafion are essentially isotropic, showing two distinct rings centered at ca. q=1.31 $nm^{-1}$ (d= 4.8 nm) and ca. q=0.4 $nm^{-1}$ for the ionomer and the matrix knee, respectively. In contrast, the SAXS profiles of the transverse plane for the nanohybrid membranes are clearly anisotropic, indicating that the bundles of polymeric aggregates tend to align parallel to the membrane surface, while they are uniformly distributed along the thickness of the membrane. At the same time, the orientation of the polymeric lamella peak is orthogonal to that from the ionic

Downloaded by CORNELL UNIV on June 22, 2012 | http://pubs.acs.org
Publication Date (Web): March 11, 2010 | doi: 10.1021/bk-2010-1034.ch012

Downloaded by CORNELL UNIV on June 22, 2012 | http://pubs.acs.org
Publication Date (Web): March 11, 2010 | doi: 10.1021/bk-2010-1034.ch012

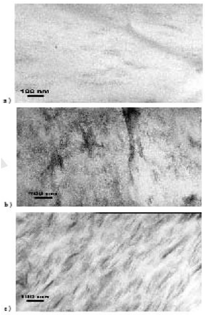

*Figure 1. TEM images of cross-sections of 10wt% MMT-H$^+$/Nafion membrane. (Reproduced with permission from reference (40). Copyright 2009 Elsevier Ltd.)*

domains in agreement with previous reports for moderately stretched pure Nafion (*47*). This observation further supports the conclusion that the matrix knee peak primarily arises from a repeat that is perpendicular to the polymer chain axis (*48*, *49*). The ionomer peak and the matrix knee peak are displaced to higher q values with increasing clay loading due to the suppression of the ionic domains and the fragmentation of the lamellar superstructure induced by MMT-H$^+$.

It has been observed in a number of systems (*52*, *53*) that clay platelets tend to align parallel to the membrane surface, under certain conditions. Presumably, this preferential orientation originates from gravitational forces experienced by the platy nanoparticles while remaining well dispersed in a low viscosity medium. The aligned arrays of stiff platelets effectively template, in turn, the organization of the polymer. A schematic representation of the organization of polymeric bundles is shown in Figure 3a and 3b for plain Nafion and nanohybrid membranes respectively. Note the short-range order of polymeric aggregates in pure Nafion, as opposed to the long-range order in nanohybrid membranes.

Anisotropic Nafion membranes have been prepared before by applying electrical field (*54*) or uniaxial deformation (*55*, *56*). In our system, the alignment of the polymeric bundles in the MMT-H$^+$/Nafion nanohybrid membranes has been produced in the absence of any external field and it is solely induced by the 2-D nature of the nanoparticles.

## 3. Functionalized Silica/Nafion Membranes (HS30SIT/Nafion and TEOS:SIT/Nafion)

Two types of Nafion hybrid membranes based on functionalized silicon dioxide ($SiO_2$) have been cast from water suspensions at 180 °C, 15 psi for 6h, to allow a close comparison between different nanoparticles (*57*). In the first case (denoted hereafter as HS30SIT/Nafion), $SiO_2$ spheres with a diameter of ca. 12 nm were surface modified by 3-(trihydroxysilyl)-1-propanesulfonic acid (PSA) followed by replacement of sodium counter ions by H$^+$, so that the resultant nanoparticles were densely covered by sulfonic acid groups (-$SO_3H$). The ion exchange capacity of the modified $SiO_2$ nanoparticles was 1.46 meq/g.

Downloaded by CORNELL UNIV on June 22, 2012 | http://pubs.acs.org
Publication Date (Web): March 11, 2010 | doi: 10.1021/bk-2010-1034.ch012

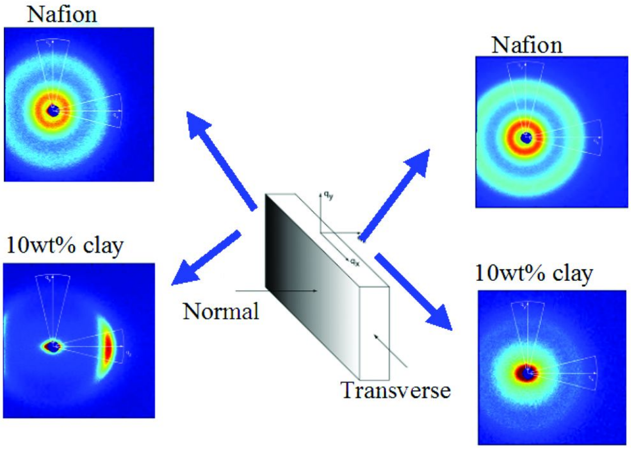

*Figure 2. SAXS patterns of pure Nafion and a 10wt% MMT-$H^+$/Nafion nanocomposite obtained in two orthogonal directions: normal plane (surface parallel to the membrane surface) and transverse plane (cross-section of the membrane). (Reproduced with permission from reference (40). Copyright 2009 Elsevier Ltd.)*

Besides HS30SIT/Nafion membranes, another class of hybrid materials containing silica particles was also synthesized in-situ by a sol-gel reaction following a procedure described previously by Adjemian et al. (*58*). A 1:2 mixture of tetraethoxysilane (TEOS) and PSA was allowed to react with water, before being blended with aqueous Nafion dispersions to give Nafion-silica hybrids, abbreviated here as TEOS:SIT/Nafion. During casting, water is evaporated, thus promoting further polymerization and cross-linking between hydrolyzed TEOS and PSA. The ion exchange capacity of these networks exceeds 2 meq/g.

TEM images of 7wt% HS30SIT/Nafion and 16wt% TEOS:SIT/Nafion nanohybrid membranes suggest that the nanoparticles are uniformly distributed within the matrix. Additionally for both classes of nanohybrid membranes, the SAXS patterns of normal and transverse planes were isotropic.

## 4. Nafion/Clay Hybrids with a Network Structure

An alternative approach was developed to produce hybrid membranes with a unique microstructure by exploiting phase separation based on depletion aggregation. Application of depletion interactions to induce phase separation has raised a substantial interest in experiments (*59*, *60*), theory (*61*, *62*), and simulations (*63*, *64*) over the last decades.

Addition of a non-adsorbing polymer to a colloidal suspension induces interparticle depletion attractions, whose range and depth can be tuned independently by altering either the polymer's molecular weight or concentration (*65*, *66*). Such attractive interactions arise due to osmotic pressure differences

Downloaded by CORNELL UNIV on June 22, 2012 | http://pubs.acs.org
Publication Date (Web): March 11, 2010 | doi: 10.1021/bk-2010-1034.ch012

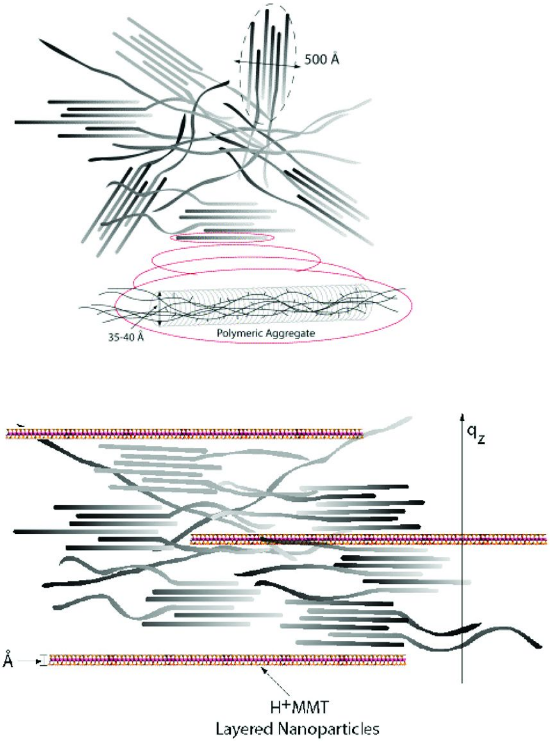

*Figure 3. Schematic representation of bundles consisting of locally ordered polymeric elongated aggregates (adopted from reference (50)) (top). Schematic of MMT-H$^+$/Nafion membrane morphology: bundles of polymeric aggregates oriented parallel to the membrane surface (bottom). (Reproduced with permission from reference (40). Copyright 2009 Elsevier Ltd.)*

surrounding the particles and can lead to particle clustering and, in some cases, formation of a percolated network of particles, which eventually leads to gelation.

Nafion possesses charges of the same sign as the clay surface, therefore it can serve the role of the non-absorbed, non-interacting polymer when added in a clay suspension (here MMT-Na$^+$ in water). The phase diagram of MMT-Na$^+$/Nafion in water is shown in Figure 4. Sol/gel boundaries were detected by tube inversion, a simple method that is sensitive to yield stress of the sample. The dividing line separates samples that form a gel (immobile) from those that remain either in suspension (homogenous, mobile) or flocculate and phase separate (inhomogeneous). Clay suspensions even in the absence of a polymer are known to form a gel primarily through edge-to-face interactions. As Figure 4 suggests gelation at lower clay concentrations can be induced in the presence of Nafion.

Addition of Nafion leads to either flocculation as the laminated face-to-face aggregates grow in size or gelation, promoted by several edge-to-face interactions (Figure 5).

Figure 6a presents a cryo-TEM image of 23wt% MMT-Na$^+$/Nafion gel before any drying. Thin face-to-face aggregates composed only of a few layers

Downloaded by CORNELL UNIV on June 22, 2012 | http://pubs.acs.org
Publication Date (Web): March 11, 2010 | doi: 10.1021/bk-2010-1034.ch012

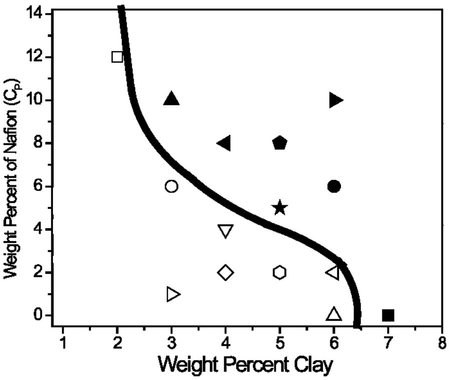

*Figure 4. Phase diagram for the MMT-Na$^+$/Nafion system in water. Filled symbols represent gel samples (immobile). Samples that have not led to a gel (sols) are shown with non-filled symbols. (Reproduced with permission from reference (41). Copyright 2009 Elsevier Ltd.)*

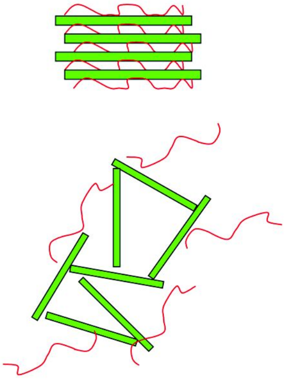

*Figure 5. Schematic representing clay-polymer systems: face-to-face aggregation (top) and edge-to-face aggregation (bottom). (Reproduced with permission from reference (41). Copyright 2009 Elsevier Ltd.)*

are connected with each other into a network structure via several edge-to-face interactions.

A series of composite membranes (abbreviated as MMT-Na$^+$/Nafion(dep)) was prepared by casting hybrid gels at 160°C and 160 psi for 6 h. During casting (at conditions far away from supercritical drying) surface tension forces can cause serious defects to the network microstructure. This can be confirmed by the TEM micrograph of the 23wt% hybrid membrane shown in Figure 6b. Clearly, more face-to-face aggregation is present at the expense of edge-to-face aggregates seen in the gels.

Downloaded by CORNELL UNIV on June 22, 2012 | http://pubs.acs.org
Publication Date (Web): March 11, 2010 | doi: 10.1021/bk-2010-1034.ch012

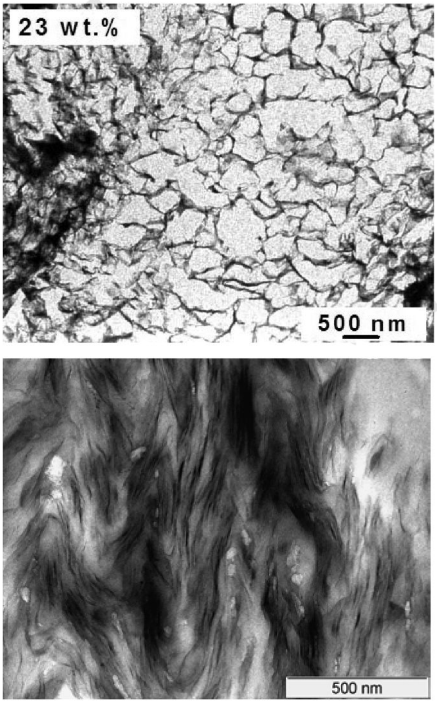

*Figure 6. Cryo-TEM of MMT-Na$^+$/Nafion hybrids; a) before any drying (top) and b) after drying (bottom). (Reproduced with permission from reference (41). Copyright 2009 Elsevier Ltd.)*

## Performance Characteristics of Hybrid Membranes

### 1. Mechanical Properties

The Dynamic mechanical analysis (DMA) traces of Nafion and two MMT-H$^+$ hybrid membranes are shown in Figure 7a. Pure Nafion shows a high-temperature $\alpha$ transition at around 125°C, while the $\beta$ transition falls outside the temperature window considered here. The $\alpha$ relaxation of the nanocomposites shifts to higher temperatures with clay loading. For the 20 wt% MMT-H$^+$/Nafion nanohybrid the a transition takes place at 215 °C and it appears much suppressed compared to pure Nafion. At the same time, the hybrids show significant enhancements in terms of storage modulus. The nanocomposite containing 20wt% clay shows a 6 times increase at low temperatures and orders of magnitude above ~ 100 °C.

The DMA plots of hybrid MMT-Na$^+$/Nafion(dep) membranes before acid treatment are shown in Figure 7b. Although pure Nafion shows a single relaxation, the hybrid membranes show two distinct relaxations. The first one is rather weak and it varies within the range 75 to 120 °C depending on the clay concentration, while the second relaxation is dominant and takes place around 230 °C for all hybrids.

Downloaded by CORNELL UNIV on June 22, 2012 | http://pubs.acs.org
Publication Date (Web): March 11, 2010 | doi: 10.1021/bk-2010-1034.ch012

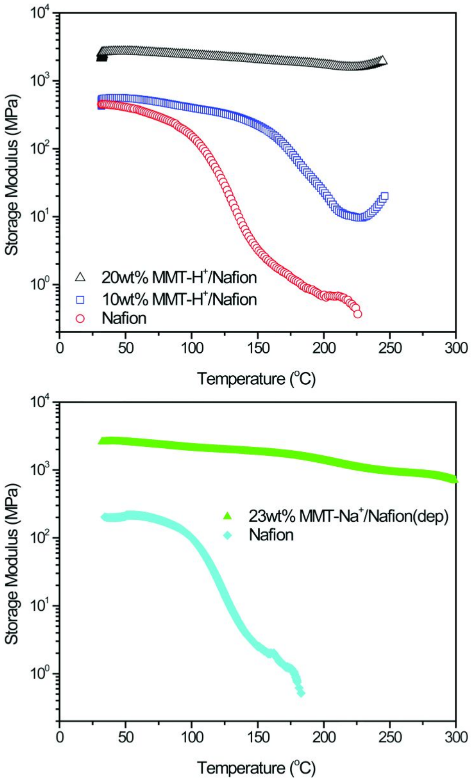

*Figure 7. Storage modulus as a function of temperature of MMT-H$^+$/Nafion hybrids (top) and MMT-Na$^+$/Nafion(dep) (bottom). (Reproduced with permission from references (40) and (41). Copyright 2009 Elsevier Ltd.)*

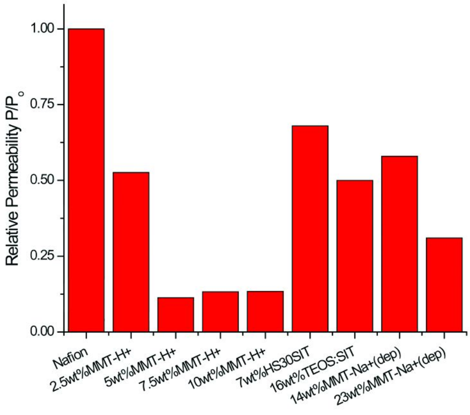

*Figure 8. Relative methanol permeability for Nafion nanohybrid membranes. (Data from references (40) and (41)).*

Downloaded by CORNELL UNIV on June 22, 2012 | http://pubs.acs.org
Publication Date (Web): March 11, 2010 | doi: 10.1021/bk-2010-1034.ch012

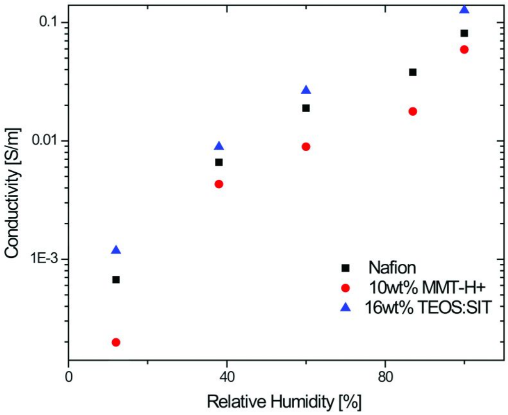

*Figure 9. Ionic conductivity as a function of relative humidity of Nafion nanohybrids membranes. (Data from references (40, 57)).*

Given that the Na$^+$-exchanged Nafion shows a distinct *α* (ca. 240 °C) and weak *β* (ca. 150°C) relaxation (*67*) a partial ion exchange reaction between the polymer protons and the clay counter ions can contribute to the enhanced dynamics of hybrid membranes. However, even in the acid treated membranes (where Na$^+$ was essentially eliminated) the a relaxation occurs at 160°C, e.g much higher than that observed for pure Nafion. In addition to the temperature shift, the hybrids show dramatic increases in modulus (Figure 7b).

For example, the sample containing 23wt% clay shows at room temperature a storage modulus about 10 times that of Nafion and several orders of magnitude higher at elevated temperatures.

The overall DMA analysis reveals that both types of clay/Nafion hybrid membranes are much stiffer and can withstand higher temperatures compared to pure Nafion. Both of these characteristics are highly desirable for use in fuel cell applications. A higher modulus might allow the use of a thinner membrane circumventing problems associated with the membrane resistance. Additionally, the mechanical strength at high temperature enables application requiring temperatures in excess of 100 °C. The profound displacement and suppression of α-relaxation observed for all hybrids can be directly related to the molecular confinement in the vicinity of polymer-clay interface that drastically hinders the polymer chain motions.

## 2. Transport Properties

### *a. Methanol Permeability*

As mentioned in the introduction methanol permeability through the electrolyte membrane is a critical performance parameter of a DMFC. Methanol permeability was measured using a two-compartment cell. Permeability values were normalized to the value for pure Nafion ($P_0$= 6.08×10$^{-6}$ cm$^2$/s).

Downloaded by CORNELL UNIV on June 22, 2012 | http://pubs.acs.org
Publication Date (Web): March 11, 2010 | doi: 10.1021/bk-2010-1034.ch012

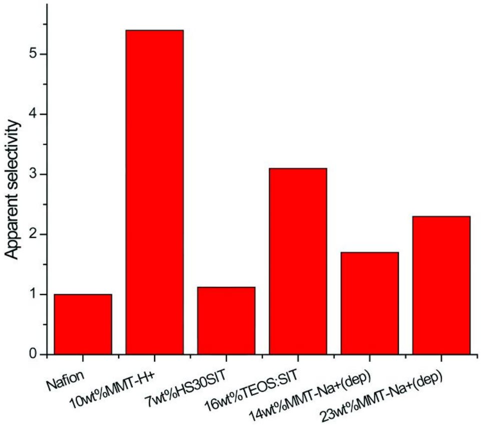

*Figure 10. Apparent selectivity of various Nafion nanohybrid membranes. (Data from references (40) and (41)).*

A pronounced decrease of methanol permeability was observed for 5-10wt% MMT-$H^+$/Nafion nanohybrid membranes as shown in Figure 8.

Methanol permeability was also found to decrease, albeit to a lesser extend in both classes of silica/Nafion membranes. For the MMT-$Na^+$/Nafion membranes containing 14wt% and 23wt% clay, the relative permeability was approximately 0.5 and 0.3, respectively. Higher amounts of functionalized silica particles are required in order to achieve a substantial decrease in permeability compared to those based on clay.

## *b. Ionic Conductivity*

Enhanced ionic conductivity is a crucial requirement for PEM fuel cells. In our work, ionic conductivity was measured at room temperature in a closed vessel under a controlled relative humidity (RH) environment. The resistance and ultimately the conductivity ($\sigma$) of the membrane was measured by alternating current (AC) impedance spectroscopy, using a two-point probe. We note that, in the specific configuration employed here, the conductivity measured is a combination of both normal (through-plane) and transverse (in plane) direction and thus we cannot rule out any anisotropy for the conductivity of nanocomposites.

The ionic conductivity of pure Nafion is compared with 10wt% MMT-$H^+$/Nafion nanohybrid at various RH in Figure 9.

The hybrid membrane follows a similar trend to the pure Nafion; the conductivity increases with increasing RH. At the same time, the differences in conductivity between Nafion and the hybrid membranes becomes progressively larger at low RH. This deviation can be attributed to the much lower intrinsic ionic conductivity of clay nanoparticles compared to Nafion. On the other hand, at fully hydrated conditions Nafion and MMT-$H^+$ exhibit comparable conductivity (ca. 0.08 S/cm and 0.01 S/cm, respectively). Very similar trends were observed for MMT-$Na^+$/Nafion(dep) membranes.

The ionic conductivity of 16wt% TEOS:SIT/Nafion membranes as a function of RH is also shown in Figure 9. We note that this membrane has not been subject to acid treatment that typically yields higher conductivity values. Nevertheless, it is remarkable that it exhibits consistently higher ionic conductivity even when compared to acid activated pure Nafion membranes.

### *c. Selectivity*

The selectivity term ($\kappa$) is defined as the ratio of ionic conductivity to methanol permeability of the membrane and is widely used as a criterion to evaluate the performance of DMFCs. Conventionally, the selectivity of Nafion is set to one. In this work, we favor the term *apparent selectivity*, to account for the highly anisotropic nature of the MMT-$H^+$/Nafion membranes. It must be clarified that selectivity values presented below have been derived for RH=100%.

Figure 10 shows the *apparent selectivity* parameters for 10wt% MMT-$H^+$/Nafion, 16wt% TEOS:SIT/Nafion, 7wt% HS30SIT/Nafion and two MMT-$Na^+$/Nafion(dep) membranes.

Clearly, all hybrids considered here exhibit a better *apparent selectivity* compared to pure Nafion. The highest apparent selectivity was obtained for 10wt% MMT-$H^+$/Nafion, mainly due to its lowest methanol permeability and its relatively high conductivity when fully hydrated. Significantly, 16wt% TEOS:SIT/Nafion also exhibit enhanced selectivity followed by the 23wt% MMT-$Na^+$/Nafion(dep) membrane. For the clay based hybrids, the decrease of ionic conductivity is more than compensated by the large suppression of methanol permeability. That coupled with improved mechanical mechanical strength makes clay-Nafion nanohybrids very attractive for DMFC applications.

## References

1. Dohle, H.; Divisek, J.; Mergel, J.; Oetjen, H. F.; Zingler, C.; Stolten, D. *J. Power Sources* **2002**, *105*, 274–282.
2. Guraua, B.; Smotkin, E. S. *J. Power Sources* **2002**, *112*, 339–352.
3. Wakizoe, M.; Velev, O. A.; Srinivasan, S. *Electrochim. Acta* **1995**, *40*, 335–344.
4. Carrette, L.; Friedrich, K. A.; Stimming, U. *Fuel Cells* **2001**, *1*, 5–39.
5. Carrette, L.; Friedrich, K. A.; Stimming, U. *ChemPhysChem.* **2000**, *1*, 162–193.
6. Li, X.; Roberts, E. P. L.; Holmes, S. M.; Zholobenko, V. *Solid State Ionics* **2007**, *178*, 1248–1255.
7. Neburchilov, V.; Martin, J.; Wang, H.J.; Zhang, J. *J. Power Sources* **2007**, *169*, 221–238.
8. Ren, X. M.; Wilson, M. S.; Gottesfeld, S. *J. Electrochem. Soc.* **1996**, *143*, L12–L15.
9. Chu, D.; Gilman, S. *J. Electrochem. Soc.* **1994**, *141*, 1770–1773.

Downloaded by CORNELL UNIV on June 22, 2012 | http://pubs.acs.org
Publication Date (Web): March 11, 2010 | doi: 10.1021/bk-2010-1034.ch012

10. Li, Q. F.; He, R. H.; Jensen, J. O.; Bjerrum, N. J. *Chem. Mater.* **2003**, *15*, 4896–4915.
11. Hogarth, W. H. J.; da Costa, J. C. D.; Lu, G. Q. *J. Power Sources* **2005**, *142*, 223–237.
12. Heinzel, A.; Barragan, V. M. *J. Power Sources* **1999**, *84*, 70–74.
13. Ren, X. M.; Zelenay, P.; Thomas, S.; Davey, J.; Gottesfeld, S. *J. Power Sources* **2000**, *86*, 111–116.
14. Smitha, B.; Sridhar, S.; Khan, A. A. *J. Membr. Sci.* **2005**, *259*, 10–26.
15. Saito, M.; Tsuzuki, S.; Hayamizu, K.; Okada, T. *J. Phys. Chem. B.* **2006**, *110*, 24410–24417.
16. Deluca, N. W.; Elabd, Y. A. *J. Polym. Sci., Part B: Polym. Phys.* **2006**, *44*, 2201–2225.
17. Hsu, W. Y.; Gierke, T. D. *Macromolecules* **1982**, *15*, 101–105.
18. Kreuer, K. D. *J. Membr. Sci.* **2001**, *185*, 29–39.
19. Li, Q. F.; He, R. H.; Jensen, O. J.; Bjerrum, N. *J. Chem. Mater.* **2003**, *15*, 4896–4915.
20. Ray, S. S.; Okamoto, M. *Prog. Polym. Sci.* **2003**, *28*, 1539–1641.
21. Zanetti, M.; Lomakin, S.; Camino, G. *Macromol. Mater. Eng.* **2000**, *279*, 1–9.
22. Schmidt, D. F. Ph.D. Thesis, Cornell University, Ithaca, NY, 2003.
23. Aliouane, N.; Hammouche, A.; De Doncker, R. W.; Telli, L.; Boutahala, M.; Brahimi, B. *Solid State Ionics* **2002**, *148*, 103–110.
24. Choudalakis, G.; Gotsis, A. D. *Eur. Polym. J.* **2009**, *45*, 967–984.
25. Giannelis, E. P. *Adv. Mater.* **1996**, *8*, 29–35.
26. Paul, D. R.; Robenson, L. M. *Polymer* **2008**, *49*, 3187–3204.
27. Kim, T. K.; Kang, M.; Choi, Y. S.; Kim, H. K.; Lee, W.; Chang, H.; Seung, D. *J. Power Sources* **2007**, *165*, 1–8.
28. Bebin, P.; Caravanier, M.; Galiano, H. *J. Membr. Sci.* **2006**, *278*, 35–42.
29. Thomassin, J. M.; Pagnoulle, C.; Caldarella, G.; Germain, A.; Jérôme, R. *Polymer* **2005**, *46*, 11389–11395.
30. Lin, Y.F.; Yen, C. Y.; Hung, C. H.; Hsiao, Y.H.; Ma, C. C. M. *J. Power Sources* **2007**, *168*, 162–166.
31. Kim, Y.; Lee, J. S.; Rhee, C.H.; Kim, H. K.; Chang, H. *J. Power Sources* **2006**, *162*, 180–185.
32. Rhee, C. H.; Kim, H. K.; Chang, H.; Lee, J. S. *Chem. Mater.* **2005**, *17*, 1691–1697.
33. Thomassin, J. M.; Pagnoulle, C.; Bizzari, D.; Caldarella, G.; Germain, A.; Jérôme, R. *Solid State Ionics* **2006**, *177*, 1137–1144.
34. Gosalawit, R.; Chirachanchai, S.; Shishatskiy, S.; Nunes, S. P. *Solid State Ionics* **2007**, *178*, 1627–1635.
35. Song, M. K.; Park, S. B.; Kim, Y. T.; Rhee, H. W.; Kim, J. *Mol. Cryst. Liq. Cryst.* **2003**, *407*, 411.
36. Song, M. K.; Park, S. B.; Kim, Y. T.; Kim, K. H.; Min, S. K.; Rhee, H. W. *Electrochim. Acta* **2004**, *50*, 639–643.
37. Jung, D. H.; Cho, S. Y.; Peck, D. H.; Shin, D. R.; Kim, J. S. *J. Power Sources* **2003**, *118*, 205–211.

Downloaded by CORNELL UNIV on June 22, 2012 | http://pubs.acs.org
Publication Date (Web): March 11, 2010 | doi: 10.1021/bk-2010-1034.ch012

38. Kim, D. W.; Choi, H. S.; Lee, C.; Blumstein, A.; Kang, Y. *Electrochim. Acta* **2004**, *50*, 659–662.
39. Zhang, W.; Li, M. K. S.; Yue, P. L.; Gao, P. *Langmuir* **2008**, *24*, 2663–2670.
40. Alonso, R. H.; Estevez, L.; Lian, H.; Kelarakis, A.; Giannelis, E. P. *Polymer* **2009**, *50*, 2402–2410.
41. Burgaz, E.; Lian, H.; Alonso, R. H.; Estevez, L.; Kelarakis, A.; Giannelis, E. P. *Polymer* **2009**, *50*, 2384–2392.
42. Hudiono, Y.; Choi, S.; Shu, S.; Koros, W. J.; Tsapatsis, M.; Nair, S. *Microporous Mesoporous Mater.* **2009**, *118*, 427–434.
43. Fujimura, M.; Hashimoto, T.; Kawai, H. *Macromolecules* **1981**, *14*, 1309–1315.
44. Gebel, G.; Aldebert, P.; Pineri, M. *Macromolecules* **1987**, *20*, 1425–1428.
45. Mauritz, K. A.; Moore, R. B. *Chem. Rev.* **2004**, *104*, 4535–4586.
46. Hsu, W. Y.; Gierke, T. D. *J. Membr. Sci.* **1983**, *13*, 307–326.
47. Rubatat, L.; Rollet, A. L.; Gebel, G.; Diat, O. *Macromolecules* **2002**, *35*, 4050–4055.
48. Schmidt-Rohr, K.; Chen, Q. *Nat. Mater.* **2008**, *7*, 75–83.
49. Van der Heijden, P. C.; Rubatat, L.; Diat, O. *Macromolecules* **2004**, *37*, 5327–5336.
50. Rubatat, L.; Gebel, G.; Diat, O. *Macromolecules* **2004**, *37*, 7772–7783.
51. Gebel, G.; Moore, R. B. *Macromolecules* **2000**, *33*, 4850–4855.
52. Dillon, D. R.; Tenneti, K. K.; Li, C. Y.; Ko, F. K; Sics, I.; Hsiao, B. S. *Polymer* **2006**, *47*, 1678–1688.
53. Yamada, E.; Nishioka, A.; Suzuki, H.; Koda, T.; Ikeda, S. *Jpn. J. Appl. Phys.* **2007**, *11*, 7371–7374.
54. Lin, H. L.; Yu, T. L.; Han, F. H. *J. Polym. Res.* **2006**, *13*, 379–385.
55. Rubatat, L.; Diat, O. *Macromolecules* **2007**, *40*, 9455–9462.
56. van der Heidjen, P. C.; de la Rosa, A.; Gebel, G.; Diat, O. *Polym. Adv. Technol.* **2005**, *16*, 102–107.
57. Herrera-Alonso, R. Ph.D. Thesis, Cornell University, Ithaca, NY, 2007.
58. Adjemian, K. T.; Lee, S. J.; Srinivasan, S.; Benziger, J.; Bocarsly, A. B. *J. Electrochem. Soc.* **2002**, *149*, A256–A261.
59. Lu, P. J.; Zaccarelli, E.; Ciulla, F.; Schoefield, A. B.; Sciortino, F.; Weitz, D. A. *Nature* **2008**, *453*, 499–504.
60. Manley, S.; Wyss, H. M.; Miyazaki, K.; Conrad, J. C.; Trappe, V.; Kaufman, L. J.; Reichman, D. R.; Weitz, D. A. *Phys. Rev. Lett.* **2005**, *95*, 238302.
61. Fuchs, M.; Schweizer, K. S. *Europhys. Lett.* **2000**, *51*, 621–627.
62. Aarts, D. G. A. L.; Tuinier, R.; Lekkerkerker, H. N. W. *J. Phys.: Condens. Matter* **2002**, *14*, 7551–7561.
63. Dijkstra, M.; van Roij, R.; Evans, R. *Phys. Rev. E.* **1999**, *59*, 5744–5771.
64. Bolhuis, P. G.; Louis, A. A.; Hansen, J. P. *Phys. Rev. Lett.* **2002**, *89*, 128302.
65. Anderson, V. J.; Lekkerkerker, H. N. W. *Nature* **2002**, *416*, 811–815.
66. Poon, W. C. K. *J. Phys.: Condens. Matter* **2002**, *14*, 859–880.
67. Cable, K. M. Ph.D. Thesis, The University of Southern Mississippi, Hattiesburg, MS, 1996.

Downloaded by CORNELL UNIV on June 22, 2012 | http://pubs.acs.org
Publication Date (Web): March 11, 2010 | doi: 10.1021/bk-2010-1034.ch012

Downloaded by DUKE UNIV on June 21, 2012 | http://pubs.acs.org
Publication Date (Web): March 11, 2010 | doi: 10.1021/bk-2010-1034.ch013

## Chapter 13

# Degradation Mitigation in PEM Fuel Cells Using Metal Nanoparticle and Metal Oxide Additives

**Panagiotis Trogadas,[1] Javier Parrondo,[2] and Vijay Ramani*,[1]**

**[1]Department of Chemical and Biological Engineering, Illinois Institute of Technology, Chicago, IL 60616**
**[2]Facultad de Ciencia y Technologia, University of the Basque Country, Leioa, Spain 48940**
***ramani@iit.edu**

The efficacy of added metal oxides and metal nanoparticles in mitigating free radical induced polymer electrolyte membrane (PEM) degradation was investigated. Freestanding and silica supported platinum, palladium, silver and gold nanoparticles, cerium oxide and manganese oxide supports, and ceria supported platinum nanoparticles were prepared. The nanoparticles were characterized by TEM and XRD to determine the particle and crystallite size. Their radical scavenging tendency was estimated by UV-vis spectroscopy using a model free radical (DPPH) as a test species. Composite membranes were prepared by adding 3 wt% of the freestanding or supported metal nanoparticles to Nafion®, followed by solvent casting. The fluoride emission rate (FER) was ascertained for each membrane from accelerated tests. The addition of Au, Pd, Pt and Ag nanoparticles led to lowering of FER by an order of magnitude, 75%, 60% and 35% respectively while the addition of $MnO_2$, $CeO_2$ and Pt on $CeO_2$ nanoparticles resulted in an order of magnitude FER reduction, indicating effective radical scavenging by the nanoparticles. Hence, the addition of metal nanoparticles and metal oxides with radical scavenging abilities is a promising route to mitigate PEM degradation.

In Functional Polymer Nanocomposites for Energy Storage and Conversion; Wang, Q., et al.;
ACS Symposium Series; American Chemical Society: Washington, DC, 2010.

Downloaded by DUKE UNIV on June 21, 2012 | http://pubs.acs.org
Publication Date (Web): March 11, 2010 | doi: 10.1021/bk-2010-1034.ch013

## Introduction

Membrane degradation is one of the most important factors limiting the lifetime of polymer electrolyte fuel cells (PEFCs) (*1–10*). Membrane degradation in a PEFC occurs via a multistep mechanism. The two major steps are: (*i*) formation of reactive oxygen radicals by reaction of hydrogen peroxide (generated in situ) with trace metal ions in the membrane electrode assembly (MEA) (*11*), and (*ii*) attack of weak links in the polymer backbone or side-chains by the radicals. Hydroxyl radicals (·OH) have been identified as the highly aggressive oxidative species responsible for the propagation of chemical degradation of perfluorosulfonic acid membranes (*2–4*, *11–15*). Mechanisms by which radicals attack the polymer have been proposed by various researchers (*11*, *16*, *17*). For Nafion® membranes, the commonly proposed mechanism is hydrogen abstraction from the reactive end groups (such as COOH) in the proton exchange membrane (PEM), leading to membrane decay (*5*).

Three approaches can be used to minimize the effect of reactive oxygen species in a fuel cell: (*i*) the use of free radical scavengers in the electrolyte (*17*, *18*); (*ii*) the use of dispersed peroxide decomposition catalysts within the electrolyte (*19*); and (*iii*) the use of dispersed peroxide decomposition catalysts in the electrodes (*20–23*). The first approach was used in our previous work (*18*) using $CeO_2$ nanoparticles as the free radical scavenger. We showed that the incorporation of these nanoparticles within a recast Nafion® membrane led to lowering the fluoride emission rate (obtained from degradation accelerated tests) by more than 1 order of magnitude, suggesting that $CeO_2$ nanoparticles have tremendous potential to greatly enhance membrane durability. In this study, we investigate the efficacy of metal nanoparticle based free radical scavengers, namely, platinum, palladium, gold and silver nanoparticles, in a PEFC environment.

There are previous reports about the incorporation of metal nanoparticles or metal oxides within a polymer electrolyte membrane (PEM) (*24–26*). Watanabe and coworkers (*24–26*) proposed new PEMs (Pt-PEM, $TiO_2$-PEM, Pt-$TiO_2$-PEM) with highly dispersed nanometer-size Pt and/or metal oxides. The Pt particles were expected to inhibit the crossover by the catalytic recombination of crossover $H_2$ and $O_2$. The hygroscopic oxide particles were expected to adsorb the water produced at Pt particles together with that produced as reaction product at the cathode and to release the water under low humidity conditions. The PEFCs with these new PEMs demonstrated the superior performances and suppression of the crossover even under non-humidified condition. It has been reported that the incorporation of hydrophilic metal oxide particles such as $SiO_2$, $TiO_2$, $ZrO_2$, $Al_2O_3$ (*27–37*) within PEM leads to an enhancement of the water retention properties and resulting proton conductivities of PEMs under high temperature operating conditions. However, the excessive incorporation of these nonconductive inorganic compounds in PEM results in a decrease of proton conductivity (*29*, *35–37*). To minimize the loss of proton conductivity caused by the addition of the inorganic compound, sulfonated groups are often grafted onto the surfaces of these inorganic compounds (*38–41*).

Several reports are available regarding the antioxidant function of metal nanoparticles (*42–46*). Esumi and coworkers (*43*) demonstrated that gold-chitosan nanocomposites had a hydroxyl radical elimination activity that was 80 times higher than that of ascorbic acid, which is a known antioxidant (*47*). The same research group (*44*) prepared gold-dendrimer nanocomposites in the presence of poly(amidoamine) (PAMAM) dendrimer. The catalytic activities of these nanocomposites for hydroxyl radical scavenging was 85 times higher than that of ascorbic acid and was found to be independent of dendrimer concentration. Endo and coworkers (*46*) investigated the catalytic activity of gold-platinum, gold-palladium and platinum-palladium dendrimer nanocomposites for scavenging 1,1-diphenyl-2-picrylhydrazyl (DPPH) radicals. The bimetallic-dendrimer nanocomposites exhibited higher catalytic activity for the scavenging reaction of DPPH radicals than that of monometallic nanocomposites.

Additionally, cerium and manganese ions have been reported to be highly effective mitigants of polymer membrane chemical degradation (*17*). $Ce^{3+}$ and $Mn^{2+}$ undergo redox reactions with hydroxyl radical (·OH) to produce $H_2O$ and the corresponding oxidized cation ($Ce^{4+}$ and $Mn^{3+}$). The greater effectiveness of $Ce^{3+}$ relative to $Mn^{2+}$ is tied to its faster rate of reaction with hydroxyl radicals. The oxidized cations must be reduced in order to capture additional hydroxyl radicals. Both $Ce^{4+}$ and $Mn^{3+}$ are reported to oxidize $H_2O_2$ to oxygen (*17*, *48–50*) since both are very strong oxidizing agents with high reduction potentials of 1.72 and 1.54 V (vs NHE).

The present study is aimed at examining and potentially applying the free radical scavenging properties of selected metal nanoparticles (Au, Ag, Pt and Pd) to mitigate free radical induced PEM degradation. Nafion® is used as a model PEM and the fluoride emission rate (FER) is used as the primary metric to monitor PEM degradation. In an attempt to minimize the potential of electrical shorting of the membrane, silica ($SiO_2$) has been used to support the metal nanoparticles. Moreover, the effect of ceria ($CeO_2$) particle size on its scavenging properties was investigated as ceria nanoparticles with varying particle sizes were incorporated within the PEM. Ceria supported Pt nanoparticles were also studied. The presence of platinum (based on the degradation mitigation reaction mechanism) should enhance the reduction of $Ce^{+4}$ to $Ce^{+3}$ ions, increasing the amount of hydroxyl radical scavengers available on $CeO_2$ surface and hence reducing the amount of harmful radicals present on composite Nafion® membrane.

## Experimental

### Reagents

Concentrated ammonia (28% w/w aqueous solution), silver nitrate ($AgNO_3$), palladium chloride ($PdCl_2$), tetraethoxysilane (99.9%), concentrated ammonium hydroxide (28% w/w aqueous solution) and trimetylammonium bromide (CTAB) were purchased from Alfa Aesar. Arabic gum, D-glucose

Downloaded by DUKE UNIV on June 21, 2012 | http://pubs.acs.org
Publication Date (Web): March 11, 2010 | doi: 10.1021/bk-2010-1034.ch013

($C_6H_{12}O_6$), tetraammineplatinum(II) chloride hydrate ($Pt(NH_3)_4Cl_2{\cdot}xH_2O$), sodium citrate ($HOC(COONa)(CH_2COONa)_2{\cdot}2H_2O$), chloroauric acid ($HAuCl_4$), tetraoctylammonium bromide ($(CH_3(CH_2)_7]_4N(Br))$ in toluene solution, sodium borohydride ($NaBH_4$), dodecanethiol ($CH_3(CH_2)_{11}SH$), hexachloroplatinic acid ($H_2PtCl_6$), hexamethylenetetramine, cerium nitrate hexahydrate, cerium oxide nanopowder ($CeO_2$, <25nm) and manganese oxide ($MnO_2$, 10μm) were obtained from Sigma Aldrich. Ethanol was purchased from Panreac, while hydrochloric acid (HCl) was obtained from Poch. The precursor solution used for the fabrication of composite membranes was 5% Nafion® (1100 EW) obtained from Solution Technologies (Mendenhall, PA).

Downloaded by DUKE UNIV on June 21, 2012 | http://pubs.acs.org
Publication Date (Web): March 11, 2010 | doi: 10.1021/bk-2010-1034.ch013

## Preparation of Metal Nanoparticles

Silver nanoparticles were prepared using ammoniacal silver salt solution (prepared using concentrated ammonia (28% w/w aqueous solution), Arabic gum as the stabilizing material and D-glucose as the reducing agent (*51*). Three different solutions ($S_1$, $S_2$ and $S_3$) were prepared: *i*) solution $S_1$ consisted of 0.84g D-glucose and 0.45g Arabic gum diluted in 9mL deionized water; *ii*) solution $S_2$ contained 4.725g silver nitrate diluted in 10.4mL deionized water and 6.8mL concentrated ammonium hydroxide; and *iii*) solution $S_3$ consisted of 0.2g Arabic gum diluted in 40mL deionized water. Solution $S_3$ placed in a bath at 80°C under continuous stirring and solutions $S_1$ and $S_2$ were added with a rate of $0.1mLmin^{-1}$ (peristaltic pump). Silver nanoparticles were recovered by treating the resulting dispersion with 6.5mL NaOH (10 M) at 85°C for 1h. After cooling at room temperature, the final mixture was centrifuged, washed with deionized water (4 times) and ethanol (1 time) to remove impurities and dried at 70°C overnight. Silver nanoparticles of approximately 20nm were obtained.

Gold nanoparticles (*52*) were prepared by mixing hydrogen tetrachloroaurate (30mL, 30mM) with tetraoctylammonium bromide in toluene solution (80mL, 50mM). The two phase mixture was stirred until the tetrachloroaurate was transferred into the organic phase, which was collected by a separating funnel. Sodium borohydride (25mL, 0.4M) and 170mg dodecanethiol were added; the borohydride reduces tetrachloroaurate to metal state in the organic phase, while dodecanethiol reacts with surface gold preventing further growth of the nanoparticles. Gold nanoparticles of approximately 2 nm were obtained.

Platinum nanoparticles were prepared following a modification of gold nanoparticles preparation method (*52*) using hexachloroplatinic acid ($H_2PtCl_6$) instead of hydrogen tetrachloroaurate. The complex formed in the organic phase between the tetrachloroplatinate and the tetraoclylammonium was very stable and could not be reduced by sodium borohydride. To circumvent this problem, 1-hexadecyl trimetylammonium bromide (CTAB) was used instead of tetraoctylammonium bromide to obtain a less stable complex that can be reduced easily. Platinum nanoparticles of approximately 2 nm were obtained.

Palladium nanoparticles were prepared in a similar manned by using palladium chloride ($PdCl_2$) dissolved in 0.5M hydrochloric acid (HCl), as described in the literature (*53*).

The loading of metal nanoparticles in the membrane used was 3wt%.

## Preparation of Silica Nanoparticles

Silica was prepared by hydrolysis of tetraethoxysilane (99.9%) in ethanol (*54*, *55*). 17mL tetraethoxysilane (99.9%) were diluted in a mixture of 600mL ethanol absolute, 32mL deionized water and 18mL concentrated ammonium hydroxide (28% w/w aqueous solution) solutions. After 2 h of stirring, 4mL tetraethoxysilane (99.9%) were added and hydrolysis was continued overnight at room temperature under mild stirring. Silica particle size was determined by the amount of water and ammonia in the medium; silica nanoparticles with a diameter close to 200nm were obtained (*55*, *56*).

To obtain the silica nanopowder, the final solution was centrifuged at 7000 rpm for 15 min and washed with deionized water (3 times) and ethanol (3 times) to remove unreacted reagents. The purified product was suspended in ethanol and dried at 70°C overnight.

Downloaded by DUKE UNIV on June 21, 2012 | http://pubs.acs.org
Publication Date (Web): March 11, 2010 | doi: 10.1021/bk-2010-1034.ch013

## Metal Nanoparticles Supported on Silica

Platinum, palladium, silver and gold nanoparticles were deposited over silica according to the procedure described by Zeng and coworkers (*57*). To produce Pt over silica, 1 g silica were dispersed in 300mL deionized water and 170mg tetraammineplatinum(II) chloride were then added. To reduce the platinum salt, 20mL sodium citrate solution (9gL$^{-1}$) was added in the mixture. The resulting suspension was heated at 70°C in a thermostatic bath and stirred overnight to allow all the metal components to be reduced. The material was centrifuged at 7000rpm for 15 min, washed with deionized water (5 times) and ethanol (3 times) and dried at 70°C overnight to obtain the metal over silica nanopowder.

Silver, palladium and gold nanoparticles deposited over silica were fabricated following the same procedure. Silver nitrate (160mg), palladium chloride (166mg) and chloroauric acid (220mg) were used as metal sources.

The loading of supported metal nanoparticles in the membrane used was 3wt%.

## Preparation of $CeO_2$ Nanoparticles

Ceria nanoparticles were synthesized in-house following a simple precipitation technique (*58*). Briefly, 0.07 g/mL (0.5 M) solution of hexamethylenetetramine (Sigma-Aldrich) and 0.016 g/mL (0.038 M) solution of cerium nitrate hexahydrate [$Ce(NO_3)3·6H_2O$; Sigma-Aldrich] were prepared and mixed separately for 30 min. The two solutions were mixed for a length of time (12, 24, 48, 72 and 96 hours) dependent upon the desired particle size and centrifuged to obtain the ceria particles.

## Pt Nanoparticles Supported on Cerium Oxide

A simple precipitation technique was employed for the synthesis of Pt on $CeO_2$ particles. Different amounts (5, 10 and 20ml) of hexachloroplatinic acid were added in 0.2 grams of $CeO_2$ and the mixture was stirred until dried at room temperature. The dried samples were heated at 400°C for 2 hours (*59*) and then washed with DI water. Samples with 0.5%, 1% and 4%wt Pt on $CeO_2$ were prepared.

## Characterization Techniques

X-ray diffraction [(XRD) Rigaku Miniflex diffractometer] studies were conducted to confirm the presence of metals on the supported metal nanoparticles and $CeO_2$ as well as to estimate their crystallite size. Diffractograms were recorded from 20° to 80° 2θ with a step of 2 min/degree.

Transmission electron microscopy (TEM) was used to determine the particle size and size distribution of metal and supported metal nanoparticles. The metal and supported metal nanoparticle dispersions in ethanol were deposited onto carbon-coated copper grids and dried at room temperature. TEM micrographs were obtained using a Philips CM200 microscope at an acceleration voltage of 200kV.

Downloaded by DUKE UNIV on June 21, 2012 | http://pubs.acs.org
Publication Date (Web): March 11, 2010 | doi: 10.1021/bk-2010-1034.ch013

## Antioxidant Activity of Metal Nanoparticles

The antioxidant properties of metal nanoparticles were determined by their ability to reduce the concentration of the stable free radical 1,1-diphenyl-2-picrylhydrazyl (DPPH) (*60*).

0.075 mmol DPPH were dissolved in 200mL ethanol solution and 50mL acetate buffer (0.1M; pH = 5.5). At the same time, 50mL ethanol solution was added to 0.2g metal nanoparticles (0.5%w/w) solution in toluene to create a suspension. Then, 1mL of metal suspension (Au, Pd, Pt or Ag) was added to 2mL DPPH solution in a test tube. The tube was heated to 80°C for 60min in a thermostatic bath and the reaction procedure was stopped by cooling down the mixture in an ice bath. When the DPPH radical is scavenged by an antioxidant and transforms to 1,1-diphenyl-2-picrylhydrazyne (DPPH-H), the color of the solution turns from purple to yellow. The extent of this change was detected by the decay in absorbance at 523nm (*61*).

## Fabrication of Composite Nafion® Membranes and MEAs

Composite membrane precursor solutions were prepared by addition of supported and unsupported metal nanoparticles and metal oxides to 5% Nafion® (1100 EW), maintaining the loading of additive constant at 3 wt%. Membranes were prepared by casting the dispersion on a 7.5 cm x 7.5 cm glass plate, followed by overnight drying at 60°C for solvent evaporation. The membranes were then peeled off from the glass plate and the edges were cut and discarded. Recast Nafion® membranes were prepared for comparison. The membranes were hot-pressed at 120-130°C and 2.75 MPa for 5 min. Membrane electrode assemblies (MEAs) were prepared with Pt/C electrocatalyst at the anode and cathode. The overall loading of platinum on each electrode was estimated gravimetrically and was maintained at 0.4±0.05 mg-cm$^{-2}$.

### MEA Testing − Performance and Durability

Linear sweep voltammetry was the first experiment performed on each cell to check for hydrogen crossover and electronic shorting in the MEA. Only cells demonstrating low hydrogen crossover (1-2 mA·cm$^{-2}$) and no shorting were chosen for further testing (these experiments were repeated at the end of the test cycle to ensure that the membranes remained uncompromised during testing). The performance of the cell was evaluated for 2 consecutive days by obtaining polarization curves at a temperature of 80°C and an inlet relative humidity (RH) of 75% (corresponding to a saturator dew point of 73°C). Air and oxygen were used as oxidants and hydrogen was used as fuel.

To monitor the PEM degradation rate, the MEAs were tested at open circuit at 90°C and 30% RH. For these accelerated degradation tests $O_2$ was used as the oxidant at the cathode and $H_2$ was used as the fuel at the anode. The flow rate for both gases was 0.2 slpm. The inlet gases were humidified by controlling the anode and cathode saturator dew points at 60°C. The test was run for 24 h for each MEA and the anode and cathode exit streams were independently condensed in cold-traps. The fluoride ion concentrations in the condensate water were measured using a fluoride ion selective electrode (Denver instruments) that was freshly calibrated before each measurement. This data, in conjunction with the condensation rate of water, was used to estimate the fluoride emission rate (FER).

Downloaded by DUKE UNIV on June 21, 2012 | http://pubs.acs.org
Publication Date (Web): March 11, 2010 | doi: 10.1021/bk-2010-1034.ch013

## Results and Discussion

### X-Ray Diffraction (XRD) Measurements

XRD (Figures 1−3) was used to confirm the presence of metal nanoparticles on silica support, the presence of $CeO_2$ in the materials synthesized in-house with varying reaction times as well the presence of Pt particles on $CeO_2$ support and to obtain a quantitative estimate of their crystallite size. XRD measurements of pure metal nanoparticles (Ag, Au, Pd and Pt) could not be conducted due to their limited available quantity.

In Fig. 1, the peaks associated with supported Ag on $SiO_2$ can be seen at 2θ values of 38°, 44°, 64° and 77° representing the (1,1,1), (2,0,0), (2,2,0) and (3,1,1) Bragg's reflections of the face center cubic (fcc) structure of silver (*62–64*). For the supported Au nanoparticles, the peaks of Au can be seen at 2θ values of

Downloaded by DUKE UNIV on June 21, 2012 | http://pubs.acs.org
Publication Date (Web): March 11, 2010 | doi: 10.1021/bk-2010-1034.ch013

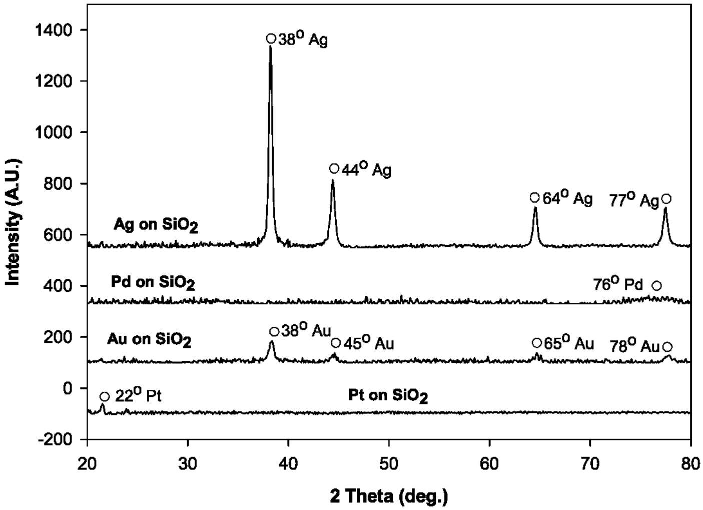

*Figure 1. XRD spectra of supported Ag, Au, Pt and Pd nanoparticles.*

38°, 45°, 65° and 78° representing the (1,1,1), (2,0,0), (2,2,0) and (3,1,1) Bragg's reflections of the fcc structure of gold (*65*). Supported Pt and Pd nanoparticles demonstrated only one very small peak at 2θ values of 22° and 76° validating the presence of platinum and palladium on the supports (*66*, *67*). Due to the low nanoparticle loadings on $SiO_2$ and small sample size, XRD data could not produce sharp peaks for all the metal nanoparticles leading to an inaccurate estimation of their crystallite size. The Scherrer equation (*68*) had been employed only for the calculation of crystallite size of Ag and Au on $SiO_2$ supported nanoparticles. The average crystallite size was similar for both at 20-25 nm.

Consistent with expectation, the synthesized in-house $CeO_2$ powder was crystalline (Figure 2) with peaks at 2θ values of 29°, 33°, 48°, 57°, 77° and 79° representing the (1,1,1), (2,0,0), (2,2,0), (3,1,1), (3,3,1) and (4,2,0) Bragg's reflections of the face center cubic (fcc) structure of ceria (*69–72*). The Scherrer equation (*68*) had been employed for the calculation of average crystallite size of the homemade $CeO_2$. The crystallite size of the ceria samples prepared in-house during 12 and 24 hours exhibited the highest crystallite size (~ 12±1.5 nm) while the ceria samples reacted for 48, 72 and 96 hours were characterized by lower crystallite size (~ 10±0.7 nm). The calculated crystallite size was similar for all different $CeO_2$ samples and further characterization measurements for particle size determination are in progress.

The peaks associated with supported Pt on $CeO_2$ can be seen at 2θ values of 46° and 68° representing the (2,0,0) and (2,2,0) Bragg's reflections of the fcc structure of platinum (*73*). $CeO_2$ support was crystalline (Figure 3) with peaks at 2θ values of 29°, 33°, 57°, 59°, 77° and 79° associated to (1,1,1), (2,0,0), (3,1,1), (2,2,2), (3,3,1) and (4,2,0) Bragg's reflections of the fcc structure of $CeO_2$ (*69–72*). The average crystallite size of commercial $CeO_2$ support was estimated by the Scherrer equation (*68*) to be approximately 13±1 nm.

Downloaded by DUKE UNIV on June 21, 2012 | http://pubs.acs.org
Publication Date (Web): March 11, 2010 | doi: 10.1021/bk-2010-1034.ch013

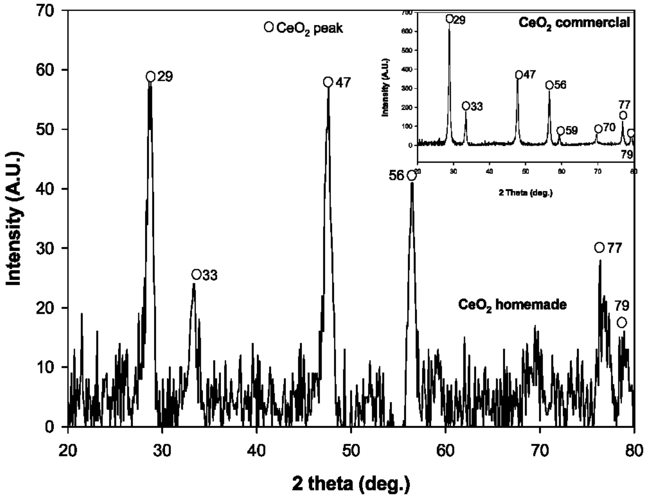

*Figure 2. XRD spectra of commercial and synthesized in-house CeO2 nanoparticles.*

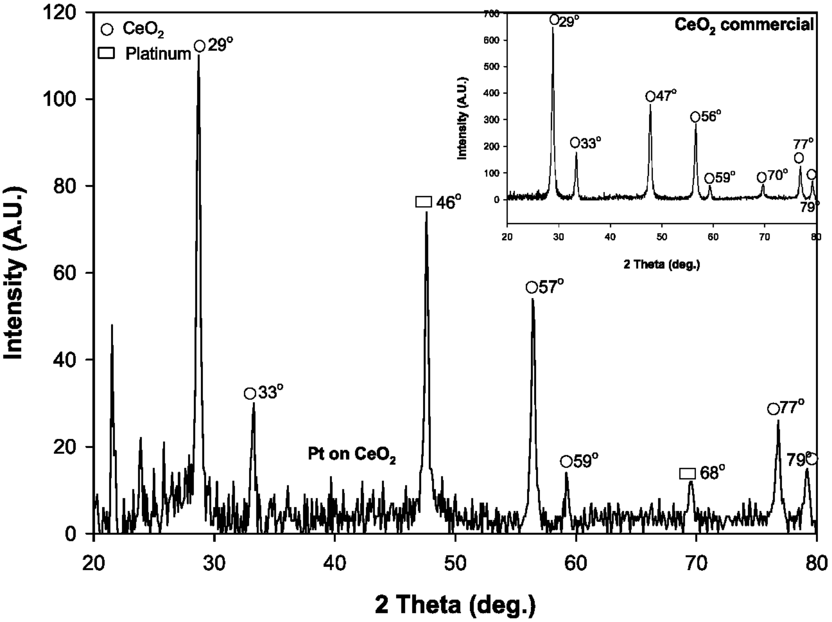

*Figure 3. XRD spectra of supported Pt on CeO2 particles.*

Downloaded by DUKE UNIV on June 21, 2012 | http://pubs.acs.org
Publication Date (Web): March 11, 2010 | doi: 10.1021/bk-2010-1034.ch013

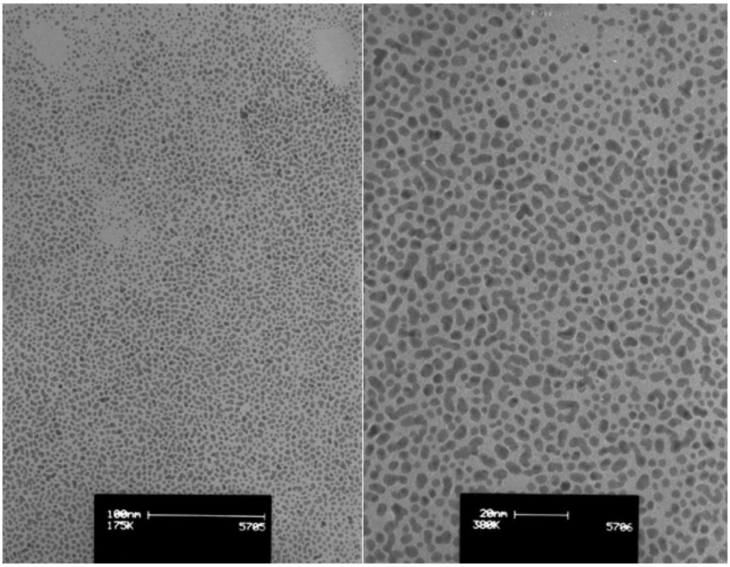

*Figure 4. TEM micrographs of Ag and Au nanoparticles (scale bar 100nm; 20nm).*

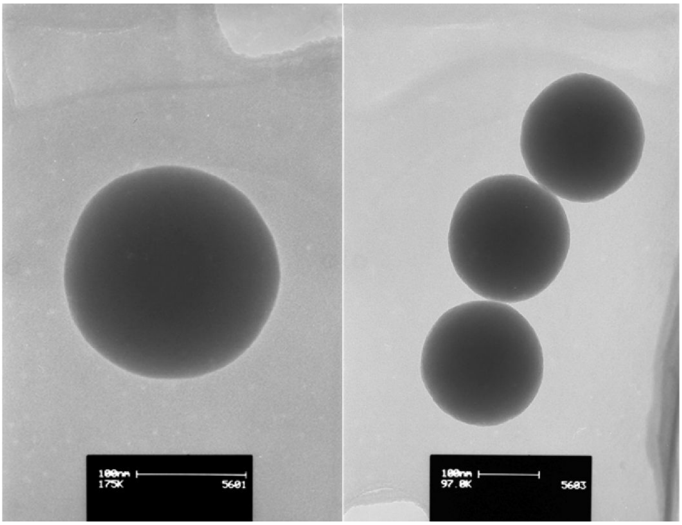

*Figure 5. TEM micrographs of $SiO_2$ support (scale bar 100 nm).*

## TEM Micrographs

TEM micrographs of Ag and Au nanoparticles, silica support and Au, Pd supported on silica are shown in Figures 4−6. These figures are representative

Downloaded by DUKE UNIV on June 21, 2012 | http://pubs.acs.org
Publication Date (Web): March 11, 2010 | doi: 10.1021/bk-2010-1034.ch013

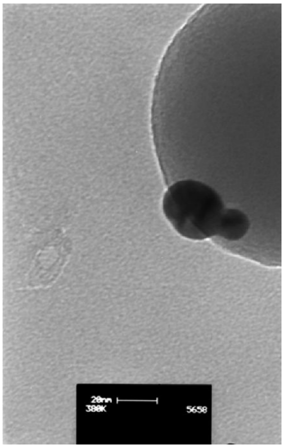

*Figure 6. TEM micrograph of Au supported on $SiO_2$ nanoparticles (scale bar 20 nm).*

**Table I. UV-vis spectra absorbance of metal nanoparticles**

| *Sample* | *Control* | *Pd NPs* | *Ag NPs* | *Pt NPs* | *Au NPs* |
|---|---|---|---|---|---|
| *Absorbance at 523nm after 30 min at 80°C* | 0.140 | 0.108 | 0.135 | 0.067 | 0.112 |

of the metal and supported metal nanoparticles studied. The dimensions of the support particles were in the range of 100 nm, while metal nanoparticles were approximately 2 nm. Supported metal nanoparticles exhibited similar particle size (~ 25nm), which is in reasonable agreement with the crystallite size estimated by XRD.

## Ex-Situ Measurement of Antioxidant Activity of Metal Nanoparticles

The ability of metal nanoparticles to catalyze the decomposition of free radicals was tested using DPPH as a stable free radical (*74*, *75*).

The starting solution contained 0.2mM DPPH and the UV-vis absorbance data obtained is shown in Table I. In the presence of Ag nanoparticles, the UV-vis signal was identical to the baseline signal, indicating that silver had no impact in lowering the concentration of DPPH free radical. A 20%-25% decrease in UV-vis absorbance was observed when Au or Pd nanoparticles were immersed in the solution, although greater decrease was observed for Pt nanoparticles. Pt nanoparticles demonstrated the highest activity against DPPH radicals as a 50% decrease in UV-vis absorbance was achieved (Table I). These preliminary results suggested that Au, Pt and Pd nanoparticles can be used as radical scavengers in order to increase the durability of polymer membrane.

Downloaded by DUKE UNIV on June 21, 2012 | http://pubs.acs.org
Publication Date (Web): March 11, 2010 | doi: 10.1021/bk-2010-1034.ch013

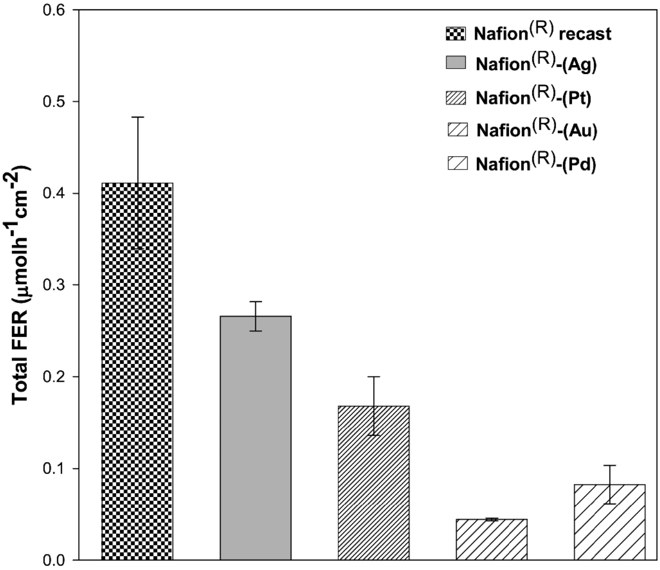

*Figure 7. Total fluoride emission rates (μmol $h^{-1}cm^{-2}$) measured for Nafion® and composite Nafion®-(metal nanoparticles) membrane based MEAs during accelerated durability testing (Operating conditions: Cell temperature: 90°C; Saturator temperature: 60°C; RH: 30%; Anode gas: $H_2$; Cathode gas: $O_2$; Flow rate: 0.2 slpm at anode and cathode; Duration: 24h).*

## MEA Testing Results – Degradation

To obtain a macroscopic estimate of the PEM degradation rate, fluoride emission rates (FERs) were obtained for each MEA tested (Ag, Pt, Au, Pd nanoparticles; Ag, Pt, Au, Pd on $SiO_2$; $MnO_2$, synthesized in-house $CeO_2$ with varying reaction times and Pt on $CeO_2$). The FERs and total FERs (in μmol/h $cm^2$) were estimated from the fluoride ion concentration in the anode and cathode condensate water and the condensation rate of water. Care was taken to ensure that the ion-selective electrode used to estimate $F^-$ concentration was calibrated prior to each measurement and verified on a standard solution (not used during calibration) prior to analyzing the desired condensate. Several MEAs of each type were tested to ensure that the results obtained and trends seen were reproducible. The total FERs (with accompanying standard errors) are reported in Figures 7, 8, 9 and 10 for the MEAs tested.

The addition of Au nanoparticles resulted in an order of magnitude reduction in the total FER while the addition of Pd nanoparticles reduced the FER by ~ 75% - 80% (Figure 7). The addition of Pt nanoparticles resulted in a ~ 60% decrease of total FER values while Ag nanoparticles, in line with expectations from our *ex-situ* studies, yielded a more modest decrease (~35%) in their FER values due to the lower antioxidant activity of Ag nanoparticles. In addition to antioxidant activity, one must consider the propensity of the metal nanoparticles and especially

Downloaded by DUKE UNIV on June 21, 2012 | http://pubs.acs.org
Publication Date (Web): March 11, 2010 | doi: 10.1021/bk-2010-1034.ch013

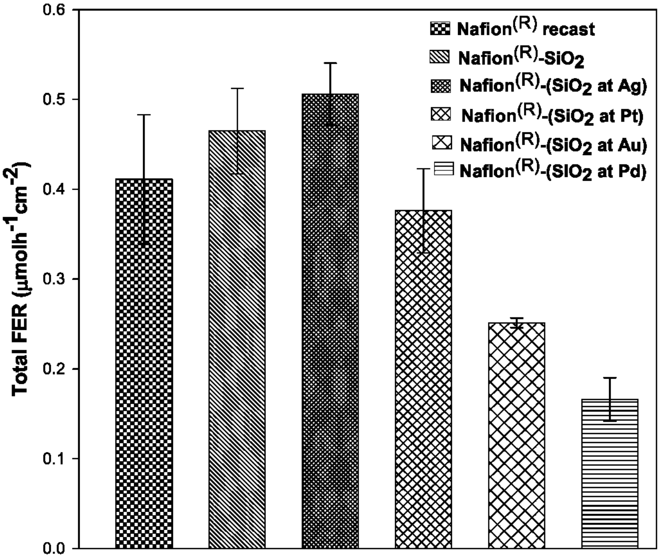

*Figure 8. Total fluoride emission rates (μmol $h^{-1}cm^{-2}$) measured for Nafion® and composite Nafion®-(metal nanoparticles supported on $SiO_2$) membrane based MEAs during accelerated durability testing (Operating conditions: Cell temperature: 90°C; Saturator temperature: 60°C; RH: 30%; Anode gas: $H_2$; Cathode gas: $O_2$; Flow rate: 0.2 slpm at anode and cathode; Duration: 24h).*

their ions to facilitate the production of free radicals from hydrogen peroxide. We note that this propensity is largest for silver (*76*, *77*). Additionally, while Pt and Pd nanoparticles (especially Pt) exhibit higher antioxidant activity than Au nanoparticles in *ex-situ* scavenging studies, they dissolve at lower potentials and concurrently augment the production of hydroxyl radicals (*78*) thereby resulting in higher total FER values.

In the case of supported nanoparticles, it is observed (Figure 8) that composite Nafion®-(Au or Pd on $SiO_2$) PEMs exhibited lower total FER values (~ 40% and ~60% respectively) than recast Nafion® MEAs, while composite Nafion®-(Ag or Pt on $SiO_2$) membrane based MEAs had similar total FER values with recast Nafion® MEAs. The observed increase of the total FER values of the composite PEMs containing supported metal nanoparticles (in comparison with their unsupported analogues) can be attributed to the larger particle size of the metal particle and resultant lowering in activity (*79*), as well as the lower concentration of metal nanoparticles in the PEM. Hence, while the silica supported additives can prevent the possibility of electronic shorting, the extent of degradation mitigation is lower when compared to unsupported metal nanoparticles.

Downloaded by DUKE UNIV on June 21, 2012 | http://pubs.acs.org
Publication Date (Web): March 11, 2010 | doi: 10.1021/bk-2010-1034.ch013

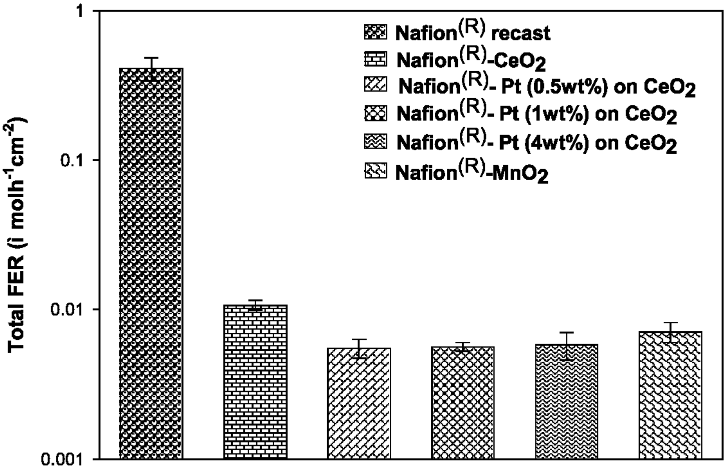

*Figure 9. Total fluoride emission rates (μmol $h^{-1}cm^{-2}$) measured for Nafion®, composite Nafion®-(Pt supported on $CeO_2$) and composite Nafion®-($MnO_2$) membrane based MEAs during accelerated durability testing (Operating conditions: Cell temperature: 90°C; Saturator temperature: 60°C; RH: 30%; Anode gas: $H_2$; Cathode gas: $O_2$; Flow rate: 0.2 slpm at anode and cathode; Duration: 24h).*

Even so, the case for further optimizing (through particle size control and enhancement of metal loading on the support) the supported metal nanoparticles for degradation mitigation is very strong when one considers in detail the issue of dissolution of unsupported metal nanoparticles in direct contact with the electrolyte. According to Pourbaix diagrams (*80*), platinum and gold metals are oxidized at potentials of approximately 1 V (vs. SHE) and 1.3 V (vs. SHE) respectively at pH value of 1 which resembles the acidic environment of a Nafion® membrane. Palladium and silver are oxidized to $Pd^{+2}$ and $Ag^{+}$ at much lower potentials, namely 0.8 V (vs. SHE) and 0.4 V (vs. SHE). As discussed in the section on proton conductivity, under normal fuel cell operating conditions, the potential distribution in the thickness dimension of the PEM is close to anode potential (0 V vs. SHE) for the most of its thickness and rises to the cathode potential (~ 0.6 - 1 V vs. SHE) in a region close to the cathode (*81*). At such high potentials Ag and Pd nanoparticles will be oxidized resulting in an increase in the concentration of metal ions impurities and hence in an increase on the formation of hydroxyl radicals as well as lowering of proton conductivity. However even Pt and Au nanoparticles, despite their relatively higher oxidation potentials at the electrolyte pH, are not completely safe. It has been documented that during PEFC start-up, the cell can experience potentials as high 1- 2V vs. SHE at either electrode (*82*, *83*). Such high potentials would facilitate the oxidation of Pt and Au in addition to Pd and Ag metal nanoparticles in the vicinity of the electrodes, potentially resulting in higher PEM degradation rate and instability issues.

)

Downloaded by DUKE UNIV on June 21, 2012 | http://pubs.acs.org
Publication Date (Web): March 11, 2010 | doi: 10.1021/bk-2010-1034.ch013

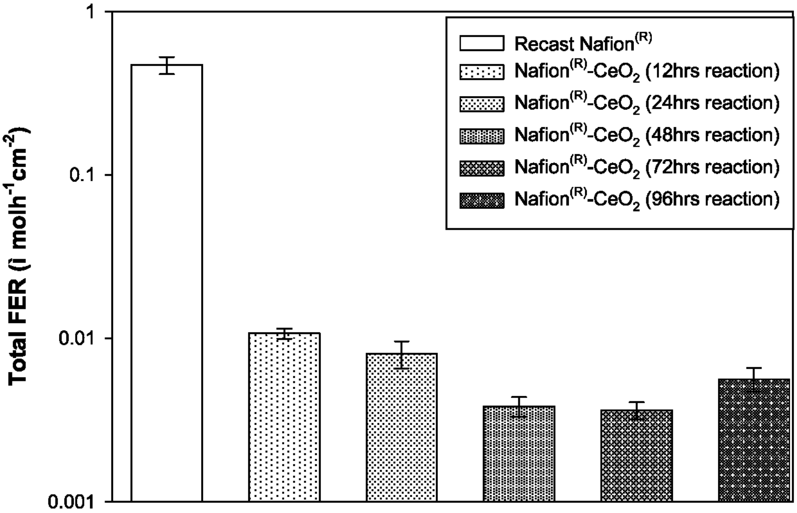

*Figure 10. FERs (µmolh$^{-1}$ cm$^{-2}$) measured for Nafion® and Nafion®-$CeO_2$ MEAs during accelerated durability testing. Operating conditions: cell temperature 90°C; saturator temperature 60°C; RH 30%; anode gas $H_2$; cathode gas $O_2$; flow rate 0.2 slpm at anode and cathode; and duration 24 h.*

In the case of metal oxides $CeO_2$ and $MnO_2$, it is observed (Figure 9) that the addition of various loadings of Pt on $CeO_2$ nanoparticles as well as the incorporation of $MnO_2$ in Nafion® membranes resulted in an order of magnitude reduction in the total FER. It can be concluded by comparison with the total FER results of composite Nafion®-($CeO_2$) membrane based MEAs that the addition of Pt on $CeO_2$ support did have a positive impact on the free radical scavenging ability of $CeO_2$ as a further reduction (approximately 45%-50%) in the total FER values was achieved, even though it was independent of Pt loading. The presence of platinum enhances the reduction of $Ce^{+4}$ to $Ce^{+3}$ ions increasing the amount of hydroxyl radical scavengers available on $CeO_2$ surface and thus mitigating the chemical degradation of Nafion® membrane (*17*). Additionally, composite Nafion®-($MnO_2$) membrane based MEAs exhibited similar FER results with composite Nafion®-($CeO_2$) membrane based MEAs indicating that $MnO_2$ is an effective mitigant of Nafion® membrane chemical degradation. This is consistent with reports in the patent literature. Work on Pt supported over manganese oxide is ongoing.

In the case of synthesized in-house ceria with varying reaction times, it is observed (Figure 10) that the reduction of $CeO_2$ particle size positively affects the total FER; $CeO_2$ particles obtained after 48, 72 and 96 hours reaction exhibited 30-50% lower FER values than ceria particles reacted for 12 and 24 hours. This phenomenon is hypothesized to be due to the alternation in the number of oxygen vacancies (defects) in cerium oxide surface structure. Tsunekawa and co-workers

Downloaded by DUKE UNIV on June 21, 2012 | http://pubs.acs.org
Publication Date (Web): March 11, 2010 | doi: 10.1021/bk-2010-1034.ch013

(*84*) reported that as the ceria particle size decreases, the $Ce^{+3}/Ce^{+4}$ ratio on ceria surface increases, enhancing its scavenging properties. The FER trend seen (Figure 10) was consistent with the crystallite size results obtained from XRD data even though it must be noted that the calculated crystallite sizes were close together. It is hypothesized that this FER trend is due to the different particle sizes (and hence $Ce^{+3}/Ce^{+4}$ ratio) of the $CeO_2$ samples and further (better resolved) characterization measurements for particle size determination, $Ce^{3+/}Ce^{4+}$ ratio estimation and and oxygen vacancy calculations are in progress.

## MEA Testing Results – Cell Performance

From the linear sweep voltammograms, the hydrogen crossover current densities were estimated for each MEA tested. Composite Nafion® and recast Nafion® membranes exhibited similar crossover current values (~1 mA/cm$^2$). Only MEAs that demonstrated this low value of hydrogen crossover (and no internal shorting) were selected for further testing. Furthermore, the linear sweep voltammograms were repeated after all tests were carried out and the data reported is drawn from MEAs that did not have any internal shorting, even at the end of the test sequence (including the accelerated durability test).

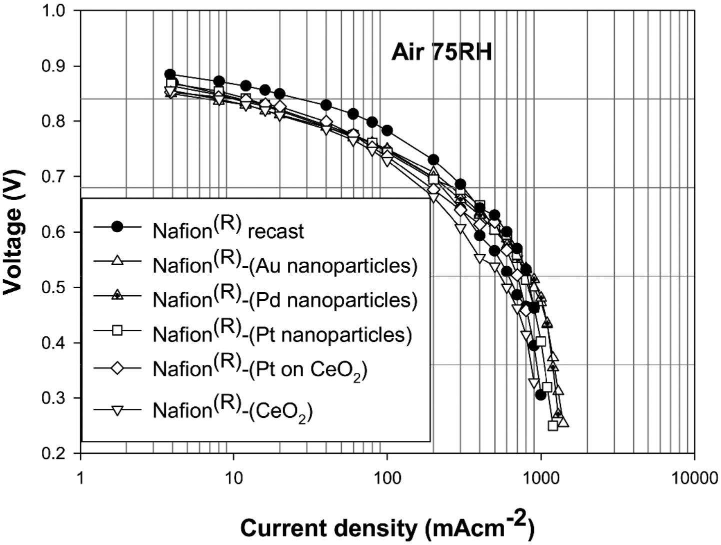

*Figure 11. Performance for Nafion® and composite Nafion®-(metal nanoparticles) membrane based MEAs at 80°C and 75% RH using air as oxidant and hydrogen as fuel (Operating conditions: Saturator temperature: 73°C; Pressure: 1atm; Anode gas: $H_2$; Cathode gas: Air; Anode stoichiometry: 4; Cathode stoichiometry: 3).*

Polarization curves were obtained with Nafion® and composite Nafion® - (Au, Pt, Pd, synthesized in-house $CeO_2$ and Pt supported on $CeO_2$ nanoparticles) membrane based MEAs that exhibited a large decrease of their FER values compared to Nafion®. All the MEAs had the same electrocatalyst loading and were tested at 80°C and 75% RH (1 atm. operating pressure), with air and oxygen as the oxidants and hydrogen as the fuel. Figure 11 demonstrates that the performance of composite Nafion® - (Au, Pt and Pd nanoparticles as well as synthesized in-house $CeO_2$ and Pt supported on $CeO_2$ nanoparticles) membrane based MEAs, when corrected for membrane resistance, were very similar to recast Nafion® MEAs, suggesting that the additives were stable within the membrane for the duration of the test.

Downloaded by DUKE UNIV on June 21, 2012 | http://pubs.acs.org
Publication Date (Web): March 11, 2010 | doi: 10.1021/bk-2010-1034.ch013

## Conclusions

The effect of incorporating metal nanoparticles and metal oxides into a Nafion® membrane on PEM conductivity and the macroscopic PEM degradation rate was studied. Unsupported and silica supported Au, Ag, Pt and Pd nanoparticles as well as $MnO_2$, $CeO_2$ and Pt supported on $CeO_2$ nanoparticles were used to prepare composite membranes with a loading of 3% wt. The metal/metal oxide nanoparticles and supports were characterized by TEM and XRD to determine their particle and crystallite size. The free radical scavenging properties of metal nanoparticles were determined *ex-situ* by UV-vis spectroscopy using a stable free radical (DPPH). A 20%-25% decrease in the UV-vis absorbance was observed when Au or Pd nanoparticles were immersed in the solution, although greater decrease was observed for Pt nanoparticles. Pt nanoparticles demonstrated the highest activity against DPPH radicals as a 50% decrease in the concentration of DPPH was achieved. Ag nanoparticles did not demonstrate appreciable antioxidant activity. MEAs were prepared using Nafion® and composite Nafion® membranes. The fluoride emission rate (FER) was ascertained for each composite membrane from multiple accelerated tests. The FER was lowered by an order of magnitude when Au was used and by 75%-80% when Pd was added to Nafion®. The addition of Pt nanoparticles resulted in a ~ 60% decrease of FER values while composite Nafion®-(Ag nanoparticles) membrane based MEAs demonstrated a more modest decrease (~ 35%) of their FER. The observed trends were rationalized based on the antioxidant activity that is in competition with the propensity of the metal to dissolve to form ions and exacerbate hydroxyl radical production. The supported metal nanoparticles in general yielded lower FER reduction than their unsupported counterparts due to larger metal particle size and smaller quantities within the PEM. By comparison with the total FER results of composite Nafion®-$CeO_2$ membrane based MEAs, it can be concluded that the addition of Pt on $CeO_2$ support did have a positive impact on the free radical scavenging ability of $CeO_2$, independent of the Pt loading. Additionally, the effect of incorporating different ceria particle sizes into a Nafion® membrane on FER production was examined. The FER trend seen was consistent with the crystallite size results obtained from XRD data even though the calculated crystallite sizes were close to one another. Finally, the use of $MnO_2$ in Nafion® membranes also resulted in an order of magnitude FER reduction, suggesting that $MnO_2$ is an effective mitigant of Nafion® membrane chemical degradation. The performance of composite Nafion® - (Au, Pt, Pd, synthesized in-house $CeO_2$ and Pt supported on $CeO_2$ nanoparticles) membrane based MEAs were very similar to recast Nafion® MEAs when corrected for membrane resistance. We conclude that the addition of metal nanoparticles with antioxidant abilities is a promising route to mitigate PEM degradation. However we caution that the propensity for metal nanoparticle oxidation (possibly yielding degradation exacerbating ions) within the PEM in the vicinity of the electrodes as well as the possibility of electronic shorting should be kept in mind. These factors are minimized when supported metal nanoparticles are used (at least in proximity to the electrodes).

Downloaded by DUKE UNIV on June 21, 2012 | http://pubs.acs.org
Publication Date (Web): March 11, 2010 | doi: 10.1021/bk-2010-1034.ch013

## References

1. Knights, S. D.; Colbow, K. M.; St-Pierre, J.; Wilkinson, D. P. *J. Power Sources* **2004**, *127*, 127–134.
2. Xie, J.; Wood, D. L.; More, K. L.; Atanassov, P.; Borup, R. L. *J. Electrochem. Soc.* **2005**, *152*, A1011–A1020.
3. Xie, J.; Wood, D. L.; Wayne, D. M.; Zawodzinski, T. A.; Atanassov, P.; Borup, R. L. *J. Electrochem. Soc.* **2005**, *152*, A104–A113.
4. Pozio, A.; Silva, R. F.; De Francesco, M.; Giorgi, L. *Electrochim. Acta* **2003**, *48*, 1543–1549.
5. Curtin, D. E.; Lousenberg, R. D.; Henry, T. J.; Tangeman, P. C.; Tisack, M. E. *J. Power Sources* **2004**, *131*, 41–48.
6. Tang, H.; Luo, Z.; Li, D.; Pan, M.; Ruan, R. *Int. J. Hydrogen Energy* **2006**, *31*, 1831–1837.
7. Sompalli, B.; Litteer, B. A.; Gu, W.; Gasteiger, H. A. *J. Electrochem. Soc.* **2007**, *154*, B1349–B1357.
8. Mittal, V. O.; Kunz, R.; Fenton, J. M. *J. Electrochem. Soc.* **2007**, *154*, B652–B656.
9. Mittal, V. O.; Kunz, R.; Fenton, J. M. *J. Electrochem. Soc.* **2006**, *153*, A1755–A1759.
10. Mittal, V. O.; Kunz, R.; Fenton, J. M. *Electrochem. Solid-State Lett.* **2006**, *9*, A299–A302.
11. LaConti, A. B.; Hamdan, M.; McDonald, R. C. In *Handbook of Fuel Cells – Fundamentals, Technology and Applications*; Vielstich, W., Lamm, A., Gasteiger, H. A., Eds.; John Wiley & Sons: New York, 2003; Vol. 3, pp 647−662.
12. Büchi, F. N.; Gupta, B.; Haas, O.; Scherer, G. G. *Electrochim. Acta* **1995**, *40*, 345–353.
13. Endoh, E.; Terazono, S.; Widjaja, H.; Takimoto, Y. *Electrochem. Solid-State Lett.* **2004**, *7*, A209–A211.
14. Panchenko, A.; Dilger, H.; Kerres, J.; Hein, M.; Ullrich, A.; Kaz, T.; Roduner, E. *Phys. Chem. Chem. Phys.* **2004**, *6*, 2891–2894.

15. Panchenko, A.; Dilger, H.; Moller, E.; Sixt, T.; Roduner, E. *J. Power Sources* **2004**, *127*, 325–330.
16. Collier, A.; Wang, H.; Yuan, X. Z.; Zhang, J.; Wilkinson, D. P. *Int. J. Hydrogen Energy* **2006**, *31*, 1838–1854.
17. Comms, F. D.; Liu, H.; Owejan, J. E. *ECS Trans.* **2008**, *16*, 1735–1747.
18. Trogadas, P.; Parrondo, J.; Ramani, V. *Electrochem. Solid-State Lett.* **2008**, *11*, B113–B116.
19. Haugen, G. M.; Meng, F.; Aieta, N. V.; Horan, J. L.; Kuo, M.; Frey, M. H.; Hamrock, S. J.; Herring, A. M. *Electrochem. Solid-State Lett.* **2007**, *10*, B51–B55.
20. Trogadas, P.; Ramani, V. *J. Power Sources* **2007**, *174*, 159–163.
21. Trogadas, P.; Ramani, V. *J. Electrochem. Soc.* **2008**, *155*, B696–B703.
22. Rajeshwar, K.; de Tacconi, N. R.; Chenthamarakshan, C. R.; Wampler, W. A.; Carlson, T. C.; Lin, W. Y. *Prepr.-Am. Chem. Soc.*; Boston, 2007.
23. de Tacconi, N. R.; Chenthamarakshan, C. R.; Rajeshwar, K.; Lin, W. Y.; Carlson, T. F.; Wampler, W. A.; Sambandam, S.; Ramani, V. *J. Electrochem. Soc.* **2008**, *155*, B1102–B1109.
24. Watanabe, M.; Uchida, H.; Seki, Y.; Emori, M.; Stonehart, P. *J. Electrochem. Soc.* **1996**, *143*, 3847–3852.
25. Watanabe, M.; Uchida, H.; Emori, M. *J. Electrochem. Soc.* **1998**, *145*, 1137–1141.
26. Watanabe, M.; Uchida, H.; Emori, M. *J. Phys. Chem. B* **1998**, *102*, 3129–3137.
27. Antonucci, P. L.; Ario, A. S.; Creti, P.; Ramunni, E.; Antonucci, V. *Solid State Ionics* 1997, *125*, 431−437, http://www.sciencedirect.com/science.
28. Malhotra, S.; Datta, R. *J. Electrochem. Soc.* **1997**, *144*, L23–L26.
29. Deng, Q.; Wikie, C. A.; Moore, R. B.; Mauritz, K. A. *Polymer* **1998**, *39*, 5961–5972.
30. Staiti, P.; Arico, A. S.; Baglio, V.; Lufrano, F.; Passalacqua, E.; Antonucci, V. *Solid State Ionics* **2001**, *145*, 101–107.
31. Adjemian, K. T.; Lee, S. J.; Srinivasan, S.; Benziger, J.; Bocarsly, A. B. *J. Electrochem. Soc.* **2002**, *149*, A256–A261.
32. Nunes, S. P.; Ruffmann, B.; Rikowski, E.; Vetter, S.; Richau, K. *J. Membr. Sci.* **2002**, *203*, 215–225.
33. Shao, Z. G.; Joghee, P.; Hsing, I. M. *J. Membr. Sci.* **2004**, *229*, 43–51.
34. Shao, Z. G.; Xu, H.; Li, M.; Hsing, I. M. *Solid State Ionics* **2006**, *177*, 779–785.
35. Arico, A. S.; Baglio, V.; di Blasi, A.; Creti, P.; Antonucci, P. L.; Antonucci, V. *Solid State Ionics* **2003**, *161*, 251–265.
36. Baglio, V.; Arico, A. S.; Blasi, A. D.; Antonucci, V.; Antonucci, P. L.; Licoccia, S.; Traversa, E.; Fiory, F. S. *Electrochim. Acta* **2005**, *50*, 1241–1246.
37. Bebin, P.; Caravanier, M.; Galiano, H. *J. Membr. Sci.* **2006**, *278*, 35–42.
38. Liu, Y. L.; Hsu, C. Y.; Su, Y. H.; Lai, J. Y. *Biomacromolecules* **2005**, *6*, 368–373.
39. Sua, Y. H.; Wei, T. Y.; Hsu, C. H.; Liu, Y. L.; Sun, Y. M.; Lai, J. Y. *Desalination* **2006**, *200*, 656–657.

Downloaded by DUKE UNIV on June 21, 2012 | http://pubs.acs.org
Publication Date (Web): March 11, 2010 | doi: 10.1021/bk-2010-1034.ch013

40. Gomes, D.; Buder, I.; Nunes, S. P. *Desalination* **2006**, *199*, 274–276.
41. Su, Y. H.; Liu, Y. L.; Sun, Y. M.; Lai, J. Y.; Wang, D. M.; Gao, Y.; Liu, B.; Guiver, M. D. *J. Membr. Sci.* **2007**, *296*, 21–28.
42. Kajita, M.; Hikosaka, K.; Iitsuka, M.; Kanayama, A.; Toshima, N.; Miyamoto, Y. *Free Radical Res.* **2007**, *41*, 615–626.
43. Esumi, K.; Takei, N.; Yoshimura, T. *Colloids Surf., B* **2003**, *32*, 117–123.
44. Esumi, K.; Houdatsu, H.; Yoshimura, T. *Langmuir* **2004**, *20*, 2536–2538.
45. Shukla, R.; Bansal, V.; Chaudhary, M.; Basu, A.; Bhonde, R. R.; Sastry, M. *Langmuir* **2005**, *21*, 10644–10654.
46. Endo, T.; Fukunaga, T.; Yoshimura, T.; Esumi, K. *J. Colloid Interface Sci.* **2006**, *302*, 516–521.
47. Nishikimi, M. *Biochem. Biophys. Res. Commun.* **1975**, *63*, 463–468.
48. Czapski, G.; Bielski, B. H.; Sutin, N. *J. Phys. Chem.* **1963**, *67*, 201–203.
49. Davies, G.; Kirschenbaum, L. J.; Kustin, K. *Inorg. Chem.* **1968**, *7*, 146–154.
50. Mahlman, H. A.; Matthews, R.W.; Sworski, T. J. *J. Phys. Chem.* **1971**, *75*, 250–255.
51. Siiman, O.; Jitianu, A.; Bele, M.; Grom, P.; Matijevic, E. *J. Colloid Interface Sci.* **2007**, *309*, 8–20.
52. Brust, M.; Walker, M.; Bethell, D.; Schiffrin, D. J.; Whyman, R. *J. Chem. Soc. Chem. Commun.* **1994**, *7*, 801–802.
53. Shen, C. M.; Su, Y. K.; Yang, H. T.; Yang, T. Z.; Gao, H. J. *Chem. Phys. Lett.* **2003**, *373*, 39–45.
54. Stoeber, W.; Fink, A.; Bohn, E. *J. Colloid Interface Sci.* **1968**, *26*, 62–69.
55. van Blaaderen, A.; Van Geest, J.; Vrij, A. *J. Colloid Interface Sci.* **1992**, *154*, 481–501.
56. Bogush, G. H.; Tracy, M. A.; Zukoski, C. F. *J. Non-Cryst. Solids* **1988**, *104*, 95–106.
57. Zeng, J.; Lee, J. Y.; Chen, J.; Shen, P. K.; Song, S. *Fuel Cells* **2007**, *7*, 285–290.
58. Zhang, F.; Jin, Q.; Chan, S. W. *J. Appl. Phys.* **2004**, *95*, 4319–4326.
59. Silva, A. M.; Costa, L. O. O.; Barandas, A. P. M. G.; Borges, L. E. P.; Mattos, L. V.; Noronha, F. B. *Catal. Today* **2008**, *133-135*, 755–761.
60. Isono, R.; Yoshimura, T.; Esumi, K. *J. Colloid Interface Sci.* **2005**, *288*, 177–183.
61. Sujia, K. P.; Jayalekshmy, A.; Arumughan, C. *J. Agric. Food Chem.* **2004**, *52*, 912–915.
62. Ding, Y.; Zhang, P.; Qu, Y.; Jiang, Y.; Huang, J.; Yan, W.; Liu, G. *J. Alloys Compd.* **2008**, *466*, 479–482.
63. Khanna, P. K.; Singh, N.; Charan, S.; Subbarao, V. V. V. S.; Gokhale, R.; Mulik, U. P. *Mater. Chem. Phys.* **2005**, *93*, 117–121.
64. Abu Bakar, N. H. H.; Ismail, J.; Abu Bakar, M. *Mater. Chem. Phys.* **2007**, *104*, 276–283.
65. Wang, L.; Song, Y.; Sun, L.; Guo, C.; Sun, Y.; Li, Z. *Mater. Lett.* **2008**, *62*, 4124–4126.
66. Chhina, H.; Campbell, S.; Kesler, O. *J. Electrochem. Soc.* **2007**, *154*, B533–B539.
67. Yang, S.; Zhang, X.; Mi, H.; Ye, X. *J. Power Sources* **2008**, *175*, 26–32.

Downloaded by DUKE UNIV on June 21, 2012 | http://pubs.acs.org
Publication Date (Web): March 11, 2010 | doi: 10.1021/bk-2010-1034.ch013

68. Zhang, F.; Chan, S. W.; Spanier, J. E.; Apak, E.; Jin, Q.; Robinson, R. D.; Herman, I. P. *Appl. Phys. Lett.* **2002**, *80*, 127–129.
69. Laberty-Robert, C.; Long, J. W.; Lucas, E. M.; Pettigrew, K. A.; Stroud, R. M.; Doescher, M. S.; Rolison, D. R. *Chem. Mater.* **2006**, *18*, 50–58.
70. Bumajdad, A.; Zaki, M. I.; Eastoe, J.; Pasupulety, L. *Langmuir* **2004**, *20*, 11223–11233.
71. Zhang, F.; Jin, Q.; Chan, S. W. *J. Appl. Phys.* **2004**, *95*, 4319–4326.
72. Sheng, P. Y.; Bowmaker, G. A.; Idriss, H. *Appl. Catal., A* **2004**, *261*, 171–181.
73. Jiang, L.; Colmenares, L.; Jusys, Z.; Sun, G. Q.; Behm, R. J. *Electrochim. Acta* **2007**, *53*, 377–389.
74. Masuda, T.; Yonemori, S.; Oyama, Y.; Takeda, Y.; Tanaka, T.; Andoh, T.; Shinohara, A.; Nakata, M. *J. Agric. Food Chem.* **1999**, *47*, 1749–1754.
75. Ionita, P. *Chem. Pap.* **2005**, *59*, 11–16.
76. Denisov, E. T.; Denisova, T. G.; Pokidova, T. S. *Handbook of Free Radical Initiators*; Wiley Interscience: Hoboken, NJ, 2003.
77. Strukul, G. *Catalytic Oxidations with Hydrogen Peroxide as Oxidant*; Springer: NY, 1992.
78. Liu, T. Z.; Lin, T. F.; Chiu, D. T. Y.; Tsai, K.-J.; Stern, A. *Free Radical Biol. Med.* **1997**, *23*, 155–161.
79. Corma, A.; Garcia, H. *Chem. Soc. Rev.* **2008**, *37*, 2096–2126.
80. Pourbaix, M. *Atlas of Electrochemical Equilibria in Aqueous Solutions*; Pergamon Press: Oxford, NY, 1966.
81. Liu, W.; Zuckerbrod, D. *J. Electrochem. Soc.* **2005**, *152*, A1165–A1170.
82. Tang, H.; Qi, Z.; Ramani, M.; Elter, J. F. *J. Power Sources* **2006**, *158*, 1306–1312.
83. Lee, S. Y.; Cho, E. A.; Lee, J. H.; Kim, H. J.; Lim, T. H.; Oh, I. H.; Won, J. *J. Electrochem. Soc.* **2007**, *154*, B194–B200.
84. Tsunekawa, S.; Sivamohan, R.; Ito, S.; Kasuya, A.; Fukuda, T. *Nanostruct. Mater.* **1999**, *11*, 141–147.

Downloaded by DUKE UNIV on June 21, 2012 | http://pubs.acs.org
Publication Date (Web): March 11, 2010 | doi: 10.1021/bk-2010-1034.ch013

# Subject Index

**A**

α-crystals/phases in PVDF, 28, 34
Antioxidant activity, of metal nanoparticles, ex-situ measurement of, 197
  with DPPH as free radical, 197
  UV-vis spectra absorbance of, 197, 197*t*
Atomic force microscopy analysis, 102
  images
    of P3HT supramolecular structures on MWCNTs, 114, 115*f*
    of P3HT-*b*-PS/CNTs, 102, 103*f*

**B**

Band offset, electronic structure at interfaces, 14, 15
Bandgap, of semiconducting polymers
  donor-acceptor approach for, 75
  as function for PV efficiencies/performance, 74
  stabilized quinoid form incorporation to, 76
β-crystals/phases in PVDF, 28, 34
Biaxially oriented polypropylene
  discharged energy density profiles
    as function of applied electric field, 33, 33*f*
    as function of discharge time, 30, 32*f*
Bulk heterojunction polymer solar cells
  devices, characteristic properties of, 76, 78*t*
  overall energy conversion efficiency, 74
  PCDTBT based with $TiO_2$ interfacial layer, 77
  recent progress on highly efficient, 71
  RR-P3HT/PCBM blend, 74
    annealing/additives effect on, 77

**C**

Cadmium (II) Sulfide QDs
  with bare ZnS, synthesis of, 140*s*, 146, 147*f*, 150, 150*f*
    by pyrolysis, 146
  ligand exchange with MPTMO, 142*s*, 147, 148*f*
Carbon nanotubes
  carboxylate group functionalized, 110
  dispersing and functionalizing using conjugated block copolymers, 95
  dispersing using P3HT-*b*-PS block copolymers, 101, 101*f*, 102, 102*f*, 103, 103*f*, 104, 104*f*, 105*f*
    in chloroform, toluene, THF solvents, 101
    schematic illustration of, 98*s*
    superhydrophobic films, normalized resistance of, 109, 112*f*
  non-invasive functionalization by P3HT-*b*-PAA and P3HT-*b*-PPEGA, 109, 110, 112*f*
  solubility in various solvents, 111
  supramolecular structures of P3HT on, 113*f*, 114, 115*f*
Carbonyl frequency
  center *versus* corresponding time delay, plot of, 62, 64*f*
  correlation with PCBM radial position
    origin of, 60
    schematic illustration of, 59, 60*f*

Downloaded by 89.163.35.42 on June 21, 2012 | http://pubs.acs.org
Publication Date (Web): March 11, 2010 | doi: 10.1021/bk-2010-1034.ix002

Downloaded by 89.163.35.42 on June 21, 2012 | http://pubs.acs.org
Publication Date (Web): March 11, 2010 | doi: 10.1021/bk-2010-1034.ix002

Carbonyl stretch/bleach, in CN-MEH-PPV/PCBM blend, 55, 57*f*
  integrated area *versus* time delay, 56, 58*f*
  spectra in 2D surface plot *versus* time delay, 58*f*, 59
Carboxylate group, functionalized CNTs, 110
Casting process, for Nafion nanohybrid membranes, 173
Cerium oxide nanoparticles
  supported Pt, XRD spectra of, 193, 194, 195*f*
  synthesized in-house, 193, 194, 195*f*
    total FERs, 201, 201*f*
Charge mobility, 126
  of P3HT/$C_{60}$ films, tailoring of, 123
Chloroform solvent, 101, 111, 113*f*
Chloroform vapors, treated on P3HT/$C_{60}$ films, 126, 127*f*, 128, 128*f*, 130*f*, 131, 132, 132*f*, 133*f*
  hole mobility as function of time, 125*f*, 126, 130, 132, 133*f*
Clay
  dispersion, 173
  platelets, 174, 175
  and polymer systems
    aggregation, schematic representation of, 177, 178*f*
CNTs. *See* Carbon nanotubes
Conjugated block copolymers, for dispersing and functionalizing CNTs, 95
Contact angle
  *versus* etching time, 87, 88, 88*f*, 90*f*
  hysteresis *versus* etching time, 87, 88, 88*f*, 90*f*
Copolymerization, of ethylene/Vac in $scCO_2$, 145
  reactivity ratios *versus* reaction temperature and pressure, 145, 146*f*
  in situ FTIR waterfall plot of, 144*f*, 145
Crystalline morphology, characterization in P(VDF-CTFE)-*g*-PS *graft* copolymers, 28, 30*f*

**D**

Defect states, of insulators, 14
Density, induced charge, 12
Density functional theory
  computational results on system structural parameters, 11, 12*t*
  for eigenvalue equation, 11
  GGA calculations within, 11
  LDA calculations within, 11
  as quantum mechanics-based method, 11
1,2-Dichlorobenzene vapors, treated on P3HT/$C_{60}$ films, 127, 128, 128*f*, 130*f*, 131, 132, 132*f*, 133*f*
  hole mobility as a function of time, 125*f*, 126, 130, 132, 133*f*
Dielectric permittivity constant
  determination by Maxwell equation, 12
  local profile, 11, 13
  *versus* loss tangent
    of $BaTiO_3$-P(VDF-TrFE-CTFE)/P(VDF-CTFE)-$BaTiO_3$, 40*f*, 42
    of $TiO_2$-P(VDF-TrFE-CTFE)/P(VDF-CTFE)-$BaTiO_3$, 45*f*, 46
  of multilayer systems, 11
  optical and static, 11
  in $SiO_2$-polymer interface system, 11, 13, 14, 15*f*
Dielectric polarization. *See* Dielectric permittivity constant
Dielectric response
  at surfaces and interfaces, 11, 13
  temperature dependency of, 41*f*, 42, 47*f*, 48
Differential scanning calorimery curves/profiles
  of $BaTiO_3$-P(VDF-TrFE-CTFE)/P(VDF-CTFE), 44*f*, 45
  of P(VDFCTFE)-g-PS *graft* copolymers, 28, 30*f*
  of $TiO_2$-P(VDF-TrFE-CTFE), 49*f*, 50

In Functional Polymer Nanocomposites for Energy Storage and Conversion; Wang, Q., et al.;
ACS Symposium Series; American Chemical Society: Washington, DC, 2010.

Dimethyl formamide, 173
Dimethyl sulfoxide, 173
1,1-Diphenyl-2-picrylhydrazyl free radical, for metal nanoparticles antioxidant activity, 197
Discharged energy density
  as function of applied electric field
    for BOPP, 33, 33*f*
    for PVDF, 33, 33*f*
    for P(VDF-CTFE)-g-PS, 33, 33*f*
  as function of discharge time
    for BOPP, 30, 32*f*
    for PVDF, 30, 32*f*
    for P(VDF-CTFE)-g-PS, 30, 32*f*
Dispersion medium, for Nafion nanohybrid membranes, 173
  DMF, 173
  $Me_2SO$, 173
  water, 173, 174
Dissipation factor, for PVDF/P(VDF-CTFE)/P(VDF-CTFE)-g-PS *graft* copolymers, 34, 34*f*
Donor-acceptor copolymer blends
  as method for low bandgap polymers, 75
  morphology control on, 77
  with PCBM, 75
    energy levels bandgap, PV performance of, 75*t*
    structures of, 73*f*
Dynamic mechanical analysis, on montmorillonites/Nafion, 179, 180*f*

E

Edge-to-face aggregation, of MMT-$Na^+$/Nafion, schematic representation of, 177, 178*f*
Eigenvalue equation, solved by DFT, 11
Electric circuit, LCR/capacitor, 27*f*
Electric field
  applied, as function for discharged energy density profiles, 33, 33*f*
  assisted free carrier formation, 64
  at CN-MEH-PPV/PCBM blend interface
    formation, 60, 61*f*
    variation of, 61*f*, 62
Electrical energy density, of polymers and nanocomposites, 43, 43*f*, 48*f*, 49
Electrical energy storage, from ferroelectric polymer based nanocomposites, 37
Electron transfer, interfacial, dynamics of, 55
  in CN-MEH-PPV/PCBM blend, 55, 57*f*
    carbonyl stretch/bleach, 55, 57*f*
Electronic structure at interfaces, 14
  band offset and defects states, 14, 15
Electronic wave function, 14, 16
Electron-phonon interactions, 17
  in $Al_2O_3$-polymer and $SiO_2$-polymer, 18, 18*f*
Electrons radial motion, 59
  correlated to carbonyl frequency
    origin of, 60
    schematic illustration of, 59, 60*f*
Electro-osmotic drag coefficients, of nanocomposites as function of T, 164*f*, 165
Energy dispersive X-ray analysis, 101
  spectrum of P3HT-*b*-PS/CNTs, 102, 102*f*
Energy levels, of semiconducting polymers, 74
Energy storage
  from first principles computations on nanodielectrics, 9
  nonlinear, in polymer-ceramic nanocomposites
    nanostructure-level modeling of, 1
    in SSCL configuration, 4, 5*f*, 6*f*, 7*f*
Etching time, 84

Downloaded by 89.163.35.42 on June 21, 2012 | http://pubs.acs.org
Publication Date (Web): March 11, 2010 | doi: 10.1021/bk-2010-1034.ix002

    and depth relationship of Au layer assisted Si in $HF/H_2O_2$, 83*f*, 84
Ethylene, and VAc
    copolymerization in $scCO_2$, 145
    reactivity ratios *versus* reaction temperature/pressure, 145, 146*f*
    in situ FTIR waterfall plot of, 144*f*, 145
Ex-situ measurement, of antioxidant activity of metal nanoparticles, 197
    with DPPH as free radical, 197
    UV-vis spectra absorbance of, 197, 197*t*

**F**

Face-to-face aggregation, of MMT-$Na^+$/Nafion, schematic representation of, 177, 178*f*
Field-emission scanning electron microscopy, cross-sectional images
    of polymer-$TiO_2$ nanocomposites, 45*f*, 46
    of P(VDF-TrFECTFE)-$BaTiO_3$ nanocomposite, 40*f*, 41
First principles
    computations on energy storage of nanodielectrics, 9
    DFT method based from, 11
    inherently parameter-free method, 10
Fluorescence spectroscopy analysis, 103
    spectra of pure P3HT-*b*-PS and P3HT-*b*-PS/SWCNT in chloroform, 104*f*
Fluoride emission rates, and total FERs, 198
    with metal nanoparticles, 198, 198*f*
    with metal nanoparticles supported on $SiO_2$, 199, 199*f*
    with metal oxides, 200*f*, 201
Fourier transform infrared spectroscopy
    in situ, waterfall plot of ethylene/Vac copolymerization in $scCO_2$, 144*f*, 145
    spectra of CdS-ZnS QDs before and after ligand exchange, 147, 148*f*
Free carrier formation
    dynamics, 62
    electric field assisted, 64
    in OPV polymer blends, ultrafast IR spectroscopy on, 53
Fuel cells
    Nafion nanohybrid membranes for, 171
    PEM, degradation mitigation using metal nanoparticle and oxides, 187
    performance of nanocomposites, cell potential *versus* current density plot, 166*f*, 167
Functionalized Silica/Nafion membranes, 175
    HS30SIT/Nafion, 175, 176
    TEOS:SIT/Nafion, 176

**G**

Generalized gradient approximation, 11
Gold layer
    assisted Si etching in $HF/H_2O_2$, 83*f*, 84*f*, 85*f*, 86, 86*f*
        etching time-depth relationship, 83*f*, 84
    effect on etching morphology, 86
    thickness, 86
        with Si surfaces, 84*f*, 86
Gold nanoparticles
    supported on silica, XRD spectra of, 193, 194*f*
    total FERs with addition of, 198, 198*f*

Downloaded by 89.163.35.42 on June 21, 2012 | http://pubs.acs.org
Publication Date (Web): March 11, 2010 | doi: 10.1021/bk-2010-1034.ix002

**H**

Highest occupied molecular orbital, 74, 75, 75*t*, 78*t*
Hole mobility, of P3HT/$C_{60}$ films as function of time, 125*f*, 126, 132, 133*f*
  in DCB and chloroform vapor treatments, 130
HOMO. *See* Highest occupied molecular orbital
Honeycomb structures, formed from P3HT-*b*-PS/MWCNT dispersions, 108
HS30SIT/Nafion membranes, 175
  apparent selectivity, 182*f*, 183
  methanol permeability, 182
  SAXS patterns of, 176
  TEM images of, 176
Hydrogen fluoride/hydrogen peroxide, Au assisted Si etching in
  etching time-depth relationship, 83*f*, 84
  SEM cross-section images of, 83*f*, 84, 84*f*, 86
  surface morphology size scale images, 85*f*, 86, 86*f*
Hydrogen fluoride/hydrogen peroxide/water, Au assisted Si etching in
  contact angle and contact angle hysteresis of, 88, 90*f*
  Si pyramid surfaces and cross sections of, 88, 89*f*, 90*f*
Hydrogen montmorillonite/Nafion membranes, 174
  apparent selectivity, 182*f*, 183
  DMA on, 179
  ionic conductivity as function of relative humidity, 181*f*, 182
  methanol permeability, 180*f*, 181, 182
  $Na^+$ replaced by $H^+$, 174
  polymeric bundles schematic representation of, 175, 177*f*
  SAXS patterns/profiles, 174, 176*f*
  storage modulus as function of T, 179, 180*f*
  TEM images of cross-sections, 174, 175*f*

**I**

Induced charge density, 12
Insulators, 14
  defects states, 14
Interfacial electron transfer,
  dynamics of, 55
  in CN-MEH-PPV/PCBM blend, 55
    carbonyl stretch/bleach, 55, 57*f*
    linear IR absorption spectrum of, 55, 57*f*
Ionic conductivity, 182
  as function of relative humidity
    montmorillonites/Nafion membranes, 181*f*, 182
    of pure Nafion, 181*f*, 182
    of TEOS:SIT/Nafion membranes, 181*f*, 182

**L**

LaDOS. *See* Layer-decomposed density of states
Layer-decomposed density of states, 15
  profile of $SiO_2$-vinylsianediol-PVDF, 16, 17*f*
Ligand exchange, of quantum dots, 147
  CdS-ZnS core-shell with MPTMO, 142*s*, 147, 148*f*
Light reflection measurement, 89
  hemispherical reflectance *versus* wavelength, 89, 91*f*
  weighted reflectance on different textured surfaces, 89, 91*t*
Light selectivity, by polymer nanocomposite films, quantum dots in, 137
Local density approximation, calculations within DFT, 11

Downloaded by 89.163.35.42 on June 21, 2012 | http://pubs.acs.org
Publication Date (Web): March 11, 2010 | doi: 10.1021/bk-2010-1034.ix002

Downloaded by 89.163.35.42 on June 21, 2012 | http://pubs.acs.org
Publication Date (Web): March 11, 2010 | doi: 10.1021/bk-2010-1034.ix002

Loss tangent, temperature dependency, 41*f*, 42, 47*f*, 48
Lowest unoccupied molecular orbital, 74, 75*t*, 78*t*
LUMO. *See* Lowest unoccupied molecular orbital

**M**

Maxwell equation, 12
Membrane electrode assembly testing, for PEM cell
  degradation of, 198, 198*f*, 199*f*, 200*f*
  performance of, 202, 202*f*, 203
(3-Mercaptopropyl)trimethoxysilane, for CdS-ZnS core-shell QDs ligand exchange, 142*s*, 147
Metal nanoparticles
  antioxidant activity, ex-situ measurement of, 197
    with DPPH as free radical, 197
    UV-vis spectra absorbance of, 197, 197*t*
  for degradation mitigation in PEM fuel cells, 187
  TEM micrographs, 196, 196*f*
  total FERs with addition of, 198, 198*f*
  XRD measurements on, 193, 194*f*
Metal oxides additives
  for degradation mitigation in PEM fuel cells, 187
  total FERs with addition of, 200*f*, 201
Methanol permeability, 181
  HS30SIT/Nafion membranes, 182
  MMT-$H^+$/Nafion membranes, 180*f*, 182
  MMT-$Na^+$/Nafion membranes, 182
  of nanocomposites as function of T, 163, 164*f*
    with PTA and ZrP, 164
  TEOS:SIT/Nafion membranes, 182

**N**

Nafion nanohybrid membranes
  for fuel cells, 171
  ionic conductivity as function of relative humidity, 181*f*, 182
  morphology and structural characteristics, 173
    clay hybrids with network structure, 176
    dispersion medium and casting process, 173
    functionalized Silica HS30SIT and TEOS:SIT, 175
    MMT-$H^+$, 174
  performance characteristics, 179
    mechanical properties, 179
    transport properties, 181, 182, 183
  polymeric bundles schematic representation of, 175, 177*f*
  SAXS patterns/profiles of, 174, 176*f*
Nanocomposites
  CNT-PMMA
    conductivity of, 106, 107*f*
    optical images before/after annealing, 106, 108*f*
  from CNTs/block copolymers dispersion, 105
  ferroelectric polymer based for electrical energy storage, 37
  polymer-$BaTiO_3$, 41
    dielectric properties, 42
    with P (VDF-TrFE-CTFE), 40*f*, 41, 42
    with P(VDF-CTFE), 40*f*, 41, 42
    structure and morphology, 41
    surface-modified particles in DMF, particle size distribution of, 38*f*, 41
    thermal properties, 45
  polymer-$TiO_2$, 46
    cross-sectional FE-SEM image, 45*f*, 46
    dielectric properties, 46
    morphology, 46
    with P (VDF-TrFE-CTFE), 45*f*, 46, 48*f*, 49, 49*f*, 50

In Functional Polymer Nanocomposites for Energy Storage and Conversion; Wang, Q., et al.;
ACS Symposium Series; American Chemical Society: Washington, DC, 2010.

Downloaded by 89.163.35.42 on June 21, 2012 | http://pubs.acs.org
Publication Date (Web): March 11, 2010 | doi: 10.1021/bk-2010-1034.ix002

- with P(VDF-CTFE), 45*f*, 46
- WAXD spectrum of, 50, 51*f*

proton exchange membrane, 155
- characterization of, 163
- fuel cell potential *versus* current density, 166*f*, 167
- interactions between organic-inorganic moieties in, 161*f*
- types of, 157*t*

with PTA and ZrP, 163, 164, 165, 167
- electro-osmotic drag coefficients as function of T, 164*f*, 165
- methanol permeability as function of T, 163, 164*f*
- relative selectivity of, 166*f*, 167
- water self-diffusion coefficients in, 165*f*, 166
- water uptake and conductivity, 162*f*, 163

SWCNT/PS
- conductivity of, 105, 107*f*
- optical images before/after annealing, 106, 108*f*

Nanodielectrics, for energy storage from first principles computations, 9

Nanostructure-level modeling, of nanocomposite nonlinear energy storage, 1

N,N-dimethylformamide, BaTiO$_3$ particles in, particle size distribution of, 38*f*, 41

Nuclear magnetic resonance, of P(VDF-CTFE)/P(VDF-CTFE)-g-PS *graft*copolymers, 28
- $^1$H and $^{19}$F spectrum of, 27*f*, 28

**O**

Open circuit voltage, 74

Organic photovoltaic polymer blends, free carrier formation ultrafast IR spectroscopy, 53

Overall energy conversion efficiency, 74, 75*t*, 78*t*

**P**

Palladium nanoparticles
- supported on silica, XRD spectra of, 193, 194*f*
- total FERs with addition of, 198*f*

Permittivity modeling, in spherical particle composites, 2
- simulations, 2
- three dimensional cellular model space, 2

[6,6]-Phenyl-$C_{61}$-butyric acid methyl ester
- blended with RR-P3HT solar cell, 74
- with CN-MEH-PPV blend
  - carbonyl stretch/bleach, 55, 57*f*, 58*f*
  - comparison of potential energy *versus* electron-hole separation, 65*f*
  - electric field formation, 60, 61*f*
  - interfacial electron transfer dynamics in, 55
  - linear IR absorption spectrum of, 55, 57*f*
- domains radial position correlation with carbonyl frequency
  - origin of, 60
  - schematic illustration of, 59, 60*f*
- as electron acceptor, 56*f*
- molecular structure of, 56*f*

Phonons band structure determination, 18

Phosphotungstic acid, effect on nanocomposites
- electro-osmotic drag coefficients as function of T, 164*f*, 165
- methanol permeability as function of T, 163, 164*f*
- water self-diffusion coefficients, 165*f*, 167
- water uptake and conductivity, 162*f*, 163

Platinum nanoparticles

- supported on $CeO_2$ particles, XRD spectra of, 193, 194, 195*f*
- supported on silica, XRD spectra of, 193, 194*f*
- total FERs with addition of, 198, 198*f*

Polyethylene, with silane-treated $SiO_2$ nanoparticles, 14
- decreased dielectric polarizability and permittivity, 14
- increased dielectric breakdown strength, 14

Poly(ethylene-co-vinyl acetate)
- nanofilms and QDs synthesis, 146, 148
  - photoluminescence emission spectra of, 149*f*, 150, 151, 151*f*
  - schematic diagram of experimental setup, 139*f*
  - 2-step method using $scCO_2$, 142*s*, 148
  - TEM images of, 150, 150*f*
  - UV-Vis spectra of, 151, 151*f*, 152, 152*f*
- sample beads before and after treatment of $scCO_2$, 148, 148*f*

Poly(3-hexylthiophene), on CNTs
- crystallization process of, 116*f*
- supramolecular structures, 114
  - AFM height images, 114, 115*f*
  - TEM images of, 113*f*, 114

Poly(3-hexylthiophene), relative crystallinity of, 129, 129*f*

Poly(3-hexylthiophene)-*b*-poly(poly(ethylene glycol)methyl ether acrylate), on MWCNTs, 109, 111
- in chloroform, toluene, methanol, DMF, photographs of, 111, 113*f*

Poly(3-hexylthiophene)-*b*-polystyrene block copolymers
- CNTs dispersion by, 101
  - AFM analysis on, 102, 103*f*
  - in chloroform, toluene, THF solvents, 101
  - EDX analysis on, 101, 102*f*
  - fluorescence spectroscopy analysis on, 103, 104*f*
  - formation of honeycomb structures from, 108, 110*f*
  - for nanocomposite fabrication, 105, 106, 107*f*, 108*f*
  - Raman spectroscopy analysis on electric properties of, 104, 105*f*
  - schematic illustration of, 98*s*
  - superhydrophobic films, normalized resistance of, 109, 112*f*
  - TEM analysis on, 101, 101*f*
  - UV-Vis absorption spectroscopy analysis on, 103, 104*f*
- synthetic scheme of, 100*s*

Poly(3-hexylthiophene)/fullerene films
- in DCB and chloroform vapor treatment
  - hole mobility as function of time, 125*f*, 126, 130, 132, 133*f*
  - TEM images of, 128, 128*f*
  - typical morphological SEM images of, 126, 127, 127*f*, 128*f*, 132, 132*f*
  - UV-vis absorption spectra of, 130*f*, 131, 132, 133*f*
- morphology and charge mobility, tailoring of, 123
- solar cells, power conversion efficiency as function of time, 131*f*, 132, 134*f*
- WAXD curves, P3HT relative crystallinity calculated from, 129, 129*f*

Polymer electrolyte membrane, fuel cells, degradation mitigation, 187, 198

Polymer nanocomposites
- films and quantum dots, for light selectivity, 137
- $SiO_2$-PVAc, TEM images of, 143*f*, 144
- synthesis using $scCO_2$, 144

Polymer-$BaTiO_3$ nanocomposites, 41

Downloaded by 89.163.35.42 on June 21, 2012 | http://pubs.acs.org
Publication Date (Web): March 11, 2010 | doi: 10.1021/bk-2010-1034.ix002

Downloaded by 89.163.35.42 on June 21, 2012 | http://pubs.acs.org
Publication Date (Web): March 11, 2010 | doi: 10.1021/bk-2010-1034.ix002

  - dielectric properties, 42
    - dielectric permittivity constant, 40*f*, 42
    - electrical energy density, 43, 43*f*
  - with P (VDF-TrFE-CTFE)
    - cross-sectional FE-SEM image of, 40*f*, 41
    - dielectric permittivity constant *versus* loss tangent, 40*f*, 42
    - DSC profiles of, 44*f*, 45
    - electrical energy density, 43, 43*f*
  - with P(VDF-CTFE)
    - dielectric permittivity constant *versus* loss tangent, 40*f*, 42
    - DSC profiles of, 44*f*, 45
    - electrical energy density, 43, 43*f*
    - TEM image of, 40*f*, 41
  - structure and morphology, 41
  - surface-modified particles in DMF, particle size distribution of, 38*f*, 41
  - thermal properties, 45
- Polymer-ceramic nanocomposites
  - energy storage in, nanostructure-level modeling of, 1
  - nonlinear inclusions, 3
    - polarization curves for, 3, 4*f*
    - SSCL configurations, 4, 5*f*
- Polymeric aggregates/bundles
  - edge-to-face and face-to-face aggregation, 177, 178*f*
  - pure Nafion and MMT-$H^+$/Nafion, schematic representation of, 175, 177*f*
- Polymeric systems
  - $SiO_2$-polymer interface, 13
    - atomic model and dielectric constant of, 15*f*
    - silane-treated and untreated, 14
  - $SiO_2$-vinylsianediol-PVDF, 16
    - LaDOS profile, 16, 17*f*
    - structure of, 16, 17*f*
- Polymers, semiconducting
  - bandgap and energy levels
    - donor-acceptor approach for, 75
    - as function for PV efficiencies/performance, 74
    - stabilized quinoid form incorporation to, 76
  - PTB, molecular structures of, 76, 78*f*
    - mixed with PCBM, characteristic properties of, 76, 78*t*
- Polymer-$TiO_2$ nanocomposites, 46
  - cross-sectional FE-SEM image, 45*f*, 46
  - dielectric properties, 46
    - dielectric permittivity constant, 45*f*, 46
    - electrical energy density, 48*f*, 49
  - morphology, 46
  - with P(VDF-TrFE-CTFE) and P(VDF-CTFE)
    - dielectric permittivity constant *versus* loss tangent, 45*f*, 46
    - DSC curves/profiles of, 49*f*, 50
    - electrical energy density, 48*f*, 49
    - microstructure, effect of $TiO_2$ nanoparticles on, 50
  - WAXD spectrum of, 50, 51*f*
- Poly(2-methoxy-5-(3,7-dimethyloctyloxy)-1,4-phenylenevinylene)
  - as electron donor and molecular structure of, 56*f*
- Poly[2-methoxy-5-(2-ethylhexyloxy)-1,4-(1-cyanovinylene-1,4-phenylene)]
  - molecular structure of, 56*f*
  - with PCBM blend
    - carbonyl stretch/bleach, 55, 57*f*, 58*f*
    - electric field formation, 60, 61*f*
    - interfacial electron transfer dynamics in, 55
    - linear IR absorption spectrum of, 55, 57*f*

Downloaded by 89.163.35.42 on June 21, 2012 | http://pubs.acs.org
Publication Date (Web): March 11, 2010 | doi: 10.1021/bk-2010-1034.ix002

- Polystyrene contents, 27*f*, 28, 29*t*
- Poly(vinylidene fluoride)
  - crystallinity, 28
    - α-crystals/phases, 28
    - β-crystals/phases, 28
  - discharged energy density profiles
    - as function of applied electric field, 33, 33*f*
    - as function of discharge time, 30, 32*f*
  - dissipation factor as function of frequency for, 34, 34*f*
  - space charge distribution, 33, 34, 35*f*
  - WAXD profiles/patterns, 28, 30*f*
    - biaxially oriented, 29, 31*f*
- Poly(vinylidene fluoride-*co*-chlorotrifluoroethylene)
  - with $BaTiO_3$ nanocomposites
    - dielectric permittivity constant *versus* loss tangent, 40*f*, 42
    - DSC profiles of, 44*f*, 45
    - electrical energy density, 43, 43*f*
    - TEM image of, 40*f*, 41
  - dissipation factor as function of frequency for, 34, 34*f*
  - $^1$H and $^{19}$F NMR spectra of, 27*f*, 28
  - SEC results for, 28, 29*f*
  - with $TiO_2$ nanocomposites, dielectric permittivity constant *versus* loss tangent, 45*f*,
- Poly(vinylidene fluoride-*co*-chlorotrifluoroethylene)-*graft*-polystyrene copolymers
  - characterization of, 28, 29*t*
  - crystalline morphological characterization in, 28, 30*f*
  - dielectric properties of, 30
  - discharged energy density profiles
    - as function of applied electric, 33, 33*f*
    - as function of discharge time, 30, 32*f*
  - dissipation factor as function of frequency for, 34, 34*f*
  - fast discharge and low loss by confined ferroelectrics/dielectrics, 23, 33, 34
  - $^1$H and $^{19}$F NMR spectrum of, 27*f*, 28
  - space charge distribution, 33, 34, 35*f*
  - synthesis of, 27*s*, 28
  - uniaxially oriented, WAXD patterns for, 29, 31*f*
- Poly(vinylidene fluoride-*ter*-trifluoroethylene-*ter*chlorotrifluoroethylene)
  - with $BaTiO_3$ nanocomposites
    - cross-sectional FE-SEM image of, 40*f*, 41
    - dielectric permittivity constant *versus* loss tangent, 40*f*, 42
    - DSC profiles of, 44*f*, 45
    - electrical energy density, 43, 43*f*
  - with $TiO_2$ nanocomposites
    - dielectric permittivity constant *versus* loss tangent, 45*f*, 46
    - DSC curves/profiles of, 49*f*, 50
  - WAXD spectrum of, 50, 51*f*
- Power conversion efficiency, of P3HT/$C_{60}$ solar cells as function of time, 131*f*, 132, 134*f*
- Pyrolysis synthesis of CdS-ZnS core-shell/CdS QDs, 146

## Q

- Quantum dots
  - bare CdS and CdS-ZnS core-shell synthesis of, 140*s*, 147*f*, 150, 150*f*
    - by pyrolysis, 146
  - ligand exchange, CdS-ZnS core-shell with MPTMO, 142*s*, 147, 148*f*
  - and PEVA nanofilms synthesis, 146, 148

Downloaded by 89.163.35.42 on June 21, 2012 | http://pubs.acs.org
Publication Date (Web): March 11, 2010 | doi: 10.1021/bk-2010-1034.ix002

- photoluminescence emission spectra of, 149*f*, 150, 151, 151*f*
- schematic diagram of experimental setup, 139*f*
- 2-step method using $scCO_2$, 142*s*, 148
- TEM images of, 150, 150*f*
- UV-Vis spectra of, 151, 151*f*, 152, 152*f*
- in polymer nanocomposite films for light selectivity, 137
- synthesis of, 146

Quantum mechanics. *See* First principles

Quinoid forms, stabilized
- incorporation to semiconducting polymers bandgap, 76
- poly(benzo[c]thiophene), 76, 76*f*
- poly(thieno[3,4-b]pyrazine), 76*f*
- poly(thieno[3,4-b]-thiophene), 76, 76*f*

**R**

Raman spectroscopy analysis, 104
- spectra of P3HT-*b*-PS/SWCNT and pristine SWCNTs, 105*f*

Reactivity ratios, of ethylene and VAc copolymerization, 145
- *versus* reaction temperature/pressure, 145, 146*f*

Reflectance
- hemispherical *versus* wavelength, 89, 91*f*
- weighted on different textured surfaces, 89, 91*t*

Regioregular poly(3-hexylthiophene)
- blended with PCBM, solar cell, 74
- as electron donor and molecular structure of, 56*f*

Relative crystallinity, of P3HT calculated from P3HT/$C_{60}$ WAXD curves, 129, 129*f*

Relative humidity, *versus* ionic conductivity of Nafion membranes, 181*f*, 182

Relative selectivity, of nanocomposites with PTA and ZrP, 166*f*, 167

**S**

Scanning electron microscopy analysis, 108
- cross-section images of Au layer assisted Si etching in $HF/H_2O_2$, 83*f*, 84, 84*f*, 86
- image of honeycomb structures formed from P3HT-*b*-PS/MWCNT dispersions, 108, 110*f*
- images of P3HT/$C_{60}$ films as function of time
  - in chloroform vapor treatment, 126, 127*f*, 132, 132*f*
  - in DCB vapor treatment, 127, 128*f*, 132, 132*f*

Selectivity, 183
- apparent
  - for HS30SIT/Nafion, 182*f*, 183
  - for MMT-$H^+$/Nafion, 182*f*, 183
  - for MMT-$Na^+$/Nafion, 182*f*, 183
  - for TEOS:SIT/Nafion, 182*f*, 183
- definition of, 183

Silane treatment on $SiO_2$-polymer interface, 14

Silica support, 196, 196*f*
- over metal nanoparticles, 193, 194*f*
  - total FERs with addition of, 199, 199*f*

Silicon dioxide-polymer interface system
- atomic model and dielectric constant, 15*f*
- dielectric permittivity, 13
- electron-phonon interactions, 18, 18*f*
- silane-treated and untreated, 14

Silicon dioxide-poly(vinyl acetate) nanocomposites, 143*f*, 144

Silicon surfaces
  etching, Au layer assisted in $HF/H_2O_2$
    contact angles and hysteresis *versus* etching time, 87, 88*f*
    etching time-depth relationship, 83*f*, 84
    SEM cross-section images of, 83*f*, 84
    surface morphology size scale images, 85*f*, 86, 86*f*
  images with Au layers of different thickness, 84*f*, 86
  for solar cell applications, 81
  two-scale structures in $HF/H_2O_2/H_2O$, 87
    contact angle and contact angle hysteresis of, 88, 90*f*
    Si pyramid surfaces and cross sections of, 88, 89*f*, 90*f*
Silver nanoparticles
  supported on silica
    TEM micrographs, 196, 197*f*
    XRD spectra of, 193, 194*f*
  TEM micrographs, 196, 196*f*
  total FERs with addition of, 198, 198*f*
Size-exclusion chromatography, results for P(VDF-CTFE)/P(VDF-CTFE)-g-PS copolymers, 28, 29*f*
Small angle X-ray scattering patterns/profiles
  of HS30SIT/Nafion and TEOS:SIT/Nafion membranes, 176
  of pure Nafion and MMT-$H^+$/Nafion, 174, 176*f*
  of P(VDF-CTFE)-g-PS, 28, 30*f*
Sodium montmorillonite/Nafion/water system
  apparent selectivity, 182*f*, 183
  cryo-TEM image of, 177, 179*f*
  DMA on, 179
  edge-to-face and face-to-face aggregation, schematic representation of, 177, 178*f*
  ionic conductivity as function of relative humidity, 181*f*, 182
  methanol permeability, 182
  phase diagram of, 177, 178*f*
  storage modulus as function of T, 179, 180*f*
Solar cells
  P3HT/$C_{60}$, power conversion efficiency as function of time, 131*f*, 132, 134*f*
  Silicon surfaces for applications of, 81
Space charge distribution, in PVDF and P(VDF-CTFE)-g-PS, 33, 34, 35*f*
Spheres-in-a-simple-cubic-lattice configurations
  ceramic-polymer composite
    stored energy
    at high saturation inclusion, 4, 6*f*
    at low saturation inclusion, 4, 5*f*
  of nonlinear inclusions
    finite difference simulations, 4, 5*f*
    schematic and geometry, 4, 5*f*
Storage modulus, of montmorillonites/Nafion, as function of T, 179, 180*f*
Supercritical carbon dioxide
  copolymerization of ethylene and Vac, 145
    reactivity ratios *versus* reaction temperature/pressure, 145, 146*f*
    in situ FTIR waterfall plot of, 144*f*, 145
  image before and after treatment to PEVA, 148, 148*f*
  polymer nanocomposites
    synthesis in, 144
  QD-PEVA nanofilms in, 2-step synthesis of, 142*s*, 148

**T**

Temperature dependency, of dielectric permittivity and loss tangent, 41*f*, 42, 47*f*, 48
TEOS:SIT/Nafion membranes, 175, 176
  apparent selectivity, 182*f*, 183

Downloaded by 89.163.35.42 on June 21, 2012 | http://pubs.acs.org
Publication Date (Web): March 11, 2010 | doi: 10.1021/bk-2010-1034.ix002

Downloaded by 89.163.35.42 on June 21, 2012 | http://pubs.acs.org
Publication Date (Web): March 11, 2010 | doi: 10.1021/bk-2010-1034.ix002

- ionic conductivity as function of relative humidity, 181*f*, 182
- methanol permeability, 182
- SAXS patterns/profiles of, 176
- TEM images of, 176

Tetrahydrofuran solvent, 101

Titanate-like nonlinear polymer-ceramic inclusions
- polarization curves for, 3, 4*f*
- SSCL configurations, 4, 5*f*

Titanium dioxide interfacial layer, 77

Toluene solvent, 101, 111, 113*f*

Transmission electron microscopy analysis, 101
- bare CdS QDs images, 146, 147*f*
- cross-sections of MMT-H$^+$/Nafion membranes images, 174, 175*f*
- dark field image of P3HT-*b*-PS/MWCNT, 102*f*
- higher resolution images
  - of homogenous coverage of CNT by P3HT-*b*-PAA, 110, 112*f*
  - of MWCNT/P3HT-*b*-PS thin layer and pristine MWCNT, 101, 101*f*
- HS30SIT/Nafion and TEOS:SIT/Nafion membranes images, 176
- micrographs images of, 196
  - Ag and Au nanoparticles, 196, 196*f*
  - Au supported on $SiO_2$ nanoparticles, 196, 197*f*
  - $SiO_2$ support, 196, 196*f*
- MMT-Na$^+$/Nafion hybrids cryo images, 177, 179*f*
- P3HT supramolecular structures on MWCNTs images, 113*f*, 114
- P3HT-*b*-PAA/MWCNT images, 110, 112*f*
- P3HT-*b*-PS/MWCNT, P3HT-*b*-PS/SWCNT images, 101, 101*f*
- P3HT/$C_{60}$ films in DCB and chloroform vapor treatments images, 128, 128*f*
- P(VDF-CTFE)-$BaTiO_3$ composites images, 40*f*, 41
- $SiO_2$-PVAc nanocomposites images, 143*f*, 144
- synthesized CdS-ZnS core-shell QDs images, 146, 147*f*, 150, 150*f*

Trap states. *See* Defects states

**U**

Ultrafast infrared spectroscopy, on OPV polymer blends free carrier formation, 53

UV-vis absorption spectroscopy analysis, 103
- spectra absorbance
  - of metal nanoparticles, 197, 197*t*
  - of pure P3HT-*b*-PS and P3HT-*b*-PS/SWCNT in chloroform, 103, 104*f*

**V**

Vinyl acetate, and ethylene copolymerization in $scCO_2$, 145
- reactivity ratios *versus* reaction temperature/pressure, 145, 146*f*
- in situ FTIR waterfall plot of, 144*f*, 145

**W**

Water self-diffusion coefficients in nanocomposite with PTA and ZRP, 165*f*, 166

Water uptake and conductivity in nanocomposite with PTA and ZRP, 162*f*, 163

Wave function, electronic, 14, 16

Wavelength *versus* hemispherical reflectance, 89, 91*f*

Downloaded by 89.163.35.42 on June 21, 2012 | http://pubs.acs.org
Publication Date (Web): March 11, 2010 | doi: 10.1021/bk-2010-1034.ix002

Wide-angle X-ray diffraction analysis, profiles/spectra/curves, 193
  of P3HT/$C_{60}$, 129, 129*f*
  of PVDF, 28, 30*f*
    biaxially oriented, 29, 31*f*
  of P(VDF-CTFE)-g-PS *graft*copolymer films, 28, 30*f*
    uniaxially oriented, 29, 31*f*
  of supported Ag, Au, Pt and Pd nanoparticles on silica, 193, 194*f*
  of supported Pt on $CeO_2$ particles, 193, 194, 195*f*
  of synthesized in-house $CeO_2$ nanoparticles, 193, 194, 195*f*
  of $TiO_2$ nanocomposites and P(VDF-CTFE-TrFE), 50, 51*f*

**Z**

Zirconium phosphate, effect on nanocomposites
  electro-osmotic drag coefficients as function of T, 164*f*, 165
  methanol permeability as function of T, 163, 164*f*
  water self-diffusion coefficients, 165*f*, 166, 167
  water uptake and conductivity, 162*f*, 163